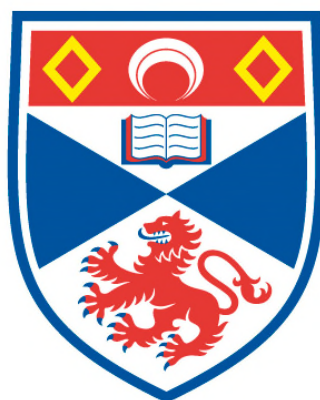


**TEMPLATING APPROACHES TO THE SYNTHESIS
OF NEW MICROPOROUS MATERIALS
FOR GAS ADSORPTION AND SEPARATION**

María Castro

**A Thesis Submitted for the Degree of PhD
at the
University of St Andrews**



2008

**Full metadata for this item is available in
St Andrews Research Repository
at:**

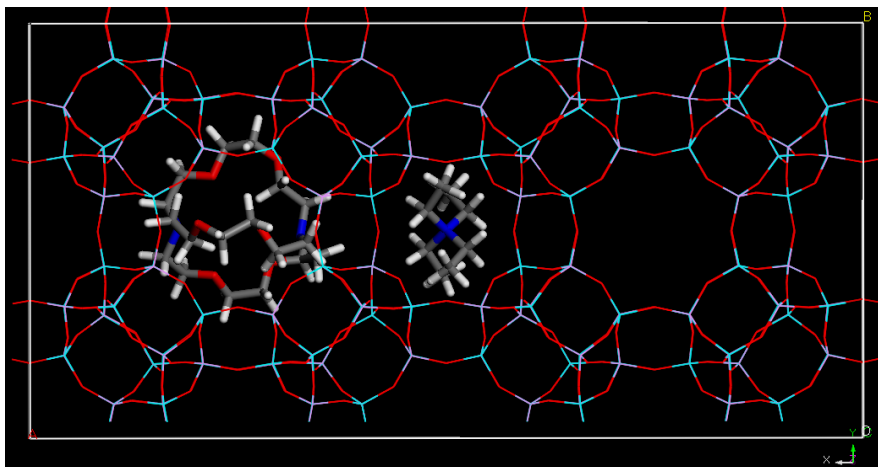
<http://research-repository.st-andrews.ac.uk/>

Please use this identifier to cite or link to this item:

<http://hdl.handle.net/10023/851>

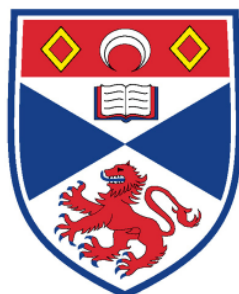
This item is protected by original copyright

Templating Approaches to the Synthesis of New Microporous Materials for Gas Adsorption and Separation



A thesis presented for the degree of
Doctor of Philosophy
in the Faculty of Science of the University of St Andrews
by María Castro

August 2008



University
of
St Andrews

Supervisor: Paul A. Wright

Declarations

I, María Castro, hereby certify that this thesis, which is approximately 48,000 words in length, has been written by me, that it is the record of work carried out by me and that it has not been submitted in any previous application for a higher degree. I was admitted as a research student in May 2005 and as a candidate for the degree of Doctor of Philosophy in 2006; the higher study for which this is a record was carried out in the University of St Andrews between 2005 and 2008.

In submitting this thesis to the University of St Andrews I understand that I wish access to it to be subject to the following conditions: for a period of one year from the date of submission, the thesis shall be withheld from use. I understand, however, that the title and abstract of the thesis will be published during this period of restricted access; and that after the expiry of this period, the thesis will be made available for use in concordance with the regulations of the University Library for the time being in force, subject to any copyright vested in the work not being affected thereby, that a copy of the work may be made available and supplied to any *bona fide* library or research worker, that my thesis will be electronically accessible for personal or research use, and that the library has the right to migrate my thesis into new electronics forms as required to ensure continued access to the thesis. I have obtained any third-party copyright permission that may be required in order to allow such access and migration.

María Castro (Candidate)

I hereby certify that the candidate has fulfilled the conditions of the Resolution and Regulations appropriate for the degree of Doctor of Philosophy in the University of St Andrews and that the candidate is qualified to submit this thesis in application for that degree.

Paul A. Wright (Supervisor)

Abstract

Structure direction in the synthesis of phosphate-based materials (aluminophosphates, AlPOs; magnesiumaluminophosphates, MgAPOs; silicoaluminophosphates, SAPOs; magnesiumsilicoaluminophosphates, MgAPSOs), has been investigated through co-templating synthesis studies supported by molecular modelling. These solids have been characterised by diffraction and solid-state NMR, and their properties in gas adsorption and catalysis have been measured.

The parameters in the hydrothermal synthesis of SAPO STA-7, St Andrews porous solid number 7, (SAV), in which the macrocycle 1,4,7,11-tetraazacyclotetradecane (cyclam) and tetraethylammonium (TEA) cations are used as co-templates, were investigated in detail. A new route involving a reversal of the mixing order of reagents leads to the formation of single crystals up to 50 μm with perfect tetragonal prismatic morphology that was not achieved via previous synthetic routes. For the first time in SAPO STA-7, X-ray diffraction locates the tetraethylammonium cation (TEA) in tg.tg. conformation. The synthesis and full characterisation of a novel aluminophosphate structure designated STA-14 (KFI) represents the first example of a designed synthesis of a zeotype. The synthesis route is based on a co-templating approach supported by molecular modelling to design the specific template for one of the two types of cages within the structure. The first, a larger type of cage, also present in AlPO-42 (LTA), is templated by the azaoxacryptand 4,7,13,16,21,41-diaza-1,10-bicyclo[8,8,8]-hexocosane ('Kryptofix 222', hereafter K222). The modelled co-template configuration, in this case TEA in the tt.tt configuration, was experimentally observed by X-ray diffraction. Modifying the gel chemistry leads to SAPO and MgAPSO STA-14, which display high pore volumes for N_2 adsorption, similar to those of STA-7 and SAPO-34 (CHA). Furthermore, during these synthetic studies, a novel fully tetrahedrally-coordinated magnesiumaluminophosphate layer phase has been prepared, with a structure of relevance to hypothetical VPI-5 (VFI) type extended structures.

Molecular modelling was also applied in another aluminophosphate-based material, that of STA-2 (SAT), to predict a template that could be prepared from inexpensive reagents. Existing routes required the use of expensive quinuclidine as a

precursor to the template 1,4-bisquinuclidinium butane. The template suggested by modelling, 1,4-diazabicyclo (2,2,2)octane butane ($\text{NC}_6\text{H}_{12}\text{N}^+-\text{C}_4\text{H}_8-\text{NC}_6\text{H}_{12}\text{N}$), labelled DABCO_C4, templated AlPO STA-2 successfully. Structure characterisation of the as-prepared form of AlPO STA-2 using X-ray synchrotron data suggest the formation of Al-OH-Al units to accommodate the positively-charged template within the neutral framework and a combination of ^{13}C , ^{14}N and ^{15}N NMR studies have been used to give further details of the template environment in the cages.

The gas adsorption behaviour of the stable materials STA-7, STA-14 and STA-2 was evaluated for CO_2 . High pressure adsorption (0 to 40 bars) on STA-7 and STA-14 shows similar behaviour due to their structural and chemical similarities. The total uptake of CO_2 for SAPO STA-7 is less than for the zeolite NaX (FAU) (3.4 and 5.2 mmol g^{-1} respectively at 373 K and 12 bars) but the usable capacity for pressure swing adsorption technology (PSA) between 1 to 20 bar for STA-7 is twice the value for NaX. The affinity of adsorption towards CO_2 and its low uptake at 1 bar made SAPO STA-7 a desirable sorbent for PSA. The zeotype affinity of adsorption for different probe gases is different, $\text{CO}_2 \gg \text{CH}_4 > \text{CO}$, to that for zeolite NaX $\text{CO}_2 \gg \text{CO} > \text{CH}_4$. Low pressure CO_2 adsorption (0 to 1 bar) in STA-7, STA-14 and STA-2 at temperatures between 273 and 303 K demonstrates that the topology and therefore the total free pore volume accessible to the gas molecules is the most important factor in determining the uptake in these solids, but that the composition and distribution of the silicon cations within the framework also has an important effect. For example at 273 K and 1 bar, the uptake of the STA-2 framework in the SAPO form is *ca.* 2wt% higher than in the AlPO form, but compared with SAPO STA-7, the uptake due to pore volume limitations is 10wt% lower under same conditions. In addition, the high quality of the SAPO STA-7 crystals obtained by the new route made them suitable in collaborations for the direct observation of diffusion of methanol by interference microscopy (IFM) and the study of their crystal growth by combined atomic force microscopy (AFM) and high resolution scanning electron microscopy (HRSEM). The catalytic applications of the STA-7 and STA-14 for the methanol-to-olefins reaction (MTO) and the argon adsorption at 87 K were also performed collaboratively. The results are reported and discussed here in the light of their structure and composition.

Publications arising from this work

- 1. Co-templating and modelling in the rational synthesis of zeolitic solids**, M. Castro, R. Garcia, S. J. Warrender, P. A. Wright*, P. A. Cox, A. Fecant, C. Mellot-Draznieks, N. Bats, *Chem. Commun.*, 2007, 3470.
- 2. A computational study of the stretching frequencies of Brønsted acid sites in SAPO STA-7: preliminary comparison with Infrared Spectroscopy**, I Déroche, G. Maurin*, P. Llewellyn, M. Castro, P. A. Wright, M. Bejblova, J. Cejka, *From Zeolites to Porous MOF Materials the 40th Anniversary of International Zeolite Conference*, R. Xu, Z. Gao, J. Chen, W. Yan (Eds.) 2007, Elsevier.
- 3. Silicon distribution in SAPO materials: A computational study of STA-7 combined with ²⁹Si MASNMR spectroscopy**, I Déroche, G. Maurin*, P. Llewellyn, M. Castro, P. A. Wright, *Microporous and Mesoporous Materials*, 2008, **107**, 268.
- 4. Adsorption of carbon dioxide in SAPO STA-7 and AlPO-18: Grand Canonical Monte Carlo simulations and microcalorimetry measurements**, I. Déroche, L. Gaberova, G. Maurin*, P. Llewellyn, M. Castro, P. A. Wright, *Adsorption*, 2008, **14**, 207.
- 5. Influence of the silicon content and chemical disorder of the SAPO STA-7 framework on the CO₂ adsorption mechanism: Grand Canonical Monte Carlo simulations combined to microcalorimetry measurements**, I. Déroche, L. Gaberova, G. Maurin*, M. Castro, P. A. Wright, P. Llewellyn, *J. Phys. Chem. C*, 2008, **112**, 5048.
- 6. Three dimensional diffusion in nanoporous host-guest materials monitored by interference spectroscopy**, L. Heinke, P. Kortunov, D. Tzoulaki, M. Castro, P. A. Wright, J. Kaerger*, *European Physics Letters*, 2008, **81**, 26002.
- 7. Nanometre resolution using high-resolution scanning electron microscopy corroborated by atomic force microscopy**, S.M. Stevens, P. Cubillas-Gonzalez, K. Jansson, O. Terasaki, M. W. Anderson*, P. A. Wright, M. Castro, *Chem. Comm.*, 2008, DOI: 10.1039/b80440f.

* Corresponding Author

Acknowledgments

I would like to thank my supervisor Dr. Paul Wright for giving me the opportunity to take part of this project, for his advice, enthusiasm and open mind to new ideas and discussion during all this time.

I must thank the assistance of: Prof. Alex Slawin for the single crystal data and pastoral advice, Ross Blackley for his help and training on the SEM-EDX, Mrs Sylvia Williamson for CO₂ adsorption at low pressures and thermal and elemental analysis, Durham University for solid-state NMR spectra and the secretarial team at the Chemistry Department of University of St Andrews for helping printing this thesis. I strongly appreciate the help and shared knowledge of all my colleagues and collaborators in and out the INDENS network; their effort have made possible this thesis.

Thanks to the members of PAW group, my sister and mother and my friends in and out St Andrews, especially Anne Schel, Gerard Sobany, Mayca Onega, Silvia Bravo, Diego Carnevale, Aga Kulczynska, David Miller, Tanja Eichelsheim, Arnald Grabulosa, and John Griffin, the new faces of WoMen Project, R2R, Yambria, Tecla's Editor and also my old friends, Amada Mendez, Marta Nieto, Jenny Ramos and Chris Law. Special thanks to the owner of my former flat and the letting office team 'Town and Gown'.

Last but not least, I thank my former boss Prof. Anthony Powell for giving me the opportunity to take part on his research and find out the fascinating world of the hydrothermal synthesis. This thesis has been sponsored by the EU with a Marie Curie Research Training Network Scholarship, many thanks to everyone that has made that possible specially Philip Llewellyn and Sergio di Virgilio, the INDENS coordinator and the EU commissioner, respectively. These acknowledgments warmly conclude including Marie Skłodowska, world wide known as Marie Curie who is an inspiration as researcher as well as human being.



*This thesis is dedicated to my mother,
Eva Castro.*

,

*'I have been writing for hours and I am happy because
I don't get tired nor do I get bored.'**

*Phrase of Juan Carlos Onetti from his first book called 'El Pozo', translation by Estrellita Plested.

Chapter Summary

| | |
|--|-----------|
| Introduction | PART 1 |
| <hr/> | |
| General Introduction | Chapter 1 |
| Literature Review | |
| Aims | |
| Techniques | Chapter 2 |
| Synthesis & Characterisation of Zeotypes | PART 2 |
| <hr/> | |
| STA-7: a double six ring zeotype | Chapter 3 |
| STA-14: a novel double six ring zeotype | Chapter 4 |
| Conclusions of the double six ring zeotypes | Chapter 5 |
| STA-2: a ABC zeotype | Chapter 6 |
| Applications of Zeotypes | PART 3 |
| <hr/> | |
| Adsorption of greenhouse gases at high and low pressures | Chapter 7 |
| Other Applications | |
| Summary & Further Work | Chapter 8 |

Contents

PART 1

Introduction to Microporous Materials & the Characterisation Techniques

| | |
|--|----|
| Synopsis | 1 |
| Chapter 1: Introduction | 2 |
| 1.1 General Introduction | 2 |
| 1.2 Introduction to Microporous Materials | 4 |
| 1.2.1 Zeolites | 4 |
| 1.2.2 Zeotypes | 6 |
| 1.2.3 Metal Organic Frameworks | 9 |
| 1.3 The Hydrothermal Synthesis | 10 |
| 1.4 The Role of Organic Molecules in the Hydrothermal Synthesis: the Concept of Templating | 14 |
| 1.4.1 Templating Effect of Organic Species in Zeotypes | 16 |
| 1.4.1.1 Alkyl Amines and Quaternary Ammonium Species | 16 |
| 1.4.1.2 Macrocycles, the ‘Co-Templating’ Effect and Gel Chemistry | 18 |
| 1.5 Molecular Modelling Applications | 19 |
| 1.6 Microporous Materials for CO ₂ Adsorption | 20 |
| 1.7 Overview of the Project and Aims | 21 |

Contents

PART 1

Introduction to Microporous Materials & the Characterisation Techniques

| | |
|--|----|
| Chapter 2: Techniques | 31 |
| 2.1 Introduction | 31 |
| 2.2 Basic Crystallography | 32 |
| 2.3 X-Ray Diffraction for the Bulk Structural Study | 34 |
| 2.3.1 X-Ray Sources | 35 |
| 2.3.2 Diffraction Phenomenon | 36 |
| 2.3.3 Solving a Crystal Structure by SXRD | 38 |
| 2.3.3.1 SXRD Experiment | 40 |
| 2.3.4 Solving a Structure from Powder Diffraction | 42 |
| 2.3.4.1 Rietveld Method for Structural Refinement | 44 |
| 2.3.4.2 PXRD Experiment | 46 |
| 2.4 Solid-State NMR Spectroscopy for the Study of Local Environments | 48 |
| 2.4.1 General Principles | 48 |
| 2.4.2 NMR in Solids | 50 |
| 2.4.3 NMR Experiments | 53 |
| 2.5 Adsorption | 57 |
| 2.6 Molecular Modelling | 63 |
| 2.7 Other Techniques | 66 |
| 2.7.1 FTIR | 66 |
| 2.7.2 SEM and EDX | 67 |
| 2.7.3 TGA | 70 |
| 2.7.4 Elemental Analysis | 71 |

Contents

PART 2

Synthesis & Structural Characterisation of Zeotypes

| | |
|--|-----|
| Synopsis | 76 |
| Chapter 3: STA-7 | 77 |
| 3.1 Introduction | 77 |
| 3.2 Experimental | 79 |
| 3.3 Results & Discussion | 84 |
| 3.3.1 Synthesis | 84 |
| 3.3.1.1 Checking Previous Synthetic Method | 84 |
| 3.3.1.2 Modifying the Synthesis Procedure | 87 |
| 3.3.1.3 Concerning Industrial Conditions (Static vs. Stirring) | 90 |
| 3.3.1.4 Variation of Framework Chemistry via Synthesis | 93 |
| 3.3.1.5 Summary | 100 |
| 3.3.2 Characterisation of As-Prepared Materials | 102 |
| 3.3.2.1 SXRD and Modelling on SAPO(20) STA-7 | 102 |
| 3.3.2.2. MAS NMR on STA-7 MgAPOs | 110 |
| 3.3.2.3 MAS NMR on STA-7 SAPOs | 112 |
| 3.3.3 Characterisation of Calcined Materials | 118 |
| 3.3.3.1 Characterisation of Calcined SAPO(20)STA-7 Material | 118 |
| 3.3.3.2 Porosity of Related STA-7 Materials | 125 |
| 3.4 Summary | 131 |

Contents

PART 2

Synthesis & Structural Characterisation of Zeotypes

| | |
|--|-----|
| Chapter 4: STA-14 | 135 |
| 4.1 Introduction | 135 |
| 4.2 Experimental | 137 |
| 4.3 Results & Discussion | 141 |
| 4.3.1 Modelling | 141 |
| 4.3.2 Synthesis | 142 |
| 4.3.2.1 Co-Template Screening in MgAPO Composition, from Hypothesis to Experiment | 142 |
| 4.3.2.2 Preparation of MgAPOs with Different Mg/P Ratios in the Gel | 147 |
| 4.3.2.3 Variation of Framework Chemistry | 149 |
| 4.3.2.4 The Morphology of SAPO STA-14 | 154 |
| 4.3.3 Characterisation of As-Prepared Materials | 158 |
| 4.3.3.1 SXRD and Modelling in MgAPO and SAPO STA-14 | 158 |
| 4.3.3.2 MAS NMR on STA-14 MgAPOs | 159 |
| 4.3.3.3 MAS NMR on STA-14 SAPOs | 163 |
| 4.3.4 Characterisation of Calcined Materials | 164 |
| 4.3.4.1 Calcined SAPO STA-14 | 164 |
| 4.3.4.2 Calcined MgAPOs STA-14 | 168 |
| 4.3.4.3 Porosity of STA-14 Materials | 169 |
| 4.4 Summary & Conclusions | 170 |

Contents

PART 2

Synthesis & Structural Characterisation of Zeotypes

| | |
|--|---------|
| Chapter 5: D6R Family Conclusions | 172 |
| 5.1. Introduction | 172 |
| 5.2. Synthetic Results from Chapter 3 and 4: the D6R Family | 173 |
| 5.3 Exploring the D6R Hypothesis: Crystal Growth in SAPO STA-7 | 177 |
| 5.4 Further Work | 183 |
| 5.4.1 Exploratory Synthesis Using the Templates of STA-7 and STA-14: Cyclam/K222/TEA | 183 |
| 5.4.2 Exploration of the Use of Three Templates; the K222/Co-Base/‘Large Template’ System in MgAPO gel; A Novel Layer Phase | 184 |
| 5.4.2.1 Modelling Results | 186 |
| 5.4.2.2 Synthesis Results | 187 |
| 5.4.2.3 SXRD of Novel Phase | 188 |
| 5.5 Conclusions | 192 |
| Chapter 6: STA-2 | 195 |
| 6.1 Introduction | 195 |
| 6.2 Experimental | 198 |
| 6.3 Results & Discussion | 204 |
| 6.3.1 Modelling | 204 |
| 6.3.2 Synthesis | 209 |
| 6.3.3 Characterisation of As-Prepared AlPO STA-2 | 214 |
| 6.3.4 Characterisation of As-Prepared SAPO STA-2 | 227 |
| 6.3.5 Porosity of STA-2 Materials | 229 |
| 6.4 Summary & Further Work | 230 |

Contents

PART 3

Adsorption Performance & other Applications of Zeotypes

| | |
|---|-----|
| Synopsis | 234 |
| Chapter 7: Applications | 235 |
| 7.1 Adsorption of Greenhouse Gases at High Pressures | 235 |
| 7.1.1 Introduction | 235 |
| 7.1.2 Experimental | 237 |
| 7.1.3 Results & Discussion | 239 |
| 7.1.3.1 CO ₂ Adsorption on SAPO STA-7 Compared with that on a Zeolite (NaX) | 239 |
| 7.1.3.2 CO ₂ Adsorption on D6R Polytypes (SAV, KFI and CHA) in SAPO Form | 240 |
| 7.1.3.3 The Polarity of the Gas Influences Adsorption in a SAPO Framework: the Basis for Gas Mixture Separation | 243 |
| 7.1.3.4 Comparison of Different Families of Materials for their Application in CO ₂ Adsorption and Separation | 246 |
| 7.1.4 Conclusions | 247 |
| 7.2 CO ₂ Adsorption at Low Pressures (0 -1 bar) | 247 |
| 7.2.1 Introduction | 247 |
| 7.2.2 Experimental | 248 |
| 7.2.3 Results & Discussion | 249 |
| 7.2.3.1 CO ₂ Adsorption on AlPO and SAPO STA-2 | 249 |
| 7.2.3.2 CO ₂ Adsorption on SAPO STA-7 with Different Silicon Distribution | 250 |
| 7.2.3.3 Heats of Adsorption | 251 |
| 7.2.4 Conclusions | 254 |

Contents

PART 3

Adsorption Performance & other Applications of Zeotypes

Chapter 7 (Continuation)

| | |
|---|-----|
| 7.3 Other Applications of Zeotypes | 255 |
| 7.3.1 Argon Adsorption as a Method to Give Details of Pore Structure Unresolved by N ₂ Adsorption | 255 |
| 7.3.2 Direct Observation of the Diffusion of Methanol in a Single Crystal of SAPO STA-7 by Interference Optical Microscopy (IFM) | 258 |
| 7.3.3 Catalysis: the Conversion of Methanol to Olefins (MTO) | 262 |
| Chapter 8: Summary & Further Work | 272 |

APPENDIX

| | |
|---|-----|
| Appendix A: Single X-Ray Data | 277 |
| Appendix B: Rietveld Refinement Data | 295 |
| Appendix C: Deconvoluted Intensities of MAS NMR Spectra | 303 |
| Appendix D: Experimental Conditions for Applications Described in Section 7.3 | 304 |

CD

Attached CD with the CIF files of SAPO STA-7 and MgAPO STA-14 and the Modelled Coordinates of Cyclam in SAPO STA-7.

List of Abbreviations

| | |
|-----------------------------|--|
| <i>a</i> | unit cell parameter |
| AFM | atomic force microscopy |
| <i>b</i> | unit cell parameter |
| <i>c</i> | unit cell parameter |
| CHN | elemental analysis for carbon, hydrogen and nitrogen |
| CIF | crystallographic information file |
| CP | cross polarization |
| DABCO | 1,4-diazabicyclo(2,2,2) octane |
| DABCO_ <i>C_n</i> | 1- <i>n</i> -diazabicyclooctane alkane |
| DEA | diethylamine |
| DIPA | di-isopropylamine |
| DIPEA | di-isopropylethylamine |
| DMA | dimethylamine |
| <i>D_nR</i> | double <i>n</i> -membered ring |
| DP | direct polarization |
| DPA | di- <i>n</i> -propylamine |
| EDX | energy dispersive X-ray analysis |
| ESRF | European Synchrotron Radiation Facility |
| GSAS | General Structure Analysis System |
| HRSEM | high resolution scanning electron microscopy |
| ICP | inductively coupled plasma (elemental analysis) |
| IFM | interference optical microscopy (diffusion) |
| IFP-Lyon | Institute Français du Pétrole Lyon |
| IGA | intelligent gravimetric analysis (adsorption) |
| IZA | International Zeolite Association |
| K222 | kryptofix |
| MAS | magic angle spinning |
| MAPO | metal aluminophosphate |
| MQ | multiple quantum |
| MTO | methanol-to-olefines reaction (catalysis) |

| | |
|------------------|---|
| <i>n</i> MR | <i>n</i> -membered ring |
| NMR | nuclear magnetic resonance |
| PIP | piperazine |
| PSA | pressure swing adsorption |
| PYR | pyridine |
| PXRD | powder X-ray diffraction |
| R _{int} | goodness of fit value |
| R _p | goodness of fit value |
| R _{wp} | goodness of fit value |
| SAPO | silicoaluminophosphate |
| SDA | structure directing agent |
| SEM | scanning electron microscopy |
| STA- <i>n</i> | St Andrews material number <i>n</i> |
| SXRD | single X-ray diffraction |
| T | atom occupying tetrahedral sites in a zeolitic material |
| TEA | tetraethylammonium cation |
| TEAOH | tetraethylammonium hydroxide |
| TMA | tetramethylammonium cation |
| TMcyclam | tetramethyl cyclam |
| TPA | tetrapropylammonium cation |
| Uiso | isotropic thermal parameter |
| XRD | X-ray diffraction |

PART 1 Introduction to Microporous Materials & the Characterisation Techniques

Introduction

- **General Introduction**
 - **Literature Review**
 - **Aims**

Techniques

Synopsis

This section introduces the fundamentals of microporous materials, their structure, composition and an updated review. It includes the aims of this thesis, which are the synthesis and structure characterisation of such materials for gas adsorption and separation. The main characteristic of these materials, from which many of their applications derive, is their regular structure, and therefore this section concludes with a description of the characterisation techniques for their structural study.

Microporous materials are interesting for industrial applications and academic investigation due to their complexity and crystallinity. The method of synthesis, ‘hydrothermal’, is dependent on many variables and is based principally on ‘trial and error’ approaches. Experimentally it is observed that the use of organic molecules in the synthesis of these materials leads to some control on the final product structures. Modelling has been applied to study this interaction.

These two ideas, the use of organic molecules in the synthesis and the application of modelling to elucidate them are the basis for the research developed in this thesis.

Chapter 1: Introduction

1.1 General Introduction

Current global energy needs are obtained by burning fossil fuels. The combustion of coal, oil or natural gas produces carbon dioxide (CO_2). Since the beginning of the Industrial Revolution the concentration of CO_2 in the atmosphere has increased by about 100 ppm* (i.e., from 280 ppm in 1850 to 385 ppm in 2008) see figure 1.1.¹ As a result, CO_2 is the major greenhouse gas affecting the Earth's climate via the greenhouse effect.²

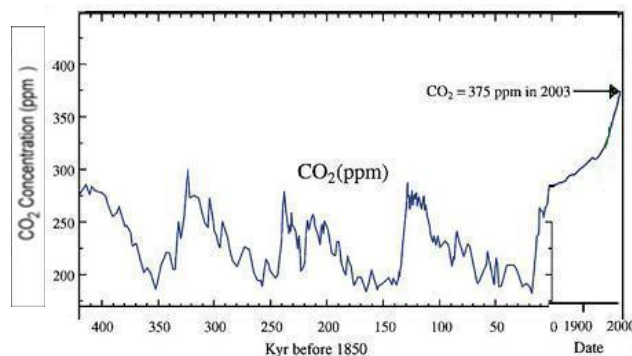


Fig. 1.1 Variation of the CO_2 concentration with the Earth history until present, adapted from reference 3.

* ppm is the abbreviation for parts per million.

CO₂ and other greenhouse gases are subjects of the Kyoto Protocol, which entered into force in 2005. The objective is the "stabilisation of greenhouse gas concentrations in the atmosphere at a level that would prevent dangerous anthropogenic interference with the climate system."⁴

In order to continue the use of fossil fuels as an energy source without harmful climate consequences, investment is required into research regarding the capture and storage of CO₂ produced. One of the options likely to be the cheapest to reduce CO₂ emissions is the Carbon Capture and Storage (CCS) method, which is a suite of technical and chemical processes that allows CO₂ to be separated, liquefied and stored. A problem common to all CCS plants is the expense and energy cost of CO₂ separation. However, the method of Pressure Swing Adsorption (PSA) can reduce the energy cost. This technique relies on switching between high and low pressure to selectively adsorb and desorb CO₂ on a molecular sieve, such as a zeolite.⁵

Zeolites are also used worldwide as catalysts for the refining of fuels and as catalysts for commodity chemicals synthesis and selective oxidation, where their activity can be classified as 'green' chemistry.⁶

The use of zeolites as molecular sieves is of particular interest to the solid state chemist due to their crystalline structure, in contrast with other porous materials such as carbon adsorbents that are amorphous. Their well defined structure enables us to understand and subsequently tailor their interaction with gas, crude oil or other chemical molecules of interest, such as methanol. Zeolites do occur as natural deposits but most of the research is focused on synthetic materials developed by public research institutions and private sector companies (Union Carbide, ExxonMobil, Chevron, IFP-Lyon...). As a result of such experimental research, it is possible to modify the structure and composition of the zeolites and to produce related materials optimised for specific industrial and environmental requirements. Following this approach, many novel zeolites, zeotypes and new families of hybrid organic-inorganic materials such as the metal organic frameworks (MOFs) have been developed.

The synthesis of these materials typically uses the hydrothermal method, which is based on an exploratory ‘trial and error’ approach. There has been slow progress in fully understanding all the aspects of the formation of these materials. Thus, more research is required to control the synthesis and optimise the materials.

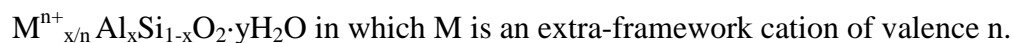
1.2 Introduction to Microporous Materials

Microporous materials (pores smaller than 20 Å) have both a huge industrial importance because of their many applications, and also an important scientific interest because of their structural complexity and diverse chemistry. The traditional applications are: ion exchange, gas separation and catalysis.^{7,8,9} However, the variety of new material compositions, particularly including organic-inorganic hybrids, promises to produce new applications such as hydrogen storage.¹⁰ The unique properties of molecular sieves arise from the uniformity of their pore size and shape that are in the order of molecular dimensions. This allows them to recognize, discriminate and organize molecules with a precision that can be better than 0.1 Å.¹¹

There is intense current activity in the synthesis of new materials. This focuses on two aspects: (i) the synthesis of new materials, giving new architectures or materials of the same architecture but different composition (often possessing different properties)¹² and (ii) the building up of an understanding of the synthesis process. In order to put the new materials into context, a summary of the different structure types of microporous solids is given below, emphasising zeotype materials.

1.2.1 Zeolites

A zeolite is a microporous aluminosilicate with a three-dimensionally connected framework of corner-sharing AlO_4 and SiO_4 tetrahedra, with the general formula:



The main characteristic of zeolites is their regular open framework, which contains channels and cavities of molecular dimensions (*ca.* 3-15 Å).¹³ The resultant molecular sieving property combined with, if appropriate, their strong acidity leads to a huge variety of applications in: (i) selective separation processes and (ii) catalysis.⁵

The substitution of Si(IV) by Al(III) imparts negative charge to the framework that is balanced by inorganic or organic cations in extraframework positions (see section 1.4). The quantity of cations required is proportional to the number of the aluminium atoms in the framework. By altering the composition it is possible to change their character from hydrophobic (high silica zeolites) to hydrophilic (aluminium-rich zeolites) and the incorporation of aluminium also enables the introduction of acid sites (Brønsted sites).

Zeolites are among the most important heterogeneous acid catalysts used in industry. The catalytic cracking of crude oil to yield fuels (gasoline) and other petrochemical feedstocks is carried out worldwide using zeolite catalysts such as zeolite Y (FAU) and ZSM-5 (MFI). The use of aluminosilicate zeolites is limited to some extent by the pore sizes available which are usually formed by a maximum of 12-membered rings (12MRs), where the pore is defined by 12 cations in tetrahedral positions linked to each other by oxygen atoms, like in the case of zeolite Y (FAU) with free diameters of 7-8 Å (Fig. 1.2).¹⁴ Recently, however, novel silicate zeolites have broken this limitation, such as the case of ITQ-33 which possess 18MRs.¹⁵

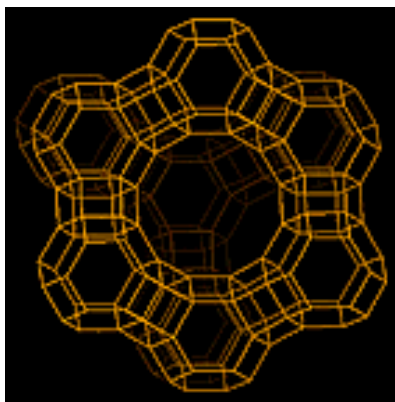


Fig. 1.2 The framework of zeolite Y or Faujasite (FAU), vertices represent the tetrahedrally coordinated (T) cations and lines represent T-O-T linkages.

1.2.2 Zeotypes

Aluminophosphates were reported in 1982 by Flanigen *et al.*¹⁶ at Union Carbide as the first family of framework oxide molecular sieves without silica. Aluminophosphates (AIPO-*n*, where *n* refers to a specific structure) are zeolite-like materials (zeotypes) with a neutral framework obtained from the connections of Al(III) and P(V) oxide tetrahedra in strict alternation (Al/P = 1, known as Flanigen's rule), see figure 1.3. The AIPO framework is the “3-5” analogue of the “4-4” pure SiO₂ (silicalite). In contrast with silicalite which shows hydrophobic behaviour, AIPOs are moderately hydrophilic due to the difference in electronegativity between aluminium (1.5) and phosphorus (2.1).

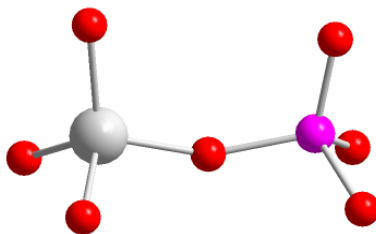


Fig. 1.3 AIPOs are made up of alternating corner-sharing AlO_4 and PO_4 tetrahedra (Al in grey, P in purple and O in red).

Many of their structures do not have analogues among zeolites due to the difficulty of forming Al-O-Al or P-O-P bonds, so only frameworks built up by even-numbered rings are formed. However an example of a zeotype material where the framework contains three-member rings has been reported: the SAPO ECR-40,¹⁷ which is analogous to the zeolite ZSM-18 (MEI) is able to take up this arrangement because it possesses Al-O-Al bonds.

They are several examples of AIPOs that have been obtained with zeolitic structures, such as AIPO-17 (ERI), AIPO-20 (SOD) and AIPO-24 (ANA). In contrast, other AIPOs were first obtained as AIPOs and afterwards obtained as silicate zeolites: examples include AIPO-5¹⁸ (AFI) and AIPO-36 (ATS), both with one-dimensional pores bounded by 12-member ring windows, which have been prepared as the silicates SSZ-24¹⁹ and SSZ-55,²⁰ respectively. Other AIPO structures are without zeolitic analogues and give novel structures with windows larger than 12-member rings, as in the case of the

remarkable VPI-5²¹ (VFI), an extra-large pore molecular sieve with 18-member ring channels with free diameters of 12.7 Å. Figure 1.4 shows the structures of AIPO-20, AIPO-5 and VPI-5. The first one is build up by stacking of sodalite cages, the second and the third possess one-dimensional channels bounded by 12 and 18-membered rings and free diameter of 7.3 Å and 12.7 Å, respectively.

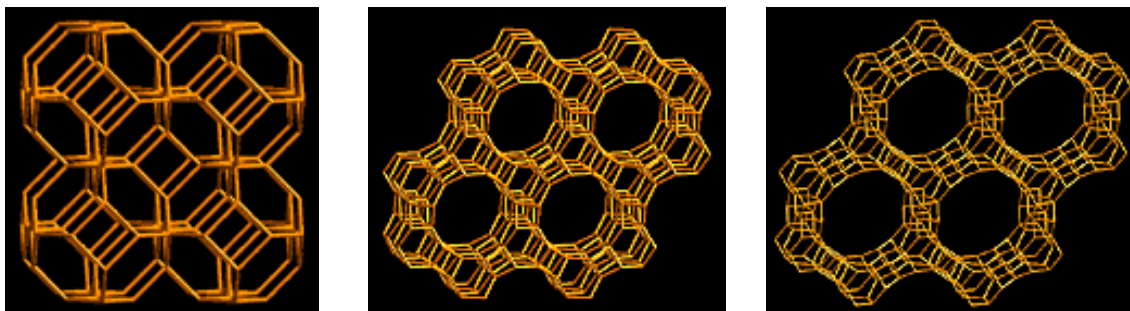


Fig. 1.4 Examples of AlPO framework, from the left to the right: AIPO-20 (SOD) along [001], AIPO-5 (AFI) along [001] and VPI-5 along [001].

Although the discovery of large pore structures offered catalytic promise, AlPOs are easily hydrolysed at high temperatures in the presence of steam, probably because framework aluminium tends to coordinate hydroxyl groups and water and ultimately Al-O-P bond cleavage occurs.²²

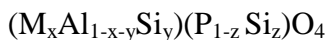
Following the discovery of AlPOs, other related classes of materials such as SAPOs²³, MAPOs^{24,25} and MAPSOs²⁶ were rapidly discovered where the addition of other elements (S = Si, M = Metal) into the reaction gel results in them being incorporated into the framework much more easily than in the case of zeolites due to the more ionic character of the AlPOs and also because the synthesis conditions (pH = 7) allow the solubility of these metal cations. The substitution can take place either for aluminium to form MAPOs or at phosphorus sites to give SAPOs. When substitution occurs in both, MAPSO materials are formed. Phosphorus, although mainly substituted by silicon, can also be replaced by titanium and vanadium.²⁷

Once calcined under oxygen, MAPO materials can be redox catalysts if they accommodate transition metals (Me = Fe, Mn, Co) into the framework. These can

undergo oxidation and reduction while remaining in framework positions.²⁸ In the specific case of MgAPOs, where Mg (II) does not have redox behaviour, the calcination under oxygen results in the formation of bridging hydroxyl groups or Lewis acid sites to balance the negative charge of the framework. Generally MgAPO applications are hindered by the loss of crystallinity upon calcination and subsequent exposure to moist air since the aluminium sites are partially hydrolysed.²⁹

In the case of SAPOs, the replacement of phosphorus by silicon gives robustness to the structures and, once calcined, Brønsted acid sites are formed to balance the negative charge of the framework.³⁰ Therefore such materials have interesting applications in industry. For example SAPO-34 (CHA) is a promising catalyst for the conversion of methanol to petrochemical products (Chapter 7). The incorporation of silicon into the AlPO framework can occur through two mechanisms, one by replacing isolated phosphorus sites Si(4Al) and the other by replacing both aluminium and phosphorus in the framework to form aluminosilicate or silica ‘islands’ Si(4Si).³¹

The general formula for substituted AlPOs obeying Flanigen’s rule is:



These materials are synthesised in the presence of amines or quaternary alkylammonium ions and many AlPOs have MAPO or SAPO analogues. For example AlPO-5 (AFI) is also obtained as MgAPO-5 or SAPO-5, but that is not always the case. Section 1.4 explains the role of the organic species and the importance of the gel composition in synthesis in more detail.

1.2.3 Metal Organic Frameworks

The most recent addition to the families of microporous solids are the metal-organic frameworks (MOFs).³² These are formed using organic linkers that connect metal clusters to give a rigid structure. Due to their organic nature they cannot compete in stability with the conventional inorganic zeolites, but their novel properties of large pores sizes, high apparent surface areas, selective uptake of small molecules and optical or magnetic responses to the inclusion of guests³³ make MOFs among the most interesting novel materials to study.

While in zeolites the access to the pores is strongly limited by the dimensions of the window rather than the size of the cavities themselves, some of the metal-organic frameworks with permanent porosity can admit considerably ‘over-sized’ guests because the windows can open to allow the guest access and then close to adsorb it into the cavity (Fig. 1.5).³⁴

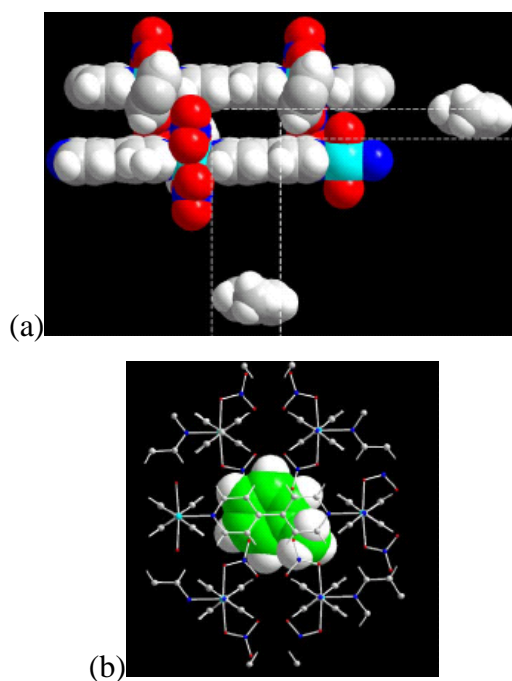


Fig. 1.5 The nickel bipyridyl nitrate framework $\text{Ni}_2(4,4'\text{-bipy})_3(\text{NO}_3)_4$ adsorbs toluene despite the pore windows being too small in a rigid model (a). That is possible because the framework flexibility allows accommodation of the toluene guest as shown by the simulation (b), representation from reference 34 and 35.

1.3 Hydrothermal Synthesis

Microporous materials are almost exclusively synthesised under hydrothermal conditions at temperatures between 100 °C and 220 °C under autogenous pressure in polytetrafluoroethylene (PTFE)-lined acid digestion bombs also called autoclaves (Fig. 1.6), under either strongly basic conditions (for zeolites), or weakly acidic or neutral conditions (for zeotypes and derivatives).³⁵ This method is very versatile and can be used not only for microporous materials but also for the synthesis of other solid-state materials such as chalcogenides.³⁶

The success of this method resides in the effective solvating ability of water under these conditions. That allows the dissolution and mixing of the solid reagents to form a homogeneous gel in the initial stage of the reaction.

The hydrothermal synthesis is very complex and involves a multiphase reaction-crystallization process, having at least one liquid phase and both amorphous and crystalline solid phases. Under these conditions it is possible to obtain thermodynamically metastable materials. For this reason, understanding of the process remains at an empirical stage.⁷

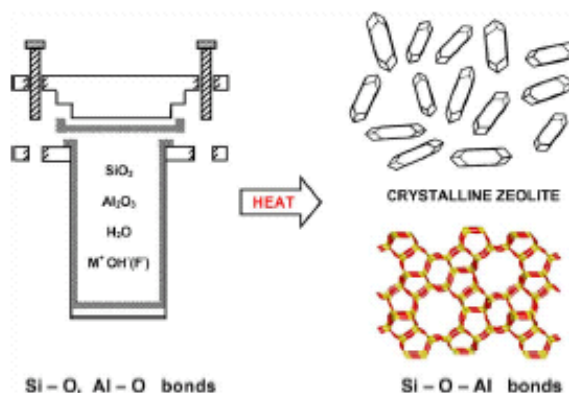


Fig. 1.6 Hydrothermal zeolite synthesis takes place in digestion bombs, also called autoclaves. The starting materials (Si-O and Al-O bonds) are converted by an aqueous mineralising medium (OH and/or F) into the crystalline product (Si-O-Al bonds) whose microporosity is defined by the crystal structure. Diagram from reference 37.

Typical variables include time, temperature, gel chemistry and pH. In general, the variation of any one of these parameters can affect several others.³⁵

Zeolites are metastable phases with respect to denser silicates and quartz. More thermodynamically unstable but kinetically-favoured phases may be formed initially and with time may evolve to more stable and denser phases. This is known as Ostwald's rule of successive transformations.³⁵

The increase of temperature increases reaction rates but can also lead to dense phase formation because it increases the autogenous pressure of water and could also affect the degree of the hydration of the extra framework cations.³⁸

The gel chemistry such as the reactant source, composition ratios and even the order of mixing are important variables that can influence the final product.³⁹ Also, when the chemical composition of the solid product is different from the initial ratios of the starting materials in the reaction, which is usually the case, the synthesis is generally inhomogeneous.³⁵

The value of pH affects the solubility of the gel components. It is necessary to dissolve the reactants in order to transfer them into the growing crystal. The use of mineralisers helps to dissolve the solid reactants and control the optimum pH. Hydroxyl ions are the mineraliser at alkali pH.⁴⁰ Fluoride ion can also act as mineraliser, typically in neutral and acidic pH.⁴¹ In addition, structure directing agents (SDAs) must be present in the gel to stabilise the open frameworks structure to favour their formation against denser phases of the same composition. These SDAs can be solvated metal or organic cations and therefore their addition to the gel influences the final pH. The role of the organic molecules as SDAs in the molecular sieve synthesis will be presented in detail (section 1.4).

In the case of organic-inorganic hybrids, where the organic moieties are part of the framework, the solvothermal method, where an organic solvent is used instead of water, is also important.

There are two mechanisms proposed for hydrothermal synthesis:

- Solid-phase transportation mechanism, where the solid hydrogel reorganizes to form the structure. The composition of the reactants matches the final product. When the initial composition of reactants is treated under hydrothermal or even dried slowly, crystallization occurs. This is illustrated in figure 1.7 a. An example is reported by Xu *et al.*⁴² in the synthesis of ZSM-35 (FER) and ZSM-5 (MFI) from non-aqueous reaction mixtures.
- Solution-mediated transport mechanism which involves the diffusion of the species from liquid phase to the nucleation centre. The nucleation occurs in the solution, allowing complete freedom of motion of the crystallising units. This is illustrated in figure 1.7 b. An example of this process is reported by Ueda *et al.*⁴³ for zeolites Y (FAU), S (GME) and P (GSI).

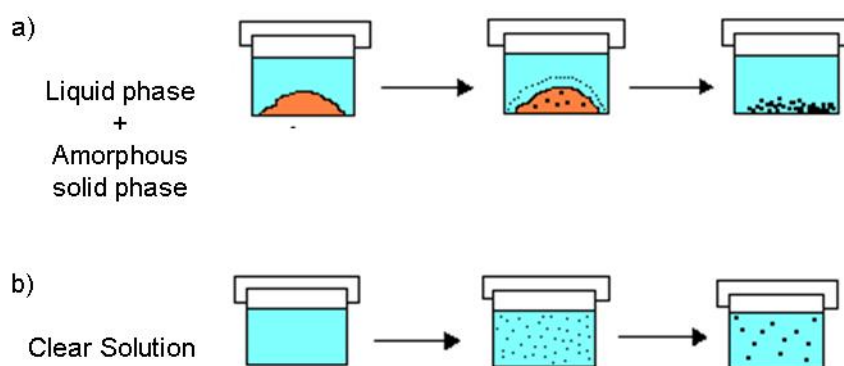


Fig. 1.7 Scheme of the two synthesis mechanisms, (a) the solid phase and (b) the solution-mediated. Adapted from Fig. 3 of reference 11.

It has been suggested that an equilibrium exists between the solid gel and the liquid phase as reported by Mintova *et al.* for zeolite A (FAU).⁴⁴ This equilibrium shifts toward the

solution when nucleation occurs, thus the gel is always dissolving in the solution, providing the constant supply of units for the crystal formation. This suggestion accommodates the hypothesis that secondary building units (SBU) are formed from the combination of primary building units, which can randomly move in suspension until they find a suitable place to crystallise.

This multi-component process is of fundamental interest and under exhaustive study using modelling and *in-situ* techniques such as X-ray diffraction and Raman spectroscopy.⁴⁵ In general the process can be ordered into three stages summarised in the following graph (Fig. 1.8):

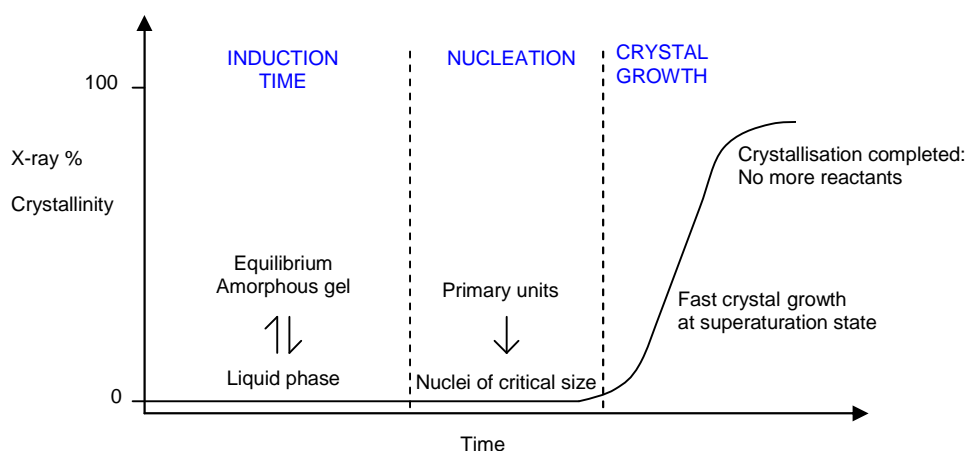


Fig. 1.8 General hydrothermal crystallisation: starting from a completely amorphous gel to slowly increase the ordering (induction time) to form the nuclei with optimum size at supersaturation conditions (nucleation) and concluding with crystal growth. Adapted from reference 46.

Crystallisation occurs when the solution reaches supersaturation, but it requires nuclei of sufficient size. The initial nuclei will be unstable, so most of them will dissolve again, but some of them may persist under these conditions. When these particles reach a critical size the crystal growth occurs by incorporating species from solution to certain preferred crystal faces. The final morphology of the crystal will reflect the growth rate at the various faces, i.e. in a needle-like crystal, growth is faster on the faces with smaller area perpendicular to the needle axis.

1.4 The Role of Organic Molecules in the Hydrothermal Synthesis: the Concept of Templating

The organic molecules in the hydrothermal synthesis are not simple pH regulators. They also direct the formation of the open framework structures with respect to dense phases via non-bonding interactions, as shown by Petrovic *et al.*⁴⁷ In some cases a close relationship exists between the structure and the organic moiety, with a strong non-bonding interaction.

The charge and size of the organic molecule strongly influences the structure and the composition. In the case of the zeolite ZK-4⁴⁸ (LTA), where tetramethylammonium cation (TMA) added into the synthesis remains occluded in the sodalite cage,⁴⁹ this must occur during synthesis since the organic cations are too large to be incorporated after crystallisation. It is said that these organic cations act as structure directing agents (SDAs) arranging the gel species around themselves to crystallise the framework. The term ‘template’ is therefore commonly used to indicate this.

The crystallisation process is very complex making it difficult to define precisely what ‘template’ means. It can be that one template forms many different structures, for example TMA forms 17 structures, or many different templates can lead to the formation of one single structure, as in the case of ZSM-5.⁵⁰ Davis *et al.* distinguish three possible roles for the organic guest molecules:⁵¹

- Space fillers, acting only to exclude water from the pores and helping to stabilise the growing framework. That is the case in the synthesis of zeolite ZSM-5 which can be achieved in the presence of numerous organic cations, where the organics are acting only as space fillers.
- Structure direction agents leading to a preferred structure via a combination of other gel parameters.
- True templates direct the framework to adopt a unique symmetry and geometry. As an example, the zeolite ZSM-18 (MEI) is templated by the triquatarnary

octahydrohexamethyl benzotripyrrolium cation. Modelling (section 1.5) shows a very close fit between the cage and the organic molecule and energy minimisation indicates that the template is unable to rotate in the cage which has the same threefold symmetry as the tri-quat (Fig. 1.9).⁵²

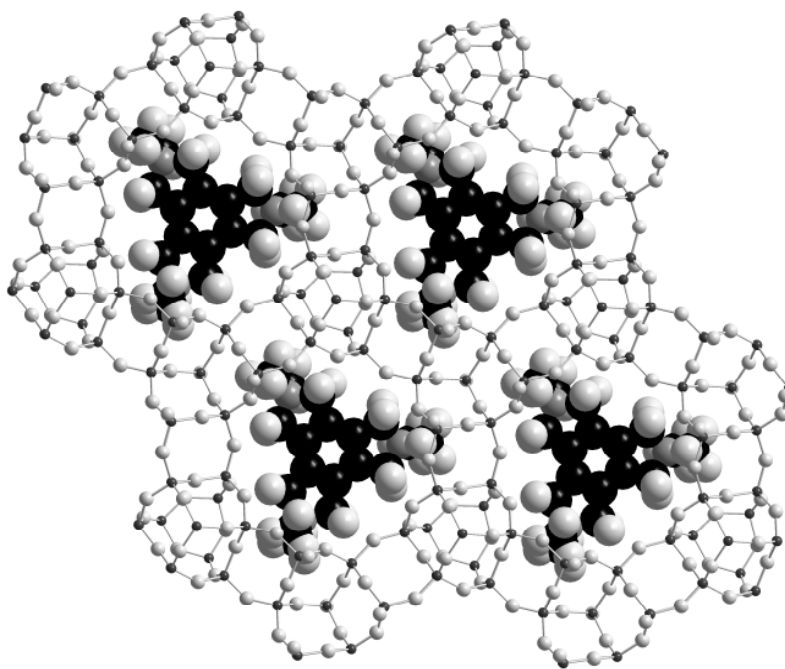


Fig. 1.9 The example of true template for ZSM-18 and the organic molecule tripyrrolium triquat $[(C_4H_4N(CH_3)_2)_3]^{3+}$, (courtesy of P. A. Wright).

Tetramethylammonium (TMA) was the first organic cation introduced in a zeolite synthesis in the 1960s by Barrer and Denny and the group of Kerr and Kokotailo.^{53,54} Since then, a wide range of quaternary ammonium ions, amines and cationic complexes has been applied in all kind of zeolite and zeotype synthesis, and is the most effective way to obtain new materials.

Normally these organic species are investigated experimentally by ‘trial and error’ and to determine their effectiveness as structure directing agents (SDAs). The flexibility of the organic species seems to be one factor that enables the formation of more than one product as the experimental conditions change (from the results of this thesis, for example, the tetraethylammonium cation (TEA) shows two distinct conformations when

templating two different types of cages, Chapter 3 and 4). Lok *et al.* showed the necessity of working in the correct gel chemistry to observe the action of the SDA (this thesis present our results in Chapter 5).⁵⁰ In addition, Corma *et al.* used the introduction of heteroatoms (Ge, Ti) into the gel as a route to synthesise new framework types.⁵⁵

1.4.1 Templating Effect of Organic Species in Zeotypes

1.4.1.1 Alkyl Amines and Quaternary Ammonium Species

The synthesis of AlPO zeotypes requires the presence of organic amines or quaternary ammonium cations. Already in 1982, Flanigen *et al.* remarked on the ‘templating’ effect of such species, since without their presence dense AlPO phases were formed.

This early work included the formation of AlPO-17 (ERI) with three different organic species with similar sizes (quinuclidine, neopentylamine and cyclohexylamine) and AlPO-20 (SOD) only obtained using the small and spherical tetramethylammonium cation (TMA) accommodated in the sodalite cage. By contrast, AlPO-5 was obtained with 23 different organic species, where due to its cylindrical channel structure and wide aperture, the organic species act merely as void fillers.

Since then a large variety of organic templates have been applied in zeotype synthesis, Table 1.1 shows the organic species commonly applied in the AlPO regime.

In fact, there is a trend towards rationalisation of the use of particular templates for specific pore sizes,⁵⁶ as in the case of the novel MgAPO STA-2⁵⁷ (SAT) using quinuclidinium ions of the form $[(C_7H_{13}N)-(CH)_n-(NC_7H_{13})]^{2+}$ ($n = 4,5$) which possesses an elongated cage where the template is occluded, figure 1.10 shows the good fit between cage and template.

Table 1.1 Common organic species applied in the AIPO synthesis.⁵⁰

| Organic Species | Typical Resulting AIPO structure |
|----------------------------|----------------------------------|
| TMAOH | AIPO-20 |
| TEAOH | AIPO-18, AIPO-5 |
| TPAOH | AIPO-5 |
| Me ₃ N | AIPO-21 |
| Et ₃ N | AIPO-5 |
| Dipropylamine | AIPO-11, AIPO-31 |
| Diisopropylamine | AIPO-11 |
| Dicyclohexylamine | AIPO-5 |
| Isopropylamine | AIPO-14 |
| Tert-BuNH ₂ | AIPO-14 |
| Diethylethanolamine | AIPO-5 |
| Dimethylethanolamine | AIPO-5, AIPO-21 |
| Ethylene urea | AIPO-12 |
| Tetraethylethylene diamine | AIPO-21 |
| Quinuclidine | AIPO-7, AIPO-16, AIPO-17 |

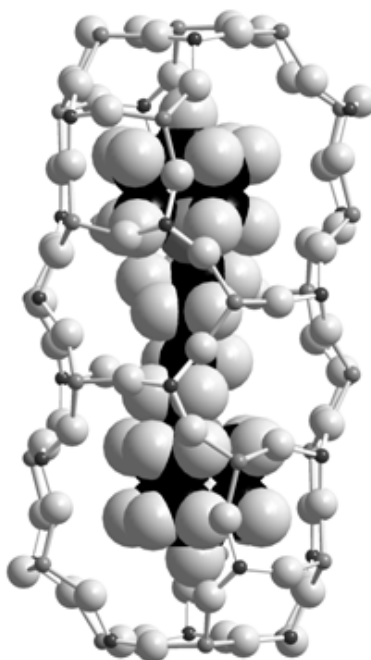


Fig. 1.10 The experimentally-determined position of the diquatery cation $[(C_7H_{13}N)-(CH)_4-(NC_7H_{13})]^{2+}$ used as template within the elongated cages of the magnesiumaluminophosphate STA-2. Template represented by a space filling model and framework by a ball and sticks model (courtesy of P. A. Wright).

1.1.4.2 Macrocycles, the ‘Co-Templating’ Effect and Gel Chemistry

Although traditionally primary, secondary and tertiary alkylamines or quaternary ammonium salts have been used, cyclic species can be alternative structure directing agents (SDAs) in the formation of frameworks containing cavities.

Such is the case for aza-crown ethers (the so-called kryptofix family, denoted with the nomenclature K22, K21, etc) and azamacrocycles (the cyclam family):

- Kryptofix 22 forms the AlPO analogue of MCM-61 Mu-13 (MSO)⁵⁸ and K222 AlPO-42,⁵⁹ which has the LTA topology. Moreover, as in the case of K21, it can be necessary to add another organic species to form the zeotype. In this specific case, K21 templates AlPO-42 in the presence of TMA. This approach is denoted ‘co-templating’ (K22, K21, K222 and TEA are described in Fig. 1.11 **1**, **2** and **3**).
- Tetramethylcyclam (TMcyclam, Fig. 1.11 **4**) templates the novel MAPOs STA-6 (SAS) and STA-7 (SAV). In this example, the synthesis of pure SAPO STA-7 needs the addition of TEA (Fig. 1.11 **5**) as a ‘co-template’.

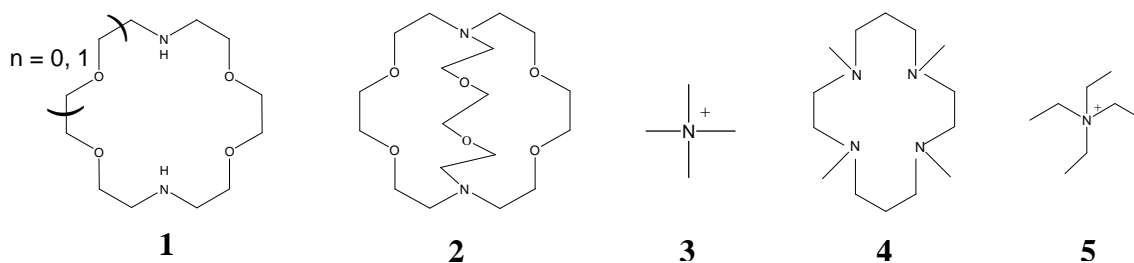


Fig. 1.11 Organic SDAs, **1** $n=1$ K22 and $n=0$ K21, **2** K222, **3** TMA, **4** TMcyclam and **5** TEA.

The ‘co-templating’ effect is studied in detail in Chapter 3 and 4 but it is important to mention that the extra template stabilises the structures by fitting into the smaller cages, in these particular examples the SOD cage of LTA and the so called A-cage of SAV.^{59,60}

As illustrated by these examples, the use of the correct inorganic gel regime is fundamental to the activity of these SDAs. As an example the substituted zeotypes DAF-

1 and several members of the STA (St Andrews) family have not been synthesised as pure AIPOs.⁶¹ It has been postulated that it is not possible to incorporate charged templates in the neutral frameworks. In the following chapters it can be seen that for the case of STA-7 this fact remains valid (Chapter 3) whereas in the case of STA-2 the formation of the pure AIPO is achievable (Chapter 6).

1.5 Molecular Modelling Applications

Modelling has been applied since the early 90's in many different areas of zeolite science. Some of them are of interest for the research presented in this thesis. The most important one is the study of the location and energies of templating agents, helping to elucidate the best template for a specific material.³⁸ Others include the discovery of hypothetical frameworks and the simulation of adsorption.^{62,63}

In particular, the application of modelling zeolite-template interactions can provide information on template location, where this cannot easily be obtained experimentally, and can also be used to propose templates for desired target structures.

Modelling can give data on template location. This in some cases can be confirmed by experimental studies by X-ray diffraction, but in other cases where this is not possible, due to the disorder and the complexity that these molecules present or because the material is only available in the form of powder, modelling can be the best way to assess the position of the molecules. Cox⁶⁴ elucidates the most likely positions of templates within the solids by a combination of Monte Carlo docking and subsequent simulated annealing routines, assuming that short-range interactions between the framework and the template molecules will determine the favoured locations, rather than coulombic forces. As an example, this approach was successfully applied for the structural characterisation of the novel materials STA-6 (SAS) and STA-7 (SAV) in the as-prepared form demonstrating the templating effect of azamacrocycles.⁶⁵

Given the ability to simulate template energies, it should be possible to tailor templates for a specific structure. This has been achieved by the automated ZEBEDDE (ZEolites by Evolutionary *De novo* Design) approach developed by Lewis *et al.*⁶⁶ in which a template is grown computationally within the pores of a zeolite. This approach successfully designed a new template for existing aluminophosphate frameworks DAF-4 (LEV) and DAF-5 (CHA).^{67,68} The method is most promising for application to structures containing pores where the space to be occupied by the organic molecules is well-defined. For this reason, the synthesis of cage structures with novel compositions, or structures where these would not be expected by simple modifications of known preparations, appears to be a designed synthesis goal that is both worthwhile and achievable.⁶⁰

Although this thesis is based on experimental synthesis of zeotypes, modelling has been performed in collaboration with A. Fecant (IFP-Lyon). Chapter 2 described the general procedure applied here and in the following Chapters 3, 4, 5 and 6 the applications are described and discussed.

1.6 Microporous Materials for CO₂ Adsorption

As mentioned in the general introduction (section 1.1) there is considerable interest in the adsorption and separation of CO₂. Its selective adsorption on microporous materials has been observed, and zeolites are of interest due to their high adsorption uptake of CO₂, minimum environmental impact and good thermal and mechanic stability.⁶⁹

The separation properties of zeolites arise from interactions between extra-framework cations with the polar molecule CO₂ through electrostatic forces and depending on the strength of the interaction the adsorption properties of the zeolites vary strongly.⁷⁰

Zeotype materials such as SAPOs have been also reported with specific sorption and catalytic activity due to their Brønsted sites.⁷¹ Moreover SAPOs can successfully separate CO₂ from CH₄/CO₂ mixtures.⁷² In this case the properties of adsorption arise from the strength of interaction between the Brønsted sites and the gas molecule and also the steric

effect of cage or channel dimensions. This combination of effects made SAPO membranes three fold more selective for gas separation compared to that of aluminosilicate ones.⁷³

When designing materials for use in PSA technologies, zeotypic materials with weaker electrostatic interactions with the target molecule than those of zeolites could be favoured because their use will not require the application of high temperatures (TSA) or vacuum (VSA) for their regeneration to remove the most strongly adsorbed carbon dioxide.

This subject is developed in Chapter 7 where the performance in CO₂ adsorption of the zeotypes synthesised during this work is measured and compared with that of commercially available materials such as zeolite Na-X and SAPO-34.

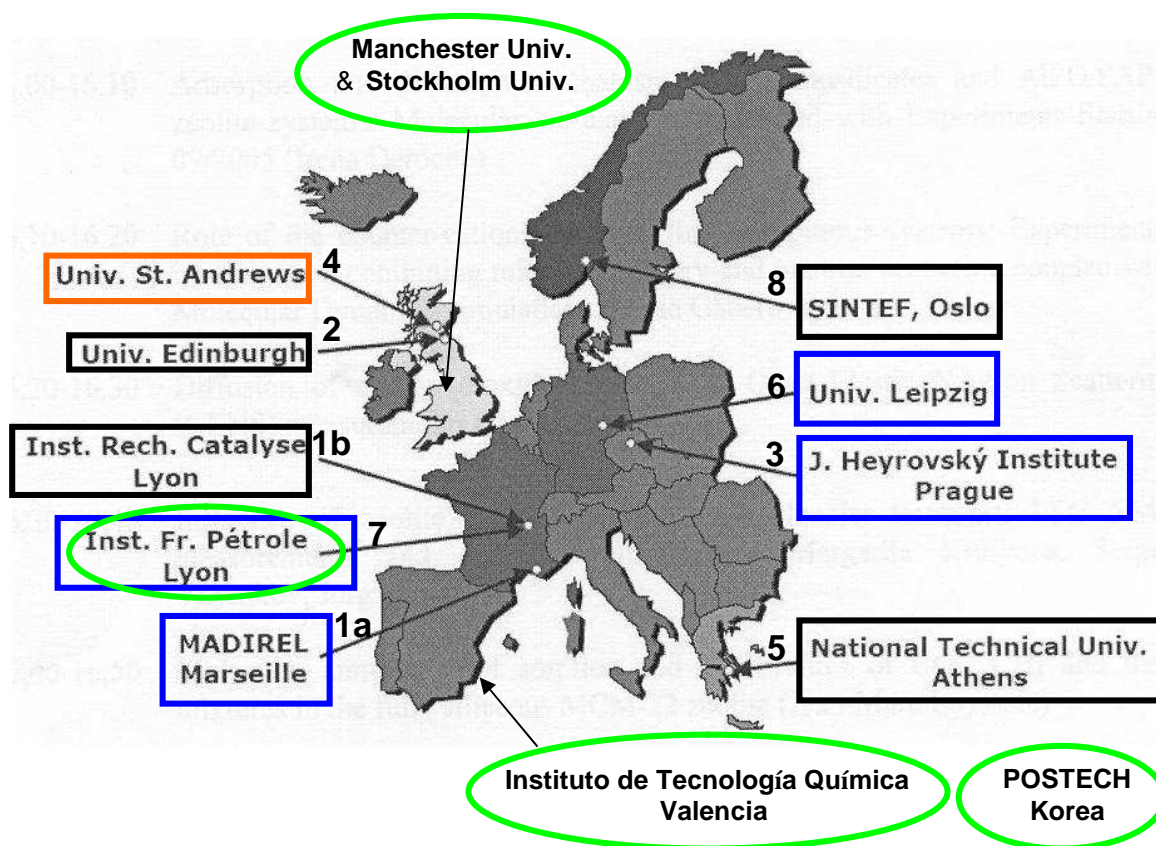
1.7 Overview of the Project and Aims

The research presented here has been sponsored during a period of three years by a Marie Curie Research Training Network funded by the European Commission named INDENS (Intelligent Design of Nanoporous Sorbents). The overall aim of this INDENS project is to combine theoretical (modelling) and experimental approaches to predict gas/solid behaviour and therefore the physicochemical properties required for the optimum sorbent. One of the initial target of the work of this thesis as a network partner was to provide selected samples with specific properties for measurements. In addition, collaborations outside the network were also undertaken (Fig. 1.12, 1.13 and 1.14).

The research area of this thesis focuses on the synthesis and structural characterisation of novel microporous materials for gas adsorption and separation, mainly concerned with zeotypes. (Some extension to metal organic frameworks was also attempted; the information is available in the First Year Report presented in 2006 at University of St Andrews under the title ‘Synthesis and Characterisation of Novel Yttrium and Ytterbium Metal Organic Frameworks for Gas Adsorption and Separation’).

The objectives for this thesis were:

- 1) To investigate the viability of a designed synthesis route through co-templating and modelling approaches. The first stage of the project was to develop and understand this co-template route for the synthesis of SAPO STA-7 and to use this as a key reference material for the project. The co-templating approach was further applied to obtain a new zeotype STA-14.
- 2) In addition, the modelling approach was taken to improve the synthesis of the known aluminophosphate STA-2.
- 3) The performance of these solids was measured in adsorption and catalysis. In particular, the adsorption of carbon dioxide at temperatures close to ambient was investigated.



Collaborations within INDENS Network

- | | | |
|----------------------------------|------------------|--|
| • Lucia Gaberova (MADIREL) | Adsorption | Microcalorimetry |
| • Youssef Belmabkhout (IFP-Lyon) | Adsorption | High Pressures Adsorption |
| • Irena Deroche (Montpellier) | Simulation | Theoretical Model for Microcalorimetric data |
| • Despina Tzoulaki (Leipzig) | Diffusion | IFM (Interference Microscopy) |
| • Jiri Cejka (Prague) | Characterisation | FTIR |

Collaborations out of INDENS Network

- | | | |
|-------------------------------------|------------------|------------------------------------|
| • Antoine Fecant (IFP-Lyon) | Modelling | Template Design |
| • Fernando Rey (ITQ, Valencia) | Adsorption | Argon at low pressures |
| • Sam Stevens (Stockholm Univ.) | Characterisation | HRSEM (High Resolution SEM) |
| • Pablo Cubillas (Manchester Univ.) | Characterisation | AFM (Atomic Force Microscopy) |
| • Suk Bong Hong (POSTECH) | Catalysis | MTO (Methanol To Olefins reaction) |

Fig. 1.12 Map of Europe showing the institutions involved in the Marie Curie training network INDENS, with partners collaborating in this thesis work marked in blue. Extra network collaborations are marked in green oval.

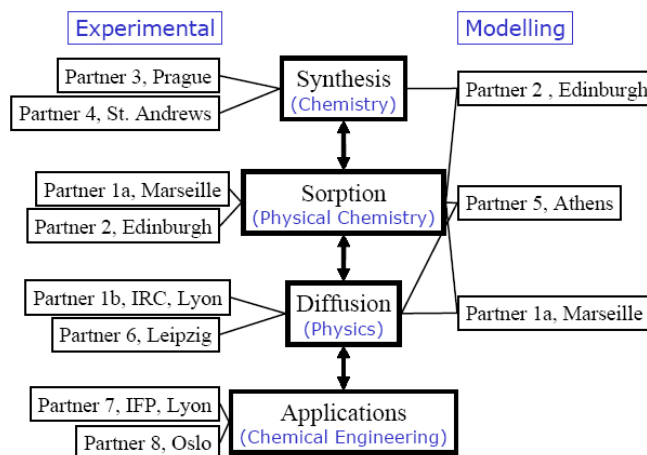


Fig. 1.13 Research Project Scheme with the areas of study and the implication of each partner (institutions labelled from 1 to 8: MADIREL, Edinburgh University, J. Heyrovsky Institute, University of St Andrews, National Technical University Athens, University Leipzig, IFP-Lyon and SINTEF).

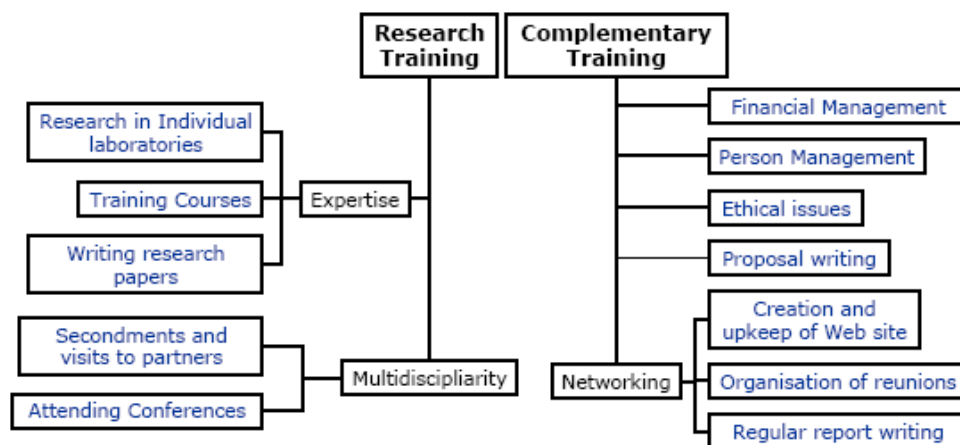


Fig. 1.14 Training provided by INDENS network during PhD period.

-
1. R. Lal, *Energy Environ. Sci.*, 2008, **1**, 86.
 2. C. T. Chou, C. Y. Chen. '*Sep. and Purification Technol.*', 2004, **39**, 51.
 3. J. E. Hansen, an Editorial Essay in *Climatic Change*, 2005, **68**, 269.
 4. Article 2, '*The United Nations Framework Convention on Climate Change*', 2005.
 5. '*Chemistry World*', RSC Publishing, October 2007, **4**, 42.
 6. R. Mokaya, M. Poliakoff, *Nature*, 2005, **437**, 1243.
 7. G. Férey, M. Latroche, C. Serre, F. Millange, T. Loiseau, A. Percheron-Guegan, *Chem. Commun.*, 2003, 2976;
 8. P. M. Forster, J. S. Chang, S. E. Park, G. Férey, A. K. Cheetham, *J. Am. Chem. Soc.*, 2003, **125**, 125.
 9. N. L. Rosi, J. Eckert, M. Eddaoudi, D. T. Vodak, J. Kim, M. O'Keeffe and O.M. Yaghi, *Science*, 2003, **300**, 1127.
 10. N. R. Rao, S. Natarajan, R. Vaidhyanathan, *Angew. Chem. Int. Ed.*, 2004, **43**, 1466.
 11. M. E. Davis, R. F. Lobo, *Chem. Mater.*, 1992, **4**, 756.
 12. G. Férey, *Chem. Mater.*, 2001, **13**, 3084; W. T. A. Harrison, *Curr. Opin. Solid St. Mater. Sci.*, 2002, **6**, 407.
 13. C. S. Cundy, P. A. Cox, *Chem. Rev.*, 2003, **103**, 663.

-
14. J. Yu, R. Xu, *Chem. Soc. Rev.*, 2006, **35**, 593.
 15. R. F. Lobo, *Nature*, 2006, **443**, 757.
 16. S. T. Wilson, B. M. Lok, C. A. Messina, T. R. Cannan, E. M. Flanigen, *J. Am. Chem. Soc.*, 1982, **104**, 1146.
 17. M. Afeworki, D. Dorset, G. Kennedy, K. Strohmaier, *Stud. Surf. Sci. Catal.*, 2004, **154**, 1274.
 18. J. M. Bennett, J. P. Cohen, E. M. Flanigen, J. J. Pluth, J. V. Smith, *ACS Sym. Ser.*, 1983, **218**, 109.
 19. R. A. Van Norstrand, D. S. Santilli, S. I. Zones, *ACS Symp. Ser.*, 1988, **368**, 236.
 20. M. G. G. Wu, M. W. Deem, S. A. Elomari, R. C. Medrud, S. I. Zones, T. Maesen, C. Kibby, C. Y. Chen, I. Y. Chan, *J. Phys. Chem. B.*, 2002, **106**, 264.
 21. M. E. Davis, C. Montes, P. E. Hathaway, J. P. Arhancet, D. L. Hasha, J. M. Garces, *J. Am. Chem. Soc.*, 1989, **111**, 3919.
 22. P. A. Wright, *'Microporous Framework Solids'*, RSC Publishing, Cambridge, 2008, 29.
 23. B. M. Lok, C. A. Messina, R. L. Patton, R. T. Gajek, T. R. Cannan, E. M. Flanigen, *J. Amer. Chem. Soc.*, 1984, **106**, 6092.
 24. C. A. Messina, B. M. Lok, E. M. Flanigen, U. S. Patent, 1985, 4544143.

-
25. S. T. Wilson, E. M. Flanigen, Eur. Pat. Appl., 1985, 132708; U. S. Patent, 1986, 4567029.
26. E. M. Flanigen, B. M. Lok, R. L. Patton, S. T. Wilson, *Pure Appl. Chem.*, 1986, **58**, 1351.
27. P. A. Wright, '*Microporous Framework Solids*', RSC Publishing, Cambridge, 2008, 31.
28. J. M. Thomas, G. N. Greaves, G. Sankar, P. A. Wright, J. Chen, A. J. Dent, L. Marchese, *Angew. Chem. Int. Ed.*, 1994, **33**, 1871.
29. P. A. Wright, C. Sayag, F. Rey, D. W. Lewis, J. D. Gale, S. Natarajan, J. M. Thomas, *J. Chem. Soc. Faraday Trans.*, 1995, **91**, 3537.
30. J. Chen, P. A. Wright, J. M. Thomas, S. Natarajan, L. Marchese, S. M. Bradley, G. Sankar, D. R. A. Catlow, *J. Phys. Chem.*, 1994, **98**, 10216.
31. G. Sastre, D. W. Lewis, C. R. A. Catlow, *Journal of Molecular Catalysis A: Chemical*, 1997, **119**, 349.
32. O. M. Yaghi, *Nature*, 2003, **423**, 705.
33. J. L. C. Rowsell, O. M. Yagui, *Micropor. Mesopor. Mater.*, 2004, **73**, 3.
34. M. J. Rosseinsky, *Micropor. Mesopor. Mater.*, 2004, **73**, 15.
35. R. J. Francis, D. O'Hare, *J. Chem. Soc., Dalton Trans.*, 1998, 3133.
36. W. S. Sheldrick, M. Wachhold, *Angew. Chem. Int. Ed.*, 1997, **36**, 206.

-
37. C.S. Cundy, P.A. Cox, *Micropor. Mesopor. Mater.*, 2005, **82**, 1.
38. R. J. Francis, D. O'Hare, *J. Chem. Soc., Dalton Trans.*, 1998, 3133.
39. X. Ren, S. Komarneni, D.M. Roy, *Zeolites*, 1991, **11**, 142.
40. E. M. Flanigen, *Adv. Chem. Ser.*, 1973, **121**, 114.
41. E. M. Flanigen, R. L. Patton, 1978, U.S. Patent 4073865.
42. W. Xu, J. Li, W. Li, H. Zhang, B. Liang, *Zeolites*, 1989, **9**, 468.
43. S. Ueda, W. Kageyama, M. Koizumi, *Proc. 6th Inter. Zeolite Conf.*, D. Olson, A. Bisio, Butterworth (Eds.), Butterworth, Surrey, 1984, 905.
44. S. Mintova, N. H. Olson, V. Valtchev, T. Bein, *Science*, 1999, **283**, 958.
45. R. J. Francis, D. O'Hare, *J. Chem. Soc., Dalton Trans.*, 1998, 3133.
46. P. A. Wright, '*Microporous Framework Solids*', RSC Publishing, Cambridge, 2008, 184.
47. I. Petrovic, A. Navrotsky, M. E. Davis, S. I Zones, *Chem. Mater.*, 1993, **5**, 1805.
48. G. T. Kerr, *Inorg. Chem.*, 1966, **5**, 1537.
49. A. Thangaraj, P. R. Rajamohanan, P. M. Suryavanshi, S. Ganapathy, *J. Chem. Soc., Chem. Comm.*, 1991, 493.
50. B. M. Lok, T. R. Cannan, C. A. Messina, *Zeolites*, 1983, **3**, 282.

-
51. M. E. Davis, R. F. Lobo, *Chem. Mater.*, 1992, **4**, 756.
52. S. L. Lawton, W. J. Rohrbaugh, *Science*, 1990, **247**, 1319.
53. R. M. Barrer, P. J. Denny, *J. Chem. Soc.*, 1961, 971.
54. G.T. Kerr, G.T. Kokotailo, *J. Am. Chem. Soc.*, 1961, **83**, 4675.; G.T. Kerr, *Inorg. Chem.*, 1966, **5**, 1537.
55. A. Corma, 'Proc. 4th Int. Zeolite Conf., Catal. Soc.', E. Van Steen, L.H. Callanan, M. Claeys (Eds), S. Africa, 2004, 25.
56. J. Yu, R. Xu, *Chem. Soc. Rev.*, 2006, **35**, 593.
57. G. W. Noble, P. A. Wright, Å. Kvik, *J. Chem. Soc., Dalton Trans.*, 1997, 4485.
58. J. L. Paillaud, P. Caullet, L. Schreyeck and B. Marler, *Micropor. Mesopor. Mater.*, 2001, **42**, 177.
59. L. Schreyeck, J. Stumbe, P. Caullet, J. C. Mougénel, B. Marler, *Micropor. Mesopor. Mater.*, 1998, **22**, 87.
60. M. Castro, R. Garcia, S. J. Warrender, A. M. Z. Slawin, P. A. Wright, P. A. Cox, A. Fecant, C. Mellot-Draznieks, N. Bats, *Chem. Commun.*, 2007, 3470.
61. P. A. Wright, 'Microporous Frameworks Solids', RSC Publishing, Cambridge, 2008, 32.
62. C. Mellot-Draznieks, S. Girard, G. Férey, J. C. Schoen, Z. Carcarevic, M. Jansen, *Chem. Eur. J.*, 2002, **8**, 4102; <http://www.hypotheticalzeolites.net>.

-
63. I. Deroche, L. Gaberova, G. Maurin, P. Llewellyn, M. Castro, P. Wright, *Adsorption*, 2008, **14**, 207.
64. A. P. Stevens, A. M. Gorman, C. M. Freeman, P. A. Cox, *J. Chem. SOC., Faraday Trans.*, 1996, **92**, 2067.
65. P. A. Wright, M. J. Maple, A. M. Z. Slawin, V. Patinec, R. A. Aitken, S. Welsh, P. A. Cox, *J. Chem. Soc., Dalton Trans.*, 2000, 1243.
66. D.W. Lewis, D.J. Willock, C.R.A. Catlow, J.M. Thomas, G.J. Hutchings, *Nature*, 1996, **382**, 604.
67. J. M. Thomas, D. W. Lewis, *Z. Phys. Chem.*, 1996, **14**, 635.
68. D.W. Lewis, G. Sankar, J.K. Wyles, J.M. Thomas, C.R.A. Catlow, D.J. Willock, *Angew. Chem. Int. Ed.*, 1997, **36**, 2675.
69. I. Deroche, L. Gaberova, G. Maurin, P. Llewellyn, M. Castro, P. Wright, *Adsorption*, 2008, **14**, 207.
70. M. D. Jia, B. Chen, R. D. Noble, J. L. Falconer, *J. Membr. Sci.*, 1994, **90**, 1.
71. U. Olsbye, M. Bjorgen, S. Svelle, K. P. Lillerud, S. Kolboe, *Catal. Today*, 2005, **106**, 108.
72. J. C. Poshusta, R. D. Noble, J. L. Falconer, *J. Membr. Sci.*, 2001, **186**, 25.
73. S. Li, J. Falconer, R. D. Noble, *J. Membr. Sci.*, 2006, **18**, 2601.

Chapter 2: Techniques

2.1 Introduction

The main characteristic that defines zeolites and related materials is their framework structure. All zeolite framework types are assigned a 3-letter code and these are published in the ‘Atlas of Zeolite Framework Types’ and on the web.^{1,2} It is necessary to know the structural details to understand their performance in applications and be able to modify and optimise them. This chapter discusses the techniques required for their structural characterisation, starting with a brief summary of the relevant crystallography and covering the main techniques applied in this thesis: X-ray diffraction and solid-state NMR.

X-ray diffraction is the most powerful method to investigate structures ordered over the long range. It can be used for simple ‘fingerprint’ identification of a known phase from its X-ray powder diffraction - published in the ‘Collection of Simulated XRD Powder Patterns for Zeolites’³ - through to more advanced structural solution and refinement. In contrast, solid-state NMR provides detailed information on local environments, such as the integrity of the organic template within the framework, which frequently shows

disorder (and cannot therefore be characterised by X-ray diffraction) and the specific distribution of silicon, aluminium and phosphorus cations within the framework.

A molecular modelling approach has been applied in collaboration with A. Fecant (IFP-Lyon) for template localisation and to design potential templates as a preliminary step to rational hydrothermal synthesis and this is described briefly. A more detailed description of this approach is presented in the relevant section.

To fully characterise calcined materials, N₂ adsorption was applied to observe the stability of the structures and FTIR was used for the observation of the Brønsted acid sites. Other techniques such as SEM, TGA and Elemental Analysis for carbon, hydrogen and nitrogen (CHN) were used to determine compositions.

The characterisation techniques were predominantly used to obtain structural details relevant to their synthesis and practical applications, and are described here at a level appropriate to this. Additional, advanced characterisation (IFM, AFM and catalytic testing) has been performed by collaborators on the samples prepared in this thesis and this is discussed briefly in the relevant sections.

Furthermore, one of the key aims of this project was to prepare adsorbents. A short introduction to adsorption principles and practice is therefore included in this section. Detailed information for specific experiments will be provided in the relevant section.

2.2 Basic Crystallography

Crystalline materials have a periodic distribution of atoms in space. Their arrangement can be defined by an imaginary array of points in space known as the crystal lattice. Each lattice point has a fixed relationship with the atoms of the crystal. Every lattice point has identical environments and therefore the same symmetry. The simplest portion of the structure which is repeated and shows its full symmetry is defined as the *unit cell*. The

unit cell describes the vectors between the lattice points by three distances (a , b and c) and three angles (α , β and γ) that are denoted as the unit cell parameters (Fig. 2.1 a).

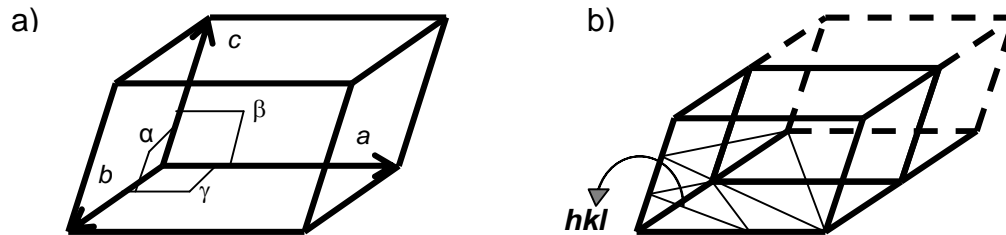


Fig. 2.1 General three-dimensional unit cell with the characteristic unit cell parameters (a) and definition of Miller indices in three dimensions (b).

In the general unit cell all the parameters can take any value because there is no symmetry relationship between them. The increase of symmetry level leads to the seven crystal systems (Table 2.1).

Table 2.1 The crystal systems ordered from the bottom to the top increasing the symmetry.

| System | Unit Cell | Essential Symmetry in the Crystal |
|--------------|--|--|
| Cubic | $a = b = c$ $\alpha = \beta = \gamma = 90^\circ$ | Four three-fold axes |
| Tetragonal | $a = b \neq c$ $\alpha = \beta = \gamma = 90^\circ$ | One four-fold axis or one inverse four-fold axis |
| Hexagonal | $a = b \neq c$ $\alpha = \beta = 90^\circ, \gamma = 120^\circ$ | One six-fold axis or one inverse six-fold axis |
| Trigonal / | $a = b = c$ | One three-fold axis |
| Rhombohedral | $a = b = c \neq 90^\circ$ | |
| Orthorhombic | $a \neq b \neq c$ $\alpha = \beta = \gamma = 90^\circ$ | Three orthogonal two-fold axes or planes |
| Monoclinic | $a \neq b \neq c$ $\alpha = \gamma = 90^\circ, \beta \neq 90^\circ$ | One two-fold axis and/or one mirror plane |
| Triclinic | No special relationships | None |

The structure of a crystal can be reproduced by the lattice type, which defines the translational periodicity, and the additional symmetry associated with the distribution of the atoms around each lattice point. In this way there are four lattice types: primitive (P), body centred (I), face centred (F) and face centred on one face only (A, B or C) and 32 point groups. The *space group* describes the 230 general combinations of both types of symmetry elements, translational and non-translational:

- Translational elements of symmetry (related to the four lattice types): screw axis, glide planes.
- Non-translational elements of symmetry (related to the symmetry around a point): inversion centre, rotation axis, mirror planes.

In this way, to fully describe a structure it is only necessary to define a minimum number of atoms, denoted as the *asymmetric unit*, which define the whole structure once the two types of elements of symmetry described by the *space group* and the *unit cell* are applied.

Miller Indices

The identical atoms in a regular 3D distribution form a series of parallel identical planes separated from each other by a distance d , which varies according to the nature of the material. For any crystal, planes exist in different orientations with characteristic d spacings. The orientation of a family of planes is designated by the Miller indices (hkl), where h , k and l are integers, positive, negative or zero (Fig. 2.1 b).

2.3 X-Ray Diffraction for the Bulk Structural Study

The diffraction phenomenon is an interference process that happens when radiation interacts with an object that has a size of the same order of magnitude as the wavelength of the incident radiation. Typical unit cell dimensions for zeolites and related materials are between 5 Å and 50 Å. Radiation of suitable wavelength to give diffraction include X-rays, neutrons and electrons. The wavelengths of these radiations are comparable to the inter-atomic distances. In this thesis the radiation applied for structural studies was X-

rays. Therefore, this section will start describe X-ray sources and interaction of this radiation with the crystalline structure giving diffraction phenomena, and also the procedure to collect and analyse the diffraction data using two techniques; single X-ray diffraction (SXRD) and powder X-ray diffraction (PXRD).

2.3.1 X-Ray Sources

In general, X-rays are produced when a metal target (anode) is bombarded with accelerated electrons. When that happens, some of the electrons have enough energy to eject an electron from the inner shell of the metal atom at the moment of collision. As a result an electron from higher energy levels fills the vacancy and its excess energy is released as an X-ray which has the characteristic frequency of the quantised atomic transition (Fig. 2.2). That is the characteristic radiation but in addition a broad and continuous spectrum of X-rays is emitted due to the deceleration process (Fig. 2.2 b) which is known as ‘white’ radiation or Brehmstrahlung (‘braking radiation’).

Many types of transitions happen in the characteristic radiation. As an example, for copper a vacancy in the K-shell can be filled by electrons from the L or M shell:

$L \rightarrow K$ transition is called K_{α} with $\lambda = 1.5418 \text{ \AA}$.

$M \rightarrow K$ transition is called K_{β} with $\lambda = 1.3922 \text{ \AA}$.

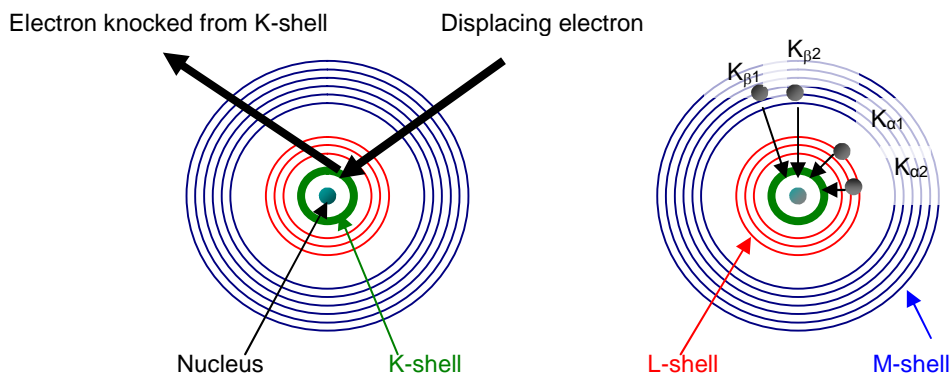


Fig. 2.2 a Scheme for the emission of the characteristic radiation for copper atom.

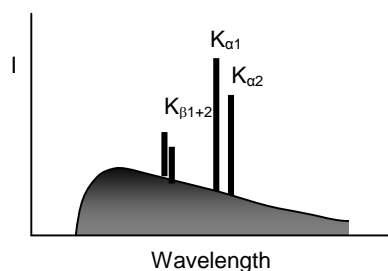


Fig. 2.2 b Spectrum of the white radiation and the characteristic radiation for a general atom.

K_{α} X-rays have lower energy than K_{β} but are more intense. For that reason K_{α} radiation is used as an intense monochromatic X-ray source. The K_{α} transition occurs as a doublet (so does K_{β}), $K_{\alpha 1}$ $K_{\alpha 2}$, with a small difference in energy and wavelength.

In a standard laboratory diffractometer the X-rays are generated commonly from Cu and Mo anodes. If more intense radiation is required the X-rays can be generated using a synchrotron source. In this case, the electrons are accelerated in a ‘storage ring’ and emitted tangentially. The desired wavelength is selected from the spectrum using monochromators. For this thesis the use of the synchrotron radiation source at the ESRF, Grenoble was applied to collect high resolution data for the structural elucidation of STA-2 (Chapter 6).

Table 2.2 Typical wavelength used in this work, (PXRD for powder X-ray diffraction and SXRD for single X-ray diffraction). The term ‘ λ bar’ is weighted average.

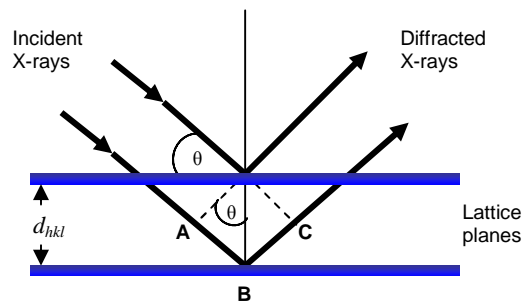
| Wavelength (Å) | Source |
|------------------|---|
| 1.5406 / 1.54178 | Cu $K_{\alpha 1}$ at laboratory PXRD / Cu ‘ λ bar’ at laboratory SXRD |
| 0.7093 / 0.71069 | Mo $K_{\alpha 1}$ at laboratory PXRD / Mo ‘ λ bar’ at laboratory SXRD |
| 0.3-0.9 | ESRF |

2.3.2 Diffraction Phenomenon

Diffraction occurs when X-rays interact with the atoms of the sample, and as a result they are re-emitted in all directions. These re-emitted X-rays interfere, giving constructive or

destructive interferences and diffracted beams are given in specific directions if the relevant geometric conditions are satisfied.

The diffraction process can be described mathematically by Bragg's Law (Fig. 2.3 and Eq. 2.1). The extra distance (AB+BC) that the lower beam has to travel is called the path difference. The interference is constructive when the diffracted beams are in phase and that happens when the path difference is an integer number of wavelengths ($n\lambda$):



$$\text{Total path difference} = AB + BC = 2d \sin\theta$$

$$\text{For constructive interference } AB + BC = n\lambda$$

$$n\lambda = 2d \sin\theta$$

Eq. 2.1

Fig. 2.3 Bragg's Law, where λ is the wavelength of the X-rays, d is the spacing between the lattice planes and n an integer value.

By varying the angle theta (θ), Bragg's law is satisfied by different d -spacings, of different planes (hkl) where the interference is constructive. Plotting the angular positions and the intensities of the resultant diffraction peaks a pattern is produced characteristic of the sample.

The structure factor, $F(hkl)$, is the amplitude of the diffracted beam in the direction of the hkl reflection and it depends on:

- The atoms types in the unit cell and their capacity to scatter the X-rays, denoted by the atomic scattering factor, f .

- The position of the atoms in the unit cell, denoted by the fractional coordinates x , y and z . The phase, ϕ , of radiation dispersed by the atoms depends on the positions of atoms in the unit cell (Eq. 2.2).

$$F(hkl) = \sum_n f_n e^{i\phi_n} \quad \text{where, } \phi_n = 2\pi (hx_n + ky_n + lz_n) \quad \text{Eq. 2.2}$$

The magnitude of $F(hkl)$ is proportional to the experimental values of intensity $I(hkl)$ as described in equation 2.3:

$$I \propto |F(hkl)|^2 \quad \text{Eq. 2.3}$$

To work from the experimental values of intensities and calculate the position of atoms in an unknown structure the ‘phase problem’ appears because $F(hkl)$ is a complex quantity (Eq. 2.4):

$$F(hkl) = |F(hkl)| e^{i\phi(hkl)} \quad \text{Eq. 2.4}$$

$|F(hkl)|$ can be determined from experimental intensities, but there is no experimental procedure to obtain $\phi(hkl)$. Unfortunately the phases contain the bulk of the structural information. There are two main X-ray diffraction techniques: Single crystal (SXRD) and Powder (PXRD).

2.3.3 Solving a Crystal Structure by SXRD

The phase problem makes the direct calculation of the electron density impossible. This problem is overcome by two approaches in single crystal diffraction technique: the Patterson method and direct methods. The Patterson method is used when the unit cell contains ‘heavy atoms’. This method is rarely applied for microporous materials because they contain atoms with similar electron density, such as Al, Si and P. ‘Direct methods’ are commonly used instead. ‘Direct methods’ determine the sign of F_{hkl} directly from the experimental intensities I_{hkl} (Fig. 2.4) by statistical methods. Direct methods were applied

in this thesis for the structure solution of STA-7 and STA-14 materials (Chapter 3 and 4 respectively).

The general procedure to solve a structure is:

- The collection of the diffraction data from a crystal of suitable quality.
- Indexing the diffraction pattern (unit cell dimensions).
- Determination of space group (from systematic absences).
- Solving the structure, obtaining the starting model by direct methods in our case.
- Complete the structure by inspection of Fourier maps and refinement.

To observe the fit between the data and the model, the model coordinates can be optimised by least squares refinement to minimise the difference (D) between observed and calculated structure factors (Eq. 2.5):

$$D = \sum w(|F_{\text{obs}}| - |F_{\text{calc}}|)^2 \quad \text{Eq. 2.5}$$

The R-factor quantifies the fit of the calculated with the observed diffraction data (Eq. 2.6):

$$R = \sum (|F_{\text{obs}}| - |F_{\text{calc}}|) / \sum |F_{\text{obs}}| \quad \text{Eq. 2.6}$$

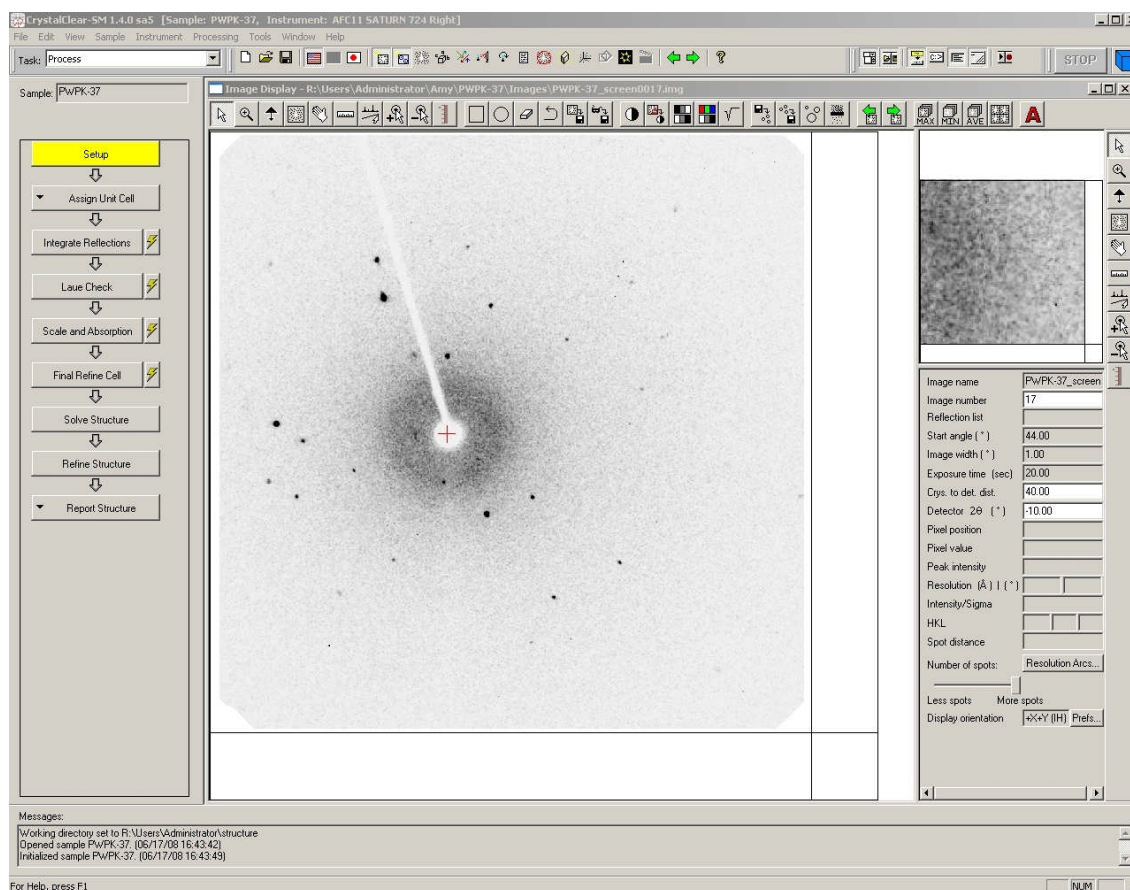


Fig. 2.4 Screen of the program *CrystalClear-SM 1.4.0 sa5* during collection of the individual reflexion peaks I_{hkl} in SXR. A good quality crystal gives a pattern of spots of varied intensities, in the figure different intensities are represented by different sizes of spot.

2.3.3.1 SXR Experiment

The collection and transformation of the intensity data on selected crystals was performed by Prof. Alex M. Z. Slawin and solved by direct methods using a routine within the program SHELX.⁴

Two Rigaku diffractometers were used, with different X-ray radiation sources: Cu and Mo respectively (the radiation used is a ‘ λ bar’ weighted average, 1.54178 Å and 0.71069 Å respectively) see figure 2.5. In order to obtain the individual reflections hkl the crystal is rotated in all possible orientations by a goniometer.

Data Collection, Indexing of Diffraction Pattern and Space Group Determination

The collected data are given in two files. They contain the starting information to solve the structure:

- The *hkl* file with the absorption-corrected reflection intensities.
- The crystallographic information file (CIF) with unit cell parameters, the lowest space group of the correct Laue group, the X-ray source radiation and $R_{\text{equivalent}}$, which gives information about the quality of the collected data by means of the quality from the equivalent reflections collected that are related by symmetry. $R_{\text{equivalent}}$ can be high either due to an error in choosing the crystal system or due to the poor quality of the crystal; so that the radiation emitted at different angles is different due the irregular shape of the crystal (for example, this problem can occur in needle-shaped crystals).

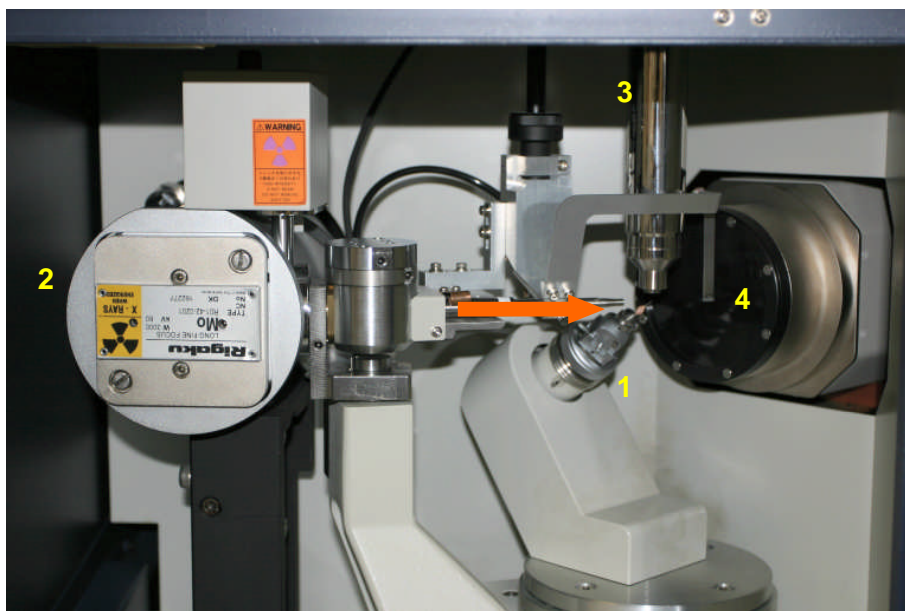


Fig. 2.5 Diffractometer for single crystals (Rigaku) employed in this work: 1) sample and goniometer, 2) X-ray source (in this case Mo K_{α}), 3) low temperature device, 4) detector, arrow indicates direction of incident X-ray beam.

Solve and Refine the Structure and Presentation of the Data for Publication

The structure is solved with SHELX97⁵⁵ giving an goodness of fit value R_{int} that depends on the quality of the structure solution and the crystal. Once the frameworks of the zeotypes were obtained, the structures were further refined. The graphic software

CAMERON (a part of the WinGX program system)⁵ showed the non assigned electron density directly, normally related to disordered template and water molecules. TGA and elemental analysis were of use to refine the structure. In this thesis, for example, regarding the structural characterisation of STA-7 and STA-14 materials, the tetraethylammonium cation (TEA) was refined using two different models: the simpler N-C1-C2 or the more complicated N-C1A-C1B-C2 where C1A and C1B are each partially occupied. In some cases the use of the second model helped to improve the refinement of the structure. The determination of these positions will generate by the 4 fold axis of symmetry the full TEA cation structure (Fig. 2.6).

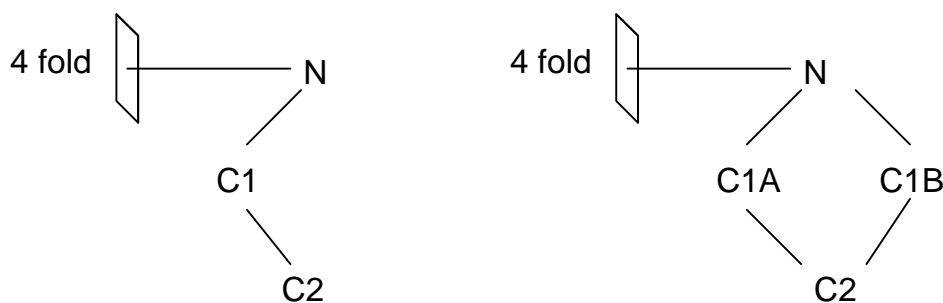


Fig. 2.6 Models used to refine the position of TEA cation within the framework cages: N1-C1-C2 model (left) and N1-C1A-C1B-C2 model (right).

Once the refinement has achieved convergence, the data are presented in a CIF file checked by the PLATON software.⁶

2.3.4 Solving a Structure from Powder Diffraction

Powder X-ray diffraction (PXRD) is used for polycrystalline samples. The diffraction process is the same as in SXRD but the diffraction from many small crystals is measured simultaneously. The small particles are randomly orientated and the individual hkl diffraction intensities appear overlapped, particularly at high diffraction angles. There is a cone of diffraction for each diffracting lattice plane at the specific 2θ value (Fig. 2.7). The diffraction pattern is made from rings rather than spots. The X-ray powder pattern from a powder X-ray diffractometer can be described as a slice through the diffraction rings.

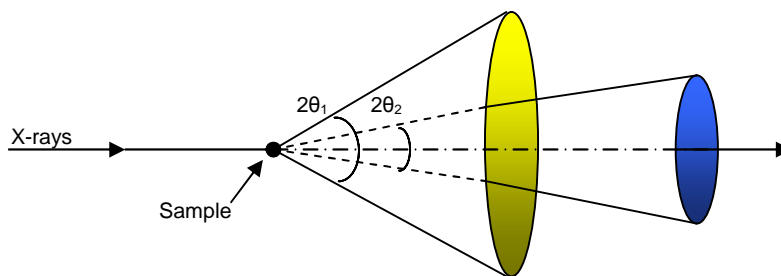


Fig. 2.7 Diffraction cones obtained from polycrystalline sample. Each cone consists of very close dots originated from each single crystallite diffracted by a particular set of crystalline planes.

SXRD and PXRD techniques give the same information: peak positions (in terms of 2θ) and the intensities. The positions depend only on dimensions and shape of the unit cell, whereas the intensities depend on the atomic types and their position in the unit cell. In the case of single crystal the information is spread in three dimensions (I_{hkl}) but in powder diffraction the information is compressed into a single dimension ($y(2\theta)$). Because each reflection maximum has a finite peak width there is considerable peak overlap and therefore loss of information (Fig. 2.8).

Although both techniques suffer the phase problem, in the case of single crystal diffraction mathematical approaches such as the direct methods overcome the problem. That is possible because there is no overlap in the information collected. For powder data, the loss of information due to peak overlap makes the use of direct methods less likely to succeed.

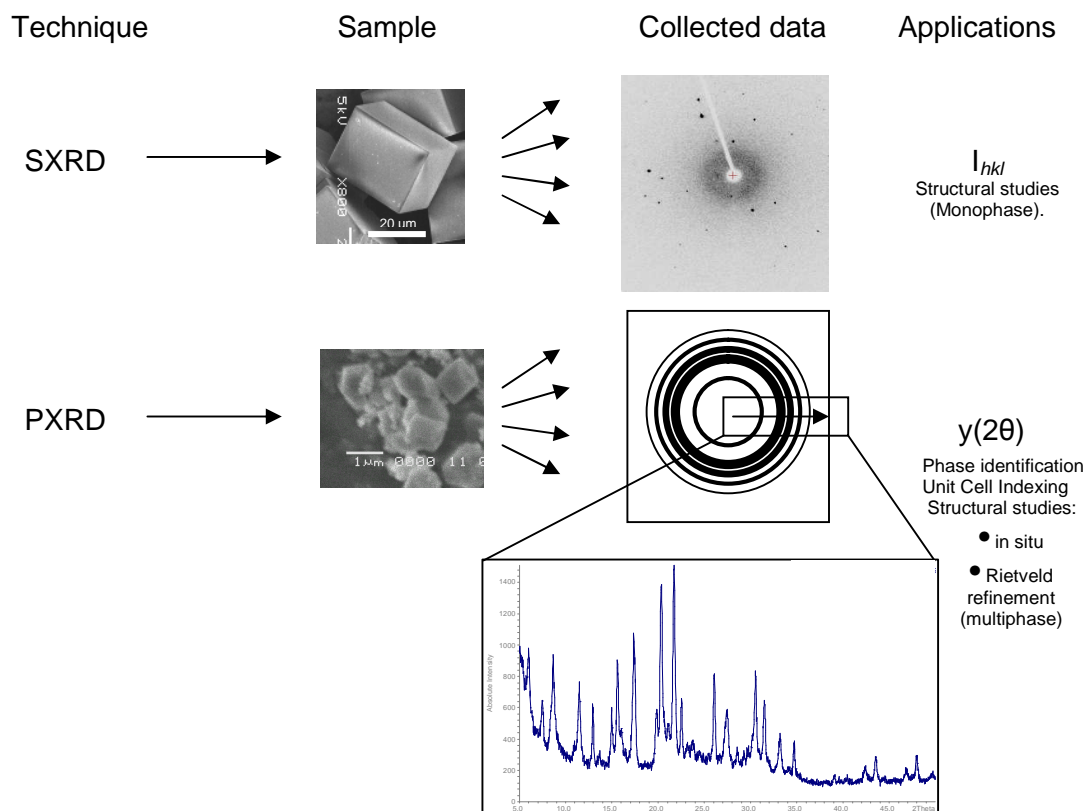


Fig. 2.8 Schematic description of SXRD and PXRD showing their differences in sample type, data collected and applications. The PXRD diffractometer scans around the sample along the circumference of a circle cutting through the diffraction cones in direction of increasing 2θ values (denoted by the arrow). As a result the pattern compress the information to one dimension, $y(2\theta)$. Adapted from reference 7.

2.3.4.1 Rietveld Method for Structural Refinement

In the absence of single crystal data, powder data can be used to solve or refine the structure. In particular, the Rietveld method⁸ enables the structure to be refined against the X-ray diffraction pattern. This method fits the whole profile ($y_{\text{obs}}(2\theta)$), without the need to separate the individual reflections, but requires a starting model of the structure ($y_{\text{cal}}(2\theta)$).⁹ In this work, the SXRD structure is normally used as a starting model. This model is refined by least-squares minimizing the difference, D , with the collected data using a suitable weight (w) at each 2θ step (Eq. 2.7):

$$D = \sum w (y_{\text{obs}} - y_{\text{cal}})^2 \quad \text{Eq. 2.7}$$

In contrast with the single crystal refinement, this method needs to include in the refinement the profile parameters:

- Profile parameters take into account instrumental effects including the diffractometer zero point, the scale factor, background and peak shape. Several parameters are used to model the peak shape and width. For X-rays a pseudo-Voigt function is commonly used (a combination of Lorentzian and Gaussian functions).
- Structural parameters include the unit cell, atom positions, occupancy and thermal parameters.

The refinement of the structural model starts by fitting the background, peak shape, zero point, scale factor and unit cell. Once the model is as similar as possible, the atom positions and occupancy are refined. To maintain chemical sense of the model restraints are applied, for example bond distances and angles can be restrained between determined values. The refinement can be performed for groups of atoms by constraining them in a chemical sense for the refinement of i) atom positions (i.e. for the atoms of the framework excluding the atoms of template) ii) fractional occupancies or thermal parameters. The use of constraints and restraints are also applicable to the structural parameters refined in SXRD. The thermal parameter can be refined isotropically or anisotropically. These include the thermal motion of the atoms above the absolute zero point and different sample and instrumental effects, so that the term ‘atomic displacement parameter’ is more appropriate. Difference Fourier maps can be inspected to complete the structure as in the SXRD case (one example is described in Chapter 6).¹⁰

The good fit between model and experimental data is expressed by the ‘profile R-factor’ and the ‘weighted profile R-factor’, R_p (Eq. 2.8) and R_{wp} (Eq. 2.9) respectively:

$$R_p = \Sigma |y_{obs} - y_{cal}|^2 / \Sigma |y_{obs}| \quad \text{Eq. 2.8}$$

$$R_{wp} = (\Sigma w (y_{obs} - y_{cal})^2 / \Sigma w (y_{obs})^2)^{1/2} \quad \text{Eq. 2.9}$$

The validation of the fit is given by the R_{wp} . The good fit is represented in a plotted histogram (Fig. 2.9), which include the experimental and model profiles and their difference. In addition, this method allows multiphase refinements to calculate the percentage of each phase present in the sample (as in the two phase refinement of MgAPO-42 and MgAPO STA-14 reported in Chapter 4).

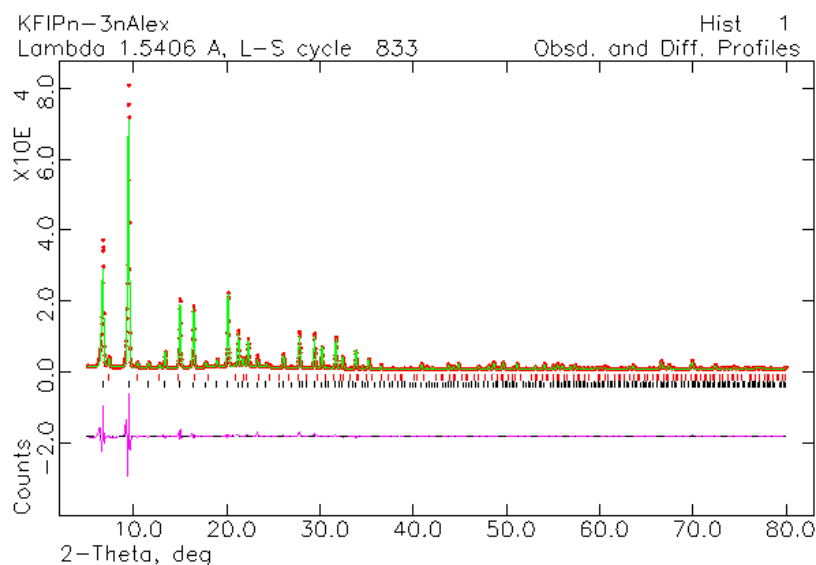


Fig. 2.9 Rietveld refinement plot of MgAPO STA-14 (KFI) with extra phase as impurity of MgAPO-42 (LTA) showing the fit between experimental data (red crosses), the model (green line) and their differences (purple line). The marks in black show the reflexion peaks for KFI phase whereas the red marks show the reflexion peaks from LTA phase.

2.3.4.2 PXRD Experiment

In this thesis, PXRD has been applied for:

- Phase identification.
- Phase indexing.
- Refinement of calcined samples, where although the crystals were large enough for SXRD the resulting data were of poor quality (Chapter 3 and 4).
- Structural study of as-prepared samples using experimental data obtained from synchrotron radiation for a multi crystalline sample (Chapter 6).

Two Stoe STADI P X-ray diffractometers operating in transmission mode with Cu $K_{\alpha 1}$ (λ 1.5418 Å) were used in this work: one in transmission mode and the other for capillaries. The first one was used for phase identification, where the sample is spread between two thin film layers with paraffin and the second mainly for long runs for the refinement of calcined and dehydrated samples, sealed in 0.7 mm quartz capillaries (Fig. 2.10). Both diffractometers rotate the sample during the data collection to minimise preferred orientation. As in the case of SXRD diffractometers, these comprise an X-ray source, sample holder and detector and between detector and sample there is a radiation stopper. The data are collected at room temperature.

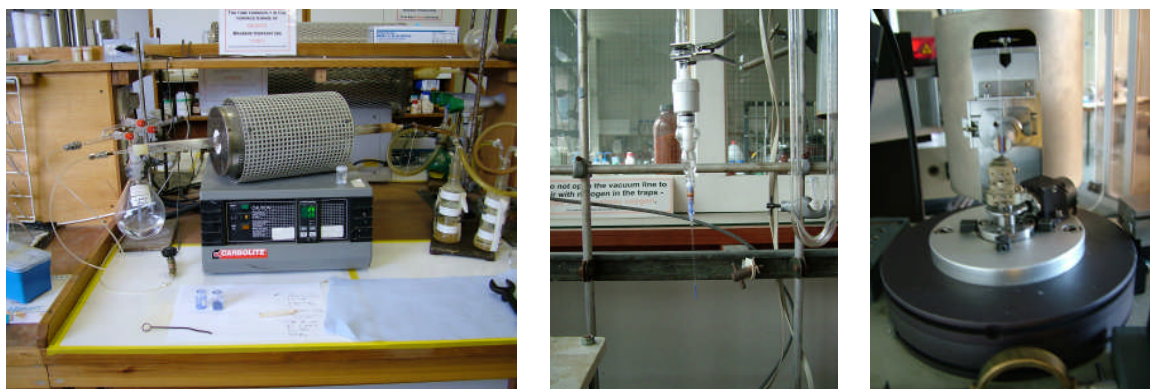


Fig. 2.10 *The three steps for the sample to collect data for Rietveld refinement in calcined form: calcination, dehydration (capillary loaded with fresh calcined sample attached to vacuum line to be heated) and once sealed mounted in the X-ray diffractometer.*

Typical run details:

- For Phase identification: 1.5 hours, 5-50 2θ and 0.5 seg/step.
- For Rietveld refinement: overnight, 5-80 2θ and 0.1 seg/step.

The data collected are analysed with software packages:

- Phase identification and indexing use the Stoe software.
- Rietveld method is performed via GSAS program.¹¹

Once the data are analysed, the results are presented in a similar format to those of SXRD.

2.4 Solid-State NMR Spectroscopy for the Study of Local Environments

2.4.1 General Principles^{12,13}

Nuclear magnetic resonance (NMR) spectroscopy is applicable to the study of nuclei with spin quantum number $I \neq 0$. A nucleus has $(2I + 1)$ spin energy levels, which are degenerate and distinguished by the quantum number m_I ($m_I = -I, -I + 1 \dots +I$). These levels split in the presence of a strong external magnetic field (B_0). This splitting is called the Zeeman effect (Fig. 2.11).¹⁴ The resonance phenomenon occurs when a radiation of energy $h\nu$ matches the energy gap (ΔE) between the permitted transition levels (selection rule: $\Delta m_I = \pm 1$). The ‘resonance frequency’ ν depends on the chemical environment of the atom (i.e. a chemical shift, δ_{iso}). As a consequence this technique is applied here for the structural study of local environments.

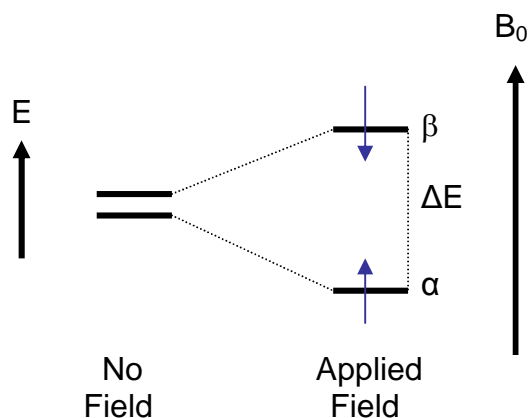


Fig. 2.11 The Zeeman effect for a nucleus ($I = 1/2$) in presence of a magnetic field B_0 .

The nuclear spin transitions are characterised by extremely small energy differences. The simple application of radiofrequency pulses (rf) enables the observation of the resonance phenomenon. The resonance frequencies depend also on the magnetic field strength. In order to make comparable experiments performed with different instruments, these frequencies are reported as chemical shifts (δ_{iso}) in ppm relative to an external standard compound.

The simplest NMR experiment can be visualised by a vector model and can be divided into three parts, once the nuclear spin is placed into an external magnetic field B_0 : i) the perturbation by applying a pulse of rf radiation, ii) the detection of the resonance during its evolution until the signal decay to zero and iii) recovery time referred to as the relaxation delay to achieve the re-establishment of the initial state prior to the perturbation (Fig. 2.12).

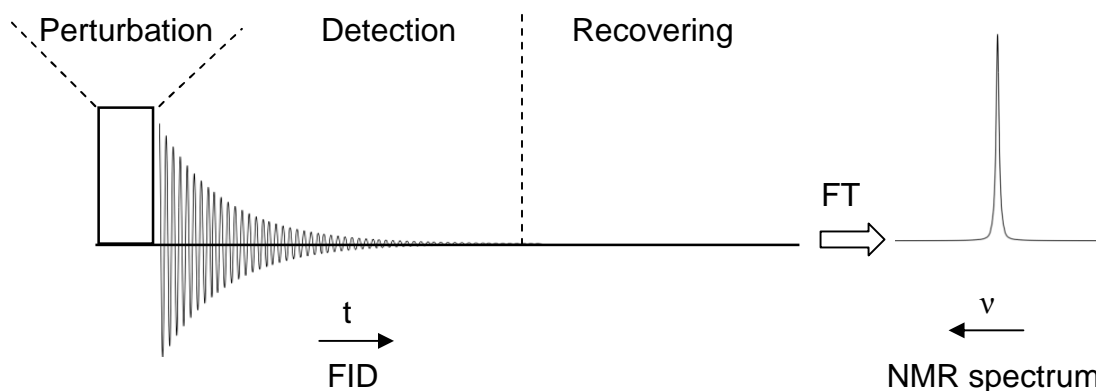


Fig. 2.12 Schematic representation of the three steps in a typical NMR experiment.

In the presence of an external magnetic field B_0 , a bulk magnetisation (M) is generated along the z axis due to the slight excess of population in the α -state over that in the β -state. This M can be seen as the sum of all the magnetic vectors (Fig. 2.13 a) precessing on the surface of a cone at the Larmor frequency (the equivalent to the resonance frequency of that nucleus). In a frame rotating at ω_{rf} (the frequency of an applied pulse) the effect of the pulse is to rotate M into the xy plane (transverse magnetisation M_{xy} , Fig. 2.13 b). In the detection stage after the application of the rf pulse, the system tends to the equilibrium condition (relaxation). In this way, the transfer magnetisation dephases along the xy plane with a characteristic relaxation time T_2 . This dephasing induces a voltage in the coil which is recorded as a function of time and is called a Free Induction Decay (FID). The FID, a time-domain signal, is converted by the mathematical procedure Fourier transformation (FT) into a frequency-domain spectrum. In the recovery step the equilibrium populations are allowed to fully re-establish according to a characteristic relaxation time T_1 .

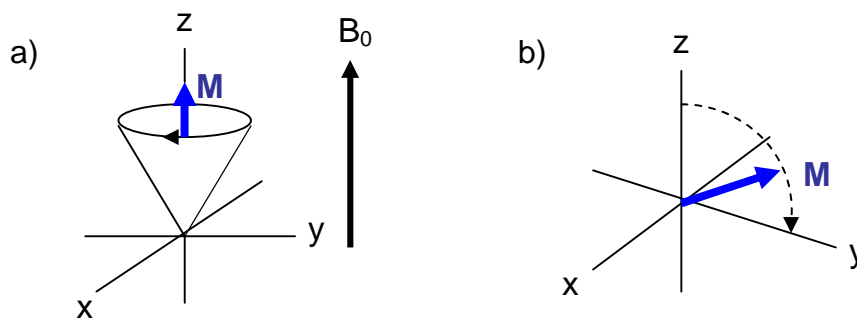


Fig. 2.13 Schematic representation of the bulk magnetization (M) in presence of B_0 (a) and the torque of M when the rf pulse is applied (b).

2.4.2 NMR in Solids¹⁵

The interactions detected by NMR are anisotropic, they depend upon orientation with respect to the applied magnetic field B_0 . In solution state, these interactions are averaged, due to the fast tumbling motion becoming isotropic, but in the solid state the molecules can be considered effectively static. This produces broadened signals as a consequence of collecting the signal of all the spins in their different orientations. The main interactions responsible for the broadening are i) the dipolar interaction, ii) the chemical shift anisotropy (CSA) and iii) the quadrupolar coupling.

Dipolar Coupling

The dipolar coupling or dipole-dipole coupling is the through space magnetic interaction of pairs of nuclei (the local magnetic field B_{loc} at a nucleus I generated by a nucleus S) and is independent of the applied field. This interaction depends on the positions of the nuclei and it is angular dependent via a factor equal to $(3\cos^2\theta_{IS} - 1)$. This interaction is often the most influential for nuclei with spin $I = 1/2$.

Chemical Shift Anisotropy (CSA)

The chemical shift is produced by the interaction of the electrons which shield the nucleus and the applied magnetic field (B_0). The distribution of those electrons is not always spherically symmetric; therefore the chemical shift is anisotropic depending on the orientation of the nuclei of the sample with respect to B_0 and its influence in

broadening increases with the strength of the external field applied.¹⁶ Nevertheless, like the dipolar interactions the chemical shift anisotropy (CSA) depends on $(3\cos^2\theta_{IS} - 1)$.¹⁷

Quadrupolar Coupling

The nuclei with spin $I > 1/2$ have a non-spherically symmetrical distribution of the nuclear charge and possess an electric quadrupole moment (eQ) which interacts strongly with any electric field gradient (EFG) generated at the nucleus by the surrounding electron density. The magnitude of this quadrupolar interaction is described by the quadrupolar coupling constant C_Q . This interaction is most significant for nuclei with spin $I > 1/2$ and is sometimes so important that the signals disappear beyond detection. The quadrupolar interaction is often so large (many MHz) that the effect on the NMR spectrum needs to be considered to both first and second order.

Magic Angle Spinning (MAS) and Multiple Quantum (MQ) MAS NMR

Solid-state NMR requires Magic Angle Spinning (MAS) to obtain high resolution spectra. In MAS NMR, the sample is rotated at 10-30 kHz around an axis at an angle of 54.736° to the applied magnetic field B_0 .¹⁸ At this angle the function $(3\cos^2\theta - 1)$ becomes zero. Therefore the broadening due to the dipolar coupling and the CSA are removed. The resultant spectra for nuclei with $I = 1/2$ have narrow resonances related to specific local environments of the nuclei in the framework. In contrast, for nuclei with $I > 1/2$ the spectra show additional broadening due to second order quadrupolar interactions. In this case the Multiple Quantum (MQ) MAS NMR¹⁹ experiment enables the separation of isotropic and anisotropic information in two-dimensional (2D) spectra, thereby improving the resolution between different sites.

2D spectra²⁰ can be generally generated in four steps: preparation (P), evolution (E), mixing (M) and detection (D) as described in figure 2.14.

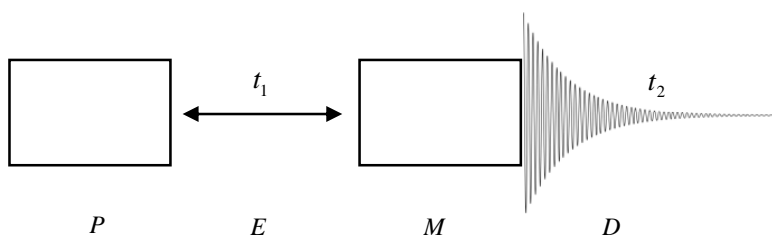


Fig. 2.14 Schematic representation of a typical 2D NMR experiment.

In the preparation period one or more pulses perturb the system to evolve in a period of time t_1 . The information is converted into observed signals by an analogous scheme of pulse(s) in the mixing period which are detected in the period of time t_2 . The t_1 period is varied providing the indirect time dimension for the two-dimensional FT spectrum (Fig. 2.15).

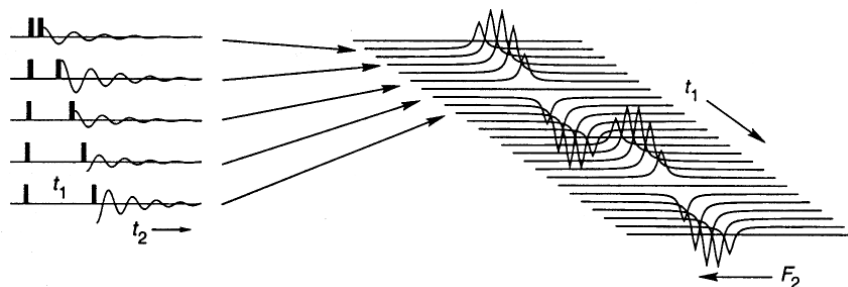


Fig. 2.15 Generation of a 2D spectrum by variation of t_1 and detection of the signals in t_2 , from reference 21.

For the specific MQ MAS NMR experiment after a shearing transformation, the projection along F_1 gives the isotropic spectrum and F_2 the quadrupolar frequencies.

Cross Polarisation Experiment

Spectra can be detected using the Cross Polarisation (CP) technique to increase the signal of the nuclei under study by transferring the magnetization from abundant nuclei such as ^1H . CP is mainly applied to enhance ‘weak’ signals of nuclei that have low natural abundance, such as ^{13}C and ^{29}Si . This technique involves the application of simultaneous pulses on both nuclei for a period of time referred to as the contact time. In this interval the transverse magnetisation (M_{xy}) previously created on the high abundant nuclei is transferred, via the dipolar interaction, to the less sensitive nuclei (Fig. 2.16).

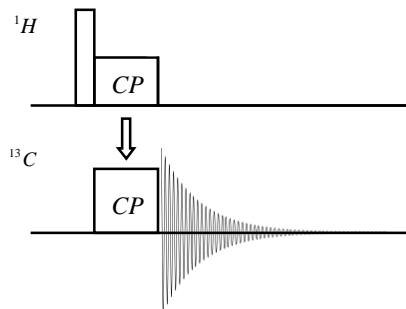


Fig. 2.16 *Schematic representation of a typical CP NMR experiment.*

CP spectra are not quantitative because nuclei closer to ^1H are preferentially enhanced. For quantitative data the spectra need to be collected using Direct Polarisation (DP). Table 2.3 summarises the natural abundance and spin of the nuclei studied in this thesis:

Table 2.3 *Relevant NMR information of the nuclei studied in this work.*²²

| Nucleus | Natural abundance % | Spin |
|------------------|---------------------|------|
| ^1H | 99.99 | 1/2 |
| ^{13}C | 1.07 | 1/2 |
| ^{14}N | 99.63 | 1 |
| ^{15}N | 0.37 | 1/2 |
| ^{27}Al | 100 | 5/2 |
| ^{29}Si | 4.70 | 1/2 |
| ^{31}P | 100 | 1/2 |

2.4.3 NMR Experiments

^{13}C , ^{15}N MAS NMR gave information about the organic molecule used as template. Commonly ^{13}C NMR is used to show that the molecule remains intact within the pores.

The nuclei ^{31}P , ^{29}Si and ^{27}Al are part of the framework and MAS NMR of these gives information about local environments (Table 2.4).

Table 2.4 Typical chemical shifts for the nuclei of the framework in their local environments, using as reference phosphoric acid, tetramethylsilane (TMS) and aluminium (III) chloride respectively.

| Nucleus | Environment | Typical chemical shift (ppm) | Ref |
|------------------|--------------|------------------------------|--------------|
| ^{31}P | Tetrahedral | P(4Mg) | –19 |
| | | P(1Al, 3Mg) | ↓ |
| | | P(2Al, 2Mg) | |
| | | P(3Al, 1Mg) | |
| | | P(4Al) | |
| ^{29}Si | Tetrahedral | Si(4Al) | –83 to –87 |
| | | Si(3Al, 1Si) | –88 to –94 |
| | | Si(2Al, 2Si) | –93 to –99 |
| | | Si(1Al, 3Si) | –97 to –107 |
| | | Si(4Si) | –103 to –114 |
| ^{27}Al | Tetrahedral | 30 - 50 | 25 |
| | 6-coordinate | 0 - 22 | |

In this thesis ^{31}P MAS NMR spectra were applied for the study of MgAPO materials at different magnesium loadings. Following the procedure of Barrie and Klinowski²³ the assignment of the resonances in the spectra assumes that the substitution of aluminium for magnesium in the AlPO lattice increases the chemical shift of the adjacent phosphorus, and this effect increases with the number of adjacent aluminium atoms

substituted. The most negative chemical shift is attributed to $P(4Al)$, the next to $P(3Al, 1Mg)$ and so on (Fig. 2.17). This study is described in detail in Chapter 4.

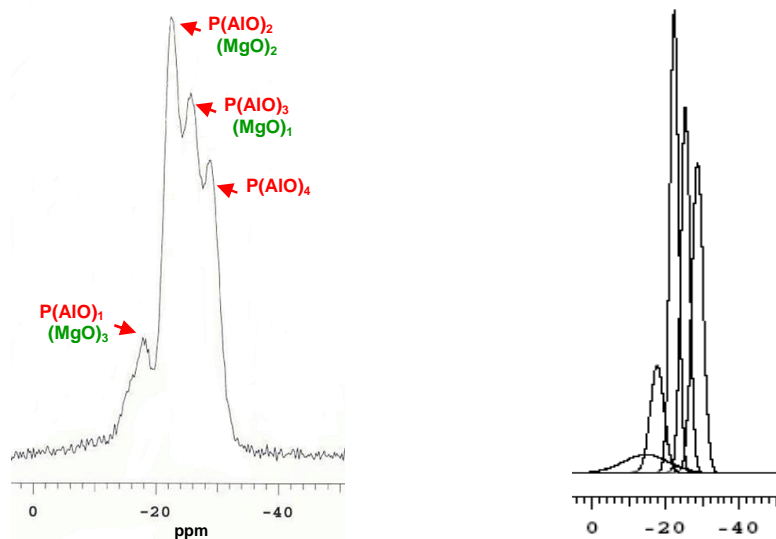


Fig. 2.17 ^{31}P MAS NMR and the deconvoluted curves for MgAPO STA-14, where magnesium substitutes 20% of the aluminium sites.

In the case of SAPO materials, ^{29}Si and ^{27}Al MAS NMR as well as ^{27}Al MQ MAS NMR were applied in this thesis to study the incorporation of silicon into the framework by replacing phosphorus sites at different loadings. ^{29}Si MAS NMR spectra show characteristic chemical shifts for specific local environments denoted as $Si(nAl, (4-n)Si)$, where n is the number of aluminium atoms and $4-n$ the number of silicon atoms (see Table 2.4 and Fig. 2.18). The incorporation of silicon into the framework influences the neighbouring aluminium atoms and therefore the ^{27}Al MAS NMR spectra. Because ^{27}Al MAS NMR is very complex due to the quadrupolar effect, ^{27}Al MQ MAS NMR was applied to observe the influence of the silicon content on the aluminium environments. As a result, it has been demonstrated by the analysis of the samples at different silicon content (from 8% up to 30% silicon content) that the weak signal at 9 ppm in the ^{27}Al MAS NMR spectra can be attributed to $Al(1Si,3P)$ environments (Fig. 2.19). The full discussion is given in Chapter 3.

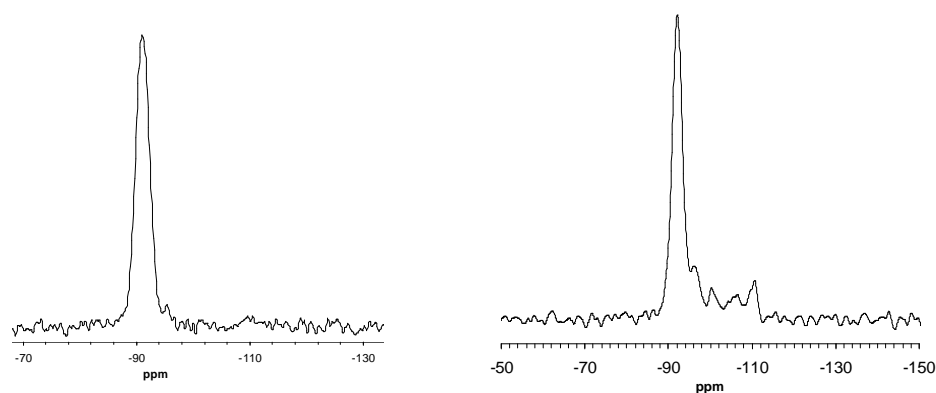


Fig. 2.18 ^{29}Si MAS NMR spectra of as-made SAPO STA-7 with Si/Al ratio ca. 0.3 in both cases but the sample on the right was synthesised by S. Warrender using fluoride anions, favouring the formation of silica islands.

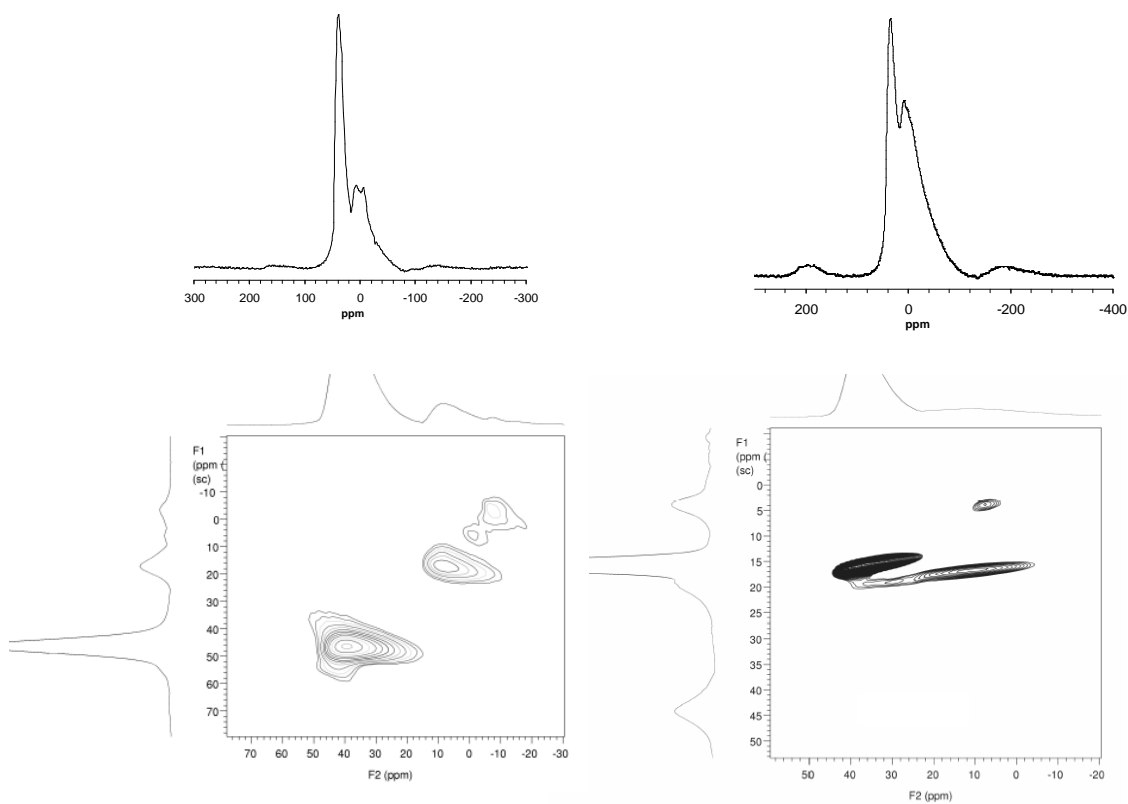


Fig. 2.19 ^{27}Al MAS NMR (top) and ^{27}Al MQ MAS NMR (bottom) spectra for SAPO STA-7 at Si/Al 0.08 and 0.30, respectively. Samples provided by S. J. Warrender.

The experimental parameters for the spectra collected in this work are summarised in each experimental section of the chapters. In general the following parameters are included:

- Freq (MHz), the resonance frequency of the specific nucleus at the magnetic field of the instrument.
- Acq time (ms), the acquisition time (t_2) for the FID collection.
- Relaxation delay (s), the recovery time required between each acquisition to allow nuclei to recover their equilibrium populations prior to the application of a new pulse cycle.
- Polarisation (abbreviated as polaris.), to denote cross polarisation (CP) or direct polarisation (DP) experiment.
- Contact time (ms), the time of transferring the magnetisation in the CP experiment.
- Pulse time (μ s), the duration of the pulse applied.
- Spin rate (kHz), the velocity at which the sample is spun at MAS conditions.

2.5 Adsorption

Adsorption is a surface phenomenon, which occurs when a gas or liquid (adsorbate or sorbate) is in contact with a solid (sorbent). The ability to sorb large quantities of sorbate molecules makes zeolites and related solids interesting for industrial applications in gas purification, separation and storage, catalysis, pollution control and also in areas of agriculture, pharmacy and medicine.²⁶

The resultant interaction can be of varying strength, depending on the chemical bonds involved. Types of interaction range from weak physisorption, based on van der Waals interactions, through to chemisorption, when a chemical bond is formed between solid and sorbate.

To determine the stability of the calcined solids the physisorption isotherms were collected to obtain data related to the structure of the sorbate. For this purpose, the adsorption of N_2 at 77.4 K was performed. The resulting adsorption isotherm is the plot of the amount adsorbed as a function of the relative equilibrium pressure (p/p_o , where p_o is the saturation vapor pressure of the adsorptive). IUPAC distinguishes six types of isotherms (Fig. 2.20).

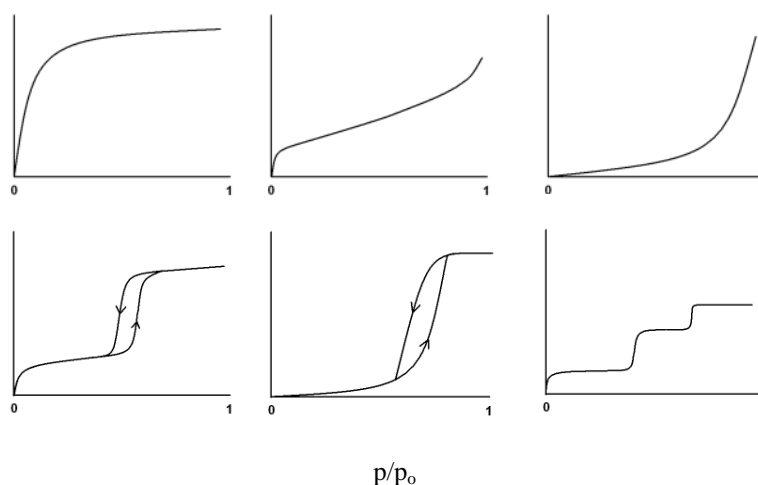


Fig. 2.20 Representation of the six isotherms types by IUPAC, adaptation from reference 27. The adsorption uptake is plotted against p/p_o , where p is the adsorbate pressure and p_o the saturated vapour pressure of the pure liquid adsorbate at the isotherm temperature.

Microporous solids have the isotherm type I for N_2 (77 K) which at low pressures increases until reaching a plateau. That shows the main interaction is the adsorbate-sorbate corresponding to the filling of the micropores by a monolayer of adsorbate atoms. IUPAC designate at pore sizes of 4 to 20 Å as in the microporous regime.²⁸

Each point of the isotherm is collected at equilibrium, so that the chemical potentials of the probe molecule in gas and adsorbed phases are the same. In the specific case of microporous solids, reaching this equilibrium state can take an extended period (> 1 hour).

The most frequently methods for the measurement of isotherms are volumetric and gravimetric.

Volumetric Method

The volumetric method is based on calibrated volumes and pressures and applies the general gas equation.²⁹ It consists of the expansion at constant temperature of the adsorbate from a pressure cell into the adsorption cell containing the activated sample that has been evacuated. The volumes of both cells (V_{prc} and V_{ads} , respectively) need to be accurately known. The difference between the initial moles of adsorbate (n_1) and the amount remaining in the gas phase after the expansion (n_2) is the quantity of the gas adsorbed by the sample (n_{ads}), figure 2.21.³⁰

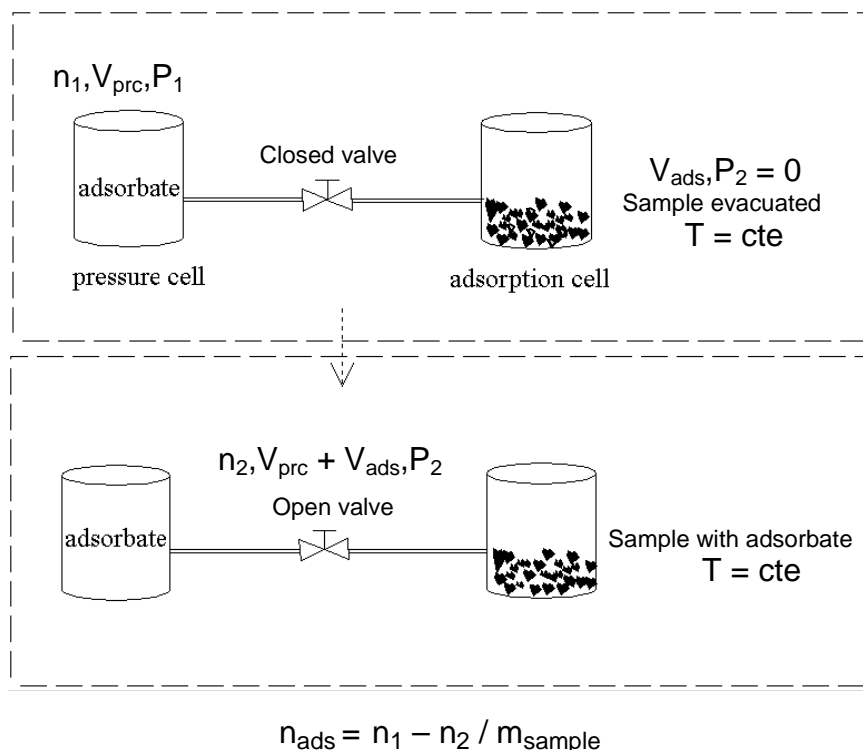


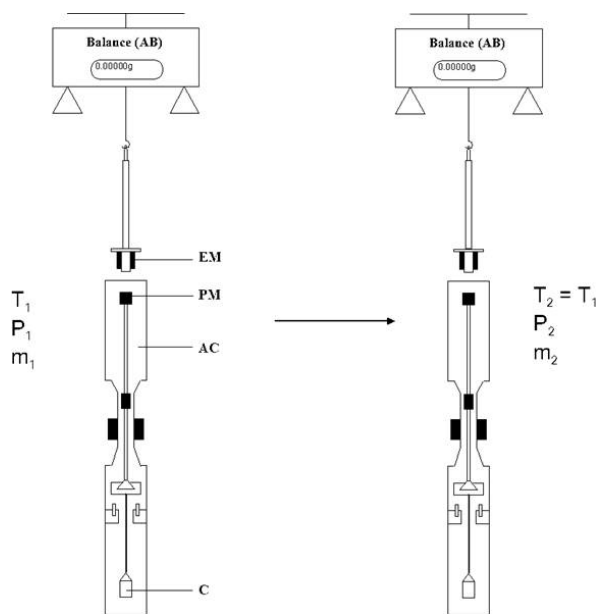
Fig. 2.21 Schematic representation of the volumetric method (courtesy of Y. Belmabkhout).

In general the method is simpler to implement and cheaper compared with gravimetric instruments. In addition, it is faster since the adsorbent is in direct contact with the thermostat. It is not readily applicable to measuring vapour adsorption, where condensation at ‘cold spots’ in the apparatus can be a problem.

Gravimetric Method

This method measures directly the amount adsorbed by the sample using a sensitive microbalance and a pressure gauge for loading the adsorbent into the adsorption chamber at constant temperature.

The different parts of the apparatus are presented in figure 2.22, which shows the magnetic balance (AB), the crucible (C) where the sample is placed hanging from a permanent magnet (PM) located in the adsorption chamber (AC). The weight increases of the sample due to the adsorption phenomenon are monitored directly by the analytical balance (AB).³¹



$$n_{\text{ads}} = m_2 - m_1 / m_{\text{sample}} M_{\text{ads}} \rightarrow [n_{\text{ads}}] = [\text{mol/g}]$$

Fig. 2.22 Schematic representation of the gravimetric method, where M_{ads} is the molar mass of the adsorbate (courtesy of Y. Belmabkhout).

This method is considered more reliable than volumetric method since it allows direct measurements and therefore is less sensitive to errors regarding pressure measurements. In contrast with volumetric methods it is more complex and expensive and takes a longer time.

During this thesis volumetric and gravimetric methods were used for the following applications:

- N_2 isotherms at 77 K at low pressures (0 to 1 bar) using either the Micromeritics or the Hiden IGA (Intelligent Gravimetric Analyser) instruments at University of St Andrews. The first instrument used the volumetric method and the second the gravimetric, figures 2.23 and 2.24 shows a typical isotherm for both methods respectively. Preferentially, the gravimetric method was applied since the volumetric method requires *ca.* 0.5 g of sample for an accurate measurement whereas in the Hiden IGA the sensitivity is such that *ca.* 50 mg of sample is enough. The measurements were carried out by Mrs Sylvia Williamson (St Andrews) and the data were used to obtain the pore volumes assuming the pores are filled with liquid N_2 .³¹ This information is used as a rate of the porosity of the materials once calcined for further applications (Chapter 3, 4 and 6).
- CO_2 isotherms on selected samples were carried out by Mrs Sylvia Williamson at low pressures (0 to 1 bar) from 273 K up to 303 K using the Hiden IGA instrument at University of St Andrews. The data are discussed in Chapter 7.
- CO_2 , CO and CH_4 isotherms at high pressures (0 to 40 bar) at 373 K using a Rubotherm instrument and the gravimetric method were carried out with Dr. Y. Belmabkhout at IFP-Lyon as a part of the INDENS project. The microbalance used here is less sensitive at low pressures (0 to 0.5 bar) than that of the Hiden IGA instrument and requires more sample (*ca.* 0.500 g as a minimum). The measurements were carried out at 373 K to improve resolution. These data are reported in Chapter 7, a typical isotherm is presented in figure 2.25.

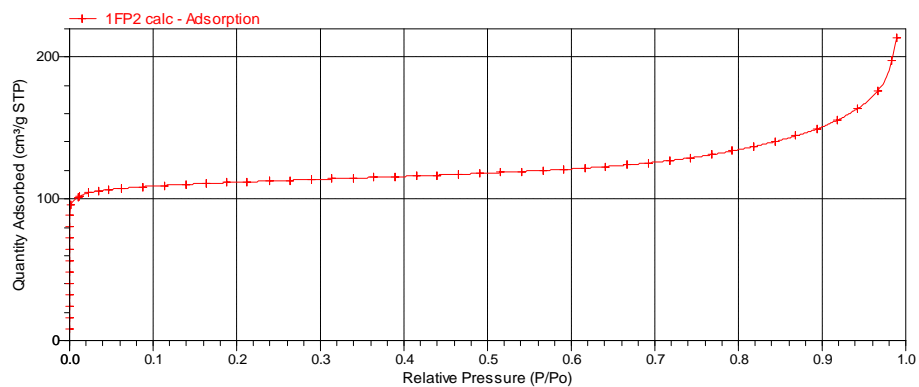


Fig. 2.23 N_2 isotherm of SAPO(20) STA-7 synthesised under industrial conditions using the volumetric instrument Micromeritics ASAP 2020.

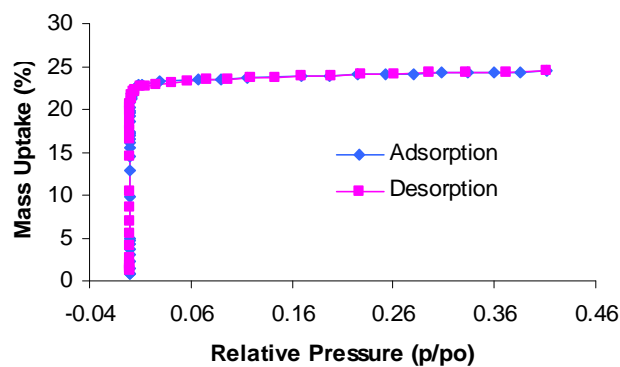


Fig. 2.24 N_2 isotherms of SAPO(20) STA-7 synthesised at laboratory conditions using the gravimetric Hiden IGA instrument.

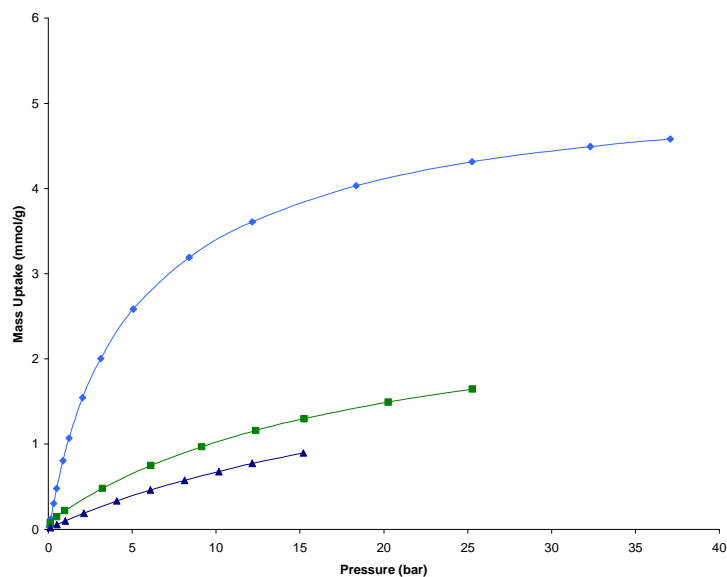


Fig. 2.25 Adsorption isotherms of SAPO(20) STA-7 at high pressures and 373 K for CO_2 (cyan), CH_4 (green) and CO (blue) measured using the gravimetric Robotherm instrument.

2.6 Molecular Modelling

Molecular modelling was performed in collaboration with A. Fecant (IFP-Lyon) using the approach developed by this group and it is fully described in his thesis.³² For the specific case of our collaboration, molecular modelling was applied to select the organic species with templating activity for target aluminophosphates structures and this is presented in the relevant sections (Chapter 3, 4, 5 and 6).

The method is based on the application of Molecular Mechanics (MM) to obtain the ‘adsorption’ and ‘torsion’ energy of the potential structure directing agents in the specific frameworks using the same criteria as those reported by Casci *et al.*³³

The MM methodology is semi-empirical, based on classic physics to describe the interaction between the framework and the template. Electrostatic interactions (long range) were ignored during modelling. Only the short range interactions (Van der Waals) between framework and the organic molecule were taken into account, making the calculations easier and less time consuming.

The semi-empirical approach enables a geometry optimisation of the frameworks and the templates and then the calculation of the minimum configuration for the ‘adsorption’ and ‘torsion’ energies. The terms ‘adsorption’ and ‘torsion’ are not really appropriate and they could be better replaced by the ‘energy of host-guest interaction’ and the ‘energy of steric constraint’. The terms ‘torsion’ and ‘adsorption’ were used for consistency with the previous work by Casci *et al.* The so called adsorption energy represents the affinity of a structure to an organic species and the torsion energy estimates the adaptability of the organic species within the structure. These two parameters were calculated using the software MS MODELLING 4.0 of Accelrys®³⁴ and the force field Universal³⁵.

Force Field Choice

Previous molecular modelling applications at IFP-Lyon were successfully performed on aluminosilicate systems using COMPASS³⁶ force field (Condensed-phase Optimised Molecular Potentials for Atomistic Simulation Studies).

COMPASS cannot be applied to aluminophosphates because it does not possess the parameters for phosphorus. The Universal force field operates with all elements of the periodic table. This forcefield as well as COMPASS were applied for the geometry optimisation of the aluminophosphate STA-7 (SAV). As can be observed in figure 2.26, after geometry optimisation, the unit cell is completely distorted by using COMPASS. Therefore the Universal forcefield was chosen.

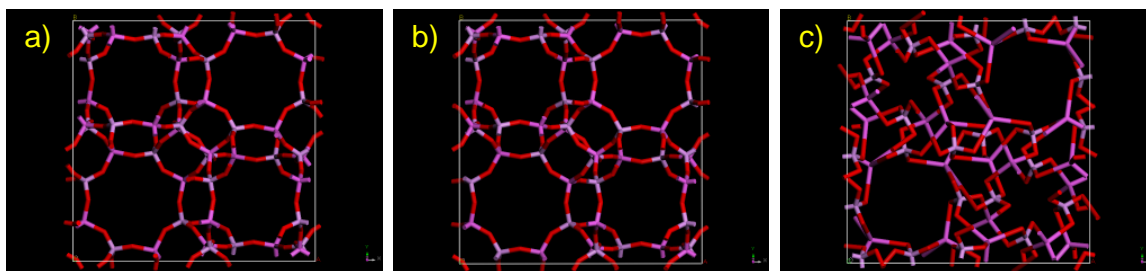


Fig. 2.26 Unit cell of the aluminophosphate STA-7 (SAV) before geometry optimization (a) and after using forcefield Universal (b) and COMPASS (c).

The Universal forcefield was tested to validate its use in AlPO systems by comparing the calculated and experimentally-measured coordinates of the organic cation tetraethylammonium (TEA), which templates the small cage of STA-7. This is fully described in Chapter 3 and demonstrates a perfect fit between theoretical and experimental values. In this way the Universal forcefield was also applied to model the hypothetical aluminophosphate structure with KFI framework and the potential template for the small cage of this structure (Chapter 4). In addition, it was applied for the design of novel templates for STA-2 material (Chapter 6).

Calculation of the adsorption energy

The adsorption energy defines the ‘host-guest’ interaction and is described as follows:

$$E_{\text{ads}} = E_{\{\text{framework} + \text{template}\}} - E_{\text{framework}} - E_{\text{template}}$$

This value requires three steps: i) geometry optimisation of the template in vacuum to obtain the optimum configuration and therefore the minimum of energy, ii) geometry optimisation of the structure by the application of the forcefield iii) random docking of different configurations of the template into the pore space to obtain the most favourable locations by geometry optimisation, see figure 2.27. The most favourable value (the most negative) is selected.

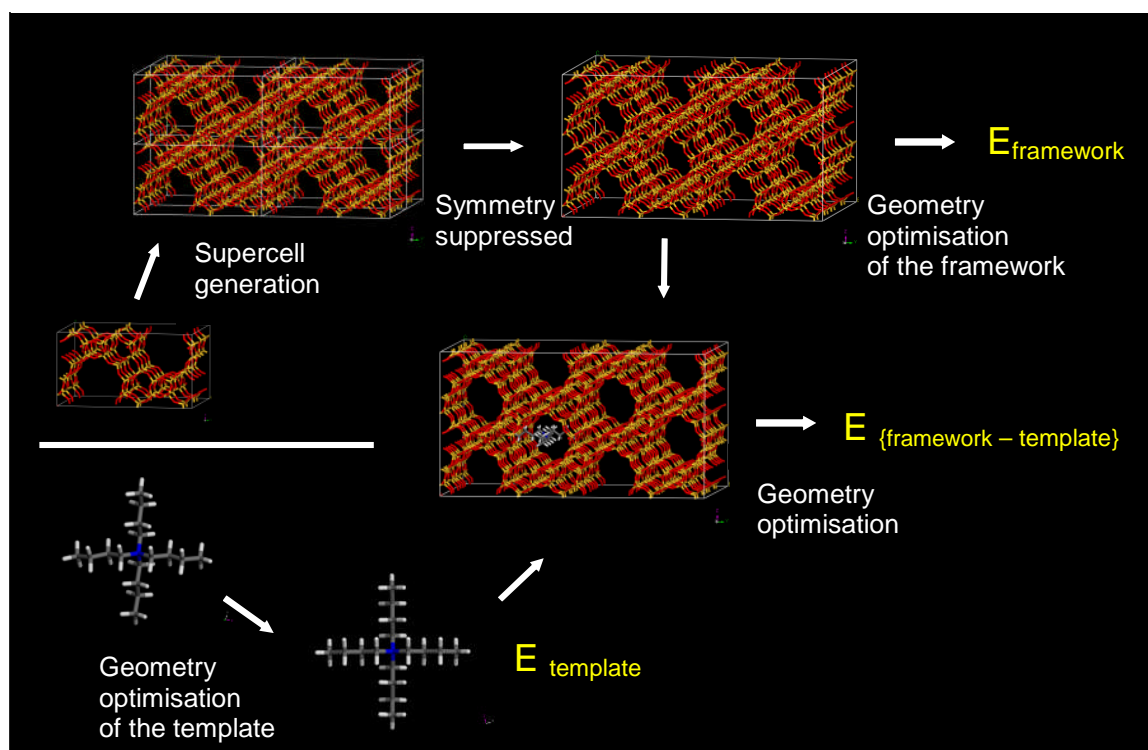


Fig. 2.27 Steps in the adsorption energy calculation (courtesy of A. Fecant).

Calculation of the torsion energy

The torsion energy defines the energy of steric constraints of the template and it is described as follows:

$$E_{\text{tor}} = E_{\text{template}}^{\text{f}} - E_{\text{template}}^{\text{i}}$$

The torsion energy is the difference between the energy of the template in vacuum with the optimum conformation within the framework and the energy of the template in vacuum with the optimum conformation in vacuum, see figure 2.28. The higher this value

the more difficulties the organic molecule will experience to adapt to the pore space within the framework.

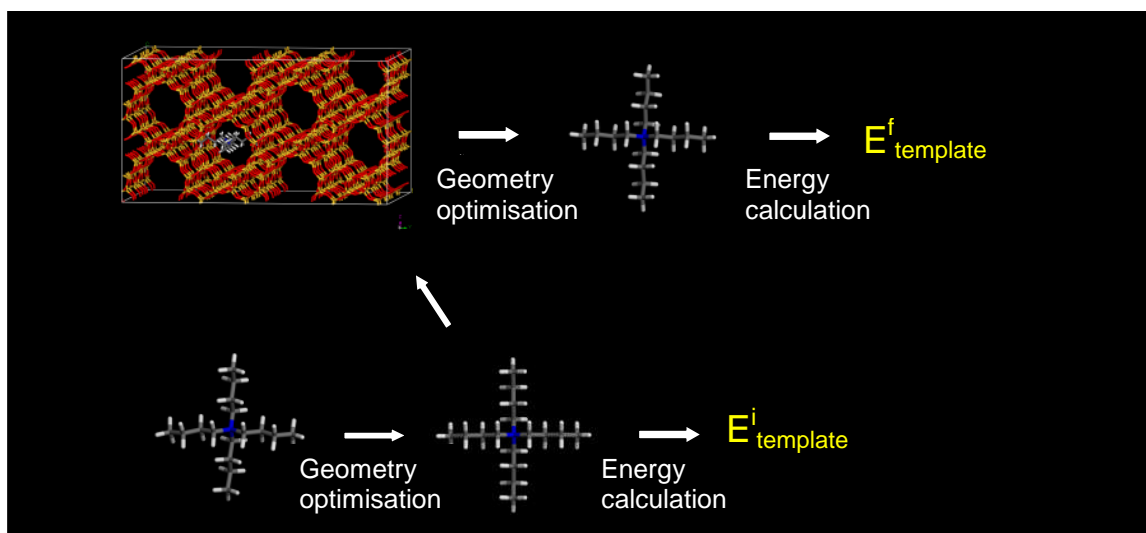


Fig. 2.28 Steps in the torsion energy calculation (courtesy of A. Fecant).

2.7 Other Techniques

2.7.1 FTIR³⁷

Fourier Transformation Infra Red (FTIR) is a spectroscopic technique like NMR, but in this case the electromagnetic radiation used ($\lambda = 10^{-6}$ m) causes vibrational transitions within the bonds in the framework section and can be used to observe the Brønsted acid sites, Si(OH)Al.

FTIR spectra can give information about the acidic strength of the material by monitoring the adsorption of basic molecules which will interact with the bridging hydroxyl group without subtracting the proton, such as deuterated acetonitrile (CD_3CN). The most useful types of excitation are the stretching vibrations (Fig. 2.29) with the following frequency ranges: Si(OH)Al at 3250 to 3660 cm^{-1} , $\text{C}\equiv\text{N}$ unperturbed at 2260 cm^{-1} and perturbed by the acid sites at 2311 cm^{-1} .^{38,39} The values observed for SAPO STA-7 are in the same range: at 3600-3625, 2258 and 2325 cm^{-1} , respectively (section 3.3.3.1).

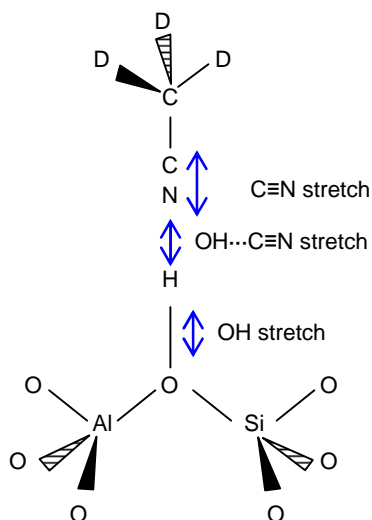


Fig. 2.29 Stretching bond vibrations that occur in the solid and the basic probe molecule deuterated acetonitrile (CD_3CN) to study the acidic strength of the Brønsted sites in SAPO materials.

2.7.2 SEM and EDX⁴⁰

Scanning Electron Microscopy (SEM) is a technique that uses electrons instead of light to form an image, and it is applied in this thesis to study the morphology of the products. In addition, Energy Dispersive X-ray spectroscopy (EDX) was used to determine the chemical composition of the samples semi-quantitatively.

As the electron beam hits the sample, a number of phenomena occur at the surface. The most important for scanning microscopy are the emission of secondary electrons for topographical information and the X-rays for EDX.

Secondary electrons are the electrons of the sample emitted by the electron beam due to electrostatic repulsion. These electrons are moving very slowly when leaving the sample. Since they are moving so slowly, and are negatively charged, they can be attracted to a positive charged detector (Fig. 2.33 f). The 3D appearance is because secondary electrons emission is dependent on topography. Regions that have direct line of sight to detector will also appear brighter, see figure 2.30 for some examples.

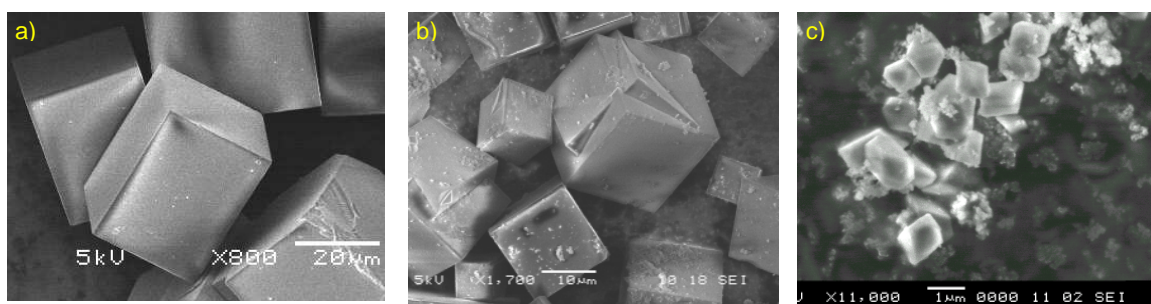


Fig. 2.30 SEM images using secondary electrons of SAPO STA-7 (a), MgAPO STA-14(b) and AlPO STA-2 (c) materials studied in Chapters 3, 4 and 6 respectively.

The interaction of the electron beam with the sample generates the emission of characteristic X-rays of the atoms contained in the sample and can be used for semi-quantitative chemical microanalysis. A flat image is formed using a suitable detector (Fig. 2.26 e). This image is an element distribution map in which the contrast variation reflects the concentration of any chosen element. Selected elements can be quantified giving an atomic percentage and from this, a weight percentage can be calculated if calibrated against a known standard. This technique is denoted as EDX and the data can be collected as a point analysis or via area mapping, examples are provided in figure 2.31 and 2.32, respectively.

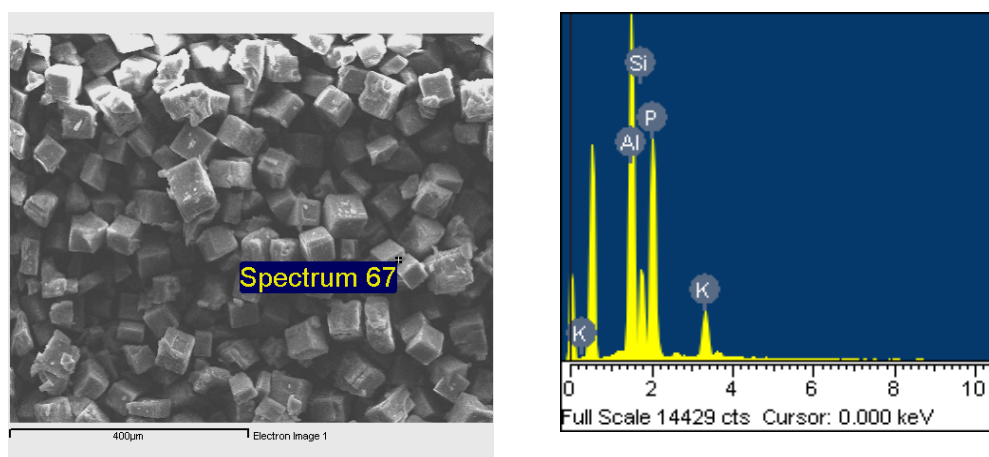


Fig. 2.31 EDX of SAPO STA-7 crystals successfully ion exchanged with potassium. On the left, the SEM image shows the point where the EDX analysis was made and the right, the X-ray spectrum emitted by the framework cations (Al, Si, P) as well as the extra framework potassium cation (K).

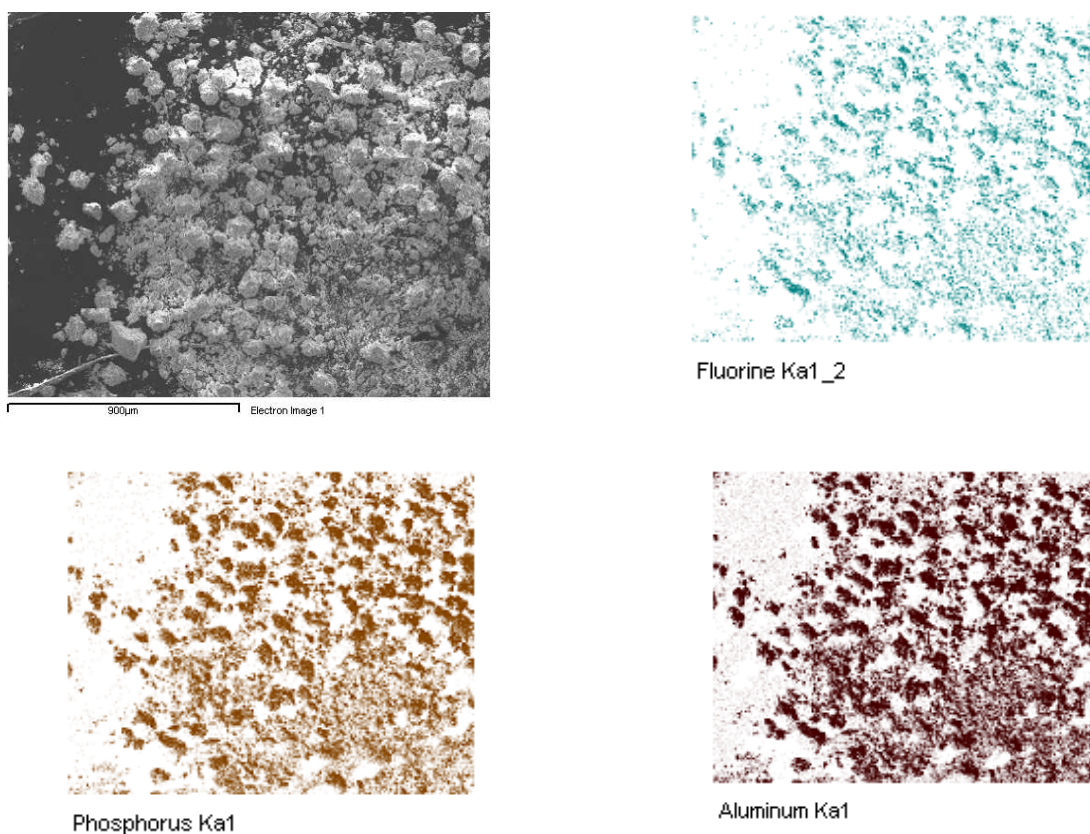


Fig. 2.32 EDX mapping from an AlPO material synthesised in the presence of fluoride ions. These results show the homogeneous incorporation of these ions in the product.

Experimental procedure

The instrument at the University of St Andrews is a Jeol JSM-5600 with a tungsten (W) filament. Maximum magnification is 300,000× with a resolution of 3.5 nm. The specimen tilting range is -10° to $+90^\circ$ and specimen rotation is 360° , accelerating voltage 30 kV. The instrument uses backscattered electrons to form the image. Figure 2.33 illustrates the parts of a SEM instrument.

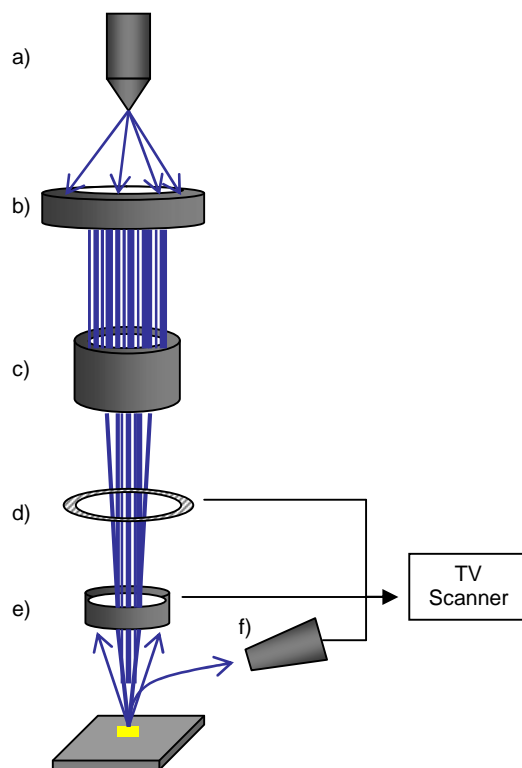


Fig. 2.33 Scheme showing the different parts of a SEM instrument. From the top to the bottom: the electron gun (a) is the source of accelerated electrons, the anode (b) and the magnetic lens (c) focus the electron beam, the scanning coils (d) move the beam along the sample, the detectors for backscattered electrons and secondary electrons (e and f, respectively) collect the emitted electron current and finally the signal is amplified and used in a cathode ray tube to obtain a image.

2.7.3 TGA⁴¹

Thermogravimetric Analysis (TGA) is applied to measure the water and the organic content to calculate the unit cell composition. The change in mass is monitored as a function of temperature under an oxygen gas flow. The figure 2.34 shows a typical TGA, in this case for SAPO STA-7. The first weight loss of *ca.* 5% at 100 °C corresponds to the removal of water molecules and the second step corresponds to the decomposition of the organic species with *ca.* 17% weight lost.

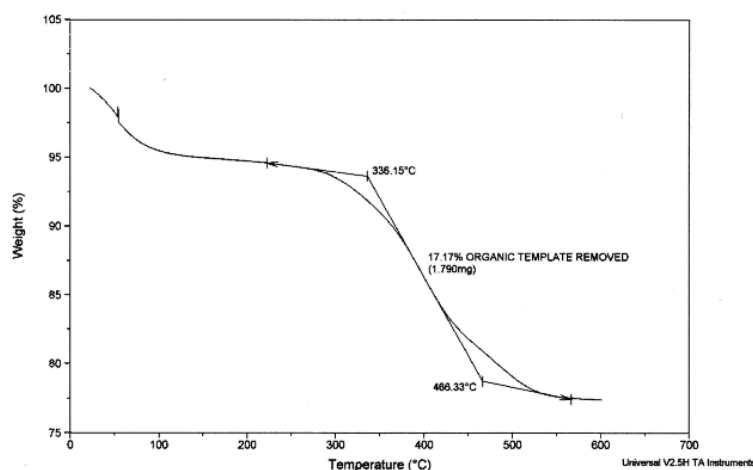


Fig. 2.34 Typical TGA thermogram of SAPO STA-7.

2.7.4 Elemental Analysis

Microanalysis is used to determine the amount and type of organic species occluded within the pores. The techniques provided percentages of carbon, hydrogen and nitrogen (CHN). These data are combined with TGA for the calculation of the unit cell composition.

For example AIPO STA-2 was synthesised with two different templates with very similar structure, and elemental analysis suggests that in both cases the templates fully occupy the elongated cages since the unit cell requires three of these molecules if they template the three cages that are contained within the unit cell. These results were corroborated by the TGA which has a weight loss corresponding to three organic molecules and 26 water molecules.

Table 2.5 Results of microanalysis of AIPOs STA-2. The calculated values used a theoretical composition of $[Al_{36}P_{36}O_{144}] \cdot R_3 \cdot (H_2O)_{26}$

| Framework | Template (R) | C%Cal | N%Cal | CHN Analysis |
|------------|--------------|-------|-------|------------------|
| AIPO STA-2 | DABCO_C4 | 9.87 | 2.88 | C% 9.89 N% 2.87 |
| AIPO STA-2 | DiQuinD4 | 11.11 | 1.44 | C% 11.06 N% 1.43 |

-
1. Ch. Baerlocher, L. B. McCusker, D. H. Olson, '*Atlas of Zeolites Framework Types*', Elsevier, London, 6th Edition, 2007.
 2. <http://www.iza-online.org/>
 3. M. M. J. Treacy, J. B. Higgins, '*Collection of Simulated XRD Powder Patterns for Zeolites*', 4th Edition, Elsevier, Amsterdam, 2001.
 4. G. M. Sheldrick, '*SHELXL97*', Gottingen, Germany, 1997.
 5. <http://www.chem.gla.ac.uk/~louis/software/wingx/index.html>
 6. <http://www.chem.gla.ac.uk/~louis/software/platon/>
 7. R. E. Morris, P. S. Wheatley, '*Introduction to Zeolite Science and Practice*', Elsevier, Amsterdam, 2007, 388.
 8. H. M. Rietveld, *Acta. Crystallogr.*, 1967, **22**, 987.
 9. A. K. Cheetham, '*Solid State Chemistry Techniques*', Eds. A.K. Cheetham and P. Day, Oxford Science Publications, 1988.
 10. C. Giacovazzo, H. L. Monaco, D. Viterbo, F. Scordari, G. Gilli, G. Zanotti, M. Catti, '*Fundamentals of Crystallography*', Oxford University Press, 1992.
 11. <http://www.ccp14.ac.uk/solution/gsas/>
 12. K. J. D. Macenzie, M. E. Smith, '*Multinuclear Solid-State NMR of Inorganic Materials*', Pergamon, Oxford, 2002.

-
13. L. M. Harwood, T. D. W. Claridge, in *'Introduction to Organic Spectroscopy'*, Oxford University Press, Oxford, 1996.
 14. P. Zeeman, *Nature (London)*, 1987, **55**, 347.
 15. M. J. Agger, *'Solid State NMR Spectroscopy: principles and applications'*, Blackwell Science, Oxford, 2002.
 16. A. Gadeon, C. Fernandez, in *'Introduction to Zeolite Science and Practice'*, Elsevier, 2007, 406.
 17. M. J. Agger, in *'Solid State NMR Spectroscopy: principles and applications'*, Blackwell Science, Oxford, 2002, 59.
 18. E. R. Andrew, A. Brandbury, R. G. Eades, *Nature*, 1959, **183**, 1802.
 19. L. Frydman, J. S. Harwood, *J. Am. Chem. Soc.*, 1995, **117**, 5397.
 20. W. P. Aue, E. Bartholdi, R. R. Ernst, *J. Chem. Phys.*, 1976, **64**, 2229.
 21. J. Keeler, in *'Understanding NMR Spectroscopy'*, Wiley, Chichester, 2005, 31.
 22. P. A. Wright, *'Microporous Frameworks Solids'*, RSC Publishing, Cambridge, 2008, Table 3.1.
 23. P. J. Barrie, J. Klinowski, *J. Phys. Chem.*, 1989, **93**, 5972.
 24. R. Garcia Salas, *Synthesis and Characterisation of Aluminophosphate-Based Materials Prepared with Nickel Complexes as Structure Directing Agents*, PhD Thesis, University of St Andrews, 2003.

-
25. G. Engelhardt, D. Mitchel, in '*High-Resolution Solid-State NMR of Silicates and Zeolites*', Wiley, New York, 1987.
27. P. Llewellyn, G. Maurin, in '*Introduction to Zeolite Science and Practice*', Elsevier, Amsterdam, 2007, 555.
27. K. S. W. Sing, D. H. Everett, R. A. W. Haul, L. Moscou, R. A. Pierotti, J. Rouquerol and T. Siemieniewska, *Pure Appl. Chem.*, 1985, **57**, 603.
28. M. Thommes, in '*Introduction to Zeolite Science and Practice*', Elsevier, Amsterdam, 2007, 496.
29. M. Thommes, in '*Introduction to Zeolite Science and Practice*', Elsevier, Amsterdam, 2007, 498.
31. Y Belmabkhout, M Frere, G DeWeireld, *Meas. Sci. Technol.*, 2004, **15**, 848.
31. M. Thommes, in '*Introduction to Zeolite Science and Practice*', Elsevier, 2007, 512.
32. A. Fecant, *Synthese de nouvelles Zeolithes possédant des ouvertures de pores à 10 et 12 atomes tétraédriques*, PhD Thesis, Ecole Normale Supérieure de Lyon, 2007.
33. P. A. Cox, J. L. Casci, R. P. G. Henney, S. Maberly, M. D. Shannon, intern report ICI n° 13676, 1992.
34. MS Modelling version 4.0, Accelrys Inc, San Diego, USA, 2006.
35. A.K. Rappé, C.J. Casewit, K.S. Colwell, W.A. Goddard, W.M. Skiff, *J. Amer. Chem. Soc.*, 1992, **114**, 10024; C.J. Casewit, K.S. Colwell, A.K. Rappé, *J. Am. Chem. Soc.*, 1992,

114, 10035; C.J. Casewit, K.S. Colwell, A.K. Rappé, *J. Am. Chem. Soc.*, 1992, **114**, 10046; A.K. Rappé, K.S. Colwell, C.J. Casewit, *Inorg. Chem.*, 1993, **32**, 3438.

38. H. Sun, *J. Phys. Chem. B*, 1998, **102**, 7338; H. Sun, P. Ren, J. R. Fried, *Computational and Theoretical Polymer Science*, 1998, **8**, 229.

37. E. L. Meijer, R. A. Van Santen, A. P. J. Jansen, *J. Phys. Chem. A*, 1999, **103**, 2553.

38. F. Schüth, K. S. W. Sing, J. Weitkamp, Eds., '*Handbook of Porous Solids*', Wiley, New York, 2002.

39. G. Pearce, S. Bordiga, Pers. Comm.

40. P. J. Goodhew, F. J. Humphreys, '*Electron Microscopy and Analysis*', 2nd Edition, Taylor and Francis, London, 1988.

41. F. W. Fifield, D. Kealey, '*Principles and Practice of Analytical Chemistry*', 3rd Edition, Blackie Academic and Professional, London, 1990.

PART 2

Synthesis & Structural Characterisation of Zeotypes

**D6R materials
STA-7 (SAV)
STA-14 (KFI)**

**ABC material
STA-2 (SAT)**

Synopsis

This section covers the study of the hydrothermal synthesis of zeotypes. The search for novel materials using this method is mainly based on trial and error, due to the complexity of this system where the variables are interrelated, making control of the synthesis difficult for targeted structures.

The so-called ‘co-templating’ approach, supported by modelling, is presented here. Its aim is to design the synthesis of materials that contain more than one kind of cage, such as STA-7 (SAV) and STA-14 (KFI). Modelling is shown to be a powerful tool as a preliminary step in planning synthesis, helping to rationalise and optimise experimental efforts to obtain desirable materials for further applications. The synthesis of the small pore aluminophosphate STA-2 (SAT) via a new route is also described here.

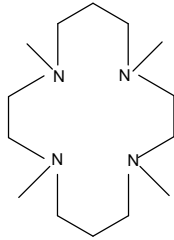
This part of the thesis includes the results and discussion of synthesis and structure characterisation of STA-7, STA-14 and STA-2.

Chapter 3: STA-7

3.1 Introduction

The novel microporous aluminophosphate-based solid STA-7 (**SAV**) was first reported by Wright *et al.* in 2000.¹ This framework was templated by the azamacrocycle tetramethylcyclam (TMcyclam) in a CoAPO gel, heated at 190 °C for two days. Depending on the gel composition, this SDA directs the crystallisation of substituted AlPOs STA-6 (**SAS**) or STA-7 (**SAV**) (Table 3.1).²

Table 3.1 Cation composition in MAPO gels and their products in presence of TMcyclam.

| Template | Cation in Gel | Product |
|--|--------------------------|------------------------|
|  tetramethylcyclam (TMcyclam) | No Cation | AlPO-21 (AWO) |
| | Mg(II), Mn(II) or Fe(II) | STA-6 (SAS) |
| | Co(II) or Zn(II) | STA-7 (SAV) |

Both structures contain cages: STA-6 has only one type, whereas STA-7 has two different types, A and B, shown in figure 3.1.

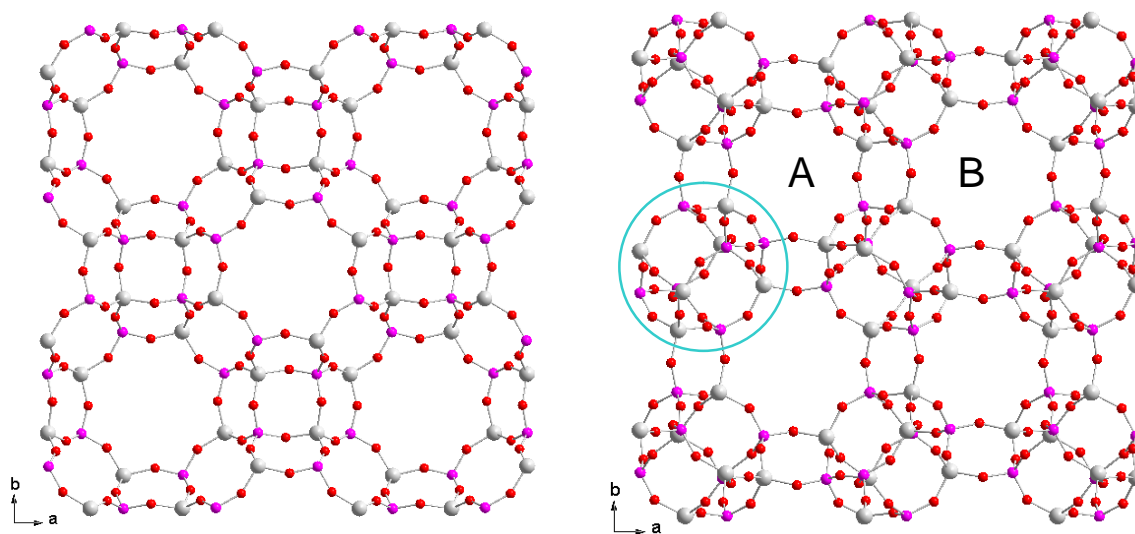


Fig. 3.1 The structures of STA-6 (left) and STA-7 with a D6R highlighted within a circle (right).

Of these two structures, STA-7 was the more promising for further applications in adsorption and catalysis due its structural similarities to SAPO-18 (AEI) and SAPO-34 (CHA), which are selective catalysts for the methanol to olefins reaction (MTO).^{3,4} Therefore the formation of STA-7 in SAPO form was an attractive target for synthesis.

CHA, AEI and SAV structure types are all composed of double 6-membered rings (D6Rs) linked differently by 4-membered rings (4MRs). The SAV structure can be described as chains of D6Rs linked along *c* by 4MRs and attached to adjacent chains by Al-O-P bonds. The two cages of STA-7 are connected three dimensionally via 8MR windows. The larger cages (B) are connected along *c* via planar 8MR windows and along *a* and *b* these cages are connected to the smaller ones (A) via elliptical 8MR windows. The framework has three different tetrahedral (T) sites with similar average T- \hat{O} -T values.

The template activity of TMcyclam in CoAPO STA-7 occurs via its inclusion within the larger cage (B) since modeling indicates that it cannot fit into the smaller cage. The use of TMcyclam in a SAPO gel forms the SAPO STA-6 structure. Therefore, a second

organic base that would fit closely into the smaller cage should favour the crystallization of the STA-7 over the STA-6 structure using TMcyclam as the primary SDA.

As a result, experimental synthesis was performed adding a second ‘co’-base. Three candidates were selected on the basis of size, di-n-propylamine (DPA), di-isopropylamine (DIPA) and tetraethylammonium cations (TEA). The addition of TEA as a co-base directs the crystallization to STA-7 rather than STA-6, whereas mixtures of STA-7 and STA-6 were obtained with DIPA and STA-6 remained favoured by the addition of DPA. Moreover, this observation was also obtained using cyclam instead of TMcyclam, being the cheaper option. Also the cost of the synthesis was decreased because the added co-base performs the second function of pH regulation, so that the final amount of azamacrocycle is lower.^{5,6}

As observed, the use of a co-base can lead to the target material and therefore this co-base was called a ‘co-template’. This chapter covers the synthesis and structural study of the STA-7 supported by modelling to understand the role of TEA as co-template in an attempt to rationalise the hydrothermal synthesis for the further synthetic research presented in this thesis.

Special attention was paid to obtain stable SAPO STA-7 material as a reference for the INDENS project and it is therefore fully characterised in the as-prepared and calcined forms. This is relevant to studies of its properties detailed in Part 3.

3.2 Experimental

Synthesis and Product Recovery

The materials reported here were obtained hydrothermally by combining sources of the metal framework species with distilled water and the desired template (and co-base where appropriated), to form a homogeneous gel. All the reagents were used as supplied without further purification (Table 3.2). The organic templates were purchased from either Aldrich or Avocado.

Table 3.2 *Inorganic reagents used in this work.*

| Reagent | Purity (%) | Supplier |
|------------------------------------|------------|-------------------------|
| Magnesium(II) acetate tetrahydrate | 99 | Fluka |
| Zinc(II) acetate dehydrate | 98.5 | BDH |
| Manganese(II) acetate tetrahydrate | 98 | Avocado |
| Cobalt(II) acetate tetrahydrate | 98 | Aldrich |
| Aluminium hydroxide hydrate | - | Aldrich |
| Aqueous orthophosphoric acid | 85 | Prolabo |
| Silica, fumed | 97 | Fluka |
| Silica, colloidal LUDOX HS-30 | - | Aldrich |
| Copper(II) acetate | 98 | Hopkin and Williams Ltd |
| HF | 48 | Aldrich |
| Silver(I) oxide | 97 | Acros |

In a typical synthesis, aluminium hydroxide was dissolved in a solution of orthophosphoric acid in water. Next, the metal acetate or the silica source was added followed by the template. Then, the co-base was introduced drop-wise until a pH of 7 was achieved. The gel was stirred until it became homogenous. Then it was loaded into a Teflon-lined stainless steel autoclave and heated under autogenous pressure in static conditions at 190 °C for two or seven days for MAPO and SAPO gels respectively (Table 3.3). The variations in gel compositions, aging, reaction temperatures, heating times and stirring conditions were investigated and are clearly marked in the text in the appropriate sections.

Table 3.3 *Typical ratios in gel, x denotes the addition drop-wise of co-base up to pH 7.⁶*

| Gel | Typical Ratios | Time (days) | Temp. (°C) |
|------|--|----------------|---------------|
| AlPO | Al : P : 40H ₂ O : 0.2HF : 0.108template : x co-base | 2 | 190 |
| MAPO | 0.2Mg : 0.8Al : P : 40H ₂ O : 0.108template : x co-base | 2 | 190 |
| SAPO | Al : 0.8P : 0.2Si : 40H ₂ O : 0.108template : x co-base | 7 | 190 |

In syntheses where metal complexes of the macrocycle were used, the complex was pre-prepared by adding the ligand to an aqueous solution of the metal acetate and this solution was then introduced to the gel.

After hydrothermal treatment, the autoclave was removed from the oven and allowed to cool. A sample of the reaction product was examined under the optical microscope to observe the crystallinity of the product. Crystalline products were separated from the resulting mixtures by filtration, washed with distilled water and dried in air. In cases where a mixture of phases was obtained, the sample was suspended in water and sonicated to separate the products by density.

Calcination

Calcination was used to remove the organic species occluded within the pores in the as-prepared materials. Selected samples were calcined overnight in a tube furnace at the desired temperature, typically 550 °C (achieved via a heating ramp of 1.5 °C/min) under dry flowing oxygen and kept at that temperature for 12 hours before allowing the sample to cool down.

Characterisation

Phase identification of the products was performed by powder X-ray diffraction using a Stoe STADIP diffractometer operating in transmission mode with Cu K $_{\alpha 1}$ X-rays. Diffraction patterns were collected over the range 5-50° 2 θ for 1.5 hours, and indexed using the Stoe software suite.⁷ For structural analysis on calcined samples, XRD was measured in 0.7 mm quartz glass capillaries sealed after dehydration at 200 °C under vacuum; data are recorded over the range 5-80° 2 θ for 12 hours and structures were refined via the Rietveld method using the GSAS program suite.⁸ Single crystal X-ray diffraction (SXRD) was applied for suitable samples: as-prepared, calcined and Cs⁺ exchanged SAPO STA-7, as-prepared MgAPO and SAPO STA-14 and as-prepared novel layer phase (Chapter 3, 4 and 5 respectively). The structures were solved by direct methods and refined using the program SHELXTL⁹ from data collected by Prof. A. M. Z.

Slawin at St Andrews University on Rigaku diffractometers using either Mo K α or Cu K α X-rays.

MAS NMR spectra were collected at the EPSRC solid-state NMR Facility in Durham University by Dr David Apperley on samples summarised in Table 3.4. ^{27}Al and ^{31}P experiments were performed on a Varian UNITY VNMRs 400 spectrometer, using a 4 mm probe and for ^{29}Si and ^{13}C a Unity Inova 300 spectrometer, using a 7.5 mm probe. Table 3.5 summarises the experimental conditions. MAS NMR spectra on samples **4** and **5** calcined were collected by Dr Philip Wormald at the University of St Andrews on a Varian UNIT plus 500 spectrometer, using a 7.5 mm probe. The 0 ppm in the spectra was defined as the shift for 1M aqueous AlCl_3 , 85% H_3PO_4 and tetramethylsilane (TMS), for ^{27}Al , ^{31}P and ^{29}Si respectively.

Inorganic chemical analysis was performed by EDX on a JEOL JSM-5600 SEM with an Oxford INCA Energy 200 analyser, and the organic component (CHN) was measured on a Carlo Erba EA 1110 CHNS analyser. TGA was performed under flowing oxygen at 5 °C/min on a TA Instruments SDT 2960 thermogravimetric analyser from room temperature to 700 °C. N_2 adsorption was performed at 77 K on dehydrated samples using an automated HIDEN gravimetric porosimeter. Elemental analysis and N_2 adsorption were performed by Mrs Sylvia Williamson at St Andrews.

Modelling and energy minimisation were calculated using the software MS MODELLING 4.0 of Accelrys®¹⁰ and the force field Universal.¹¹

Table 3.4 STA-7 samples used for MAS NMR experiments ordered according to their appearance in the text.

| Samples | | | Composition in Gel | | | | |
|----------|----------|----------|--------------------|-------|------|------|------|
| 1 | 2 | 3 | MgAPO | Mg/P | 0.50 | 0.20 | 0.10 |
| 4 | 5 | 6 | SAPO | Si/Al | 0.20 | 0.10 | 0.30 |

Table 3.5 Experimental parameters for ^{27}Al , ^{31}P , ^{29}Si and ^{13}C MAS NMR spectra on samples summarised in Table 3.4 (DP = Direct Polarisation, CP = Cross Polarisation, DD = Direct Detected, ID = Indirect Detected).

| Sample | Freq (MHz) | Acq time (ms) | Relaxation delay (s) | Polaris | Contact time (ms) | Pulse time (μs) | Spin rate (kHz) |
|------------------|---------------|---------------------|----------------------------|--------------------|-------------------------|------------------------------------|-----------------------|
| ^{27}Al | | | | | | | |
| 1 | 104.199 | 10.0 | 0.2 | DP | - | 1.0 | 14 |
| 4 | 104.198 | 20.0 | 0.2 | DP | - | 1.0 | 14 |
| ^{27}Al | | | | | | | |
| 1 | 104.199 | 5.1 | 0.2 | DD (F2) ID (F1) | | 3.4 and 1.2 | 14 |
| 4 | 104.198 | 2.5 | 0.1 | DD (F2) ID (F1) | | 3.3 and 1.4 | 14 |
| ^{31}P | | | | | | | |
| 1, 2 | 161.878 | 10.0 | 300.0 | DP | - | 3.4 | 10 |
| 3 | 161.878 | 20.0 | 300.0 | DP | - | 3.4 | 10 |
| 4 | 161.878 | 15.0 | 10.0 | CP | 3.00 | - | 10 |
| ^{29}Si | | | | | | | |
| 4 | 59.557 | 30.0 | 120.0 | DP | - | 90° | 5 |
| 5 | 59.557 | 30.0 | 1.0 | CP | 1.00 | - | 5 |
| 6 | 59.557 | 20.0 | 120.0 | DP | - | 90° | 5 |
| 4 calc. | 99.360 | 15.7 | 300.0 | DP | - | 2.5 | 5 |
| 5 calc. | 99.360 | 15.7 | 300.0 | DP | - | 3.0 | 5 |
| 6 calc. | 59.557 | 50.0 | 120.0 | DP | - | 90° | 5 |
| ^{13}C | | | | | | | |
| 4 | 75.398 | 30.0 | 1.0 | CP | 1.00 | - | 5 |

3.3 Results & Discussion

3.3.1 Synthesis

This section primarily discusses the synthesis of STA-7 in the silicoaluminophosphate (SAPO) composition, since its production was important for the INDENS project to use it as a reference material.

As part of the project, the most important issues for the SAPO and related materials were their stability after calcination for adsorption measurements and their morphology for diffusion measurements. The scale-up of production was also desirable.

3.3.1.1 Checking Previous Synthetic Method

The synthesis route previously developed by R. Garcia⁵ and S. Warrender⁶ was used as a starting point: the co-base TEOH was added before the template, in this case cyclam. The synthesis of STA-7 SAPO was studied at different Si/Al ratios on a small scale (9 g of water). Table 3.6 summarises the experiments and products obtained.

Table 3.6 Summary of the SAPO STA-7 synthesis using established procedure at Si/Al ratios 0.2, 0.1, 0.05 and 0.02, where silicon replaces 20%, 10%, 5% and 2% of the total amount of phosphorus added to the gel respectively: $Si\% = (Si/Si+P) \cdot 100$.

| Product (by XRD) | Composition in Gel | | | | | | | <i>t</i> (days) | <i>T</i> (°C) |
|---------------------|--------------------|------|------|------------------|--------|--------|-------|--------------------|------------------|
| | Al | P | Si | H ₂ O | HF(ml) | cyclam | TEAOH | | |
| STA-7 | 1 | 0.8 | 0.2 | 40 | - | 0.108 | 0.42 | 7 | 190 |
| STA-7 | 1 | 0.9 | 0.1 | 40 | - | 0.108 | 0.38 | 7 | 190 |
| STA-7 [#] | 1 | 0.95 | 0.05 | 40 | - | 0.108 | 0.38 | 7 | 190 |
| STA-7 [#] | 1 | 0.98 | 0.02 | 40 | - | 0.108 | 0.40 | 7 | 190 |
| STA-7 [#] | 1 | 0.98 | 0.02 | 40 | 0.07 | 0.108 | 0.38 | 7 | 190 |

[#]Poorly crystalline

Highly crystalline SAPO STA-7 was obtained using Si/Al 0.2 and 0.1 denoted as SAPO(20) and SAPO(10) by replacing 20% and 10% of the total amount of phosphorus added to the gel (with similar lattice parameters in both cases: SAPO(20) $a = 18.735(2) \text{ \AA}$ and $c = 9.385(1) \text{ \AA}$ and SAPO(10) $a = 18.742(6) \text{ \AA}$ and $c = 9.387(6) \text{ \AA}$). At 5% and 2% Si the STA-7 product had poor crystallinity. Addition of HF at such low silicon ratios did not increase the crystallinity of the product (Fig. 3.2).

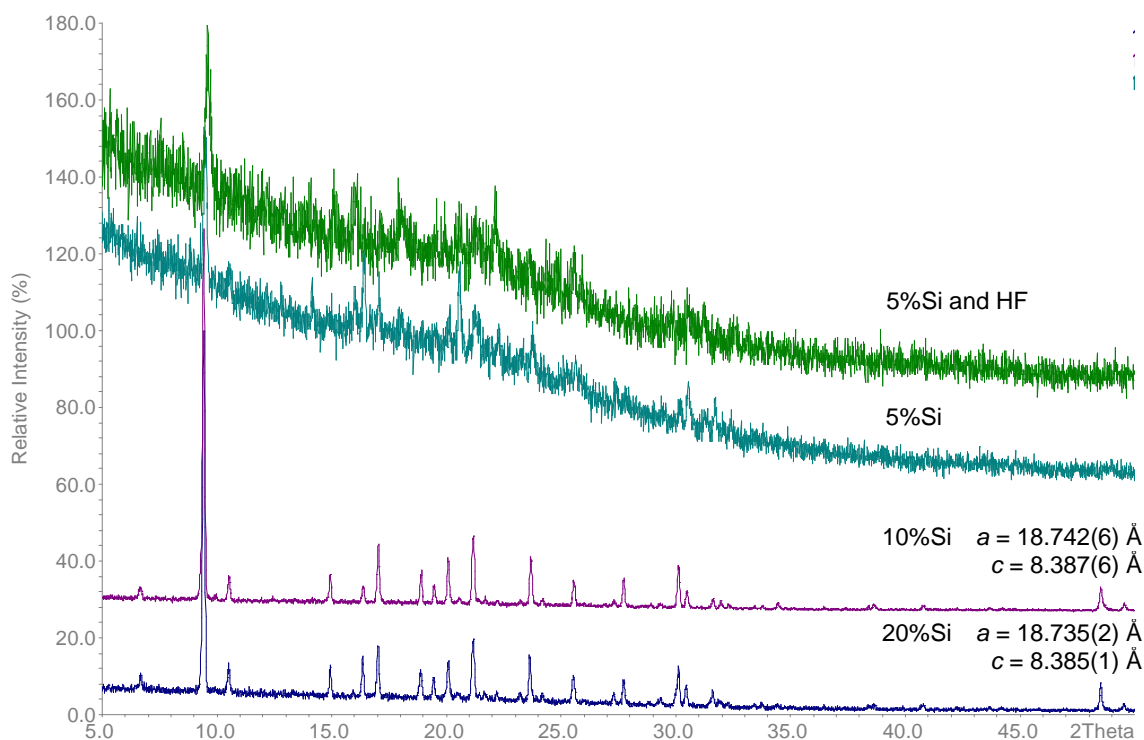


Fig. 3.2 XRD patterns of SAPO STA-7 using 20%, 10% and 5% Si in gel (blue, purple and cyan respectively). At 5% Si, the addition of HF does not help to crystalline STA-7 as observed in the pattern (green); $\text{Si}\% = (\text{Si}/\text{Si}+\text{P}) \cdot 100$.

Experimental patterns of SAPO(20) and SAPO(10) agree with the results of previous work.⁶ There is only one discrepancy, a small peak at $20.5^\circ 2\theta$ that could be attributed to SAPO-18. This material does not appear as an extra discrete phase in the product, but Atomic Force Microscopy (AFM) results suggest it could be present on the surface of already-formed STA-7 crystals (see section 5.2 for details). Once calcined at 550°C for 12 hours in a steam of dry oxygen, SAPO(20) is more crystalline than SAPO(10) as denoted by the XRD patterns and the SAPO(20) unit cell slightly shrink by the removal of

the templates (Fig. 3.3). The morphology of both samples was similar to that reported in previous work and shows cubes with some overgrowth structure that retain their shape upon calcination (Fig. 3.4). Qualitative analysis performed by EDX indicates that the level of silicon in SAPO(20) and SAPO(10) samples is Si/Al 0.3 and 0.2 respectively.

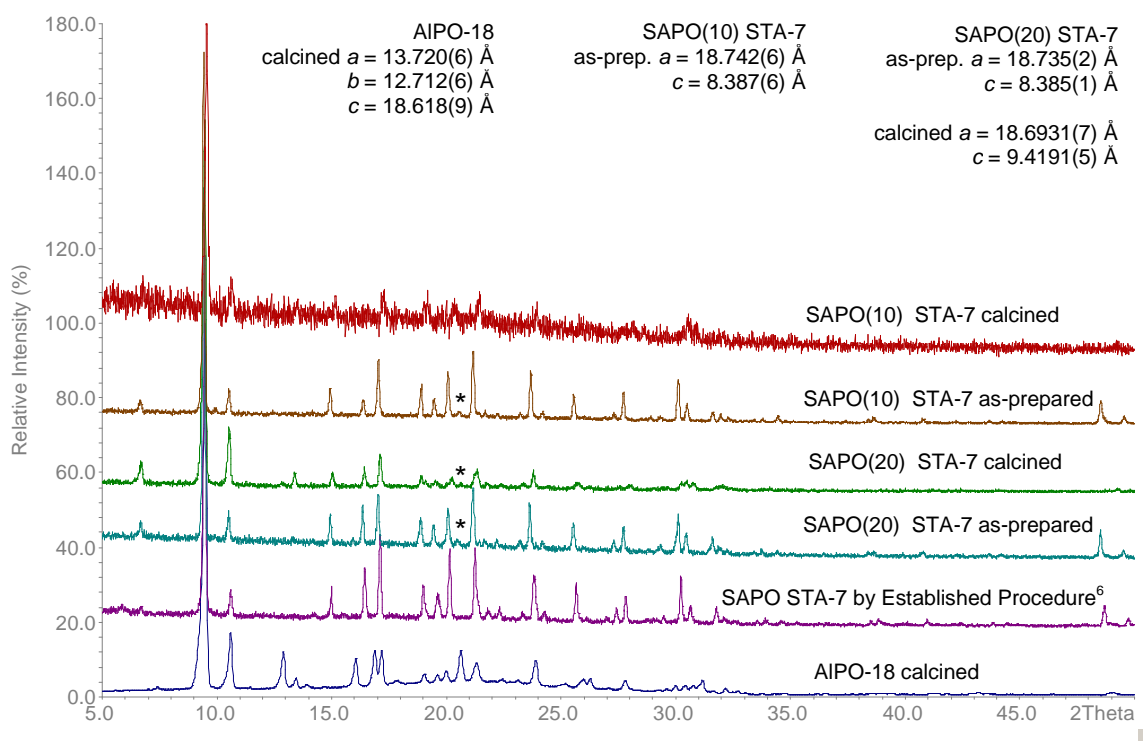


Fig. 3.3 XRD patterns of SAPO(20) and SAPO(10) STA-7 as-prepared (blue and purple, respectively) and calcined (cyan and green respectively).

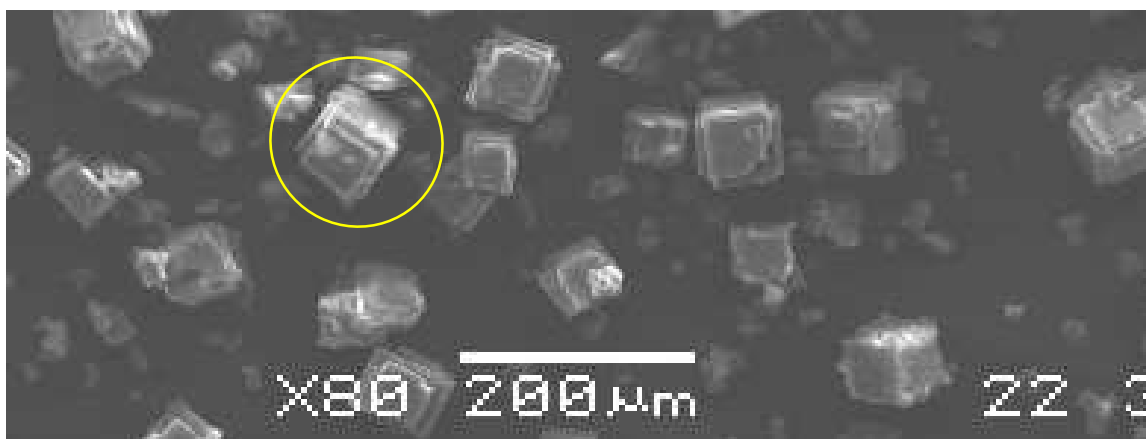


Fig. 3.4 SEM image of SAPO(20) STA-7 prepared via the method of Warrender.⁶ The typical morphology of this sample has 'overgrowth' layers on the surface.

These results show that SAPO(20) STA-7 is the most stable sample after calcination and therefore suitable for adsorption studies. The following issues arose:

- Preparing SAPO(20) with a morphology suitable for optical interference microscopy (IFM). This diffusion technique requires parallel flat faces in the single crystal with 20 μm as minimum size.
- Preparing enough sample for applications tests and for project partners. The established synthesis used 9 g of water to obtain 0.5 g of material after sonication, whereas adsorption and neutron scattering methods require 5-10 g.

3.3.1.2 Modifying the Synthesis Procedure

Changing the order of addition of the templates, adding first the cyclam and then the tetraethylammonium cation (TEA) was found to give SAPO STA-7 materials with a more regular morphology. The new SAPO(20) shows a well defined tetragonal prismatic morphology and particle sizes up to *ca.* 50 μm . Therefore, the introduction of cyclam prior the addition of TEA favours the crystallisation via the co-templating strategy.

In order to increase the amount of sample produced, larger autoclaves were used. This allowed a six fold increase in the quantity produced keeping the molar ratios constant. The crystallisation time was increased from 7 days to 10 days to allow more time for crystal growth.

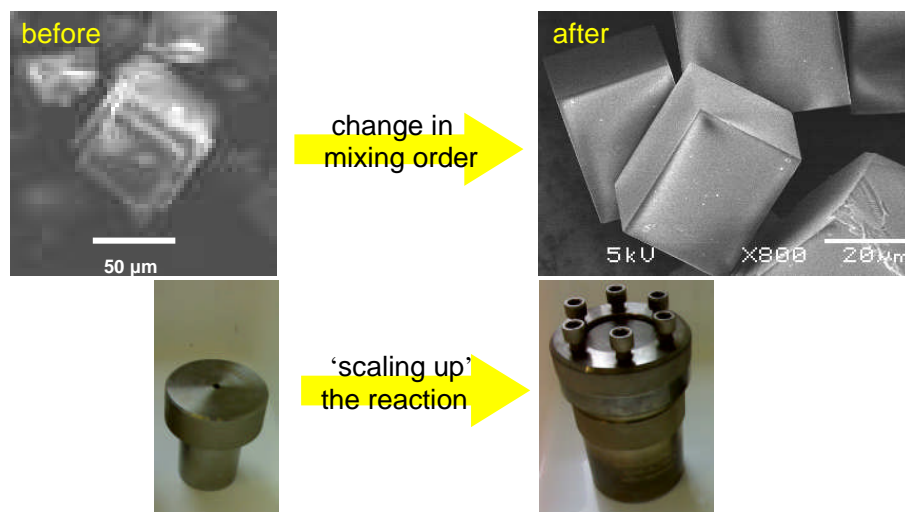


Fig. 3.5 Optimising the synthesis of SAPO STA-7.

Experiments were carried out using these new procedures with different silicon contents. The results of these reactions are summarised in Table 3.7 and having into account the final amount, thermal stability and morphology of the products the optimum Si/Al ratio is 0.20, material denoted as SAPO(20):

Table 3.7 Summary of the ‘scale-up’ synthesis changing the mixing order.* The final amounts refer to the single phase, well crystalline STA-7 recovered after sonication. This does not take into account finer grained material left with the amorphous products of the reaction after sonication.

| Si/Al in Gel | Si/Al in Product (by EDX) | Final Amount* | Yield (% on P content) | Morphology | Crystal Size (μm) | Unit Cell as-prepared (\AA) |
|-----------------|---------------------------------|------------------|------------------------------|---------------------------|--------------------------------------|--|
| 0.10 | 0.18 | 2.4 g | 20% | Tetragonal | $32(4) \times 30(4)$ | $a = 18.742(6)$ $c = 8.387(6)$ |
| 0.20 | 0.27 | 3.7 g | 32% | Tetragonal Flat Plates | $55(6) \times 42(4)$ | $a = 18.735(2)$ $c = 8.385(1)$ |
| 0.30 | 0.38 | 1.7 g | 13% | Faced Cubic Tetragonal | $53(2) \times 40(3)$ | $a = 18.733(12)$ $c = 9.413(4)$ |

SAPO(20) STA-7 shows two morphologies: flat plates and rectangular prismatic (Fig. 3.6 and Fig. 3.7 c respectively). SXRD on both morphologies on as-prepared and calcined samples was performed and showed both have the STA-7 structure. As a result, the unit cell in the calcined SAPO STA-7 material was obtained by SXRD for the first time.

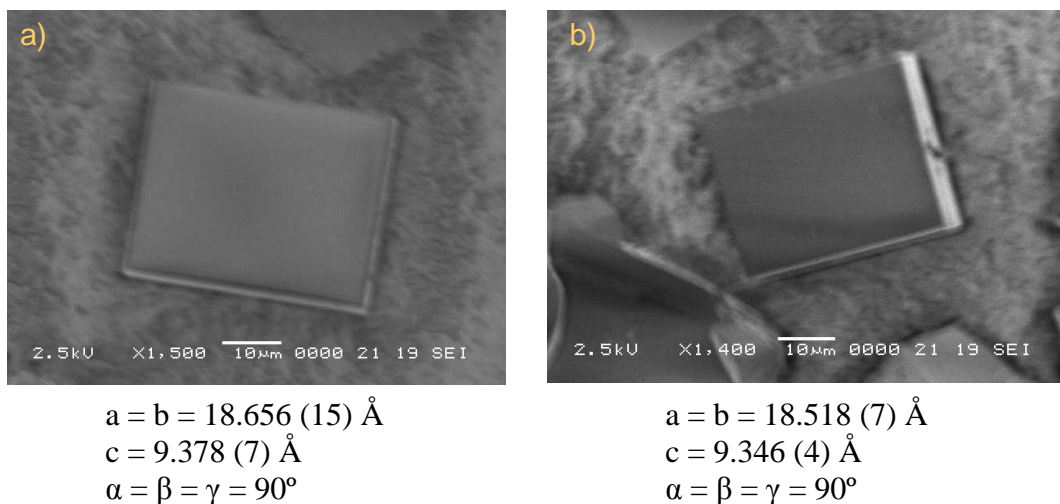


Fig. 3.6 SEM image of SAPO(20) STA-7 flat plate as-prepared (a) and calcined (b) with the unit cell parameters from SXRD.

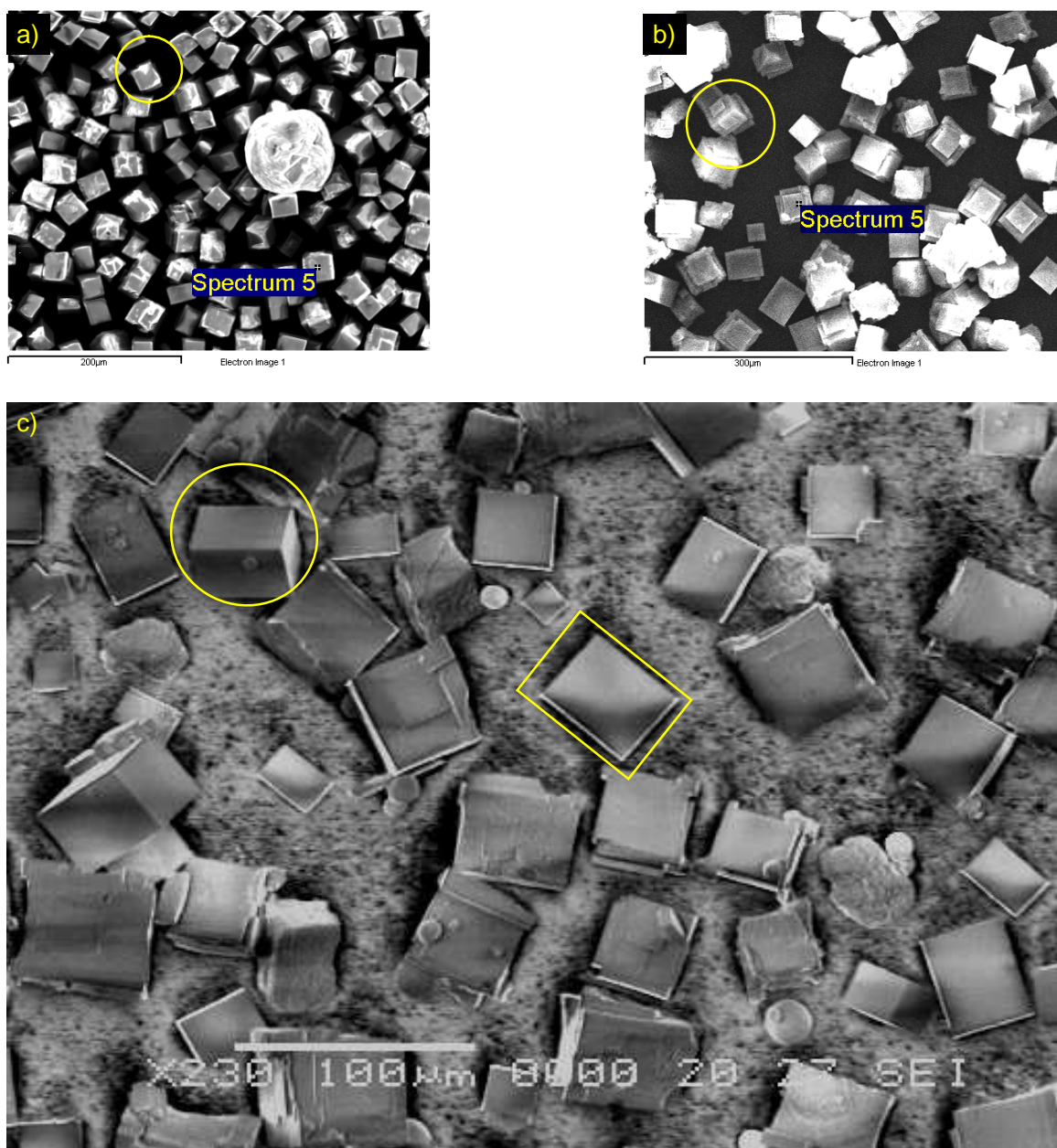


Fig. 3.7 SEM images from SAPO(10), SAPO(30) and SAPO(20) STA-7 (a, b and c respectively).

SAPO(20) STA-7 using the new order of addition of the bases was the reference material for the project. The main applications within the INDENS network covered the adsorption of CO_2 at high and low pressures, and associated microcalorimetry. Molecular modelling was performed to compare simulated uptakes and heats of adsorption with measured values (Marseille and Montpellier). In addition, quasi elastic neutron scattering

of STA-7 with CH₄ and CO₂ adsorbed was performed by the group at CNRS-Lyon and the diffusion of methanol was monitored by IFM (interference microscopy) at Leipzig.

The STA-7 synthesis was further investigated concerning industrial conditions and the variation of the framework chemistry.

3.3.1.3 Concerning Industrial Conditions (Static vs. Stirring)

The synthesis of SAPO STA-7 takes place in an autoclave with a Teflon liner reducing the reaction volume. The following study focuses on the synthesis of SAPO STA-7 in the absence of a Teflon liner, with the gel in contact with the stainless steel surface of the autoclave as performed in industrial conditions at IFP-Lyon. In this case, the synthesis takes place while stirring to homogenise the temperature in the reactor. These reactors or autoclaves are not placed in an oven for crystallization. Instead, the heating system surrounds the outside the autoclave and the whole system is isolated within a jacket (Fig. 3.8).

The following experiments were carried out:

- a) Synthesis under static conditions without liner in a 100 ml stainless steel autoclave.
- b) Synthesis while stirring without liner in a 160 ml stainless steel autoclave.
- c) In addition, samples were taken at different stages during the crystallisation period from the autoclave under stirring conditions via a valve to check the evolution of crystallisation with time.

The gel composition was the same in both reactors using the recipe previously developed (and described in this chapter) for SAPO(20) STA-7: 6.66 g Al(OH)₃ : 5.97 g H₃PO₄ (85%) : 0.8401 g SiO₂ : 54 ml H₂O : 1.62 g CYCLAM : 11.5 ml TEAOH (35%) and the conditions of crystallisation, 190 °C for 10 days, from previous synthesis work were also applied.

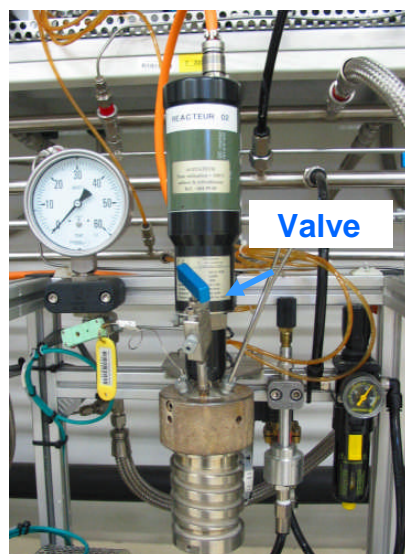


Fig. 3.8 160 ml stainless steel autoclave for the stirring conditions showing sampling valve.

The results from this study can be summarised as follows:

- The absence of a Teflon liner has little effect on the phase of the product, the only difference in the XRD pattern of the product is a small extra peak at 8.5° 2θ (Fig. 3.9).
- By using stirring conditions the extra peak at 20.5° 2θ that appears in static conditions, with and without Teflon liner, is not observed (Fig. 3.9).

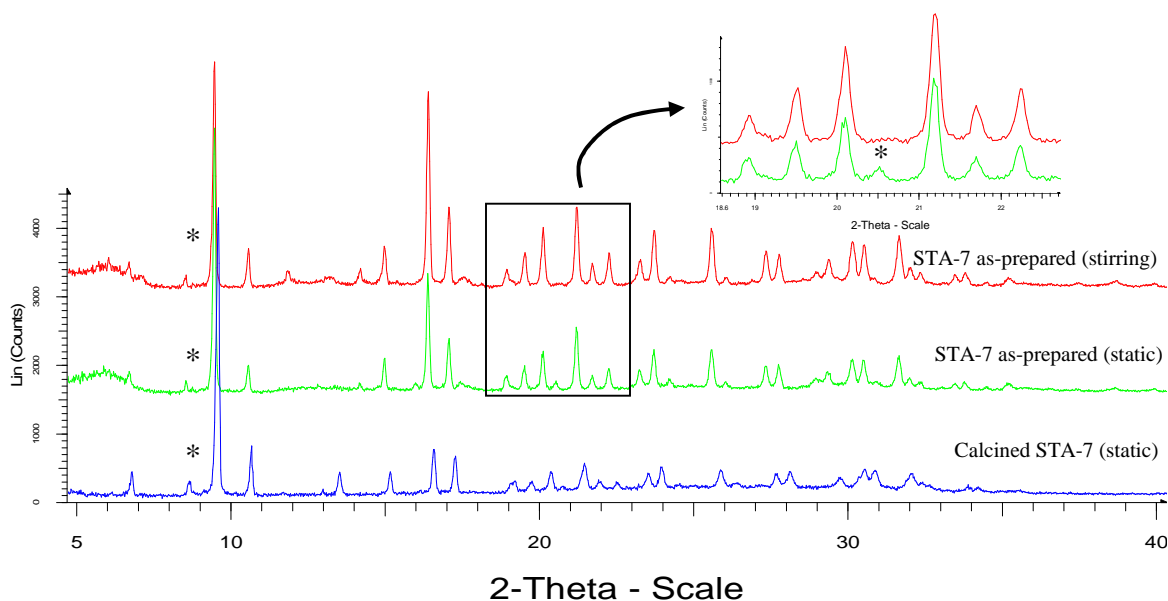


Fig. 3.9 XRD patterns of SAPO(20) STA-7 calcined and as-prepared in static conditions and as-prepared under stirring conditions using stainless steel autoclave without Teflon liner.

- The ‘static’ or ‘stirring’ conditions strongly influence the size and distribution of the crystals formed. With stirring, the crystals have uniform size (from 2 to 6 μm), since agitation promotes homogeneity in the gel generating multitude of nuclei of similar sizes. In contrast, under static conditions there is a bimodal distribution of crystal sizes with small and large crystals (*ca.* 2 μm and 80 μm), see figure 3.10. Probably the surface irregularities of the bare autoclave act as nucleation sites promoting the formation of small crystals in static conditions.

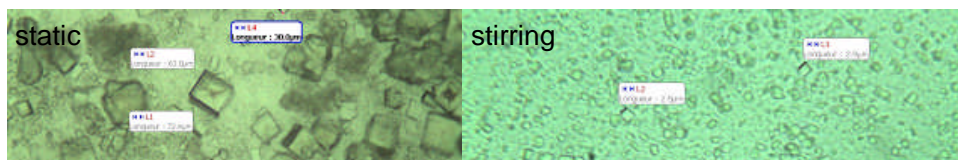


Fig. 3.10 Microscope observation of SAPO(20) STA-7 crystals obtained under static (left, $\times 250$) and stirred conditions (right, $\times 1500$) using stainless steel autoclave without Teflon liner.

- The synthesis is complete already at the third day under stirring conditions and time does not influence the crystal size once the product is formed. That is possible since stirring conditions promotes continuous nucleation event in a short period generating a multitude of nuclei of small size that cannot growth because the reactants are already exhausted (Fig. 3.11 top).
- SAPO STA-7 under static conditions is fully crystallised after just one day of hydrothermal synthesis (Fig. 3.11 bottom).

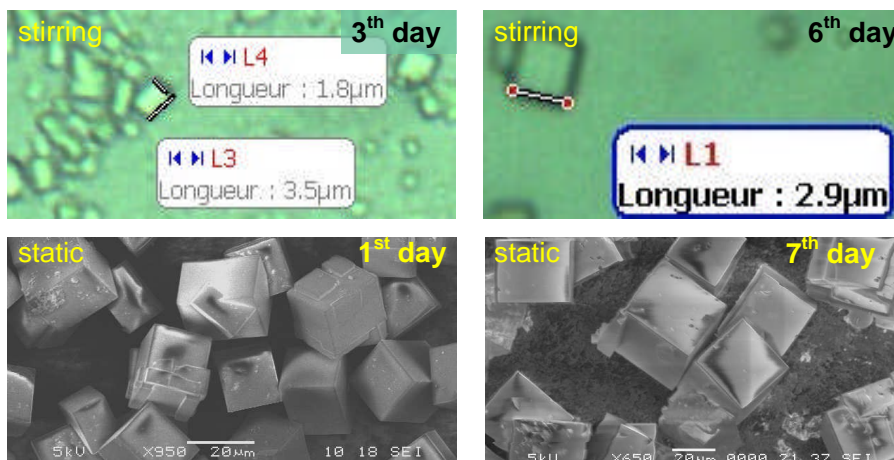


Fig. 3.11 Microscopy observation (top) of SAPO(20) STA-7 particles under stirring conditions after the 3rd (right) and 6th (left) day of hydrothermal synthesis and SEM images (bottom) of SAPO(20) STA-7 after one day (left) and seven days (right) of hydrothermal treatment under static conditions.

3.3.1.4 Variation of Framework Chemistry via Synthesis

AlPO

In contrast with SAPOs, AlPO frameworks have no charge. The addition of fluoride to the preparation may help the incorporation of the cationic organic species within the framework because fluoride ions coordinated to the aluminium could contribute a negative charge to the framework and potentially permit charge balance. Previous work by Warrender achieved (S)AlPO STA-7 with a small amount of included silicon using cyclam/TEAOH in the presence of fluoride ions, but for pure AlPO preparations only berlinite or AlPO-5 were obtained.⁶

The aim was to attempt the synthesis of pure AlPO STA-7 and to compare its adsorption properties with SAPO STA-7 to evaluate the interaction with adsorbate gas species. For example, CO₂ will interact differently with a charged framework than with a neutral one because of interactions of its quadrupole moment.

Summary of AlPO syntheses:

a) Using previous synthetic method developed by Warrender (Table 3.8).⁶

Table 3.8 Summary of AlPO synthesis performed using cyclam (or TMcyclam)/TEAOH pair with fluoride.

| Sample | Composition in Gel | | | | | | t (days) | T (°C) | Product |
|--------|--------------------|---|------------------|------|--------|-------|-------------|-----------|-------------------|
| | Al | P | H ₂ O | HF | cyclam | TEAOH | | | |
| MC245 | 1 | 1 | 40 | 0.24 | 0.125 | 0.42 | 2 | 190 | AlPO(F)-34 (UT-6) |

| Sample | Composition in Gel | | | | | | t (days) | T (°C) | Product |
|--------|--------------------|---|------------------|------|----------|-------|-------------|-----------|---------|
| | Al | P | H ₂ O | HF | TMcyclam | TEAOH | | | |
| MC260 | 1 | 1 | 40 | 0.24 | 0.125 | - | 2 | 190 | AlPO-5 |

b) Using the modified SAPO synthesis and pre-treatment of the gel (Table 3.9).

Table 3.9 Summary of AlPO synthesis performed using cyclam/TEAOH pair in non fluoride media.

| Sample | Composition in Gel | | | | | | Aging | | t (days) | T (°C) | Product |
|--------|--------------------|---|------------------|----|--------|-------|----------|-----------|-------------|-----------|---------|
| | Al | P | H ₂ O | HF | cyclam | TEAOH | t (h) | T (°C) | | | |
| MC30 | 1 | 1 | 40 | - | 0.108 | 0.30 | 1 | 80 | 7 | 190 | AlPO-18 |
| MC49 | 1 | 1 | 40 | - | 0.108 | 0.30 | 1.5 | 80 | 10 | 190 | AlPO-5 |
| MC57 | 1 | 1 | 40 | - | 0.108 | 0.30 | 5 | 60 | 7 | 190 | AlPO-5 |
| MC60 | 1 | 1 | 40 | - | 0.108 | 0.30 | 7 | 60 | 3 | 190 | AlPO-5 |

In previous work, AlPO gels containing non-metallated cyclam were prepared with DPA and TEAOH as co-bases. Gels containing DPA/cyclam crystallised as spherulitic assemblages of plate-like crystals with the [F,cyclam]-AlPO-CHA structure denoted UT-6.¹² This structure was synthesised previously by Morris *et al.* in the presence of cyclam only, and therefore DPA did not appear to influence this system.¹³

The present study shows again the formation of [F,cyclam]-AlPO-CHA in the presence of fluoride ions and AlPO-18 (AEI) in non-fluoride media. Both materials are part of the D6R family. Elemental analysis on these products suggest that AlPO-18 (AEI) contains a mixture of *ca.* one cyclam to four TEA, where $(C/N)_{\text{measured}} = 5.6$ instead of 8 as expected for TEA only. AlPO-34 (CHA) contains only cyclam and the value $(C/N)_{\text{measured}} = 2.3$ agrees closely with the expected 2.5. The pure AlPO STA-7 was not obtained and it can be concluded the STA-7 structure is favoured by having silicon in the framework and it may be that the STA-7 framework cannot readily coordinate fluoride ions. Notably, calcined AlPO-34 and AlPO-18 remain stable if kept dry and with similar unit cell parameters as the reference materials¹⁴ SAPO-34 and AlPO-18 in calcined form, see figure 3.12 for unit cell parameters. Therefore both samples have been used for CO₂ adsorption experiments.

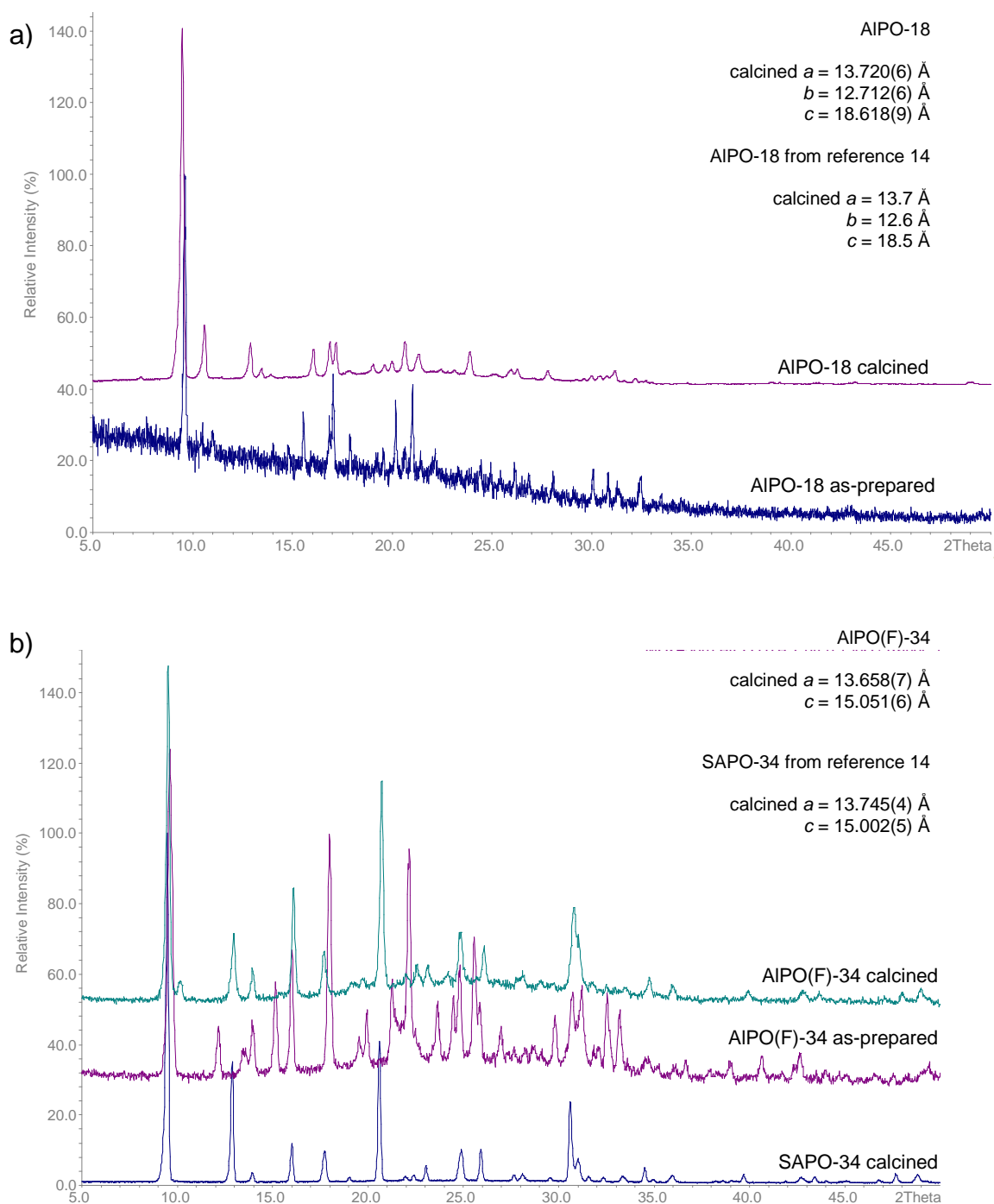


Fig. 3.12 XRD patterns of (a) AlPO-18 in the as-prepared (blue) and calcined (purple) forms and (b) AlPO(F)-34 in the as-prepared (purple) and calcined (cyan) forms; pattern of SAPO-34 for comparison (blue) synthesised using reference 14.

MAPO ($M = \text{Co}^{2+}, \text{Mg}^{2+}$)

It is also possible to introduce divalent metal cations into aluminophosphate frameworks, by substitution for aluminium. These MAPOs tend to be less stable than SAPOs upon calcination but possess good crystal quality. For this thesis CoAPO STA-7 was synthesised for examination as an adsorbent (Fig. 3.13) and MgAPOs were prepared at different Mg^{2+} contents for study by NMR in the as-prepared form (Table 3.10).

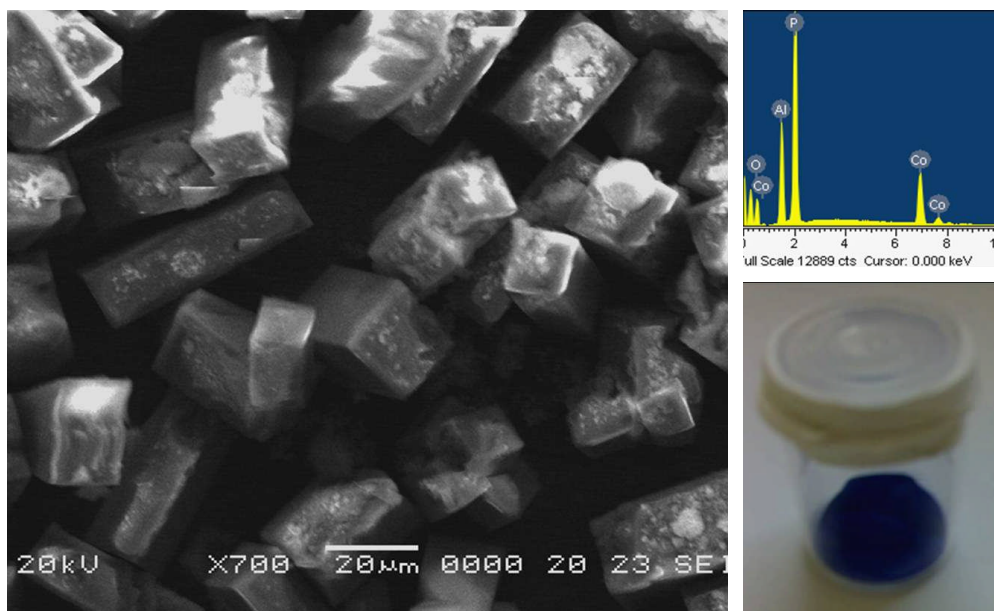
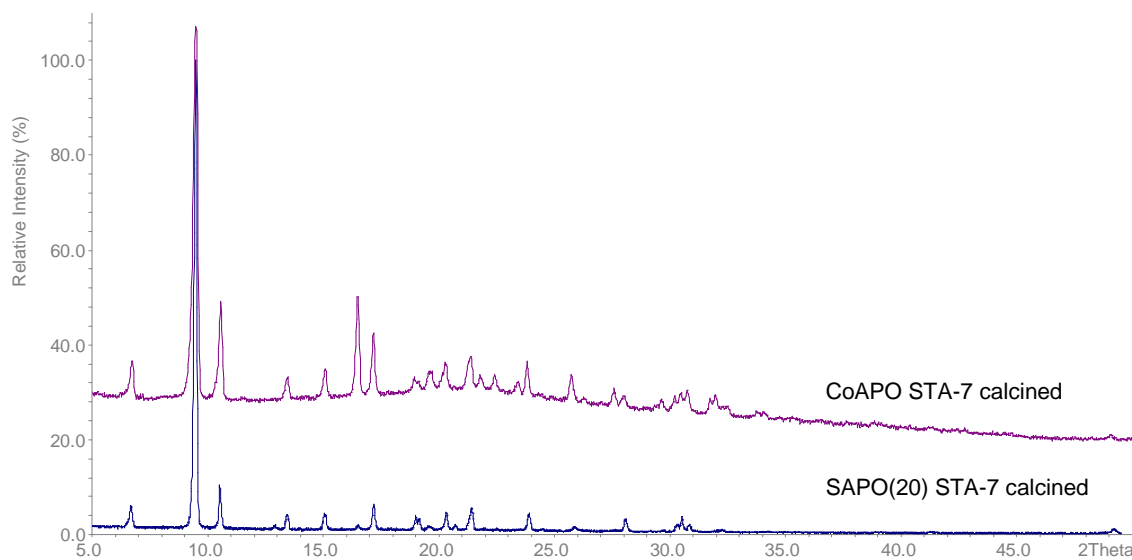


Fig. 3.13 (Above) XRD Pattern of CoAPO and SAPO(20) STA-7 calcined, (below) SEM image, EDX spectrum and characteristic blue colour of as-prepared CoAPO STA-7.

Cobalt (Co^{2+} , d^7) is paramagnetic, so CoAPOs cannot be studied quantitatively by NMR. However, ^{31}P MAS NMR of MgAPO STA-7 materials enables the mode of incorporation of the divalent Mg^{2+} into the framework to be studied.

Table 3.10 *Summary of MgAPO STA-7 synthesis.*

| Template | Co-base | Mg/P in gel | Product (by XRD) |
|----------|---------|-------------|-----------------------------------|
| cyclam | TEAOH | 0.15 | STA-7 |
| | | 0.20 | STA-7 |
| | | 0.50 | CHA/SAV/AEI intergrowth (by SXRD) |
| TMcyclam | DIPA | 0.50 | STA-7 mainly |

The product using Mg/P ratios 0.15 and 0.20 gives STA-7, denoted as MgAPO(15) and MgAPO(20) STA-7, with only a small additional peak at 20.5° 2θ (as in the case of SAPO STA-7) which might be attributed to AlPO-18 (Fig. 3.14).

The XRD pattern of the product prepared from a Mg/P ratio of 0.5 shows a mixture of phases; some peaks are related to AEI (MgAPO-18) and others to SAV and CHA (MgAPO-34). SXRD analysis did not yield data of sufficient quality to solve the structure, but gave indications that the crystals consisted of an intergrowth of phases rather than the compound being a mixture of discrete phases. The SEM image shows only one kind of morphology that indicated the phases are intimately intergrown (Fig. 3.15).

The samples MgAPO(15) and (20) prepared with the cyclam/TEA template pair were examined by ^{31}P MAS NMR. In addition, a mixture of MgAPOs prepared using a Mg/P ratio of 0.5 in the gel was obtained with the TMcyclam/DIPA pair (Fig. 3.16), TMcyclam is known to be a strong template for STA-7.¹ The pattern exhibits minor extra peaks due to impurity, but the sample was also included in the NMR study and denoted as MgAPO(50) STA-7. The lattice parameters increase as magnesium content increases, consistent with magnesium 2^+ (tetrahedral) being larger than aluminium 3^+ (tetrahedral), 0.57 \AA vs. 0.39 \AA respectively (see lattice parameters in Fig. 3.16).

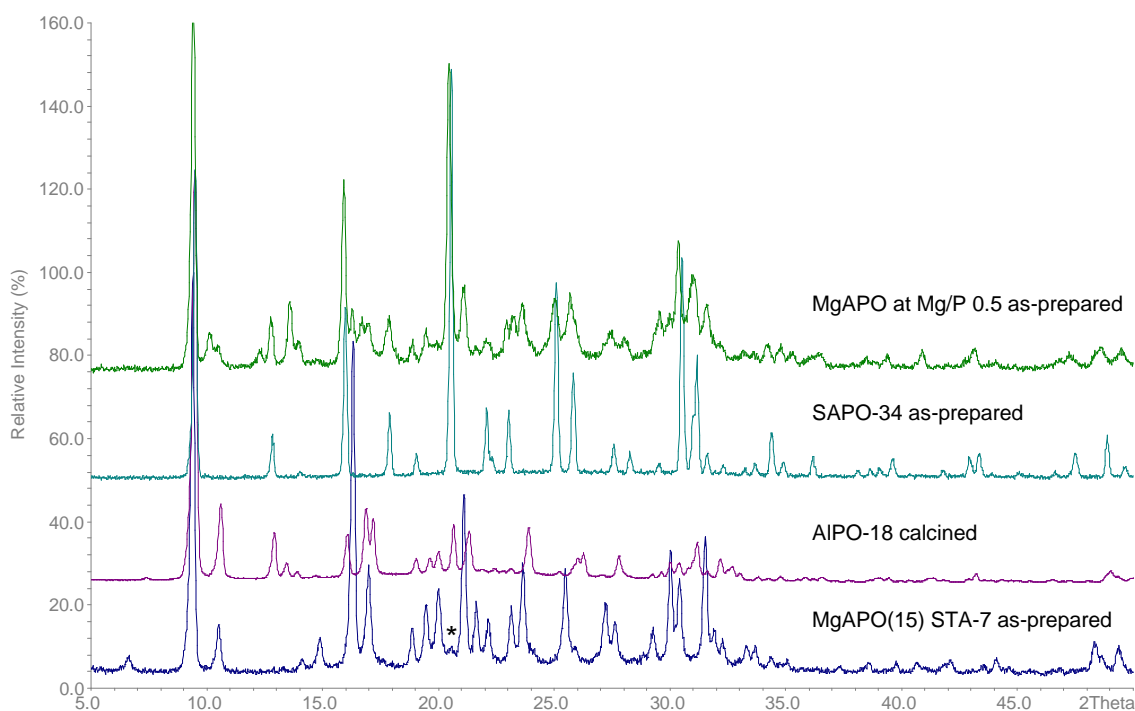


Fig. 3.14 XRD patterns. From bottom to top: MgAPO(15) STA-7, AlPO-18, SAPO-34 and MgAPO product using 50 %Mg in the gel, where the MgAPOs synthesis used the cyclam/TEA pair . The asterisked peak in MgAPO(15) STA-7 could be from AlPO-18.

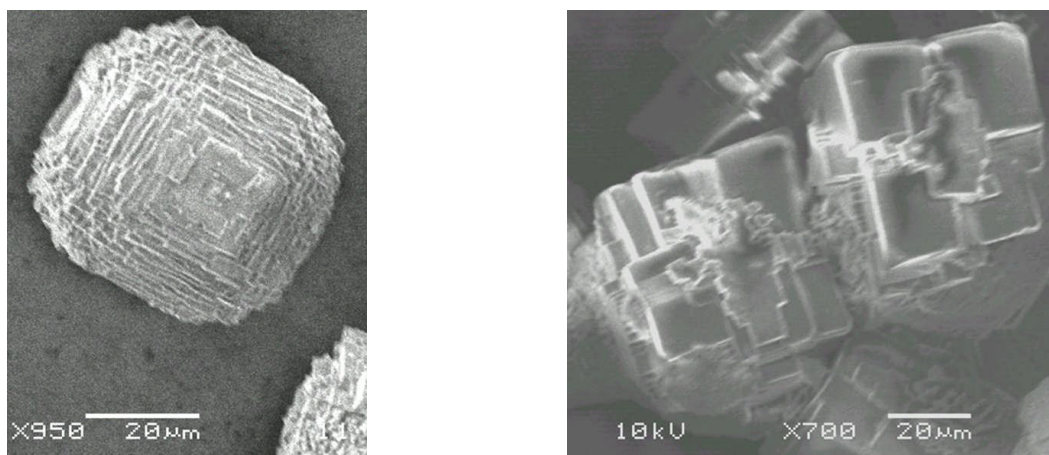


Fig. 3.15 SEM images of MAPO(15) STA-7 (left) and MgAPO product of the synthesis using Mg/P ratio 0.5

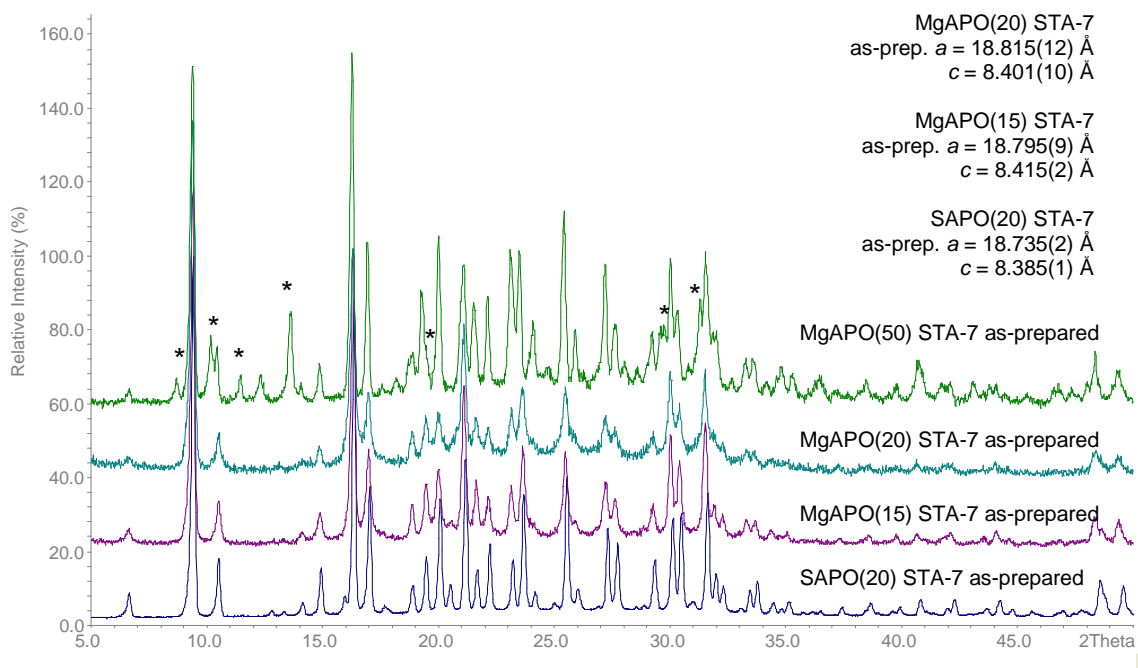


Fig. 3.16 XRD patterns of SAPO(20), MgAPO(15), MgAPO(20) and MgAPO(50) STA-7, where the MgAPO(50) used the TMcyclam/DIPA pair. Impurities in MgAPO(50) marked with asterisks.

MAPSO

The introduction of divalent metals $M(II) = Mn, Mg, Zn$ and Co to replace aluminium in a SAPO gel was studied, and the stability to template removal was measured.

The most thermally stable form was the MnAPSO STA-7. As prepared the sample has a yellow color and once calcined the oxidation stage of manganese changed from II to III and the sample colour turned to purple-blue. The lattice parameters of the MnAPSO as-prepared form are larger than the pure SAPO(20) STA-7, consistent with Mn^{2+} (tetrahedral) being larger than Al^{3+} (tetrahedral), 0.66 Å vs. 0.39 Å respectively. The framework as expected shrinks due to the removal of the template (see Fig. 3.17 for the XRD patterns and the lattice parameters of as-prepared and calcined MnAPSO sample).

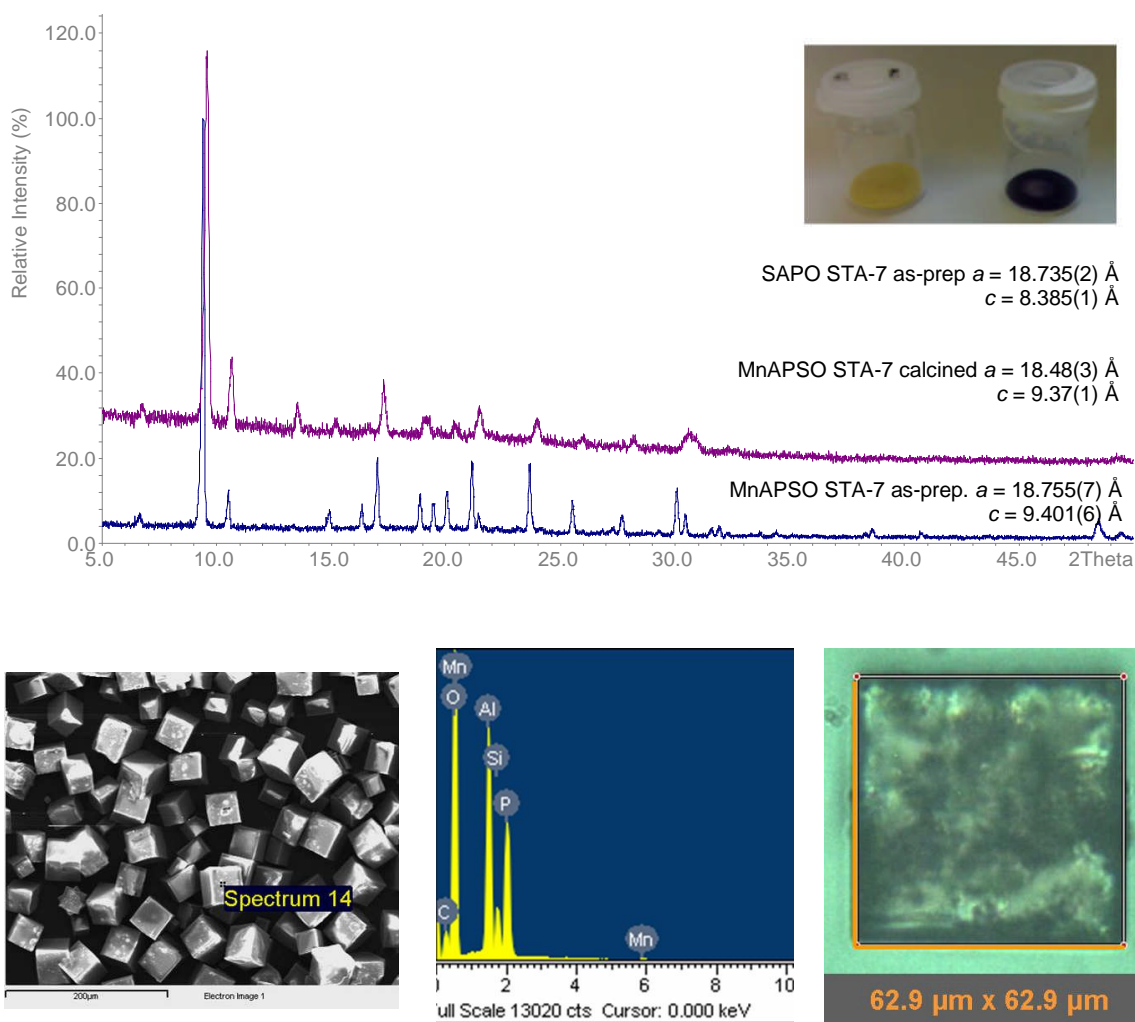


Fig. 3.17 XRD pattern of MnAPSO STA-7 (top); SEM, EDX and light microscope image showing a cuboidal single crystal (bottom, from the left to right).

3.3.1.5 Summary

Pure SAPO STA-7 product was obtained by using Si/Al ratio 0.2 in the gel, denoted as SAPO(20) STA-7. Changing the mixing order of templates gives a well developed tetragonal prismatic morphology. This is suitable for Interference Microscopy (IFM) studies of diffusion.


The crystallisation of SAPO STA-7 is much faster than suggested from previous synthetic studies, under both stirring and static conditions.

The same modified preparation method enabled MAPO and MAPSO STA-7 to be prepared. MgAPOs were analysed by NMR in the as-prepared form, and are denoted as MgAPO(15), MgAPO(20) and MgAPO(50) STA-7.

The synthesis of pure AlPO STA-7 was not achieved, so the introduction of silicon into the synthesis is required to favour STA-7 crystallisation. It is interesting that related materials of the D6R family were obtained from AlPO synthesis at different template ratios: AlPO-18 contains a mixture of *ca.* one cyclam to four TEA and AlPO(F)-34 contains only cyclam.

Table 3.11 summarises the co-templating approach applied in the hydrothermal synthesis:

Table 3.11 *The incorporation of silicon from the gel (molar ratios) into the final product (u.c. abbr. unit cell). The organic content in the unit cell was calculated from CHN and TGA analysis.*

| SAPO(20) STA-7 Si/Al = 0.20 in Gel | Hydrothermal  treatment | SAPO(20) STA-7 Si/Al = 0.27 in Product (by EDX) | | |
|---|--|--|----------|----------------|
| P : cyclam :TEAOH | | P | : cyclam | : TEAOH |
| 0.8 0.108 0.4 | | 17 atoms | 2 molec | 2 molec (u.c.) |
| 1 0.135 0.5 | | 1 | 0.118 | 0.118 |

There is an excess of both cyclam and TEA in the gel over that required for full crystallisation of SAPO STA-7. The excess is slight in the case of the cyclam, and much higher (around four times) for TEA, which acts both as co-template and a pH regulator. Notably, the experimental patterns of STA-7 show an extra small peak at $20.5^\circ 2\theta$ that could be attributed to SAPO-18 (see section 5.2 for details). In fact the formation of AlPO-18 is favourable in the presence of TEA cations as reported here using the cyclam/TEA pair and the TEA/cyclam ratio would increase as synthesis proceeds, favouring the SAPO-18 form. As further work it would be interesting to observe the SAPO and MgAPO synthesis using different ratios of TEA and cyclam.

3.3.2 Characterisation of As-Prepared Materials

This section focuses on understanding the hydrothermal synthesis and rationalising further synthetic studies. In this way, the co-templating approach is studied via SXR and modelling in SAPO(20) STA-7 to observe the bulk structure and its interaction with the template and the co-base (TEA), showing the role of TEA as a co-template. MAS NMR is applied to study the magnesium incorporation in MgAPOs STA-7 and investigate the hypothesis of the formation of secondary building units (SBUs) made of double six rings (D6Rs) since this material is build up of only D6Rs as well as the AEI and CHA structures that have been obtained in the previous section. To conclude this section, the distribution of silicon within the STA-7 framework, as observed by ^{29}Si , ^{27}Al and ^{31}P MAS NMR, is discussed.

3.3.2.1 SXR and Modelling on SAPO(20) STA-7

In previous work, the energy minimised location of TEA in the A cage of STA-7 and two possible configurations of tetramethylcyclam within the B cage were obtained from a combined Monte Carlo-Simulated Annealing approach.¹ Furthermore, the single crystal structure of CoAPO STA-7 templated by Ni-TMcyclam/TEAOH revealed the square planar NiN_4 configuration and the positions of disordered carbon atoms of TMcyclam and TEA.⁶

The SAPO(20) STA-7 obtained via the synthesis route of section 3.3.1 was suitable for single crystal diffraction. From this study, the framework structure and the conformation of TEA were measured and the latter compared with the modelled position of TEA. Modelling was also used to find likely positions for cyclam. This approach confirms the co-templating effect of TEA and cyclam in SAPO STA-7.

SXR

The structure of SAPO STA-7 was solved by single crystal diffraction in the tetragonal space group $P4/n$. These data confirm the Al-P ordering and the position of TEA in the smaller cages, which is disordered over two symmetrically-related positions and shows

tg.tg conformation*. Distinction between phosphorus and silicon was not made due to their similar electron density. The mean (Si-P)-O bond lengths for framework sites were 1.528(6) Å, 1.548(6) Å and 1.531(6) Å for T1, T2 and T3 sites respectively. These values are slightly larger than P-O bond lengths (1.52 Å) indicating the inclusion of silicon into the framework, since tetrahedral Si-O is normally 1.62 Å. The (Si-P)-O bond of T2 is larger than T1 and T3 indicates a possible preference of silicon for this site (Table 3.12 and Fig. 3.18). The residual electron density determined by Fourier mapping forms a disk within the larger cage and was attributed to disordered cyclam molecules (Fig. 3.19). The inclusion of cyclam in a modelled position (see later) slightly improved the fit, but the associated displacement parameters refined to an unreasonably large value. The positions of some extra-framework density were refined as extra-framework oxygen atoms. The structure was refined to final $R_{\text{int}} = 0.22$ (full details are given in Appendix A, from Table A.1 to A4 and the CIF file attached on CD).

Table 3.12 Summary of data from SXR D in SAPO(20) STA-7.

| $a = b$ (Å) | c (Å) | Space Group | T1-O (Å) (A cage) | T2-O (Å) (B cage) | T3-O (Å) (6R) | Unit Cell Composition |
|-------------|----------|----------------|-------------------------|-------------------------|---------------------|---|
| 18.656(15) | 9.378(7) | P4/n | 1.528(6) | 1.548(6) | 1.531(6) | $\text{Al}_{24}\text{P}_{18.5}\text{Si}_{5.5}\text{O}_{96}$ |

*tg.tg is the abbreviation for the trans-gauche conformer.



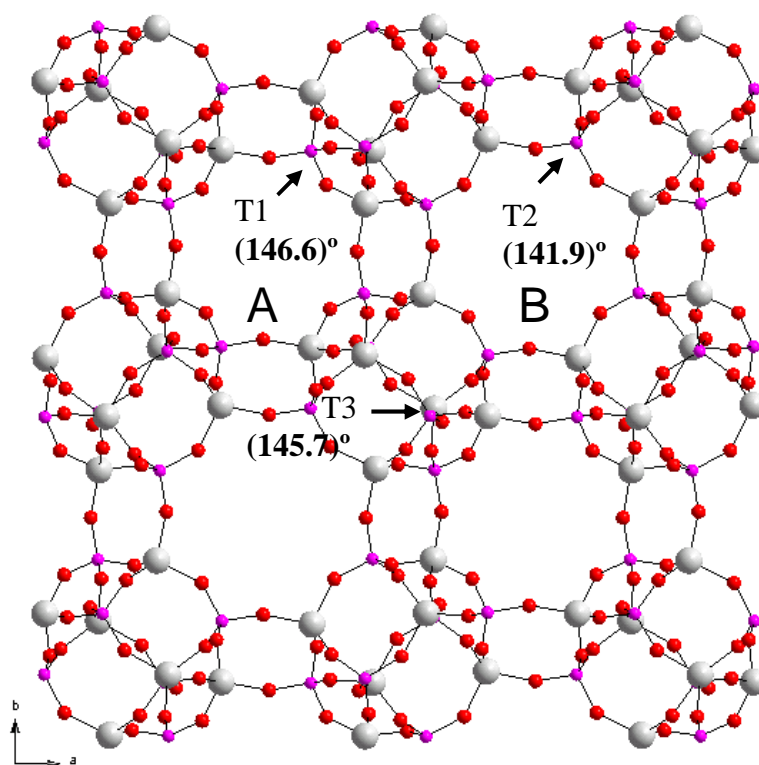


Fig. 3.18 The three T sites in SAPO(20) STA-7 and their mean T- \hat{O} -T angles.

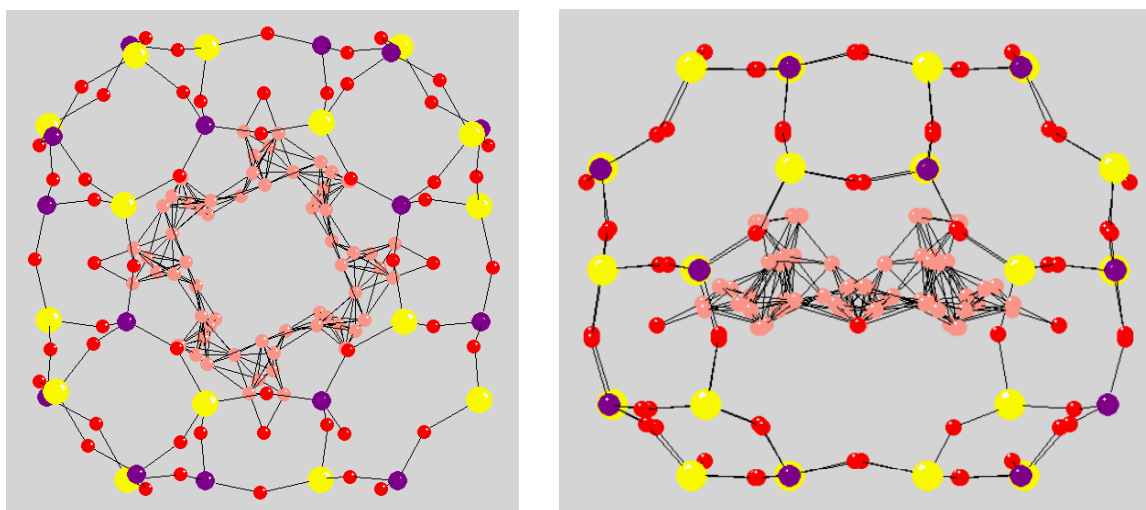


Fig. 3.19 Electronic density attributed to cyclam in the larger cage of SAPO(20) STA-7.

The determination of the TEA positions was achieved from the Fourier map using a model in which the carbon atoms adjacent to the nitrogen are disordered over two sites - C1A and C1B - but the methyl carbons (C2) are located in a single position. The ethyl groups of the TEA molecule point to the corners of the A cage, showing a good fit between the organic species and the cage which may be important for the TEA to act with a co-templating effect (Fig. 3.20).

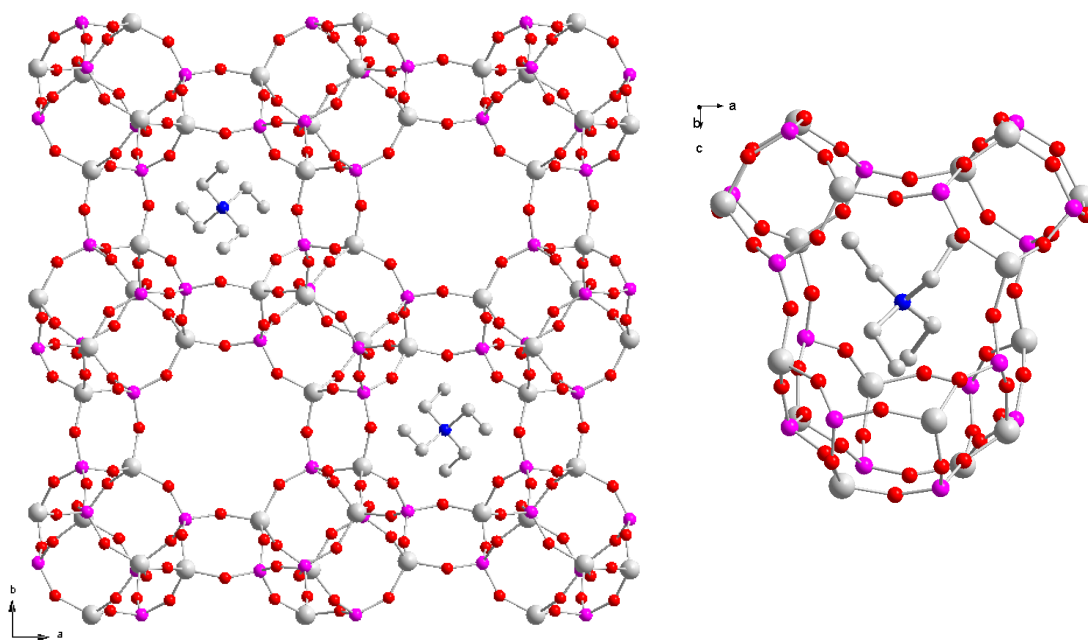


Fig. 3.20 Structure of STA-7 (left) with the TEA cations the in A-cages. The measured *tg.tg* configuration of TEA in the smaller cage of STA-7 as determined from SXRD (right). One of two symmetry-related configurations is shown.

Modelling

The initial aim of modelling was to locate cyclam within the host framework to improve the single crystal structure refinement. This work was done in collaboration with A. Fecant at IFP-Lyon as described in section 2.6. The energy-minimised locations of bases within a theoretical aluminophosphate SAV framework were obtained by molecular modelling. The coordinates of STA-7 were taken from the SXRD.

The first step was to find the appropriate parameters to model an AIPO framework. To assess the potentials that were used, the modelled coordinates of TEA were compared

with experimental values from SXRD. The framework coordinates were constrained at their measured values and TEA was placed into the small cage of STA-7 ready to run a geometry optimisation using the Universal forcefield. The following figure 3.21 shows the good agreement between modelled and experimental coordinates.

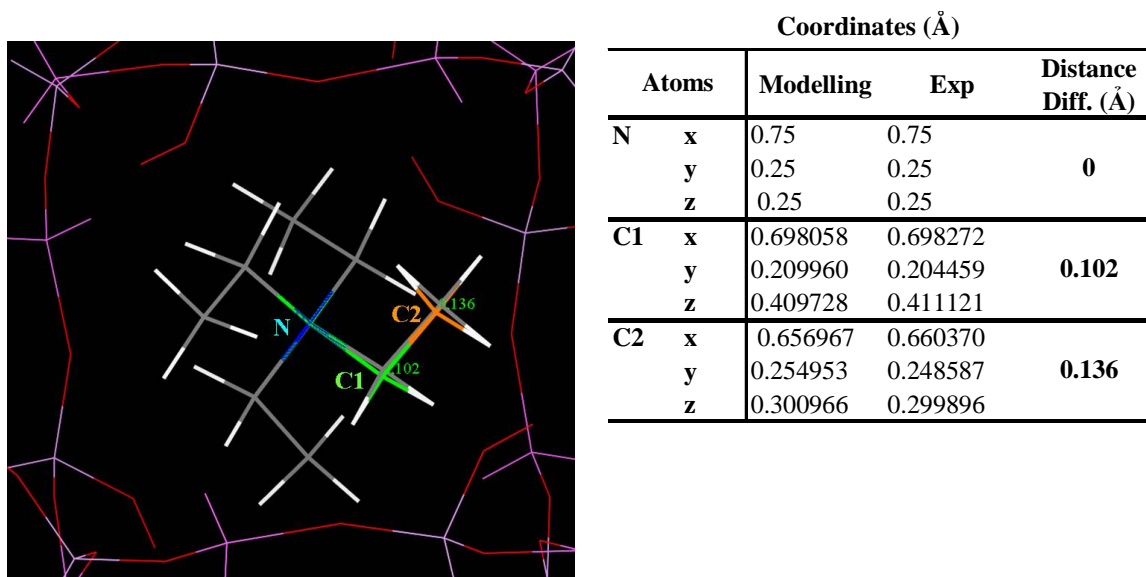


Fig. 3.21 Comparison between modelled (grey) and experimental (coloured) coordinates of TEA in A cage of AlPO STA-7 framework.

The second step in the molecular modelling was to suggest locations for the cyclam moiety within the cages. Before modelling the template position inside the framework, its own geometry was modelled alone. For that, the molecule was drawn and geometry optimization applied.

The best configurations for cyclam and $\text{H}_2\text{cyclam}^{2+}$ are shown in figure 3.22.

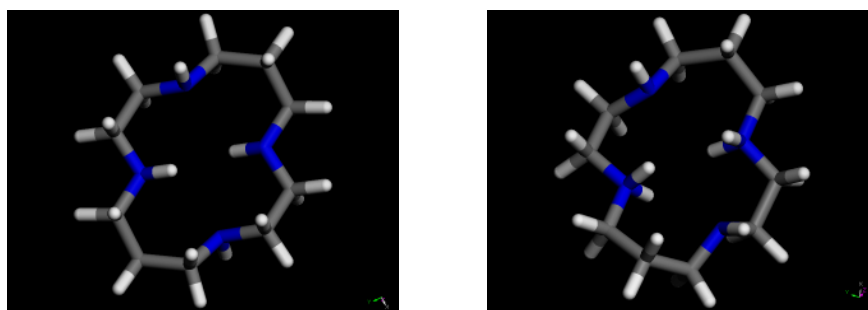


Fig. 3.22 Best configuration found for cyclam (left) and $\text{H}_2\text{cyclam}^{2+}$ (right) with values $E = 24.53 \text{ kcal/mol}$ and $E = 29.70 \text{ kcal/mol}$ respectively.

Cyclam is a base with several basicities (Fig. 3.23).¹⁵ It was important to know which species are involved in the crystallisation of STA-7 where the initial pH of the gel is seven. According to the data of figure 3.23, the first basicity of cyclam is a strong base, so in solution cyclam becomes Hcyclam^+ . The volume of HCl added at the inflexion point is equivalent to one basicity of the template. Then at $\text{pH}=7$, all the hydroxide created by Hcyclam^+ reacted, and $\text{H}_2\text{cyclam}^{2+}$ is the main species. From this observation, it seems that $\text{H}_2\text{cyclam}^{2+}$ rather than cyclam directs the synthesis of the large cage of STA-7, in agreement with the chemical composition of the unit cell which has six silicon atoms suggesting that most of cyclam is included as the 2^+ cation (see Table 3.11 and 3.12 for details).

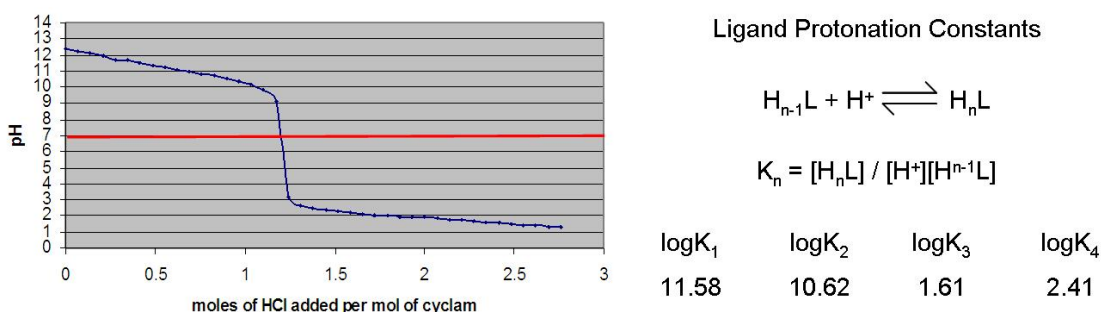


Fig. 3.23 Titration curve of cyclam (left) and ligand protonation constants (right) from reference 16.

As a third step, the potential positions of cyclam and $\text{H}_2\text{cyclam}^{2+}$ within the B cages of STA-7 were modelled, using the coordinates of SAPO STA-7 (with TEA cation) from

SXRD in an AIPO framework (Fig. 3.24). Only one position for the CH₂ aliphatic group of TEA was adopted (position C1A). To be able to place the cyclam in the framework, the space group was changed from P4/n to P-1 or P1 (coordinates of cyclam or H₂cyclam²⁺ in P-1 or P1 symmetry in CD).

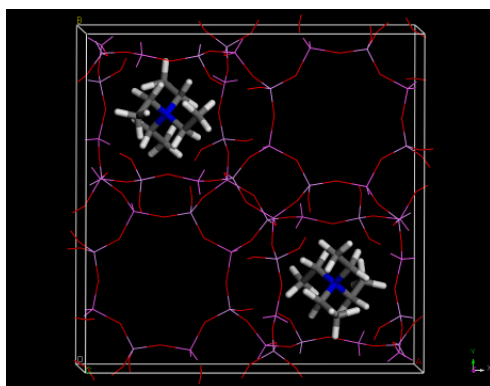


Fig. 3.24 Model of STA-7 and TEA created with MS MODELLING (courtesy of A. Fecant, IFP-Lyon).

Cyclam or H₂cyclam²⁺ was placed into the B cages of STA-7. The atom positions other than those of cyclam or H₂cyclam²⁺ were constrained and geometry optimisation allowed them to move freely. The snapshots in figure 3.25 show the good fit of the modelled positions of cyclam and H₂cyclam²⁺ within the B cage of STA-7. That supports its templating effect experimentally observed.

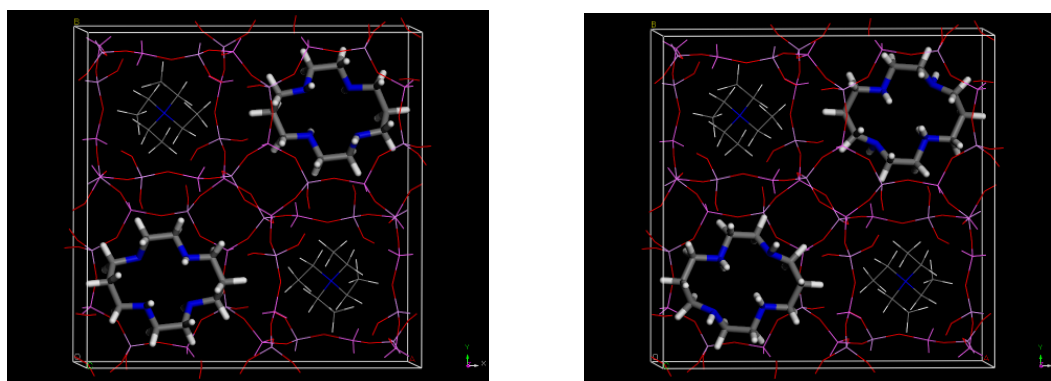


Fig. 3.25 Cyclam and H₂cyclam²⁺ within the large cage of modelled AIPO STA-7 framework.

The coordinates of cyclam and H₂cyclam²⁺ obtained from modelling were used in the refinement of the single crystal data and the occupancy refined, but this did not

significantly improve the R factor and the displacement parameters of the template refine to physically unreasonably large values. A disk of electron density was observed in the large cage of STA-7 however.

Molecular dynamics simulations were performed, allowing framework and template atoms to relax. TEA shows little movement within its cage, but cyclam rotates readily in the plane normal to [001] and therefore the template atoms have large displacement parameters (Fig. 3.26 and 3.27).

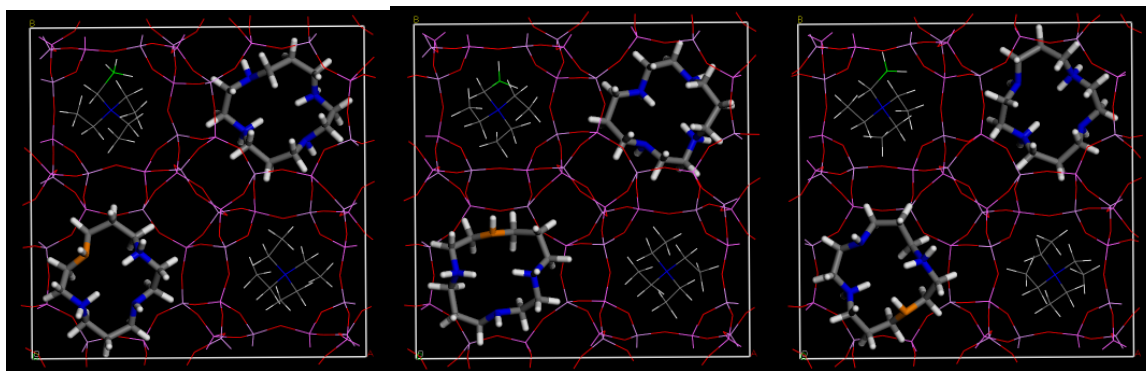


Fig. 3.26 Molecular Dynamics shows the rotation of cyclam in the plane normal to [001] (one nitrogen atom is denoted in orange to show motion whereas TEA is almost stationary (as shown by labeled 'green' C atom).

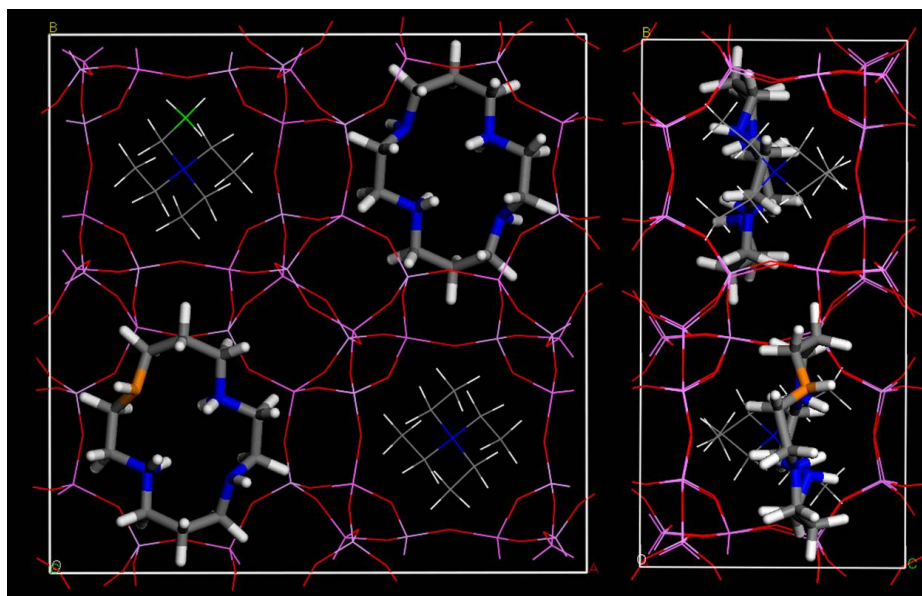


Fig. 2.27 Molecular Dynamics detail from [001] and <100> view.

Finally, an XRD pattern was simulated for SAPO(20) STA-7 with TEA and H₂cyclam²⁺ (Fig. 3.28). Compared to the experimental pattern, there is quite good agreement, except maybe for the peak at 21.1° – 21.2° 2θ which shows a lower intensity. One peak is missing at about 20.8°, but synthesis studies suggest that this peak does not arise from STA-7.

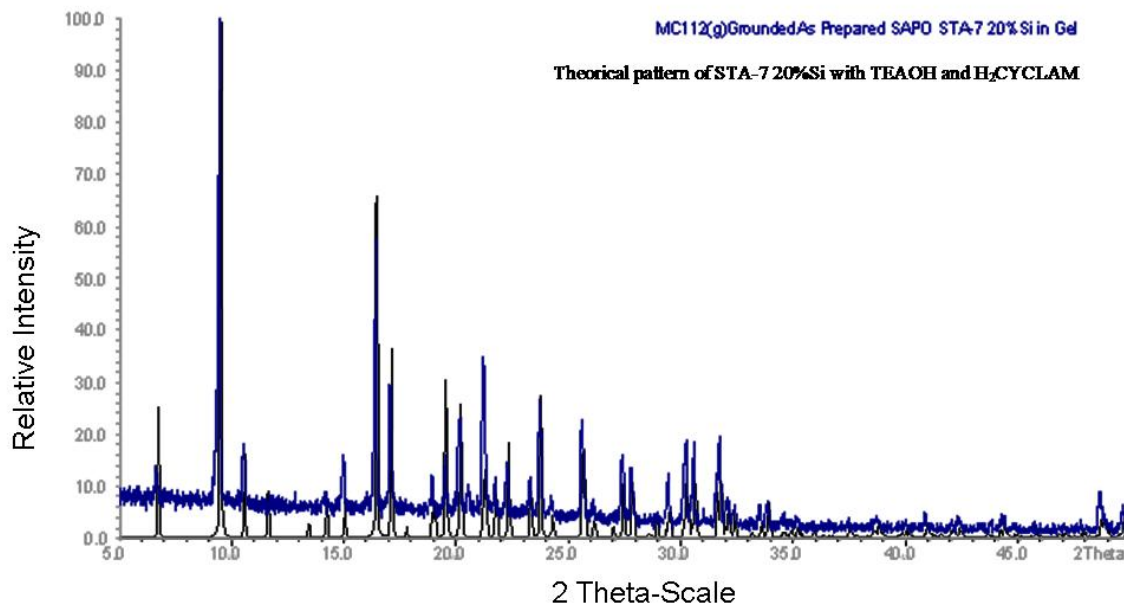


Fig. 3.28 Comparison of experimental and theoretical XRD pattern for SAPO(20) STA-7 with structure directing agents inside the framework.

3.3.2.2 MAS NMR on STA-7 MgAPOs

A ³¹P solid-state MAS NMR study of MgAPO STA-7 with different magnesium contents was performed to understand the mechanism of the magnesium incorporation into the framework. Three MgAPO STA-7 samples were studied, denoted MgAPO(15), MgAPO(20) and MgAPO(50) STA-7 with Mg/P ratios 0.18, 0.20 and 0.31 respectively (by EDX).

The major resonance in the ²⁷Al spectra is centred at 36.6 ppm indicating that most of the aluminium is in tetrahedral coordination within the STA-7 framework, where it is surrounded by four phosphorus second nearest neighbours Al(OP)₄. An extra weak resonance at –6.9 ppm is attributed to six fold coordinated aluminium.⁶ The ²⁷Al MQ

NMR spectrum showed only one signal, related to the three crystallographically distinct but unresolved tetrahedral (T) sites (Fig. 3.29).

The ^{27}Al MAS NMR spectra indicate that magnesium substitutes aluminium forming various phosphorus environments arising from the different compositions of the P second coordination sphere, i.e., P(4Al), P(3Al, 1Mg), P (2Al, 2Mg), etc. These different P environments are manifested in the ^{31}P MAS NMR spectra and can under suitable conditions be quantified to give the framework Mg content.¹⁶ ^{31}P MAS NMR spectra of the MgAPO STA-7 samples exhibit four resonances: one strong and broad centred at -22 ppm assigned to overlapping of P(2Al, 2Mg) and P(3Al, 1Mg) and two weak signals at -28 and -17 ppm attributed to P(4Al) and P(1Al, 3Mg). The overlap makes calculation of the magnesium content in the framework impossible. An extra broad resonance is attributed to an amorphous phosphorus-containing impurity.

At high magnesium content MgAPO(50) STA-7, extra resonances appear in the ^{31}P MAS NMR spectra because not all of the magnesium can be incorporated into the STA-7 framework. By EDX, the total amount of aluminium replaced by magnesium in the samples is 31%. The reason that STA-7 cannot incorporate unlimited magnesium into its framework could be explained by charge balance and/or an ordered magnesium incorporation that restricts higher magnesium content. The extra environment is attributed to a crystalline magnesium phosphate phase (the ^{27}Al MAS NMR spectrum of this sample shows only tetrahedrally-coordinated aluminium of the STA-7 framework, suggesting that there is no aluminium in this extra phase).

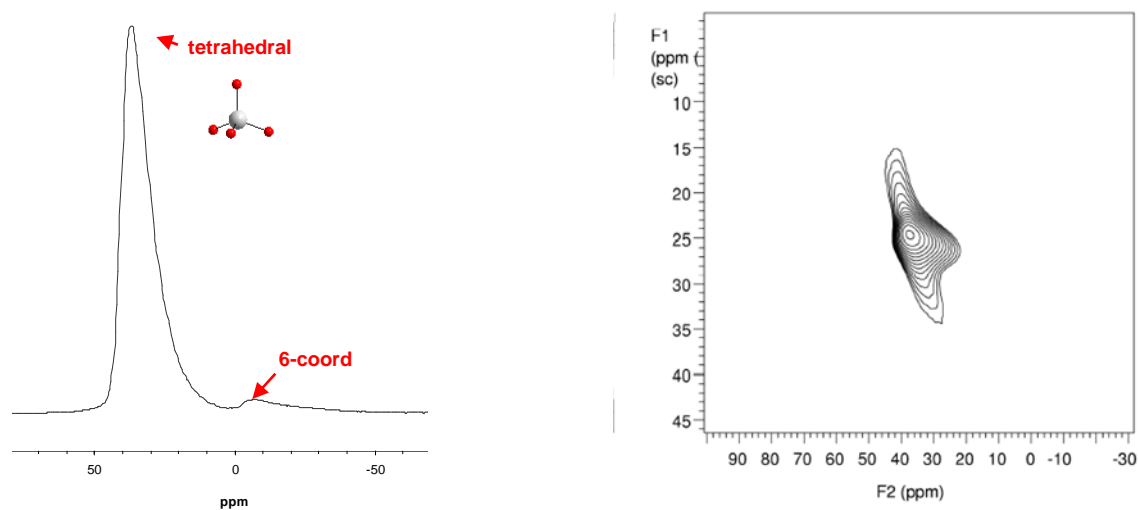


Fig. 3.29 ^{27}Al MAS NMR spectrum (left) and ^{27}Al MQ MAS NMR spectrum (right) of MgAPO(50) STA-7.

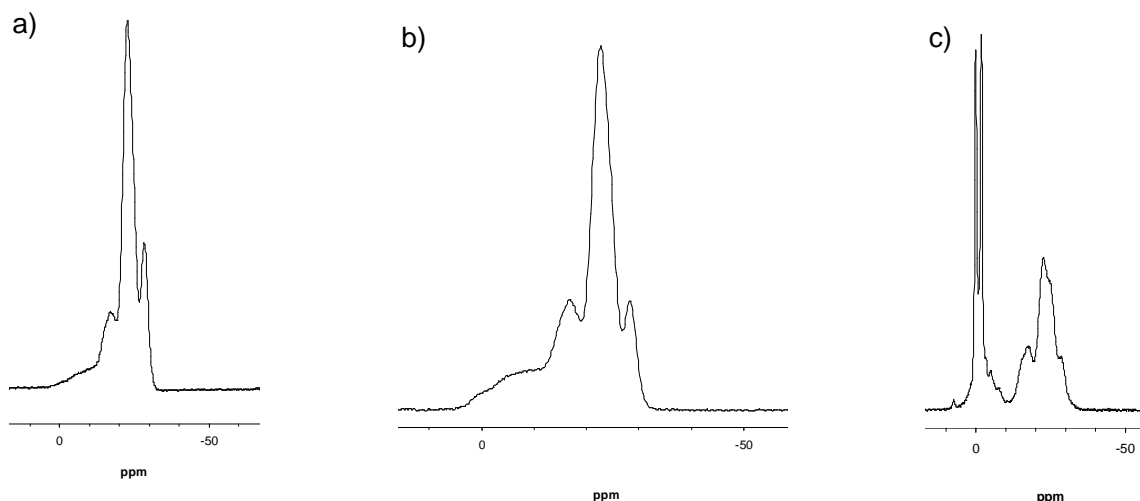


Fig. 3.30 ^{31}P MAS NMR spectra of MgAPO(15), MgAPO(20) and MgAPO(50) STA-7.

3.3.2.3 MAS NMR on STA-7 SAPOs

For the reference material of the project SAPO(20) STA-7, the ^{27}Al and ^{31}P MAS NMR spectra show the framework is tetrahedrally-connected, with main resonances centred at 36.7 ppm and -28.4 ppm for ^{27}Al and ^{31}P respectively, the spectrum of ^{27}Al shows also an extra signal at 8.6 ppm (Fig. 3.31).¹⁷

The ^{13}C MAS NMR spectrum showed two sharp resonances at 7.8 ppm and 52.9 ppm attributed to the CH_3 and CH_2 groups of TEA, respectively, while the broader resonances at 45, 26.2, 20.0 and 11.1 ppm are attributed to cyclam (Fig. 3.32). That indicates that the

organic species have been incorporated intact proving their role as SDAs. Elemental analysis support these results where the $(C/N)_{\text{measured}} = 3.78$, was between that of the two organic species with a 1 : 1 mix ($18/5 = 3.6$), see Table 3.13.

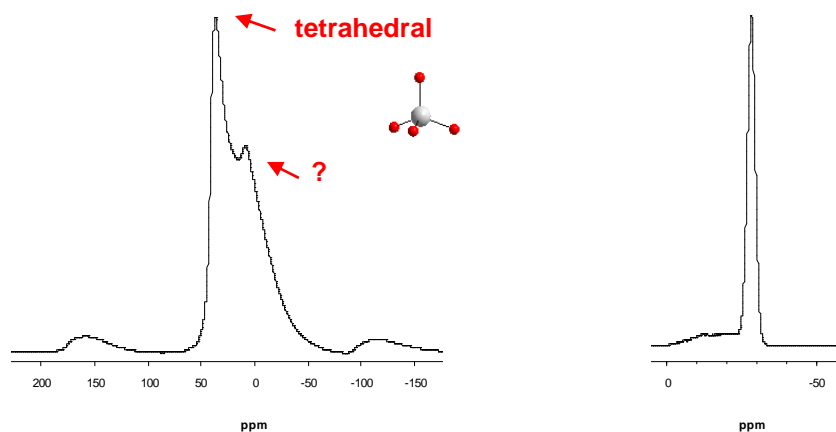


Fig. 3.31 ^{27}Al MAS NMR spectrum (left) and ^{31}P MAS NMR spectrum (right) of SAPO(20) STA-7.

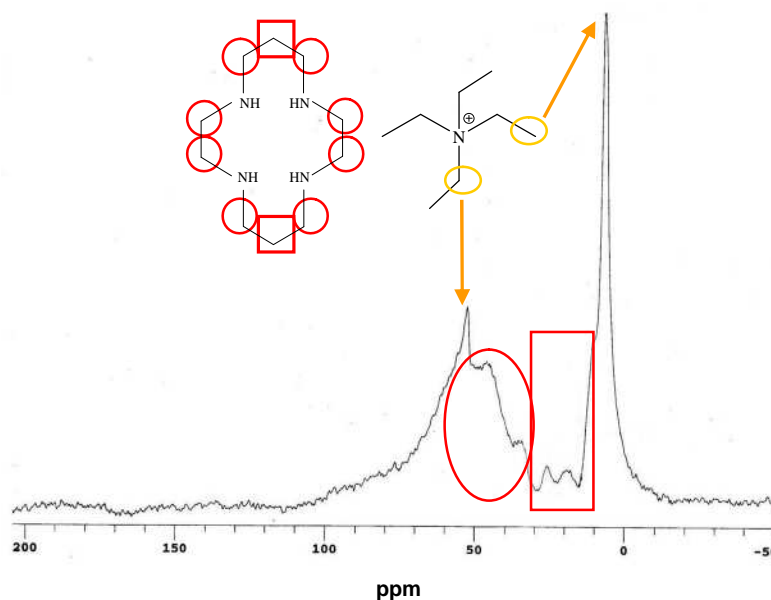


Fig. 3.32 ^{13}C MAS NMR spectrum of SAPO(20) STA-7.

Table 3.13 Results of microanalysis for SAPO(20) STA-7.

| SAPO(20) STA-7 | %C | | %H | | %N | |
|---|-----------|--------|-----------|--------|-----------|--------|
| | Predicted | Actual | Predicted | Actual | Predicted | Actual |
| $\text{Al}_{24}\text{P}_{18.5}\text{Si}_{5.5}\text{O}_{96}(\text{H}_2\text{O})_{11}(\text{cyclam})_{1.8}(\text{TEA})_{1.8}$ | 10.49 | 10.50 | 2.73 | 2.54 | 3.40 | 3.33 |

The ^{27}Al MAS NMR spectrum has an extra weak broad resonance at 8.6 ppm that could be related to Al with a higher coordination or to the influence of Si on the Al environment. For further investigation an ^{27}Al MQMAS NMR experiment was performed (Fig. 3.33). This spectrum showed three resonances, and an additional one attributed to an artefact of the experiment. Two of the three resonances are close to each other, one related to aluminium in the tetrahedral position and the other related to the weak broad resonance obtained by 1D NMR which could be related to Al(1Si, 3P) environments. The third is related to aluminium with additional coordination. For the resonance of aluminium in the tetrahedral Al(4P) site, the three crystallographically distinct sites are not resolved, presumably due to their similar mean T- $\hat{\text{O}}$ -T values.

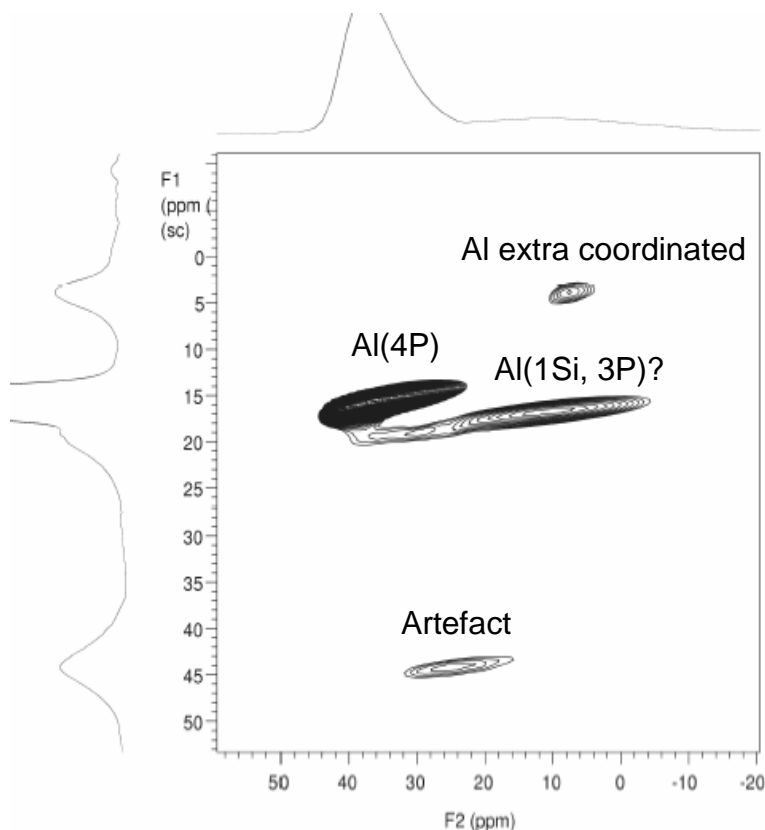


Fig. 3.33 ^{27}Al MQ MAS NMR spectrum of SAPO(20) STA-7.

The silicon distribution in the samples at different silicon content was investigated via ^{29}Si MAS NMR to observe the possible formation of silica islands or aluminosilicate domains (AS) (Fig. 3.34). Three samples were studied: SAPO(10), SAPO(20) and SAPO(30) STA-7 with Si/Al ratios 0.18, 0.27 and 0.38 respectively (by EDX, Table 3.7). For SAPO(10) and SAPO(20) the ^{29}Si MAS NMR spectrums show a sharp and strong resonance centred at -91.6 ppm related to Si(4Al) environment implying that silicon substitutes at phosphorus positions (Fig. 3.35 a and b). The framework at these levels of silicon shows silicon randomly distributed in a tetrahedral position replacing phosphorus. For SAPO(30) the resonance is slightly broader (Fig.3.35 c), but there is no evidence for the formation of silica islands or aluminosilicate domains (AS). Up to a Si/Al ratio of 0.38, the product has silicon distributed mainly in Si(4Al) environments.

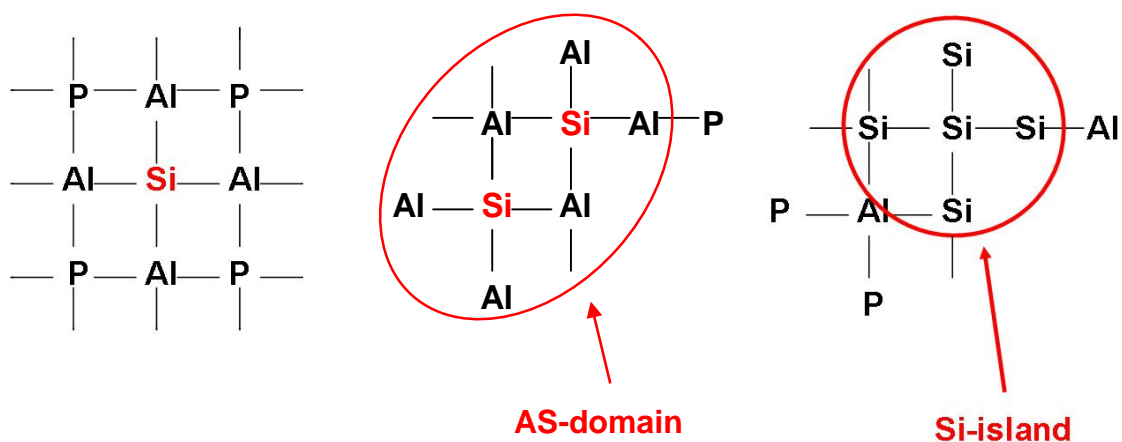


Fig. 3.34 Diagrams of the silicon distribution, from the right to the left: Si(4Al), Si (nSi)(4-nAl) and Si(4Si) environments.

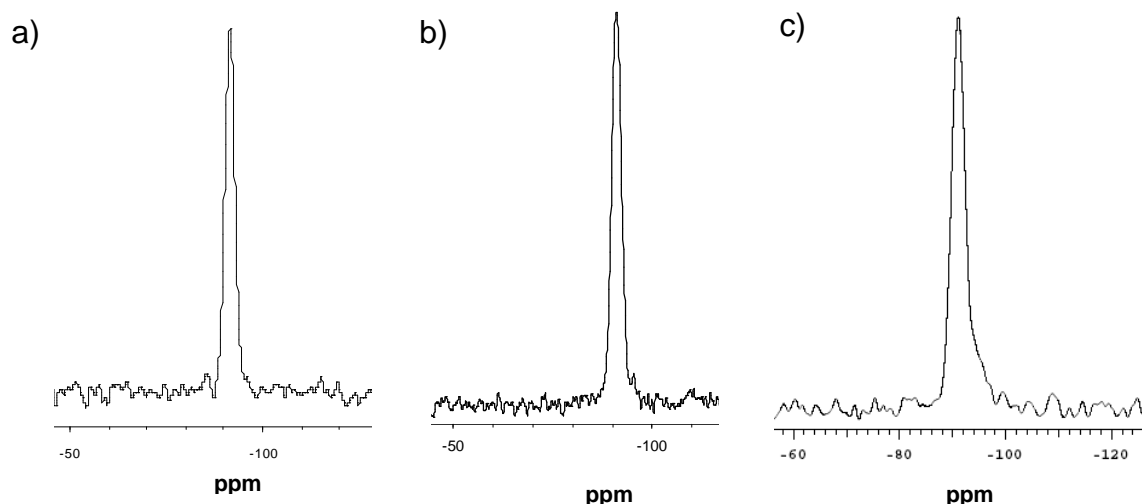


Fig. 3.35 ^{29}Si MAS NMR spectra from the left to right of SAPO(10), SAPO(20) and SAPO(30) STA-7.

The ^{27}Al MQMAS NMR spectra of SAPO and MgAPO STA-7 are different because of the extra resonance in the ^{27}Al MAS NMR for the SAPO (Fig. 3.33). That SAPO and MgAPO MAS NMR spectra are different has to be due to the influence of silicon into the aluminium environment. To investigate this further, ^{27}Al MQ MAS NMR was performed on a reference material with very low Si/Al ratio equal to 0.8 denoted as SAPO(8) STA-7 supplied by S. Warrender from fluoride-containing syntheses and compared with a sample with high silicon content.

Comparing the ^{27}Al MQ MAS NMR in SAPO(8) and SAPO(30) STA-7 samples (Fig. 3.36), the extra signal appears with increasing silicon content. In SAPO(8) with low silicon content, this broad resonance does not appear and its 2D spectrum does not have the extra resonance close to the T sites signal. So it can be concluded that the extra weak broad resonance at 8.6 ppm in the 1D ^{27}Al MAS NMR spectrum comes from the Al(1Si,3P) environment. Similar observations have been made in the literature for the ^{27}Al MQ MAS NMR spectrum of SAPO-37 (FAU), where a resonance close to the tetrahedral signal was attributed to Al(1Si,3P),¹⁸ but this is more convincingly demonstrated here by the analysis of samples with different silicon content. For SAPO(8) STA-7, ^{27}Al MQMAS NMR has two extra resonances, which are thought to be related to Al-F environments.

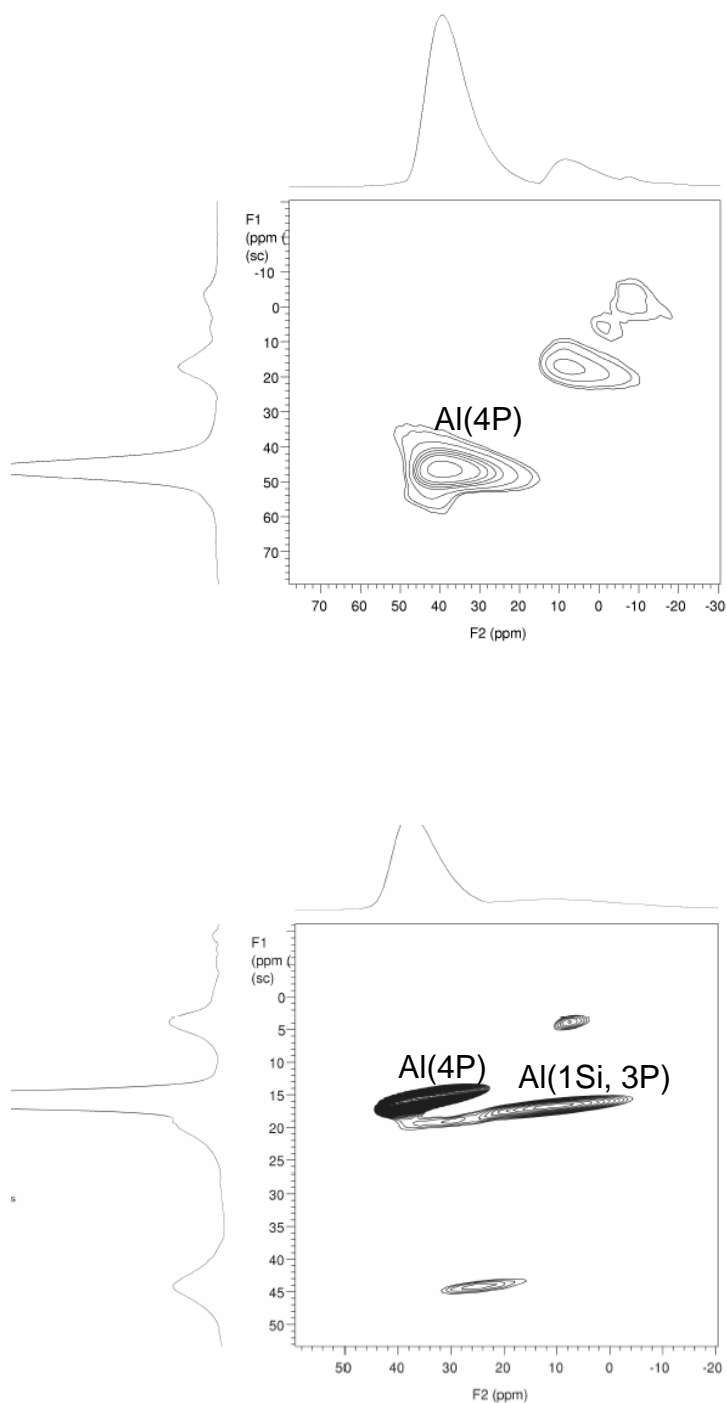


Fig. 3.36 ^{27}Al MQ MAS NMR spectra in SAPO(8) and SAPO(30) STA-7, top and bottom respectively.

3.3.3 Characterisation of Calcined Materials

This section includes the characterisation of the calcined forms of STA-7 for their applications in adsorption, diffusion and catalysis.

3.3.3.1 Characterisation of Calcined SAPO(20) STA7 Material

TGA

TGA profiles are influenced by the topology of the sample rather than the organic species present therein.⁶ STA-7 possesses a three-dimensionally connected pore system, connected via 8MR windows. As a consequence, the rate of loss of organic species upon calcination is swift, with all organic species being removed in a single event with a weight lost of *ca.* 17% (template content per unit cell of *ca.* 90%), despite there being two different organic species present (Fig. 3.37).

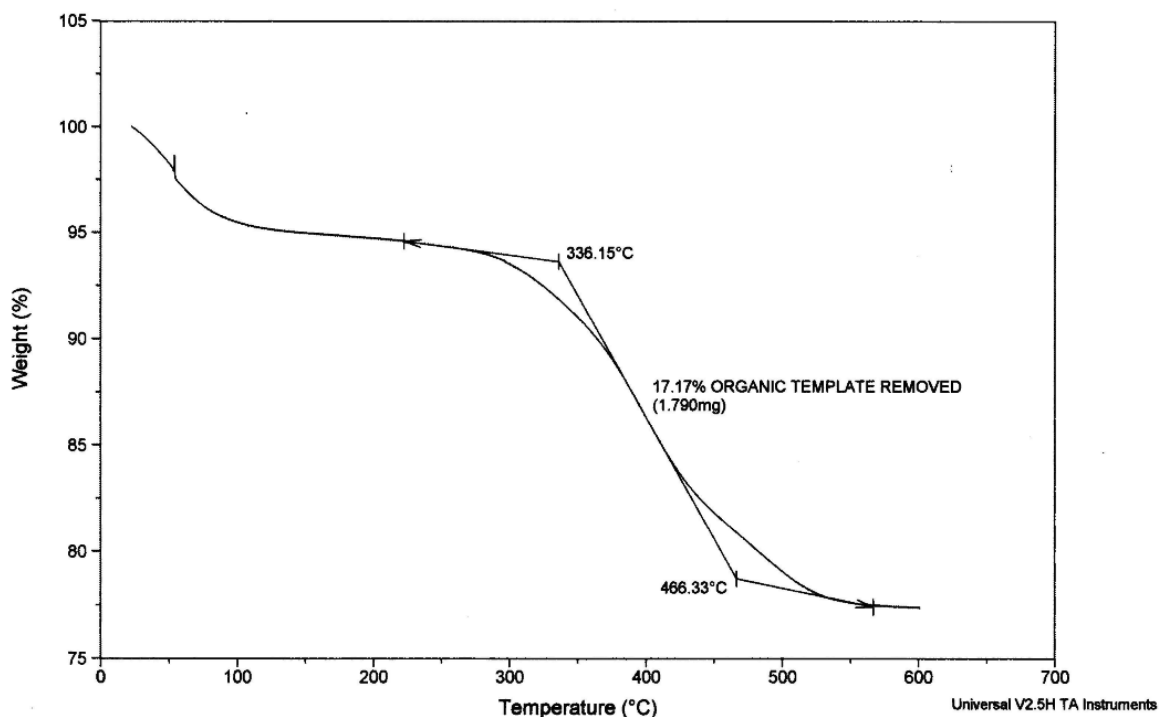


Fig. 3.37 Typical TGA thermogram of SAPO(20) STA-7.

The TGA profile shows a weight lost of *ca.* 17% related to the removed organic. That means a 90% of organic content per unit cell. The optimum calcination conditions to remove the organic species to obtain the free void volume are 550 °C in a stream of dry

oxygen (Fig. 3.38). These conditions were used for experimental calcinations, where the temperature was increased from room temperature to the desired maximum at 1.5 °C/min and held at the final temperature for 12 hours. The slow rate ramp and long dwell time was used to ensure all template was removed. Once the templates were removed, X-ray powder diffraction was conducted to check crystallinity (see Fig. 3.3 for the XRD patterns).

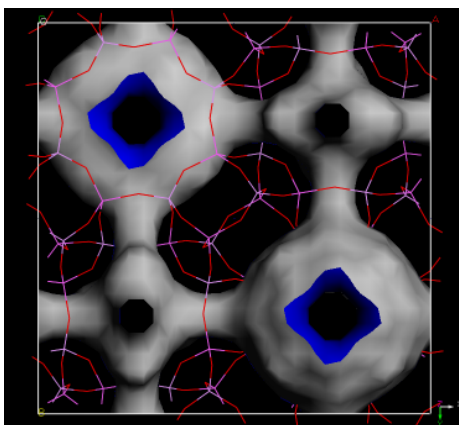


Fig. 3.38 Free void space in STA-7 framework upon calcination, as shown by A. Fecant (IFP-Lyon).

SXRD and Refinement

Previously, the as-prepared structure of SAPO(20) STA-7 has been discussed in detail. It is also important to observe the structure once the material is calcined, because it is the calcined sample that possesses adsorptive and catalytic properties. For the first time SXRD was performed on a calcined SAPO STA-7 crystal (Table 3.14).

Rietveld refinement of the calcined structure against laboratory powder data was performed with the GSAS program suite using the atomic coordinates determined by SXRD of the as-prepared material (given in Table A.1, Appendix A) as a starting model. Instrumental parameters (background -type 2-, zero point, peak profile coefficients (pseudo-Voigtian peak shape) and structural parameters (unit cell, atomic coordinates, displacement parameters) were refined, constraining the displacement parameters to a single value, which refined to 0.0020(2) Å² and restraining bond lengths, in order to maintain a chemically reasonable framework geometry. The final fit was achieved with

$R_{wp} = 7.8\%$ and $R_p = 5.4\%$, with regions between $12.6 - 13.0$, $15.9 - 16.1$ and $20.5 - 20.8^\circ 2\theta$ excluded due to minor AlPO-18 (AEI) intergrowth at the surface of the crystals (the refined atomic coordinates and thermal parameters as well as bond lengths and angles are provided in Tables B.1, B.2 and B.3 in Appendix B). Figure 3.39 shows the plot of this refinement.

The refined unit cell parameters obtained are $a = b = 18.6931(7) \text{ \AA}$ and $c = 9.4191(5) \text{ \AA}$ in $P4/n$ and bond lengths $P-O = 1.53(6) \text{ \AA}$ and $Al-O = 1.74(7) \text{ \AA}$ (the unit cell values are higher than those observed by SXRD analysis, see Table 3.14 for a comparison of the unit cell values in the as-prepared and calcined using the different structural methods available. For the unit cell refinement, Rietveld method is more accurate than SXRD due to the geometry of the instrument).

Table 3.14 Unit cell parameters for SAPO(20) STA-7 in as-prepared and calcined from different structural methods (*STOE software, **GSAS software, space group $P4/n$).

| Structural Method | $a = b \text{ (\AA)}$ | $c \text{ (\AA)}$ |
|------------------------------------|-----------------------|-------------------|
| SXRD (as-prepared) | 18.656(15) | 9.378(7) |
| SXRD (calcined hydrated) | 18.518(7) | 9.246(4) |
| PXRD* (as-prepared) | 18.7347(19) | 9.3849(14) |
| Refinement** (calcined dehydrated) | 18.6931(7) | 9.4191(5) |

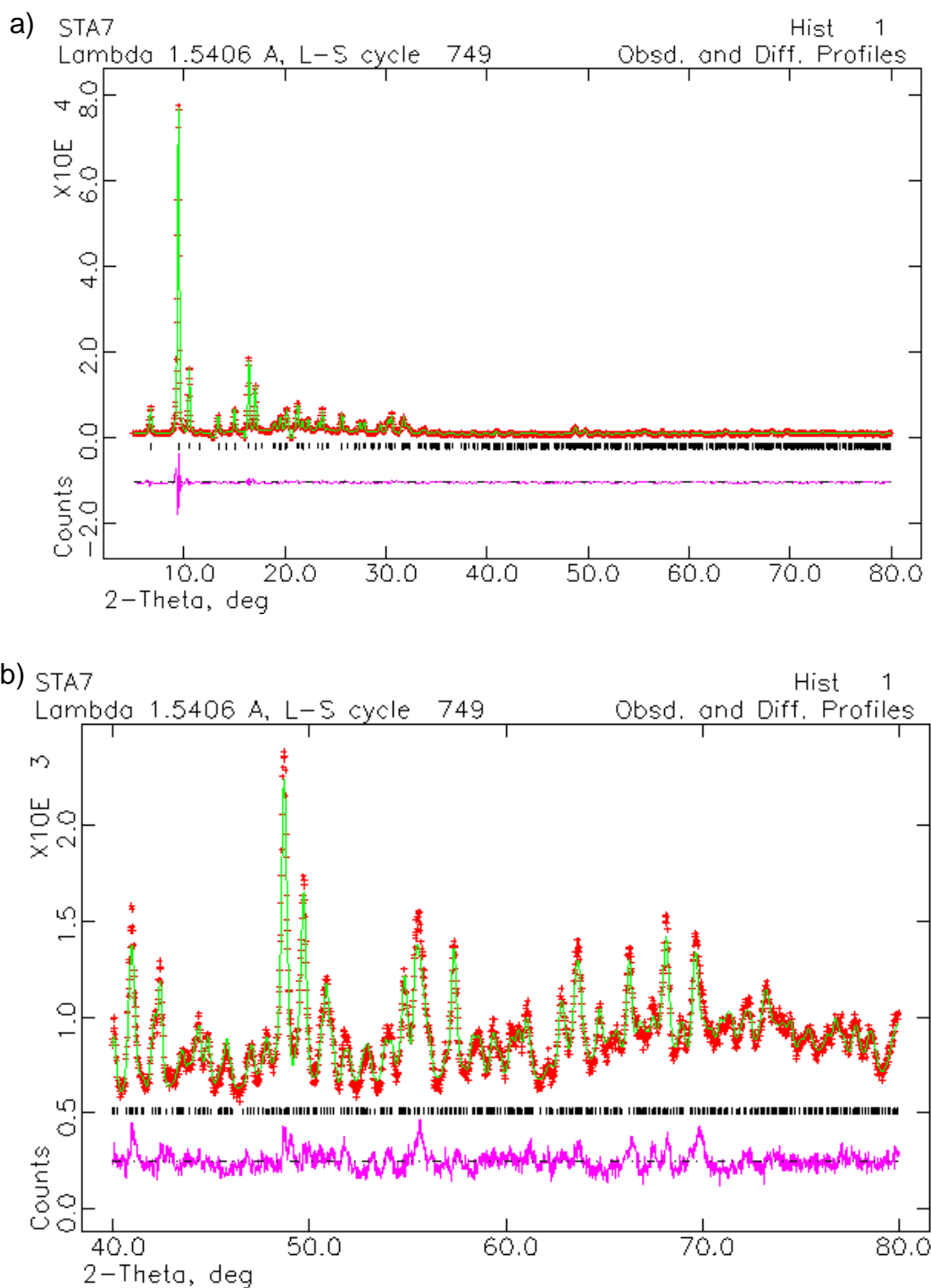


Fig. 3.39 (a) Rietveld refinement plot of calcined SAPO(20) STA-7 (red: experimental data, green: simulated pattern, purple: difference plot), (b) expanded high angle region.

Solid State NMR of calcined SAPO

Solid-state NMR was performed on calcined SAPO(10), SAPO(20) and SAPO(30) STA-7 to study the silicon and aluminium coordination in the framework. The crystallinity of calcined SAPO materials depends strongly on the uptake of water, because the materials suffer hydrolysis after a long period of hydration. This is an important consideration for sample storage, delivery and activation. That issue is reported in literature for the case of SAPO-34 (CHA) where long-term hydration of a calcined sample over two years produces a loss of crystallinity by breaking Si-OH-Al bonds.¹⁹

The ^{29}Si MAS NMR (DP) spectra of calcined samples lose resolution compared with those of as-prepared materials.²⁰ For SAPO(10) and SAPO(20), the spectra show a broad resonance, possibly with more than one peak corresponding to different crystallographic sites, at -94.8 and -95.2 ppm respectively, attributed to Si(4Al) as expected.²¹ At higher silicon contents the silicate islands resonance that is poorly defined in the as-prepared material is more obvious in the spectrum of the calcined solid, with an extra signal at -108.6 ppm related in literature to Si(4Si).⁴ The main signal at -89.4 ppm is in the region related to Si(4Al) and Si(3Al,1Si), although it is rather broad and signal related to Si(2Al,2Si) could also be present (Fig. 3.40).

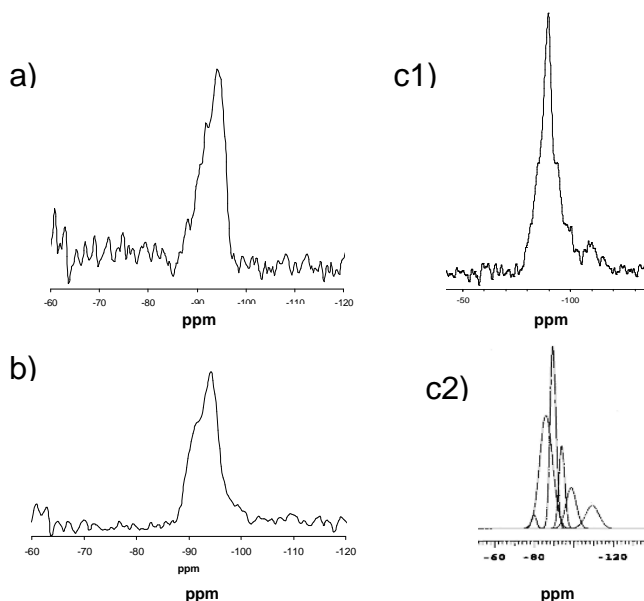


Fig. 3.40 ^{29}Si MAS NMR spectra of SAPO(10), SAPO(20) and SAPO(30) STA-7 (a, b and c1 respectively, c2 is the deconvoluted curves of c1 spectrum).

The ^{27}Al MAS NMR spectrum of sample SAPO(30) shows an acute decrease of the signal related to aluminium in tetrahedral position at 33.7 ppm and in contrast a sharper signal at -11.6 ppm arises. This extra signal is attributed to 6-coordinated Al in the literature;²² probably Al is coordinated to water molecules from moisture, leading to partial removal of aluminum from the framework. As a result, ^{31}P MAS NMR shows an extra shoulder, probably due to Al-O-P broken bonds and the ^{29}Si MAS NMR shows the formation of silica islands in a more predominant manner than in the as-prepared form. The XRD pattern of the SAPO(30) STA-7 after one year after calcination does not show any remarkable loss of crystallinity (Fig. 3.41). Therefore, SAPO materials once calcined remain stable although moisture can cause local redistribution of the framework atoms.

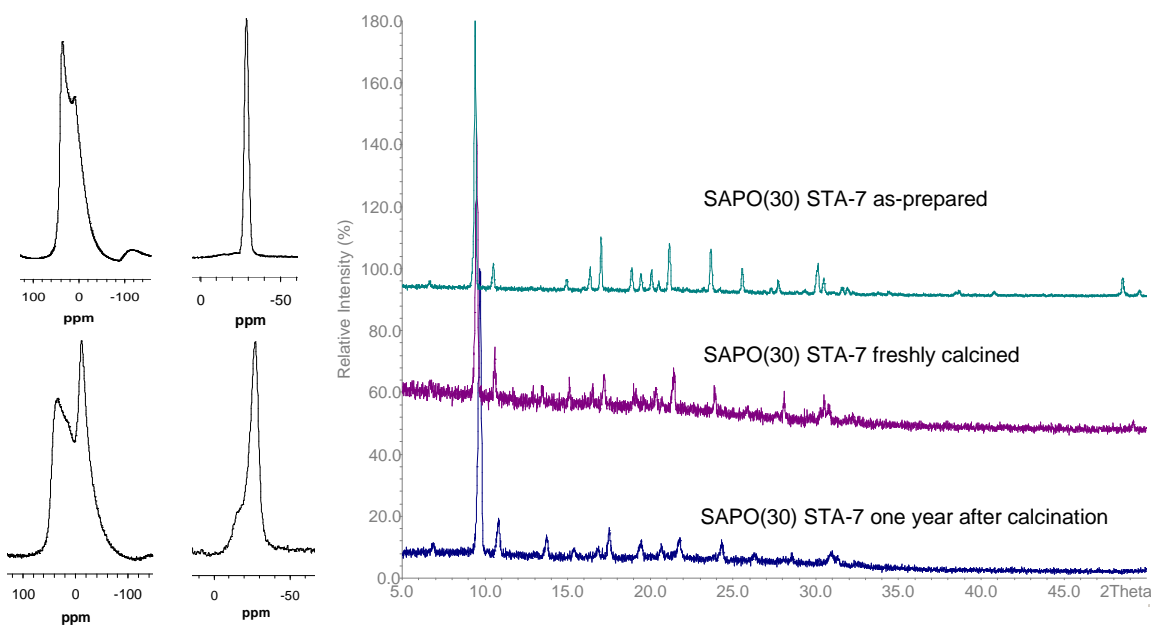


Fig. 3.41 (left) ^{27}Al and ^{31}P MAS NMR spectra of SAPO(30) STA-7 in the as-prepared and calcined form (top and bottom, respectively). (right) XRD patterns of SAPO(30) STA-7 in the as-prepared, freshly calcined and taken after one year of calcination (from top to bottom).

N₂ adsorption

Nitrogen adsorption was conducted gravimetrically on a calcined sample of SAPO(20) STA-7 at 77 K. The resulting isotherm exhibits a typical type I profile. A maximum uptake of 25% by mass suggests an internal pore volume of 0.29 cm³/g, assuming adsorbed N₂ to have a density similar to that of liquid nitrogen at 77 K (0.81 g/cm³), see figure 3.42. The adsorption properties of this and other related materials obtained from this work will be discussed in detail in part three.

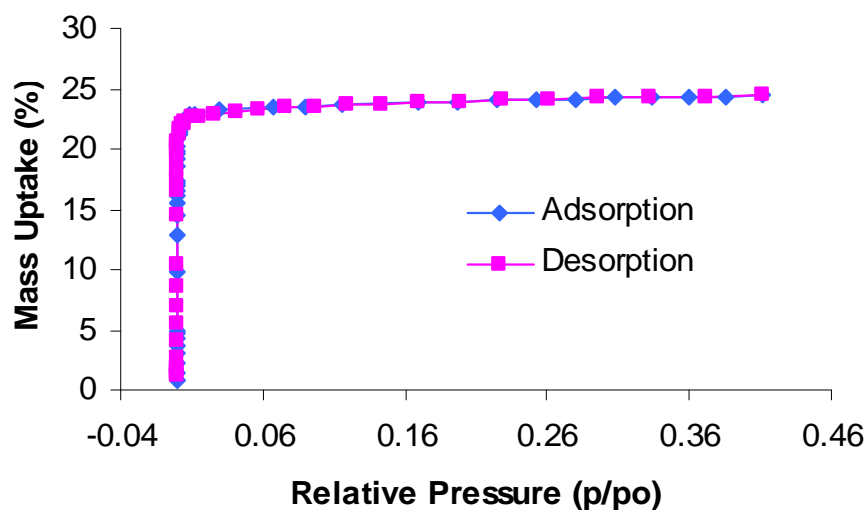


Fig. 3.42 Nitrogen adsorption/desorption isotherm for calcined SAPO(20) STA-7.

FTIR

FTIR spectroscopy provides information about the bridging hydroxyl groups (OH) formed upon calcination. The introduction of silicon into the neutral AlPO forms a negatively charged framework that is balanced by the positive template in the as-prepared material. During calcination the negative charge is balanced by protons attached to bridging oxygen atoms from the T positions where phosphorus atoms have been substituted by silicon atoms. These bridging hydroxyl groups are the Brønsted acid sites available for catalytic applications.

The following spectrum shows two bands (Fig. 3.43): a sharp and intense one between 3600-3625 cm⁻¹ and a broader one between 2900-2800 cm⁻¹. The first one is related to the hydroxyl bridging groups (O-H stretching vibrations)²³. Probably this signal is a

contribution of two bands related to two different Brønsted sites as reported in literature that are not fully resolved in the spectra.²⁴ The second band is related to water molecules adsorbed from moisture. This band decreases upon heating the sample, so that between 250 °C and 350 °C most of the water is removed and the signal disappears. For that reason, 300 °C was the temperature used to activate the materials for adsorption and diffusion experiments.

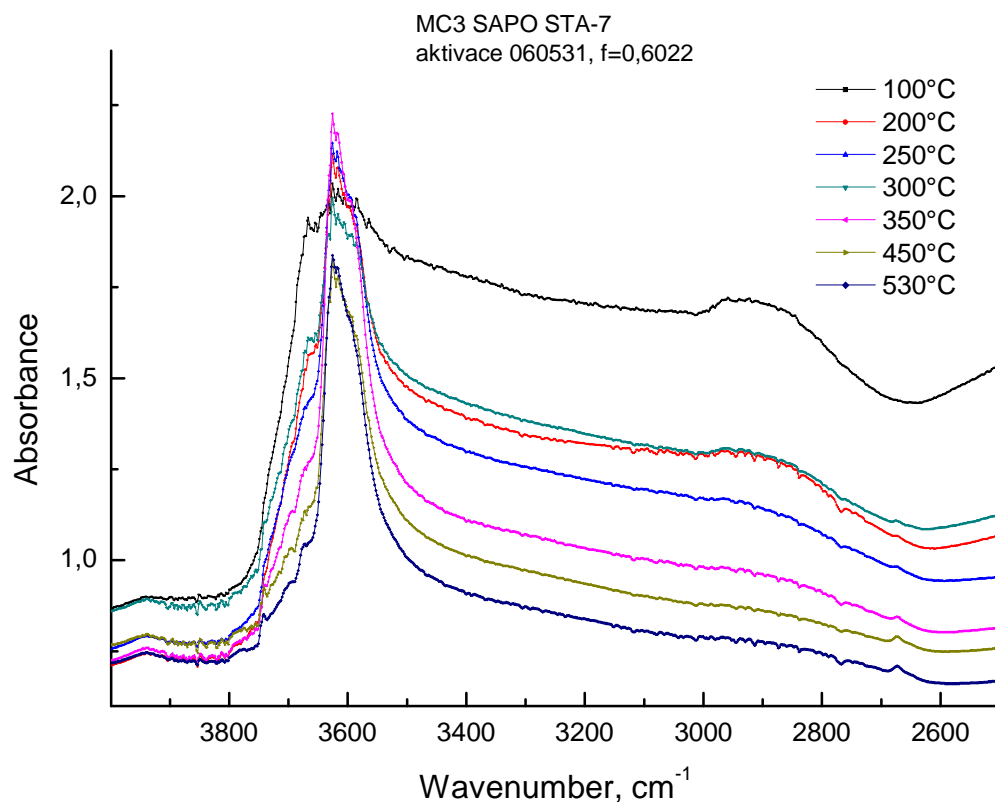


Fig. 3.43 FTIR spectrum of SAPO(20) STA-7 (courtesy of Prof. Jiri Cejka, J. Heyrovsky Institute).

Once the existence of the hydroxyl bridging groups was confirmed, d₃-acetonitrile (CD₃CN) was adsorbed to observe their acidity because acetonitrile acts as a base, interacting via the nitrogen lone pair. From the following spectra (Fig. 3.44), it can be observed that acetonitrile is indeed adsorbed, which resulted in a substantial decrease in the hydroxyl group band intensity. Two new bands appear at 2258 and 2325 cm⁻¹, due to free and chemisorbed acetonitrile respectively.²⁵

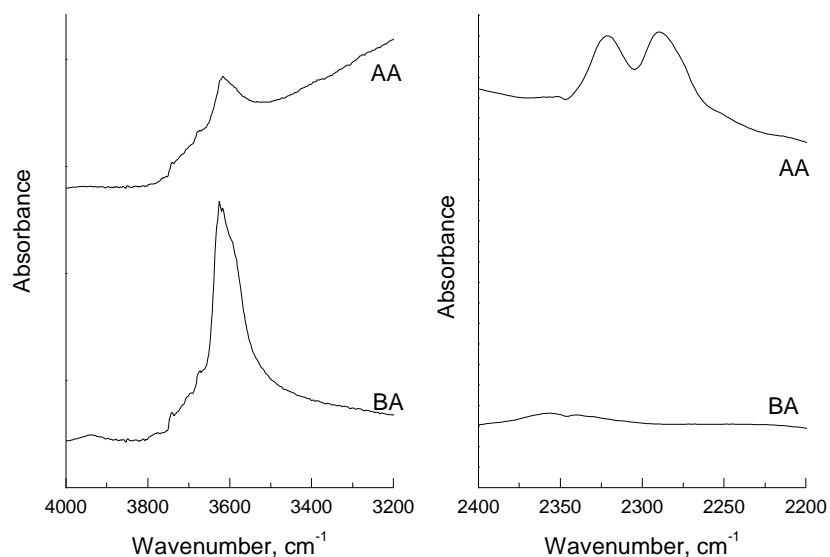


Fig. 3.44 FTIR spectra from d_3 -acetonitrile adsorption in SAPO(20) STA-7, BA (before adsorption) and AA (after adsorption) (courtesy of Professor Jiri Cejka, J. Heyrovsky Institute, Prague).

3.3.3.2 Porosity of Related STA-7 Materials

SAPO(20) STA-7 with extra framework cations by post synthesis treatment

Within the INDENS project, not only was the role of framework composition on adsorption to be studied, but also the interaction of gas molecules with extra framework cations. SAPO(20) STA-7 was used as a starting material for further attempts to introduce extra framework cations via two procedures:

a) in situ, as previously performed by R. Garcia and S. Warrender.^{5,6} The use of azamacrocyclic metal complexes as templates results, once calcined, in extra framework cations within the pores. Cation inclusion is achieved in a convenient two-step process rather than a three-step sequence of synthesis, calcinations and subsequent ion exchange, which itself may not be entirely efficient, or may result in structural degradation.

In this work the effect on STA-7 crystallisation using Cu-cyclam and the new order of addition of reagents was studied. The purple as-prepared Cu-SAPO STA-7 became turquoise upon calcination indicating that the template has been removed leaving Cu^{2+} in the pores. In addition, the new synthetic method gives crystals of different morphology from those observed previously. Whereas previous preparations show clear evidence of

intergrowth crystals, the new method produces tetragonal prismatic crystals. These appear to be an aggregation of layers, particularly at the surface. If tetragonal prisms of SAPO(20) STA-7 were used as seeds in the synthesis, the morphology changes to form large stratified cubic crystals (up to 50 μm) and tiny well shaped cubes (Fig. 3.45). Copper content in the larger crystals is proved by EDX analysis.

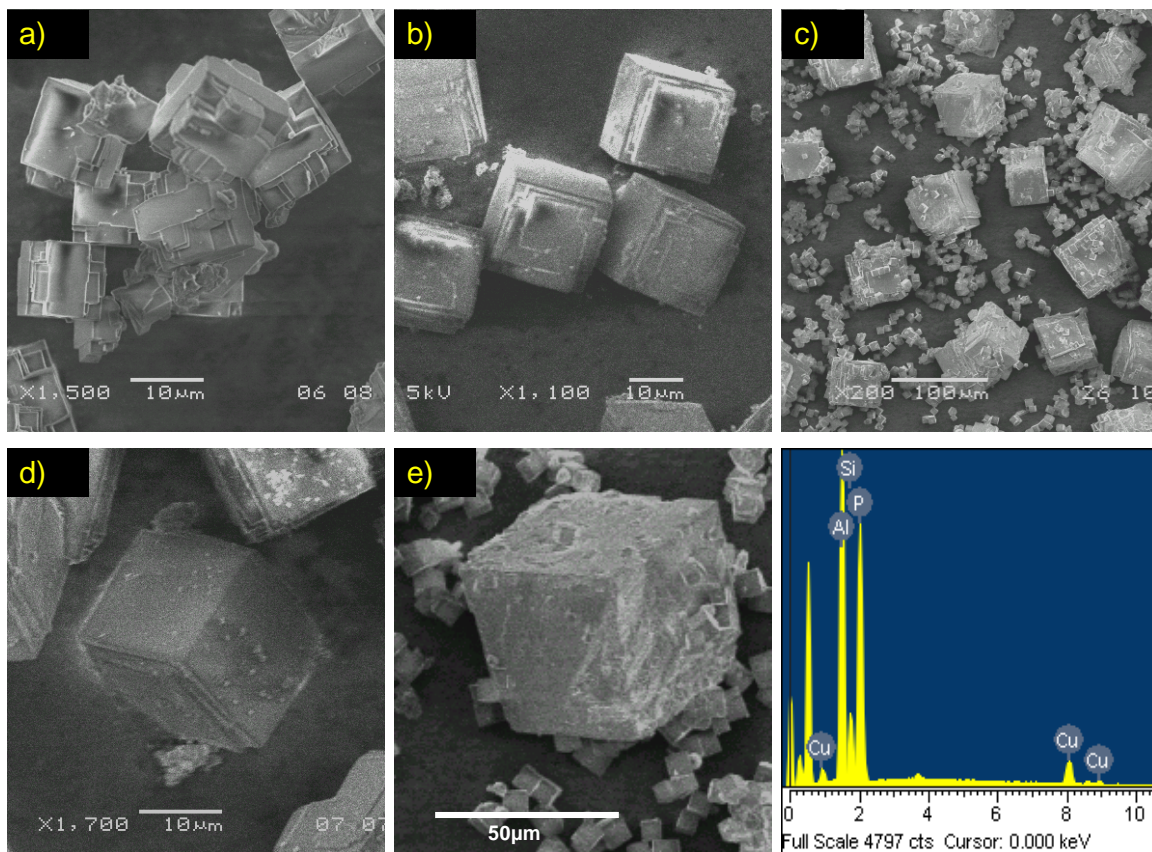


Fig. 3.45 SEM images of Cu-SAPO(20) STA-7: using previous synthetic methodology (a), via the new methodology (b, d) and incorporating SAPO(20) STA-7 crystals as seeds (c, e). EDX of the crystals showed in e) indicates the presence of copper.

b) Post synthesis ion exchange. In this approach the ability to ion exchange calcined SAPO STA-7 was measured. Ion exchange was performed using aqueous nitrate solutions. As a starting point 1M solutions (50 ml) of alkali metal cations (K^+ , Cs^+) and earth metal cations (Mg^{2+} , Ca^{2+}) were used for 0.5 g of STA-7 sample. The exchange procedure was repeated two or three times (each time for about 2 hours) at 70 $^{\circ}\text{C}$ under stirring conditions.

SEM showed significant change in the morphology of the crystals after ion exchange and the XRD patterns show a loss of crystallinity (Fig 3.46 and 3.47). ICP-AES (inductively coupled plasma atomic emission spectroscopy) reveal the limited ion exchange capacity (*ca.* 10%) for divalent cations and the more significant cation exchange for monovalent cations (*ca.* 50%), see Table 3.15. It may be that divalent cations are not readily able to enter the structure because of the large size of their hydrated ions.

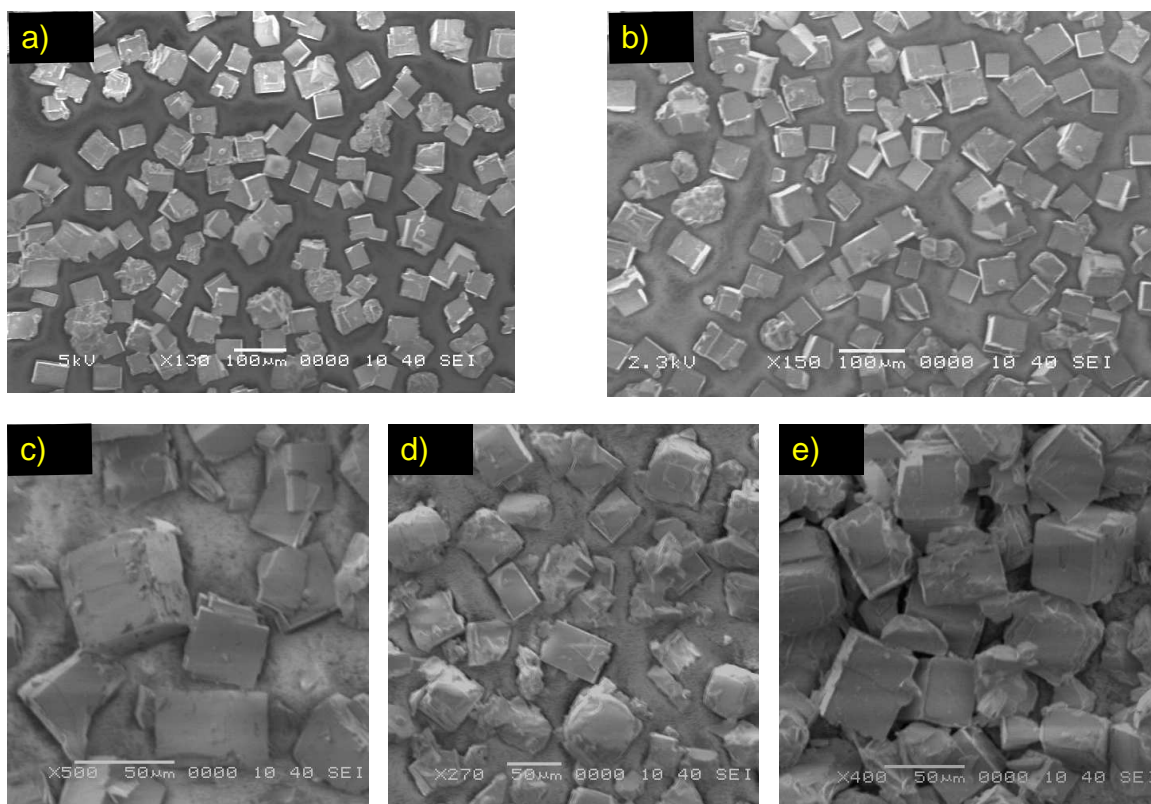


Fig. 3.46 SEM images of SAPO(20) STA-7 as made (a), calcined (b), after K^+ (c), Mg^{2+} (d) and Ca^{2+} (e) ion-exchange.

Table 3.15 ICP-AES analysis on SAPO(20) STA-7 ion exchanged

| Sample | Al% | Si% | P% | Cation% | Exchanged |
|-------------------|------|-----|------|---------|-----------|
| K-SAPO(20) STA-7 | 15.3 | 4.6 | 13.8 | 2.1 | ~ 50% |
| Ca-SAPO(20) STA-7 | 16.3 | 5.3 | 14.0 | 0.5 | ~ 10% |
| Mg-SAPO(20) STA-7 | 16.0 | 4.6 | 14.2 | 0.3 | ~ 7% |

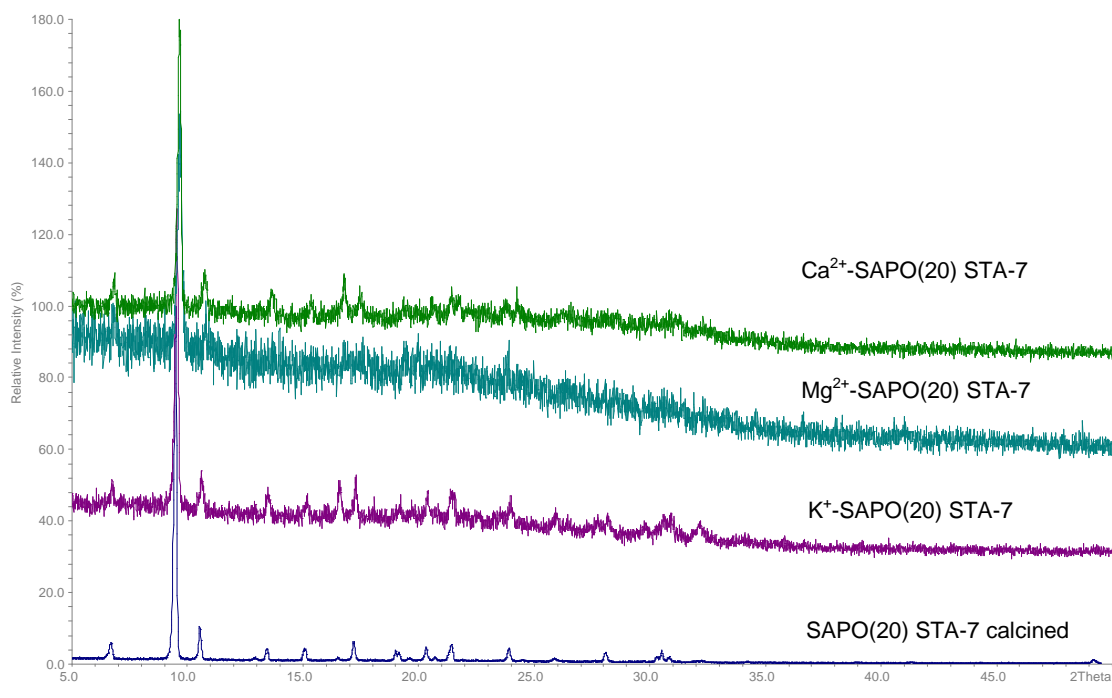


Fig. 3.47 XRD patterns of SAPO(20) STA-7 calcined (blue), after K^+ (purple), Mg^{2+} (cyan) and Ca^{2+} (green) ion-exchange.

The main cause of the loss of crystallinity is likely to be due to slow hydrolysis of the framework. Therefore, several attempts were made, changing experiment time, number of repetitions, temperature and alkali metal cation sources. For K^+ the best results were obtained using 1M KCl, repeating the procedure twice (each time for about 1 hour) heating at 60 °C and stirring at 375 rpm; for Cs^+ , the procedure was followed only once, using the same conditions as K^+ but with 0.4M nitrate solution.

For these conditions, the XRD patterns indicate that the material remained crystalline and SEM images show no significant change in the crystal morphology (Fig. 3.48 and 3.49). EDX shows 63% and 31% ion exchange for K^+ and Cs^+ respectively under these conditions assuming 100% exchange corresponded to a positive charge for every Si atom in the framework. SXRD analysis was possible for the Cs^+ form of SAPO STA-7. Although the data quality was poor ($R_{int} = 0.26$) it indicated the inclusion of Cs^+ . The cation can be located in the 8MR window of the large cage of the STA-7 structure with a Cs-O bond of *ca.* 3.3 Å (Fig. 3.50). EDX analysis suggests that the level of Cs^+ is one third of the maximum calculated on the silicon level of the STA-7, but SXRD locates

only around a quarter of this (occupancy of 0.0625 in general position). The atomic coordinates and related SXRD details are in Tables A.5, A.6, A.7 and A.8, Appendix A.

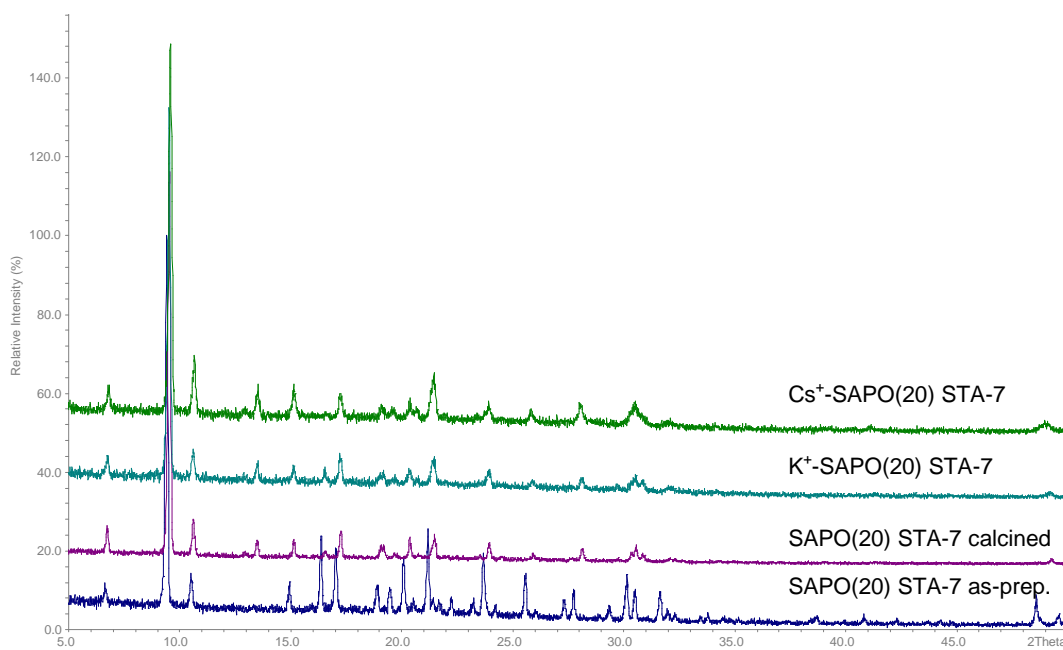


Fig. 3.48 XRD patterns of SAPO(20) STA-7 as-prepared (blue), calcined (purple), for K^+ (cyan) and Cs^+ (green) ion exchange.

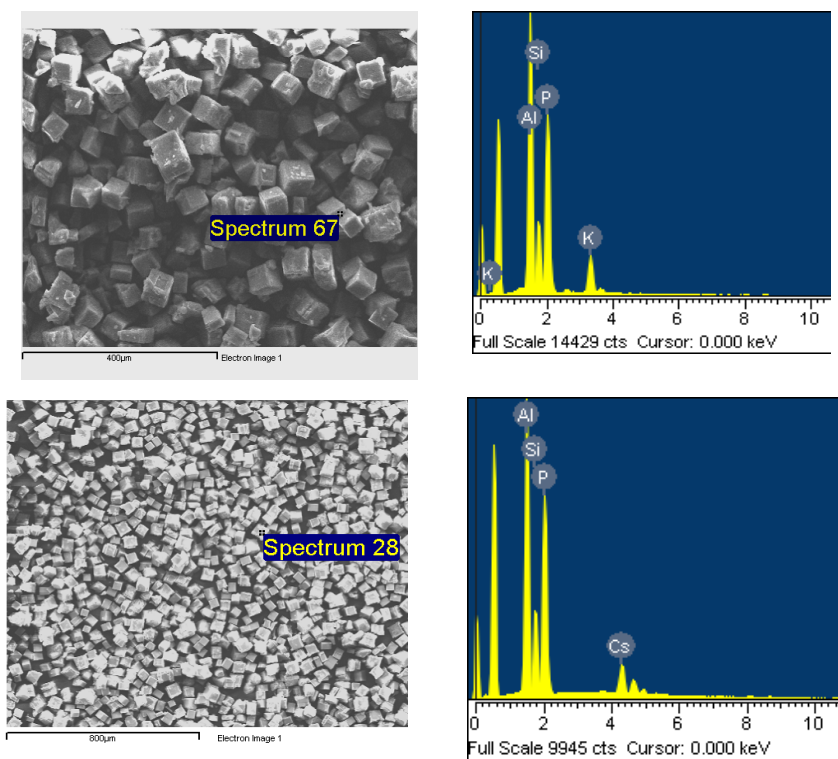


Fig. 3.49 SEM image of SAPO STA-7(20) after K^+ (top) and Cs^+ (bottom) ion exchange.

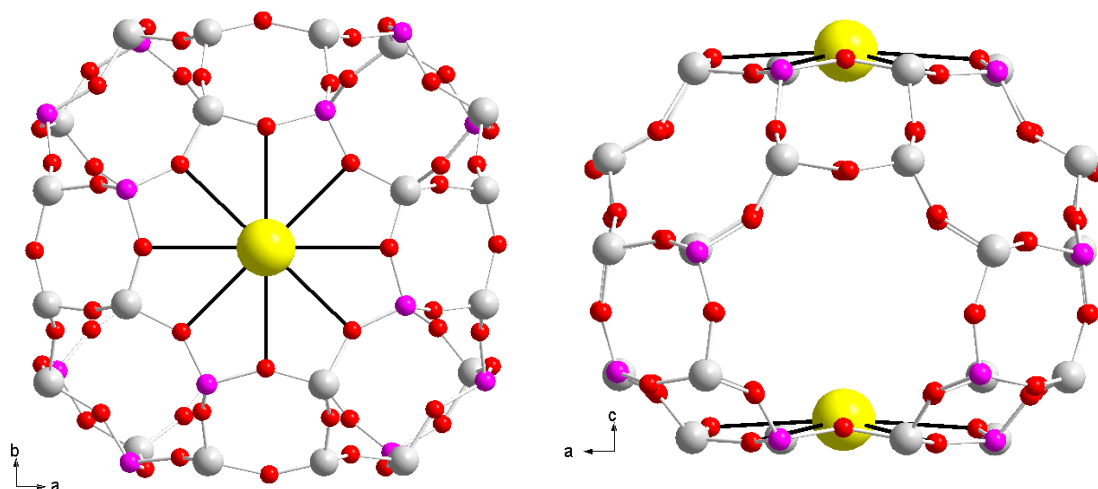


Fig. 3.50 Coordinated environment of Cs^+ in SAPO(20) STA-7.

Porosities of STA-7 materials

Table 3.17 summarises the values of the total volume uptake from N_2 isotherms of each material here synthesised stable after calcination to show their suitability as adsorbents:

Table 3.16 Summary of materials with potential adsorption properties.

| N_2 Isotherms | | | |
|------------------------|-----------------------|-----------|------------------------------------|
| STA-7 | | | |
| Sample | Extraframework Cation | % by mass | Pore Volume cm^3/g |
| SAPO(20) STA-7 | | 24.43 | 0.30 |
| SAPO(30) STA-7 | | 14.67 | 0.18 |
| SAPO(10) STA-7 | | 18.95 | 0.23 |
| SAPO(20) STA-7 | K | 14.89 | 0.18 |
| SAPO(20) STA-7 | Cu | 18.63 | 0.23 |
| CoAPO STA-7 | | 17.45 | 0.22 |
| MnSAPO STA-7 | | 20.67 | 0.26 |
| MgSAPO STA-7 | | 22.14 | 0.27 |

These data show that the STA-7 materials prepared could be used for CO_2 adsorption. The most promising for this purpose are SAPO(20) STA-7, the reference material, and also the MgAPSOs and CoAPO. The samples with ion exchange have a lower pore volume due to reduction of free pore space by the inclusion of cations, but they have retained porosity and so are potential CO_2 adsorbents.

3.4 Summary

The hydrothermal synthesis of the aluminophosphate-based STA-7 material has been explored in detail and a new route to high quality single crystals suitable for further applications has been established.

Structural characterisation of the as-prepared material combined with modelling, elucidates the co-templating effect of the co-base, tetraethylammonium cation (TEA). The inclusion of SiO_2 into the AlPO gel results in silicoaluminophosphate frameworks. The mechanism of incorporation can be monitored by ^{29}Si MAS NMR and also, ^{27}Al MQ MAS NMR. These show that silicon substitutes mainly by phosphorus, giving $\text{Si}(4\text{Al})$ and, as a consequence, $\text{Al}(1\text{Si},3\text{P})$ sites for samples up to Si/Al ratio 0.27. At higher content, a small number of silica islands are formed.

The study of calcined SAPO STA-7 by ^{27}Al MAS NMR shows that this is stable, porous and acidic, but needs to be stored dry.

-
1. P. A. Wright, M. J. Maple, A. M. Z. Slawin, V. Patinec, R. A. Aitken, A. Welch, P. A. Cox, *J. Chem. Soc., Dalton Trans.*, 2000, 1243.
 2. V. Patinec, P. A. Wright, P. Lightfoot, R. A. Aitken, P. A. Cox, *J. Chem. Soc., Dalton Trans.*, 1999, 3909.
 3. W. G. Song, J. F. Haw, J. B. Nicholas, C. S. Heneghan, *J. Am. Chem. Soc.*, 2000, **122**, 10726; W. G. Song, J. F. Haw, *J. Am. Chem. Soc.*, 2001, **123**, 4749.
 4. J. Chen, P. A. Wright, J. M. Thomas, S. Natarajan, L. Marchese, S. M. Bradley, G. Sankar, C. R. A. Catlow, P. L. Gai-Boyes, R. P. Townsend, C. M. Lok, *J. Phys. Chem.*, 1994, **98**, 10216.
 5. R. Garcia Salas, *Synthesis and Characterisation of Aluminophosphate-based Materials Prepared with Nickel Complexes as Structure Directing Agents*, PhD Thesis, University of St Andrews, 2003.
 6. S. J. Warrender, *Structure Direction in the Formation of Zeolitic Materials*, PhD Thesis, University of St Andrews, 2007.
 7. STOE Win XPOW (version 1.04), STOE & Cie GmbH, Hilpertstrasse, D-64296, Darmstadt, 1999.
 8. A. C. Larson, R. B. von Dreele, Generalized Crystal Structure Analysis System, Los Alamos National Laboratory, USA, 1988.
 9. SHELXTL 6.14, G M Sheldrick, Bruker AXS, Madison, 2004.
 10. MS Modelling version 4.0, Accelrys Inc, San Diego, USA, 2006.

-
11. A.K. Rappé, C.J. Casewit, K.S. Colwell, W.A. Goddard, W.M. Skiff, *J. Amer. Chem. Soc.*, 1992, **114**, 10024; C.J. Casewit, K.S. Colwell, A.K. Rappé, *J. Am. Chem. Soc.*, 1992, **114**, 10035; C.J. Casewit, K.S. Colwell, A.K. Rappé, *J. Am. Chem. Soc.*, 1992, **114**, 10046; A.K. Rappé, K.S. Colwell, C.J. Casewit, *Inorg. Chem.*, 1993, **32**, 3438.
 12. S. Oliver, A. Kuperman, A. Lough, G. A. Ozin, *J. Mater. Chem.*, 1997, **7**, 807.
 13. P. S. Wheatley, R. E. Morris, *J. Solid State Chem.*, 2002, **167**, 267.
 14. H. Hobson, K. P. Lillerud, 'Verified Synthesis of Zeolitic Materials', 2nd Edition, Elsevier, Amsterdam, 2001.
 15. J. F. Desreux, E. Merciny, M. F. Loncin, *Inorg. Chem.*, 1981, **20**, 987.
 16. P. J. Barrie, J. Klinowski, *J. Phys. Chem.*, 1989, **93**, 5972.
 17. C. S. Blackwell, R. L. Patton, *J. Phys. Chem.*, 1988, **92**, 3965.
 18. T.-H. Chen, B.H. Wouters, P.J. Grobet, *Colloids and Surfaces A: Physicochemical and Engineering Aspects*, 1999, **158**, 145.
 19. M. Briend, R. Vomscheid, M. J. Peltre, P. P. Man, D. Barthomeuf, *J. Phys Chem.* 1995, **99**, 8270.
 20. H. J. Jung, C.-H. Shin, S. B. Hong, *J. Phys. Chem. B*, 2005, **109**, 20847.
 21. C. S. Blackwell, R. L. Patton, *J. Phys. Chem.*, 1988, **92**, 3965.
 22. R. Vomscheid, M. Briend, M.J. Peltre, P.P. Man, D. Barthomeuf, *J. Phys. Chem.*, 1994, **98**, 9614.

23. S. A. Zubkov, L. M. Kustov, V. B. Kazansky, I. Girnus, R. Fricke, *J. Chem. Soc. Faraday Trans.*, 1991, **87**, 897.

24. I Déroche, G. Maurin, P. Llewellyn, M. Castro, P.A. Wright, M. Bejblova, J. Cejka, *From Zeolites to Porous MOF Materials the 40th Anniversary of International Zeolite Conference*, R. Xu, Z. Gao, J. Chen, W. Yan (Eds.), Elsevier, Amsterdam, 2008, 1660.

25. G.M. Pearce, S. Bordiga, Pers. Comm.

Chapter 4: STA-14

4.1 Introduction

Having prepared the SAPO form of STA-7 using a co-templating strategy arrived at via a trial and error approach, this strategy was developed in attempts to synthesise, as an aluminophosphate, a structure type that had not previously been prepared as an AlPO-based solid, but which had been observed as an aluminosilicate zeolite, ZK-5(KFI), one of the first synthetic zeolites to be discovered.¹

Like the SAV (and also CHA and AEI) framework types, KFI is built up from double 6-membered rings (D6Rs) only, but with a different stacking arrangement. Furthermore, the (001) surface of the SAV structure is topologically identical to the {100} surfaces of KFI. It was therefore thought likely that an AlPO-based KFI structure could be prepared under similar gel compositions to those that give the substituted (MAPO, SAPO) versions of AlPO-18 and -34, and STA-7, if suitable structure directing agents could be found.

The ZK-5 structure, like that of STA-7, has two types of cages. In ZK-5, these are the so-called α -cage (also found in the structure of zeolite A and the isostructural AlPO-42 (LTA)) and a smaller cage found in the structure of zeolite merlinoite (MER) (Fig. 4.1).

Previous studies have shown that the azaoxacryptand 4,7,13,16,21,24-hexaoxa-1,10 diazabicyclo[8.8.8]hexacosane (K222, see figure 4.2) is a good template for AlPO-42 and its substituted derivatives, and must reside in the α -cage.^{2,3}

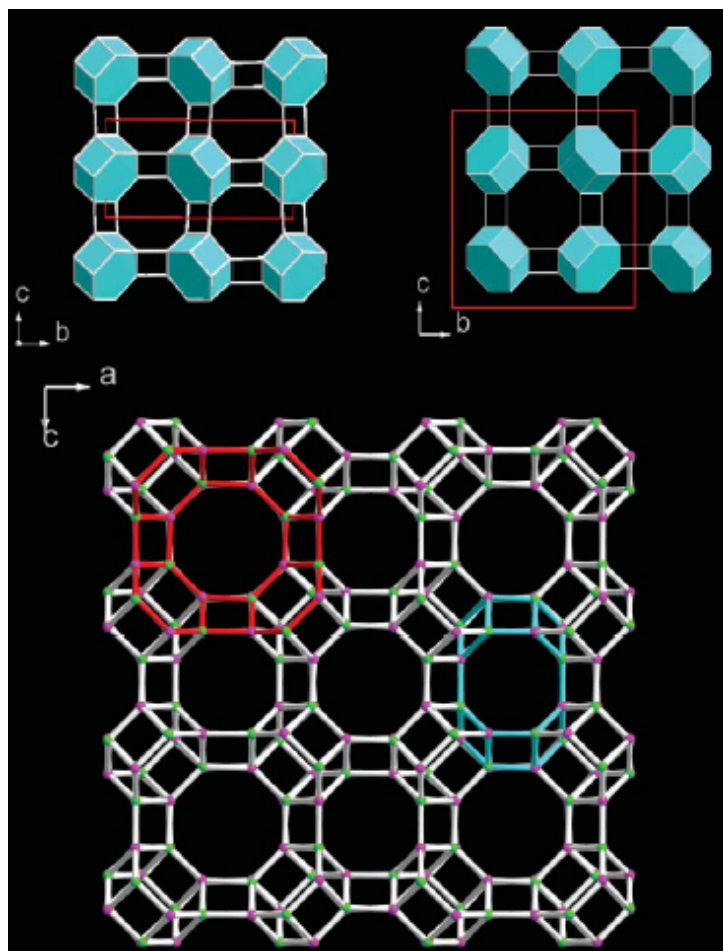


Fig. 4.1 The basis of the hypothesis for the design of a novel zeotype isostructural to zeolite ZK-5. The structures SAV (top left) and KFI (top right), both made of D6Rs (in blue), viewed along the a -axis. In SAV, layers are stacked along the c -axis by translation, whereas in KFI the adjacent layers are related by a mirror plane perpendicular to the c -axis. (Bottom) The KFI structure, with oxygen atoms omitted, with the α - and MER cages outlined in red and cyan, respectively.

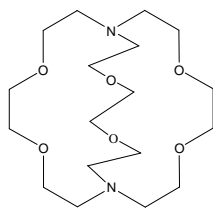


Fig. 4.2 The azaoxacryptand K222 applied in the synthesis of AlPO-42 the zeotype version of zeolite A (LTA).

Using the co-templating approach, a selection of readily available amines and alkylammonium cations were screened computationally for their fit within the MER cage and the results used to guide the synthesis. The modelling results were compared with the products, and the more interesting phases were structurally characterised for further applications.

4.2 Experimental

Synthesis of gels

A typical MgAPO synthesis with gel composition 0.2 Mg : 0.8 Al : P : 40 H₂O : 0.108 K222 : x co-base, denoted in the text as MgAPO(20) STA-14, was prepared by adding Al(OH)₃ to H₃PO₄ (85%) in water, prior to the addition of Mg(OAc)₂. Co-base was added until pH 6.8 was achieved, followed by the addition of K222. This gel was stirred until homogenous. Then, the gels were loaded in Teflon-lined stainless steel autoclaves and heated in the oven at 190°C for two days. After this period, the autoclave was removed from the oven and allowed to cool. For the SAPO gel the procedure is the same but using five days of hydrothermal treatment. The syntheses were performed based on 4.5 ml of water, in order to reduce the cost due to the expensive K222. As a result, *ca.* 0.15-0.20 g of product was obtained once sonicated and dried.

Crystallography, Modelling and Unit Cell composition

The single crystal data were collected on appropriate crystals of this MgAPO product and integrated and analysed in several cubic space groups. The best R_{int} (= 0.19) was obtained in the space group, Pn-3n, which permitted strict Mg,Al/P ordering within tetrahedral cation sites of the framework. Atomic coordinates and bond lengths are included in Appendix A (Tables A.9 to A.12), and details of the single crystal solution are given in the cif file (available on attached CD). TEA was located on a special position in the smaller cages, disordered over two positions, with *ca.* 80% in the tt.tt configuration. Its conformation was refined using the model N-C1-C2 (see section 2.3.3.1 and Fig. 2.6 for details). A small amount of residual electron density in the smaller cage was refined (C3) as disorder in the TEA configuration (20%). Electron density in the Fourier map within

the large pore was located, presumably due to the template K222, but it was not possible to determine the position of the template (Fig. 4.3).

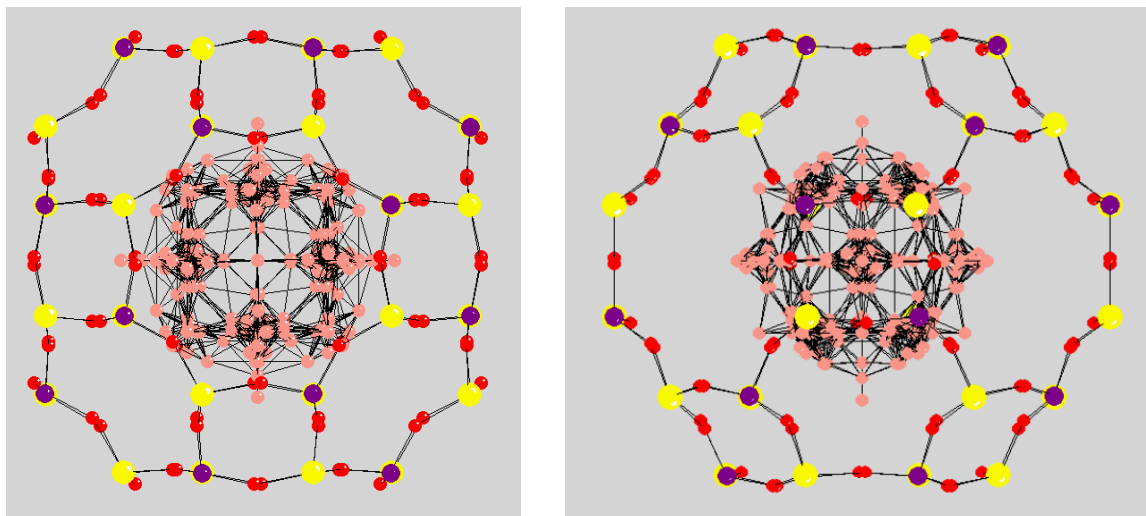


Fig. 4.3 Electronic density attributed to K222 in α -cage of MgAPO(20) STA-14.

Modelling was used to obtain the K222 coordinates to improve the final R_{int} value (Fig. 4.4), but its flexibility made it difficult to find a real energy minimum configuration: many similar conformations were obtained with similar energies. Including K222 in a modelled position slightly improved the fit, but the thermal parameters refined to an unreasonable large value. Some extra density in the large cage was refined as oxygen and nitrogen atoms.

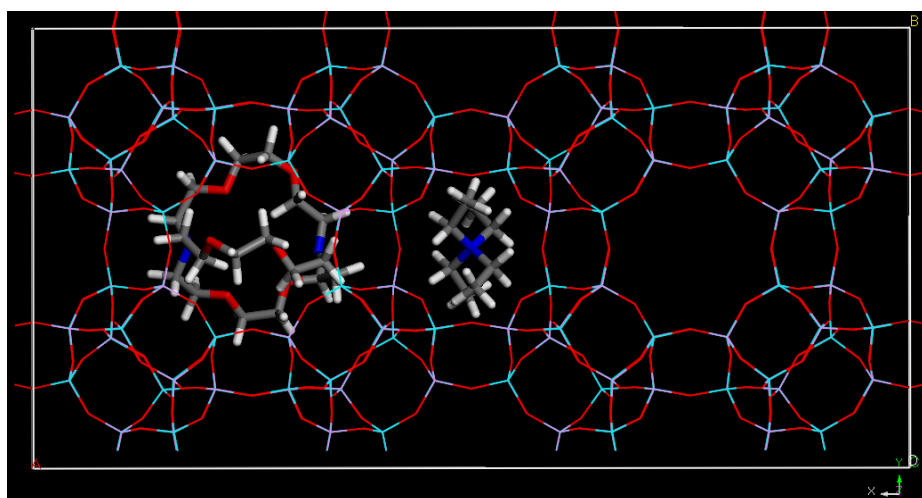


Fig. 4.4 K222 and TEA modeled in the AlPO KFI framework.

Combining TGA, EDX, CHN and assuming full occupancy of the MER cages by TEA gives a unit cell composition of $[\text{Mg}_{10}\text{Al}_{38}\text{P}_{48}\text{O}_{192}] (\text{TEA}^+)_6 (\text{H}_2\text{Kryptofix}^{2+})_1 (\text{NH}_4^+)_2 \cdot 40 \text{H}_2\text{O}$.

Synchrotron data

High resolution X-ray powder diffraction data were collected on station ID-31 of the ESRF synchrotron at Grenoble using radiation of wavelength 0.800020 Å, on a calcined sample of MgAPSO(2:3) STA-14 by S. Miller and P. Wright.

Solid-state NMR

MAS NMR spectra were collected at the EPSRC solid-state NMR Facility in Durham University by Dr David Apperley on samples summarised in Table 4.1. ^{27}Al and ^{31}P experiments were performed on a Varian VNMRs 400 spectrometer, using a 4 mm probe and for ^{29}Si and ^{13}C a Unity Inova 300 spectrometer, using a 7.5 mm probe. Table 4.2 summarises the conditions of the experiments. As an exception, the ^{27}Al spectrum of sample **1** was measured on a Unity Inova 300 spectrometer with a 4 mm probe. Zero ppm was defined as the shift for 1M aqueous AlCl_3 , 85% H_3PO_4 and tetramethylsilane (TMS), for ^{27}Al , ^{31}P and ^{29}Si respectively.

Table 4.1 STA-14 samples used for MAS NMR experiments ordered as appearance in the text.

| Samples | | | Composition in Gel | | | | |
|----------|----------|----------|--------------------|-------|------|------|------|
| 1 | 2 | 3 | MgAPO | Mg/P | 0.20 | 0.10 | 0.50 |
| 4 | 5 | | SAPO | Si/Al | 0.20 | 0.30 | |

Table 4.2 Experimental parameters for ^{27}Al , ^{31}P , ^{29}Si and ^{13}C MAS NMR spectra on samples summarised in Table 4.1, (DP = Direct Polarisation, CP = Cross Polarisation, DD = Direct Detected, ID = Indirect Detected).

| Sample | Freq (MHz) | Acq time (ms) | Relaxation delay (s) | Polaris | Contact time (ms) | Pulse time | Spin rate (kHz) |
|---------------------|---------------|---------------------|----------------------------|--------------------|-------------------------|------------------------------|-----------------------|
| ^{27}Al | | | | | | | |
| 1 | 78.123 | 10.0 | 0.5 | DP | - | 25.7° | 16 |
| 4, 5 | 104.198 | 20.0 | 0.2 | DP | - | 1.0 μs | 14 |
| ^{27}Al MQ | | | | | | | |
| 4 | 104.197 | 5.0 | 0.1 | DD (F2) ID (F1) | - | 3.6 and 1.4 μs | 14 |
| ^{31}P | | | | | | | |
| 1 | 121.370 | 20.2 | 60.0 | DP | - | 90° | 13 |
| 2 | 161.878 | 20.0 | 300.0 | DP | - | 3.4 μs | 10 |
| 3 | 161.878 | 10.0 | 300.0 | DP | - | 3.4 μs | 10 |
| 4 | 161.878 | 15.0 | 300.0 | DP | - | 3.4 μs | 10 |
| 5 | 161.878 | 15.0 | 2.0 | CP | 3.0 | - | 10 |
| ^{29}Si | | | | | | | |
| 4, 5 | 59.557 | 30.0 | 120.0 | DP | - | 90° | 5 |
| ^{13}C | | | | | | | |
| 1 | 75.398 | 30.0 | 1.0 | CP | 1.00 | - | 5 |

4.3 Results & Discussion

4.3.1 Modelling

The following organic species were selected on the basis of their size as candidate templates for the MER cage, the smaller cage of structures with the KFI topology: tetramethylammonium (TMA), TEA and tetrapropylammonium (TPA) cations and the amines dimethylamine (DMA), diethylamine (DEA), di-n-propylamine (DPA), triethylamine (TrEA) di-isopropylamine (DIPA) and di-isopropylethylamine (DIPEA) as well as piperazine (PIP).

The modelling procedure was carried out as explained in detail for STA-7 using an AIPO (KFI) framework. The calculated enthalpies of adsorption are summarised in the following histogram (Fig. 4.5):

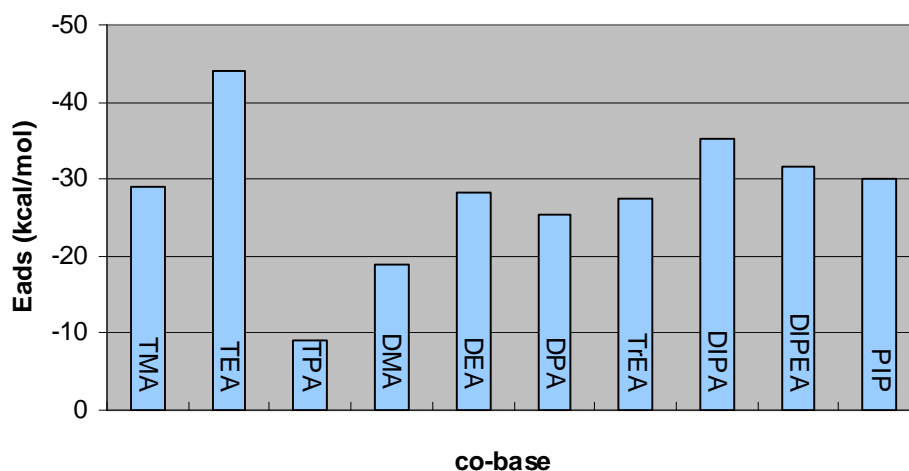


Fig. 4.5 Histogram of the non-bonding energies of potential co-templates for the MER cages of the AIPO-KFI structure indicates that TEA has most negative energies and therefore it is the most promising.

These data revealed that the most favorable fit was for TEA in the tt.tt configuration* (Fig. 4.6 c), but a number of the potential SDAs gave favorable energies. By contrast, TPA gives the less favorable interaction energy because it is too large to fit within the MER cage (Fig. 4.6 a).

* tt.tt is the abbreviation for the trans-trans conformer.



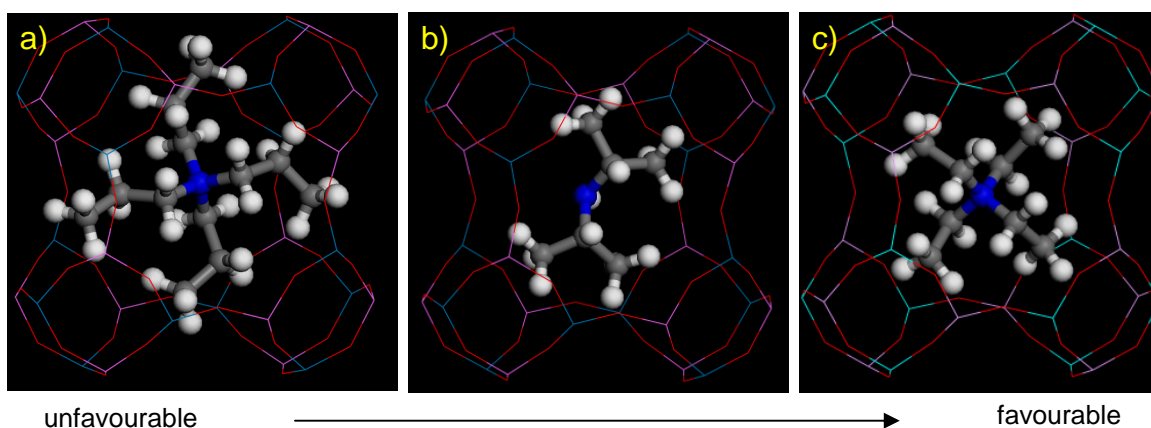


Fig. 4.6 Trend in non-bonding interaction between co-bases and MER cage: TPA (a), DIPA (b) and TEA (c).

4.3.2 Synthesis

The results of the co-template modelling prediction were used in a program of hydrothermal synthesis to assess the applicability of this approach to design a route to a target material with two cage types. The following issues are addressed here:

Issue1: MgAPO screening with K222 and potential co-templates.

Issue2: MgAPOs with different magnesium content.

Issue 3: Variation of framework chemistry.

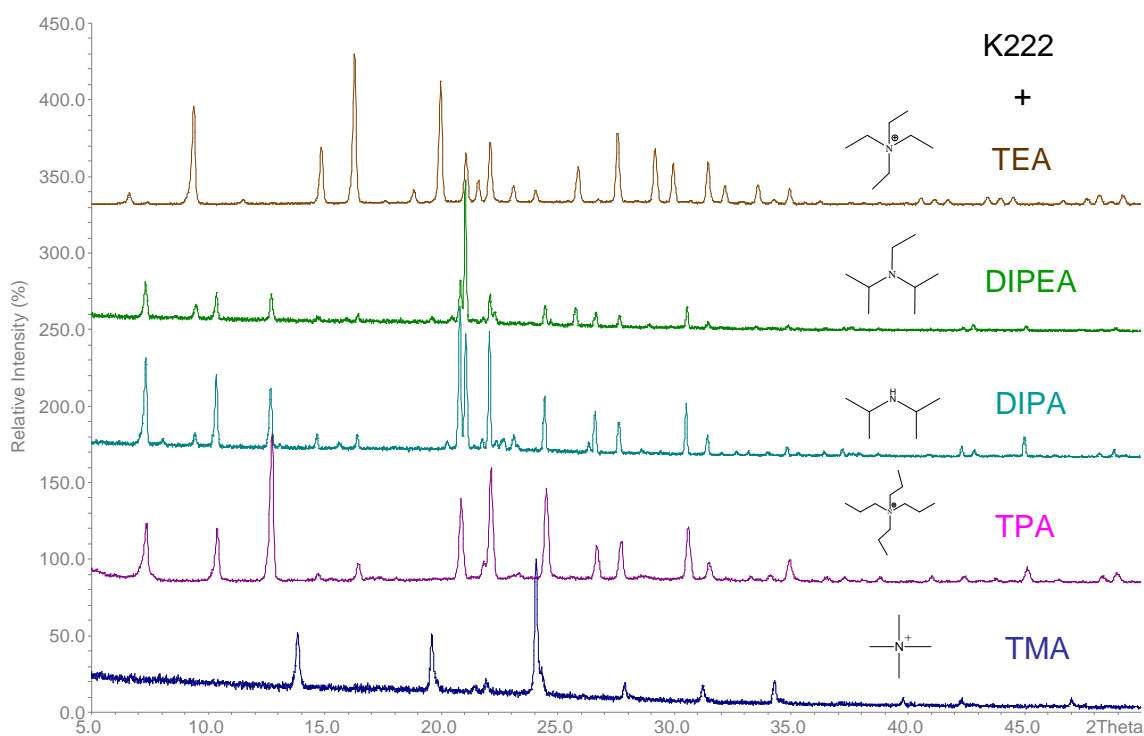
Issue 4: Modifying the morphology of STA-14.

4.3.2.1 Co-Template Screening in MgAPO Composition, from Hypothesis to Experiment

As a starting point, screening of the potential amines as co-template was applied to the crystallisation of magnesioaluminophosphate (MgAPO) gels. Such preparations are known to crystallise rapidly and give highly crystalline solids. In addition to the co-bases already mentioned, pyridine (PYR) was included due its similar size to piperazine (PIP). The solids produced are summarised in the following Table 4.3 with the XRD patterns in Fig. 4.7, 4.8 and 4.9. The identification of phases from their XRD patterns was from indexing and also comparing them against the collection of simulated XRD patterns for zeolites and zeotypes.⁴

Table 4.3 Summary of the co-base screening in MgAPO gel.

| Template | Co-base | Product (by XRD) | Indexed Unit Cell Parameter (Å) and Space Group | |
|----------|---------|-----------------------|---|-------|
| K222 | TPA | LTA | $a = 12.048(4)$ Å | Pm-3m |
| | DPA | LTA | by comparison with simulated pattern | |
| | DIPA | LTA mainly | by comparison with simulated pattern | |
| | DEA | LTA mainly | by comparison with simulated pattern | |
| | TrEA | LTA mainly | by comparison with simulated pattern | |
| | DIPEA | LTA mainly | by comparison with simulated pattern | |
| | TEA | KFI | $a = 18.8673(17)$ Å | Pn-3n |
| | TMA | SOD | by comparison with simulated pattern | |
| | PIP | LTA and SOD | by comparison with simulated pattern | |
| | PYR | LTA and MAPO-39 (ATN) | by comparison with simulated pattern | |

**Fig. 4.7** XRD patterns of the products using the template/co-template pairs: K222/TMA (blue), K222/TPA (purple), K222/DIPA (cyan), K222/DIPEA (green) and K222/TEA (brown).

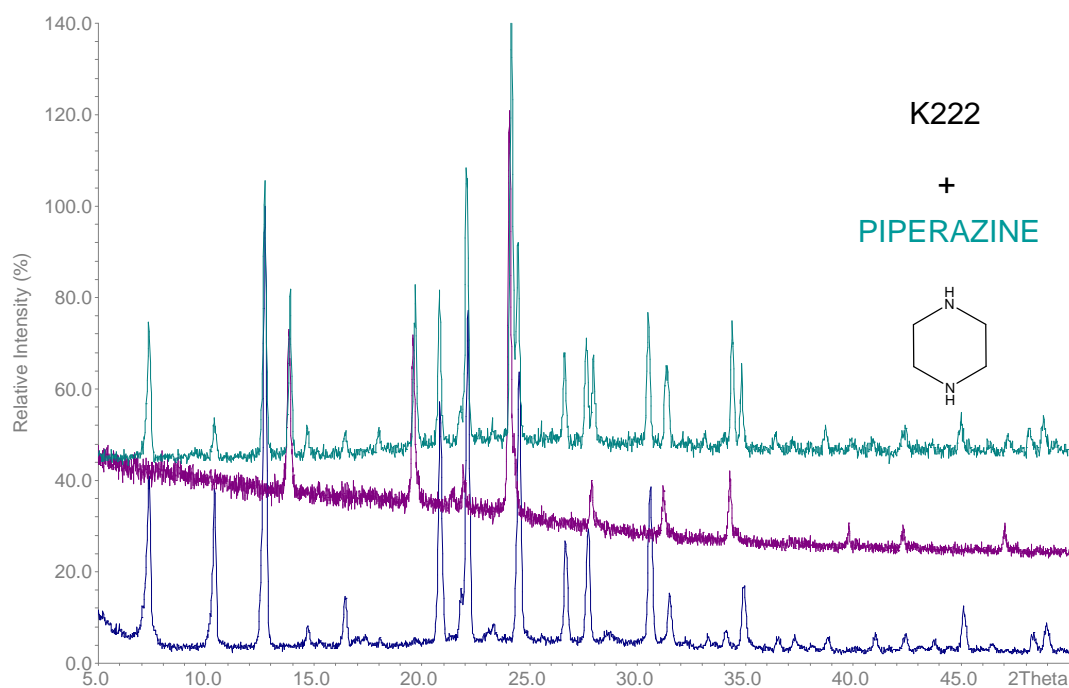


Fig. 4.8 XRD pattern of the product using the template/co-template pair: K222/piperazine. XRD patterns of LTA (blue) and SOD (purple) are included for comparison.

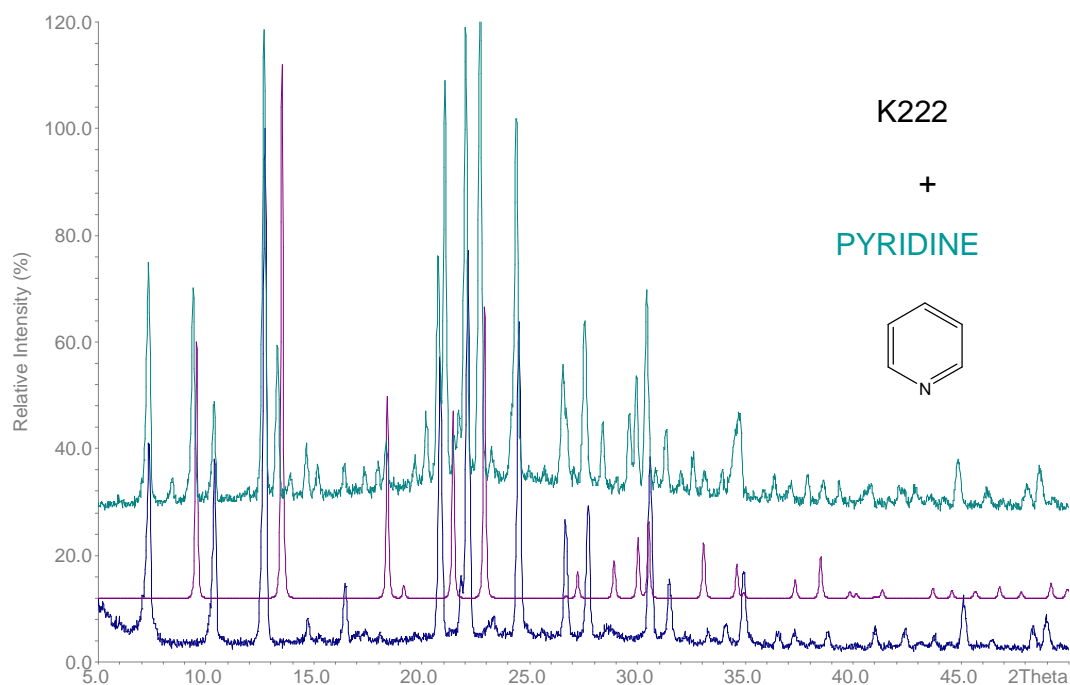


Fig. 4.9 XRD pattern (cyan) of the product using the template/co-template pair: K222/pyridine. XRD patterns of LTA (blue) and theoretical pattern of MAPO-39 (ATN) (purple) included for comparison.

The remarkable influence of the addition of co-base in the hydrothermal synthesis is observed from these results. The XRD patterns show that MgAPO preparations with the K222/TEA combination give material with the KFI structure type, whereas all other co-bases tried except TMA give MgAPOs with the LTA structure type as the dominant phase, so that the co-bases act mainly as pH regulators. Addition of TMA favours the formation of MgAPO-20 (SOD), showing TMA dominates over K222 as a SDA to form SOD against LTA or KFI topologies. The strong templating action of TMA in synthesis of the sodalite cage has previously been reported.⁵

These experimental results prove the suggestion from the modelling data and encourage the co-templating approach. The product phases indicated by the XRD patterns reflect the hypothetical fit of the co-base TEA within the MER cage that can be visualized from the modelling approach and need to be corroborated experimentally by structural techniques (Fig.4.10).

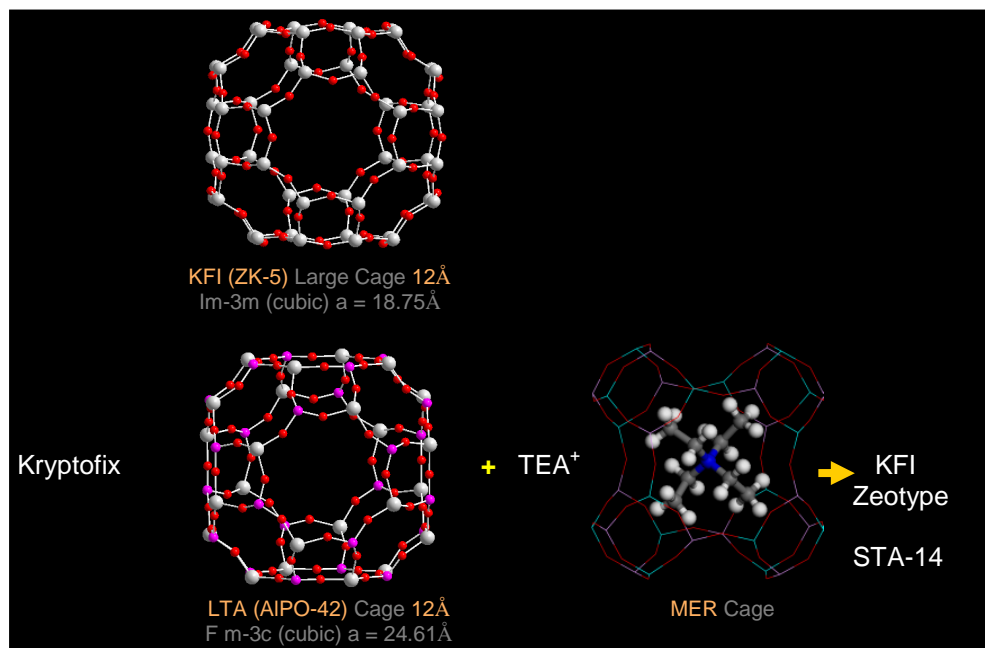


Fig. 4.10 Diagram showing that ZK-5 zeolite (KFI) and AlPO-42 zeotype (LTA) contain the same large cage. In order to move in the zeotype composition regime from LTA to KFI topology the introduction of a co-template is required to template the small cage. Without co-template LTA is formed as main phase, so the co-bases potentially act only as pH regulator and space filling, these argument visualised by modeling was experimentally proved, since, ¹³C MAS NMR demonstrated the incorporation of TEA within the solid (see section 4.3.3.2).

Once preliminary XRD had proved the formation of the KFI topology using a MgAPO gel and the template pair K222/TEA, EDX indicated that this KFI topology contained a MgAPO composition and therefore confirmed the first synthesis of an aluminophosphate version of zeolite ZK-5 labeled as STA-14. The symmetry of KFI is cubic ($a = 18.75 \text{ \AA}$) and the morphology observed in the MgAPO STA-14 by SEM shows consistent cubic morphology with a side of about $10 \mu\text{m}$ (Fig. 4.11).

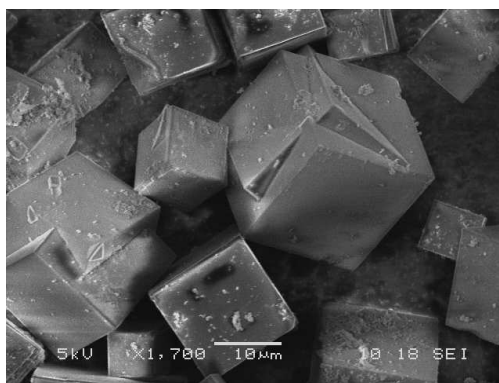


Fig. 4.11 SEM image of MgAPO STA-14.

LTA, SOD and KFI products are obtained as the major phases using K222/TPA, K222/TMA and K222/TEA respectively (Fig. 4.12 a, b and c). LTA and KFI show cubic morphology and SOD crystallizes as small spheres. A change in the phase formed and the crystal morphology of LTA and SOD products occurs when using K222/piperazine and K222/pyridine (Fig. 4.12 d and e). In the first case, SEM shows that the product is a mixture of MgAPO-42 (LTA) and MgAPO-20 (SOD) but their morphologies differ from those obtained previously using K222/TPA and K222/TMA pairs, where LTA formed cubes and SOD spherical particles, respectively change to form clusters. For the second case, although the XRD shows a mixture of LTA and MgAPO-39 (ATN), SEM shows only one kind of morphology not related to LTA or ATN morphology⁶, which tends to form small irregular platelike particles of $2.5 \times 3.3 \mu\text{m}$. MgAPO-39 is a zeotype that crystallised in tetragonal space group and contains 8-membered rings (8MR) windows with secondary building units of eight and four T sites. The SEM of this latter sample, although not related to the typical morphology of MgAPO-39, shows four fold symmetry suggesting the formation of MgAPO-39 in combination with LTA. Normally this material is synthesised in the presence of di-n-propylamine (DPA), so it may be possible

that pyridine does not remain stable during the synthesis and forms linear breakdown products (SEM images in Fig. 4.12).

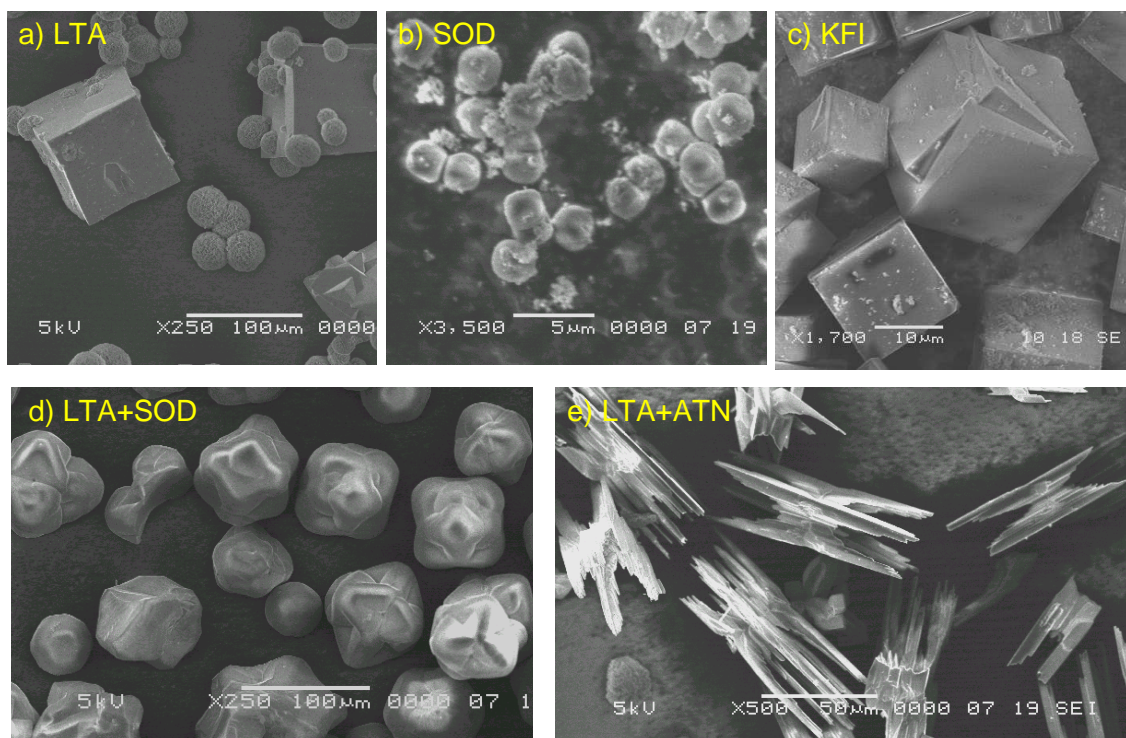


Fig. 4.12 SEM images of the products using a MgAPO gel and the template/co-template pairs: K222/TPA (a), K222/TMA (b), K222/TEA (c), K222/piperazine (d) and K222/pyridine (e).

4.3.2.2 Preparation of MgAPOs with Different Mg/P Ratios in the Gel

MgAPO STA-14 materials were synthesised with the co-templating pair K222/TEA at different magnesium loadings for a MAS NMR study of the as-prepared samples.

Table 4.4 Summary of the MgAPO STA-14 synthesis

| Template | Co-base | (Mg/P) in gel | Product (by XRD) |
|----------|---------|---------------|------------------------------|
| K222 | TEAOH | 0.15 | KFI |
| | | 0.20 | KFI |
| | | 0.50 | KFI mainly (with impurities) |

The three syntheses give MgAPO STA-14 phases and will be denoted as MgAPO(15), MgAPO(20) and MgAPO(50) STA-14 (XRD patterns in Fig. 4.13). The lattice

parameters show a very slight increase as magnesium content increases (consistent with magnesium 2^+ tetrahedral being larger than Al^{3+} tetrahedral, 0.57 Å and 0.39 Å respectively). The XRD pattern of MgAPO(50) shows extra peaks due to impurities. SEM images show that the three samples present cubic morphology and that for MgAPO(50) the cubes are embedded in a fine-grained matrix (Fig. 4.14). EDX shows that the products have Mg/P ratios of 0.18, 0.20 and 0.26 for MgAPO(15), MgAPO(20) and MgAPO(50) respectively. This indicates that magnesium can replace a maximum of *ca.* 26% of the aluminium T sites in the framework.

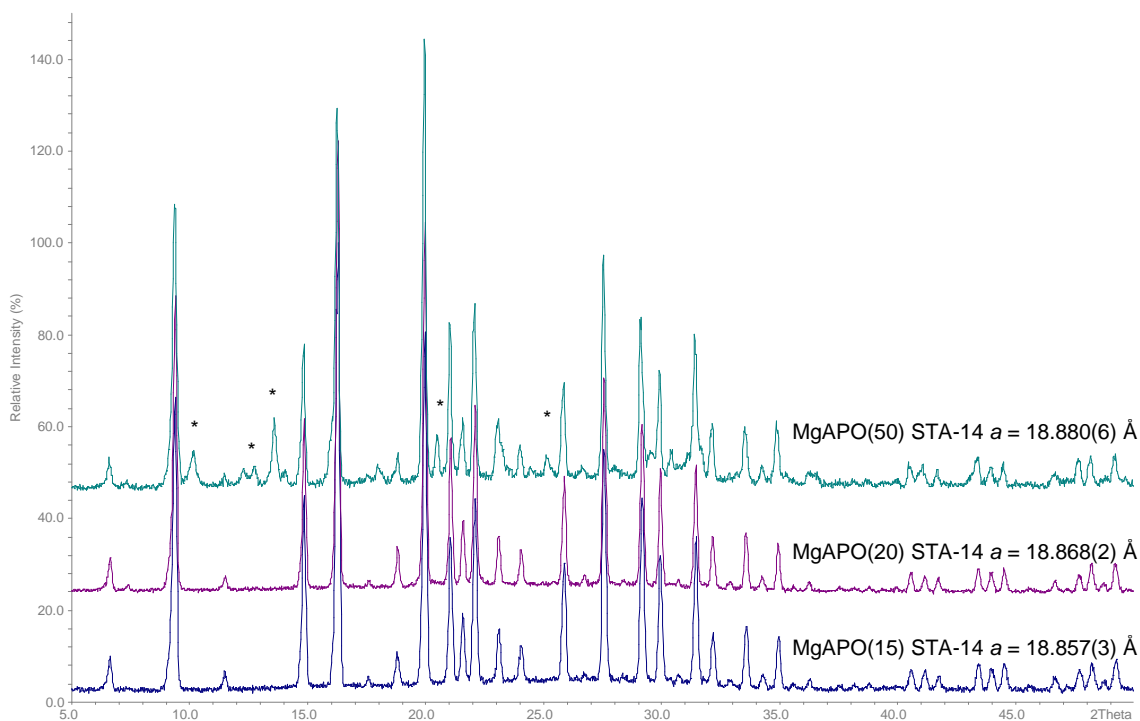


Fig. 4.13 XRD patterns of the STA-14 samples MgAPO(15) (blue), MgAPO(20) (purple) and MgAPO(50) (cyan), extra phase peaks marked with asterisks.

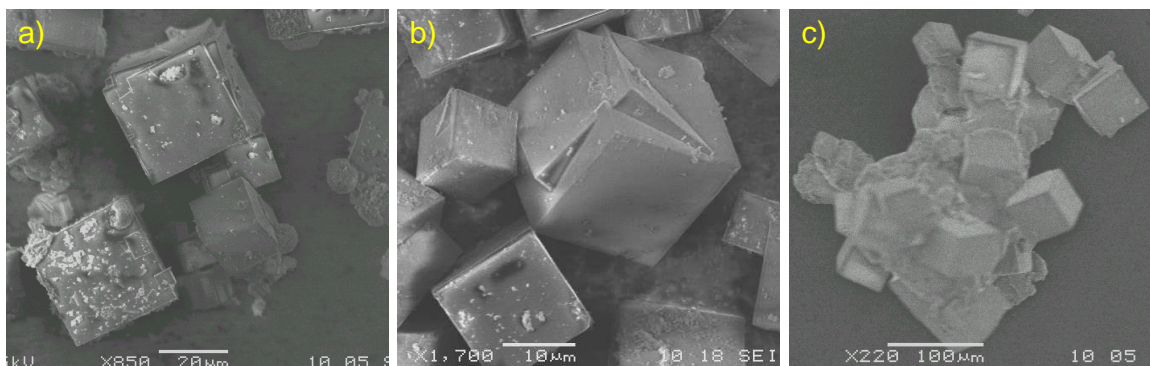


Fig. 4.14 SEM images of the MgAPO(15), MgAPO(20) and MgAPO(50) STA-14 from left to the right.

4.3.2.3 Variation of Framework Chemistry

It is known that although MgAPO materials are highly crystalline their stability once calcined is poor, so the composition of the gel was varied in order to obtain the novel zeotype in a form suitable for adsorptive and catalytic applications.

AlPO

As in the case of STA-7, the formation of pure AlPO STA-14 was not achieved and instead AlPO-42 with the LTA topology is formed (Fig. 4.15). CHN values indicate the presence of K222 alone ($C/N = 9.1$) so the TEA cation does not act as co-template probably because the neutral framework is unable to balance its positive charge.

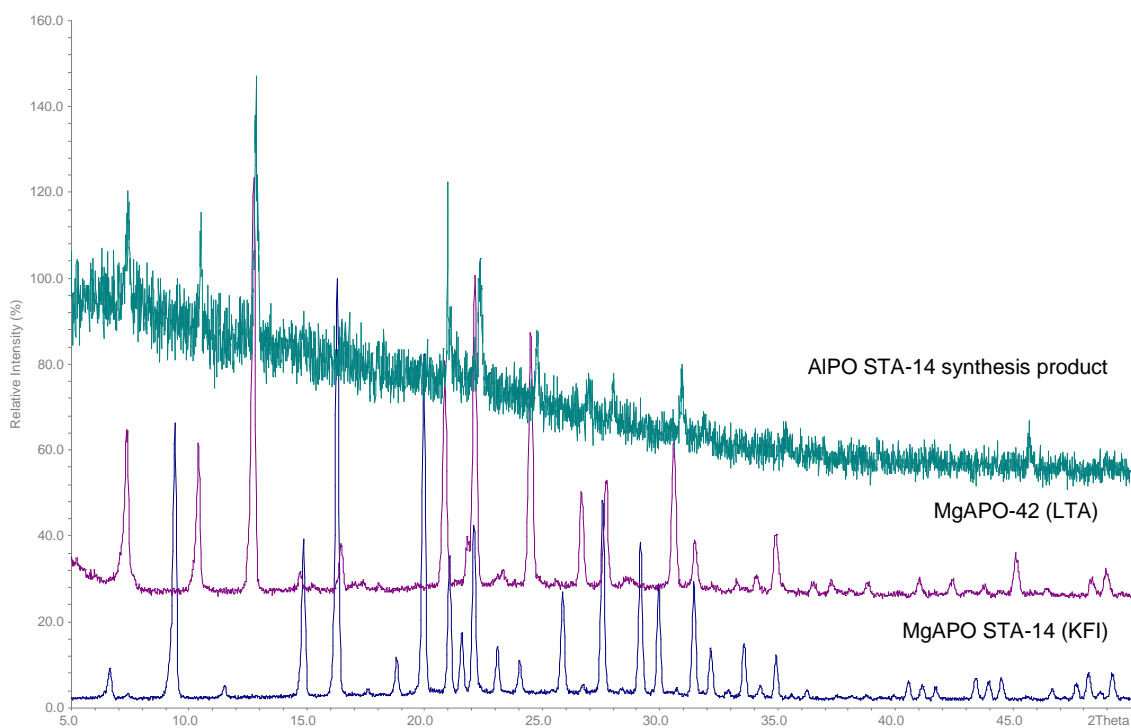


Fig. 4.15 XRD pattern of the product of AlPO STA-14 synthesis (cyan), KFI (blue) and LTA (purple).

CoAPO

The CoAPO composition has been observed in STA-7 to be more stable than the MgAPO after calcination. STA-14 can be obtained in CoAPO form for adsorption studies and with a suitable morphology for IFM applications. The sample possess the ‘cobalt blue’ colour and the lattice parameter slightly decreases with the cobalt incorporation (Fig. 4.16).

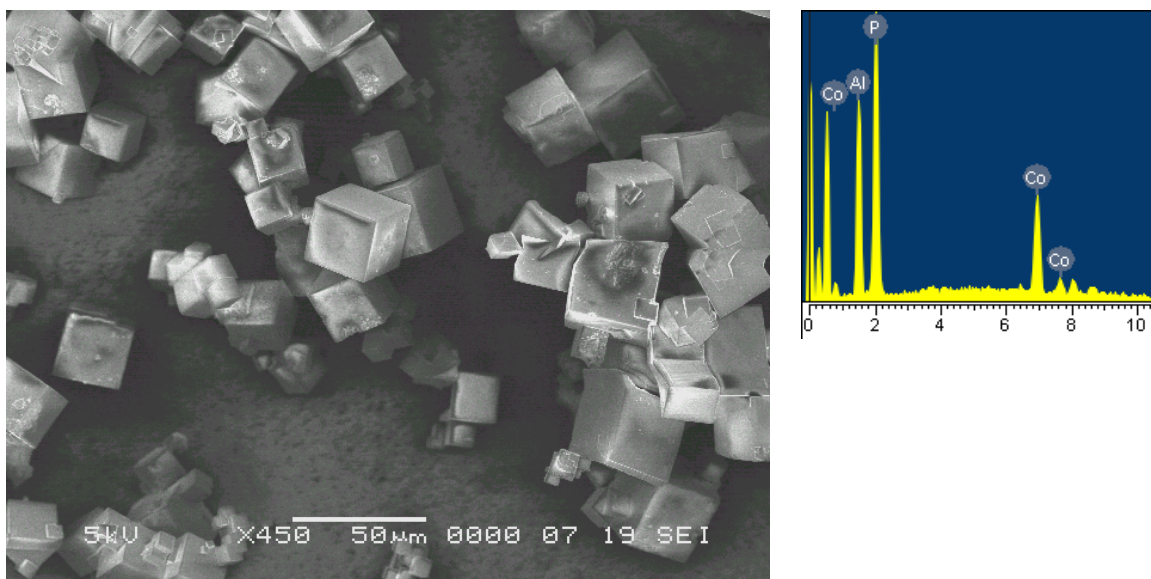
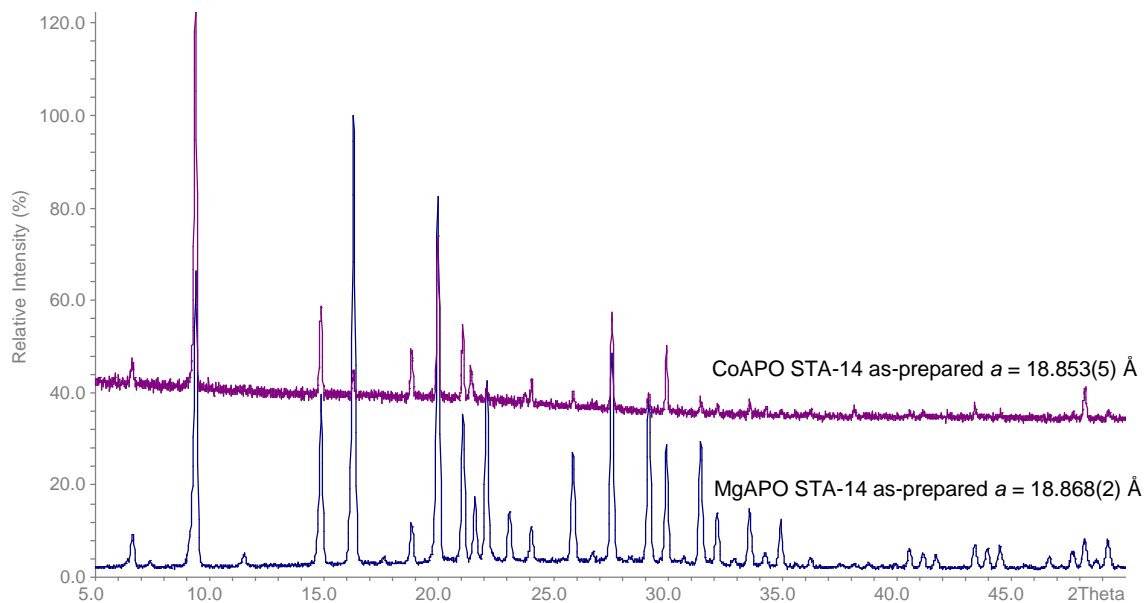


Fig. 4.16 XRD pattern of CoAPO STA-14 (purple) and MgAPO STA-14 (blue) for comparison (top). SEM image and EDX (bottom).

SAPO

The SAPO forms of aluminophosphates are known to be the most stable compositions once calcined. The incorporation of silicon into the STA-14 system was studied to obtain an optimum material for adsorption measurements and potential application in interference optical microscopy (IFM).

Synthesis using a Si/Al ratio of 0.20 in the gel successfully formed the material SAPO(20) STA-14 with a total silicon content in the product of Si/Al ratio 0.21 (by EDX), replacing *ca.* 20% of the phosphorus in framework (Fig. 4.17). The product has a small impurity (2.5%) of LTA that remained after calcination (Fig. 4.18). The lattice parameter a is slightly smaller in comparison with MgAPO STA-14 consistent with Si 4^+ (tetrahedral) being smaller than Mg 2^+ (tetrahedral), 0.26 Å and 0.57 Å respectively. Once calcined the unit cell shrinks as expected (see unit cell values in Fig. 4.17 and 4.18). The morphology of SAPO(20) STA-14 will be described in section 4.3.2.4.

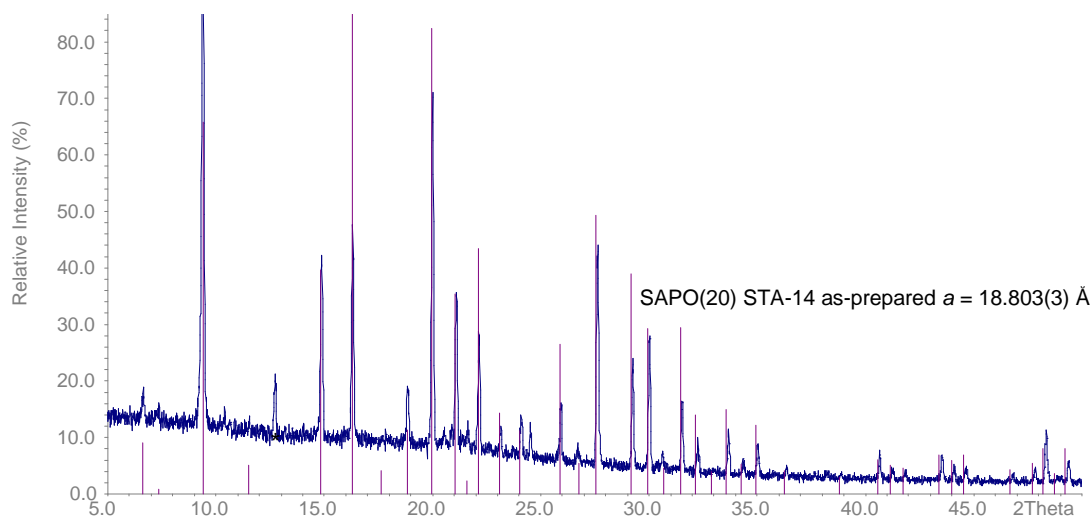


Fig. 4.17 XRD pattern of SAPO(20) STA-14 with theoretical peaks positions of KFI topology. LTA impurity peak marked with asterisk.

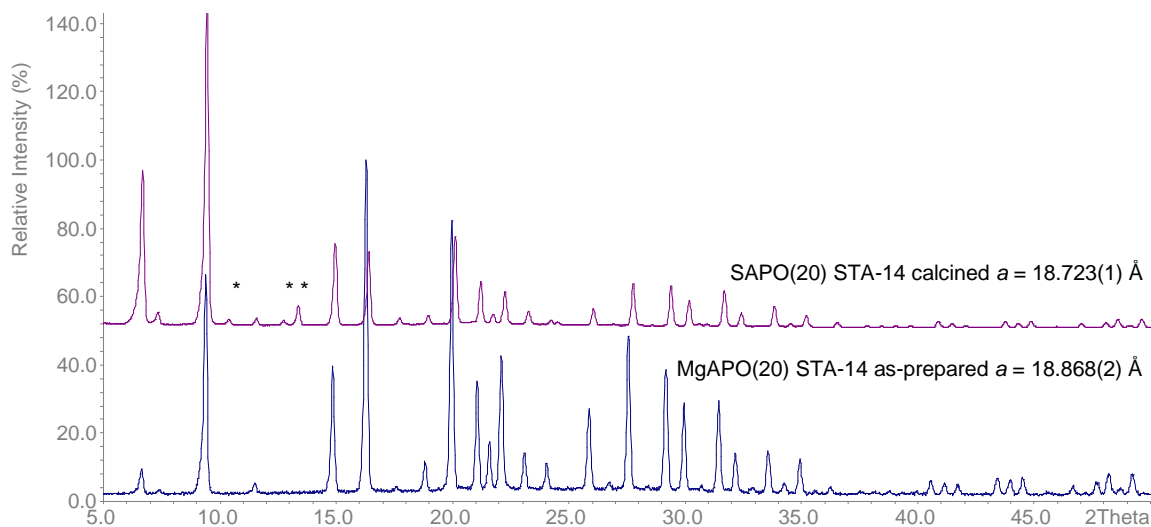


Fig. 4.18 XRD pattern of SAPO(20) STA-14 calcined (purple) and MgAPO(20) STA-14 as prepared (blue) for comparison, LTA impurity peaks marked with asterisks.

In order to obtain a pure phase the influence of the silicon content in the gel on the phase formation was studied. From the results summarised in the Table 4.5, the purest SAPO STA-14 materials were obtained using a Si/Al ratio of 0.20, followed by 0.30 and the lattice parameter a increases with the uptake of Si into the framework from $a = 18.803(3)$ Å to $a = 18.98(2)$ Å, consistent with Si 4^+ (tetrahedral) being larger than P 5^+ (tetrahedral), 0.26 Å and 0.17 Å respectively. Lower silicon levels in the gel favour SAPO-42 (LTA) formation and at higher silicon contents the product is largely amorphous (Fig. 4.19). EDX on SAPO(20) and SAPO(30) STA-14 gives a Si/Al ratio of 0.21 and 0.27 respectively.

Table 4.5 Summary of the SAPO STA-14 synthesis

| Si/Al in gel | Product (by XRD) |
|--------------|------------------------------|
| 0.10 | LTA mainly and traces of KFI |
| 0.20 | KFI mainly and traces of LTA |
| 0.30 | KFI mainly some LTA impurity |
| 0.40 | Amorphous phase mainly |

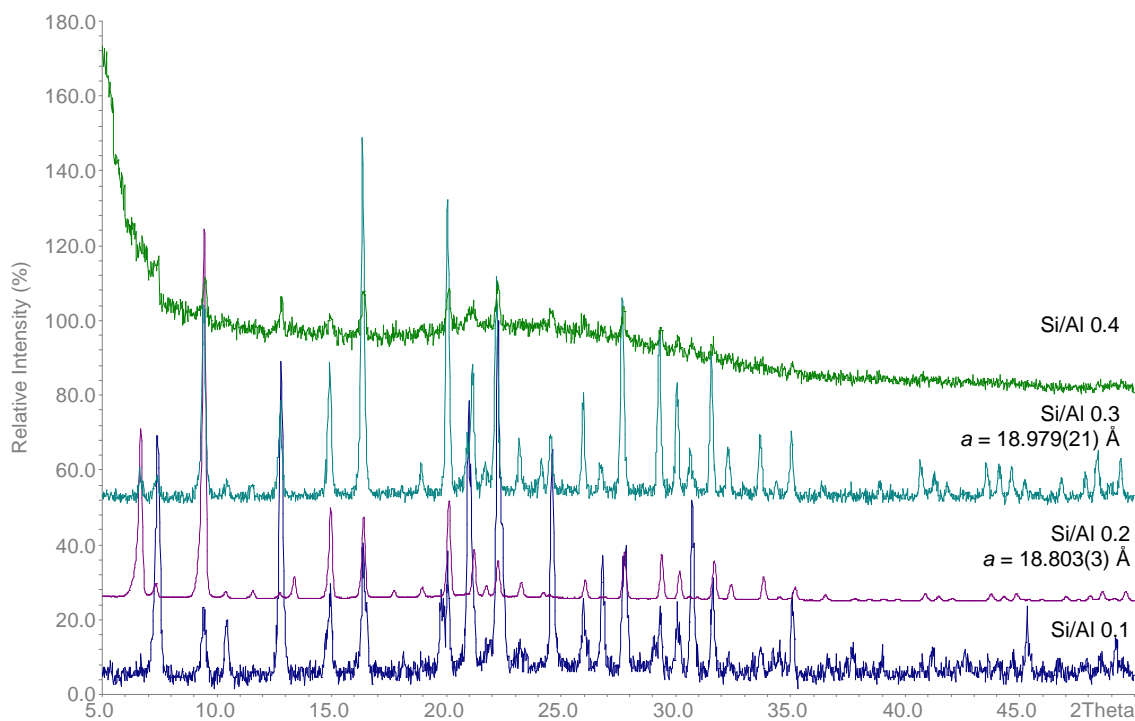


Fig. 4.19 XRD patterns of the products of SAPO STA-14 synthesis at Si/Al ratio 0.10, 0.20, 0.30 and 0.40 from the bottom to the top.

The effect of temperature on the synthesis of SAPO(20) STA-14 on a small scale (4.5 ml water) was also examined. Reducing the temperature to 160 °C did not influence the synthesis (Fig. 4.20).

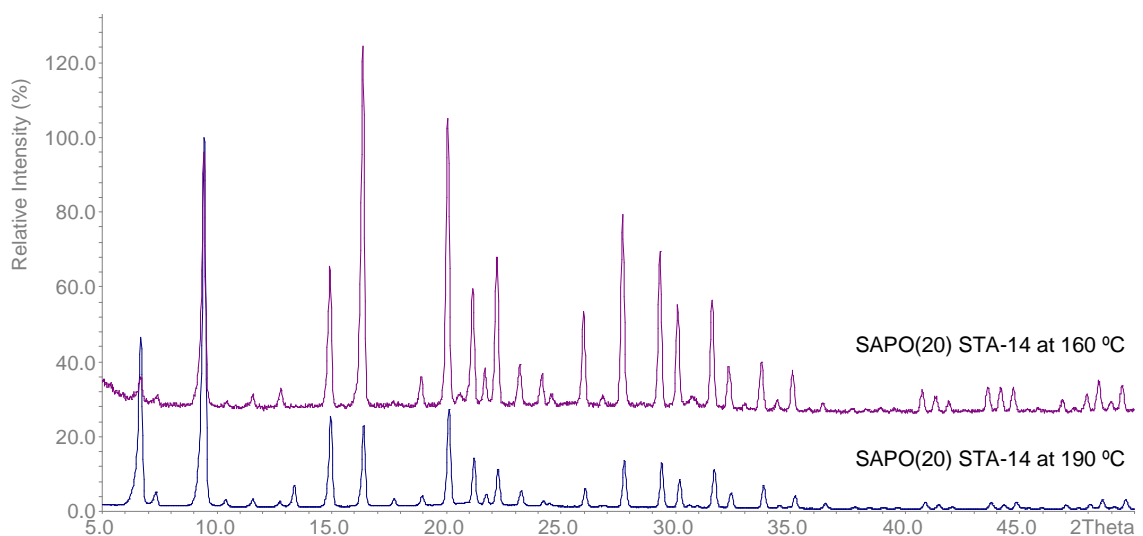


Fig. 4.20 XRD patterns of SAPO(20) STA-14 at 190 °C (blue) and 160 °C (purple).

In order to obtain enough SAPO(20) STA-14 for MAS NMR study and adsorption applications at IFP-Lyon (about 1 g) it was necessary to scale-up the reaction. For this purpose, the starting amounts were doubled so instead of 4.5 ml water, 9 ml was used. The XRD pattern in the as-prepared and calcined materials indicates the SAPO-42 impurity does not increase during this scaling-up (Fig. 4.21) and semi-qualitative analysis performed by EDX gives a Si/Al ratio of 0.23, with silicon again replacing *ca.* 20% of the phosphorus T sites in the framework (Fig. 4.21).

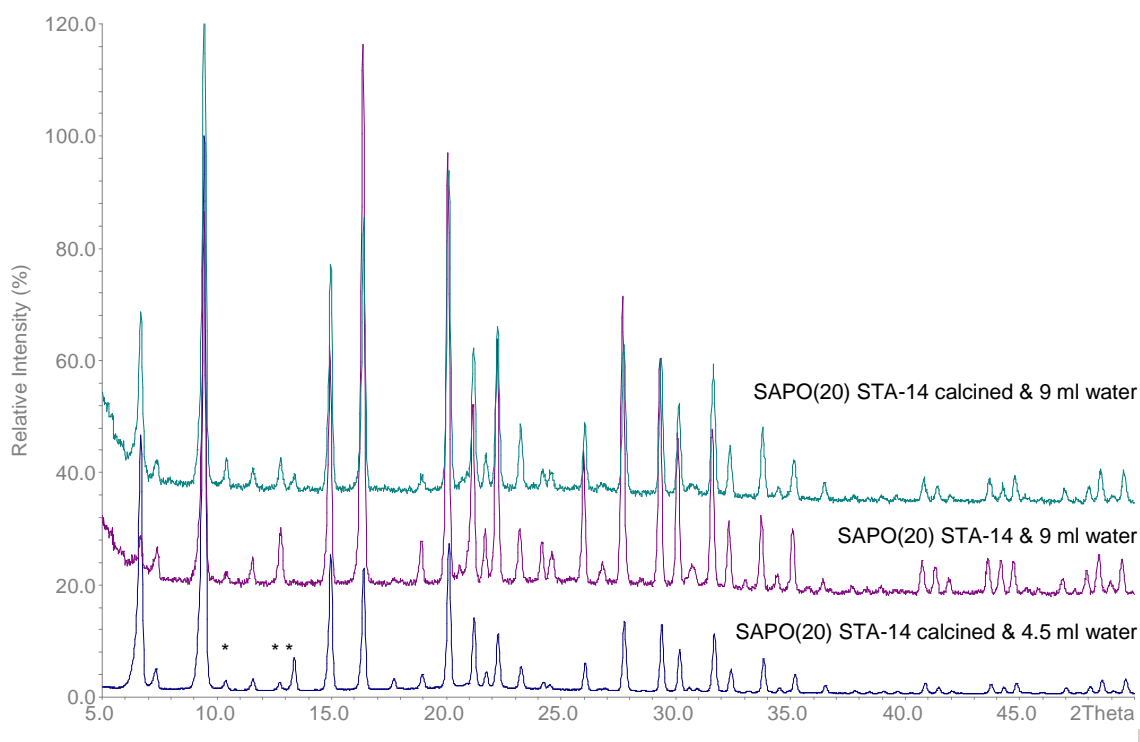


Fig. 4.21 XRD patterns of SAPO(20) STA-14 using 4.5 ml water in calcined form (blue) and with 9 ml water in as-prepared (purple) and calcined (cyan), LTA impurity peaks marked with asterisks

4.3.2.4 The Morphology of SAPO STA-14

SAPO(20) STA-14 is the most promising SAPO material for adsorption applications due to its stability once calcined and low SAPO-42 impurity content. The STA-14 morphology in the SAPO version contrasts with the single cubic crystal morphology observed in the MgAPO composition. SAPO STA-14 shows cuboctahedral morphology, with a particle size of *ca.* 10 μm (Fig. 4.22).

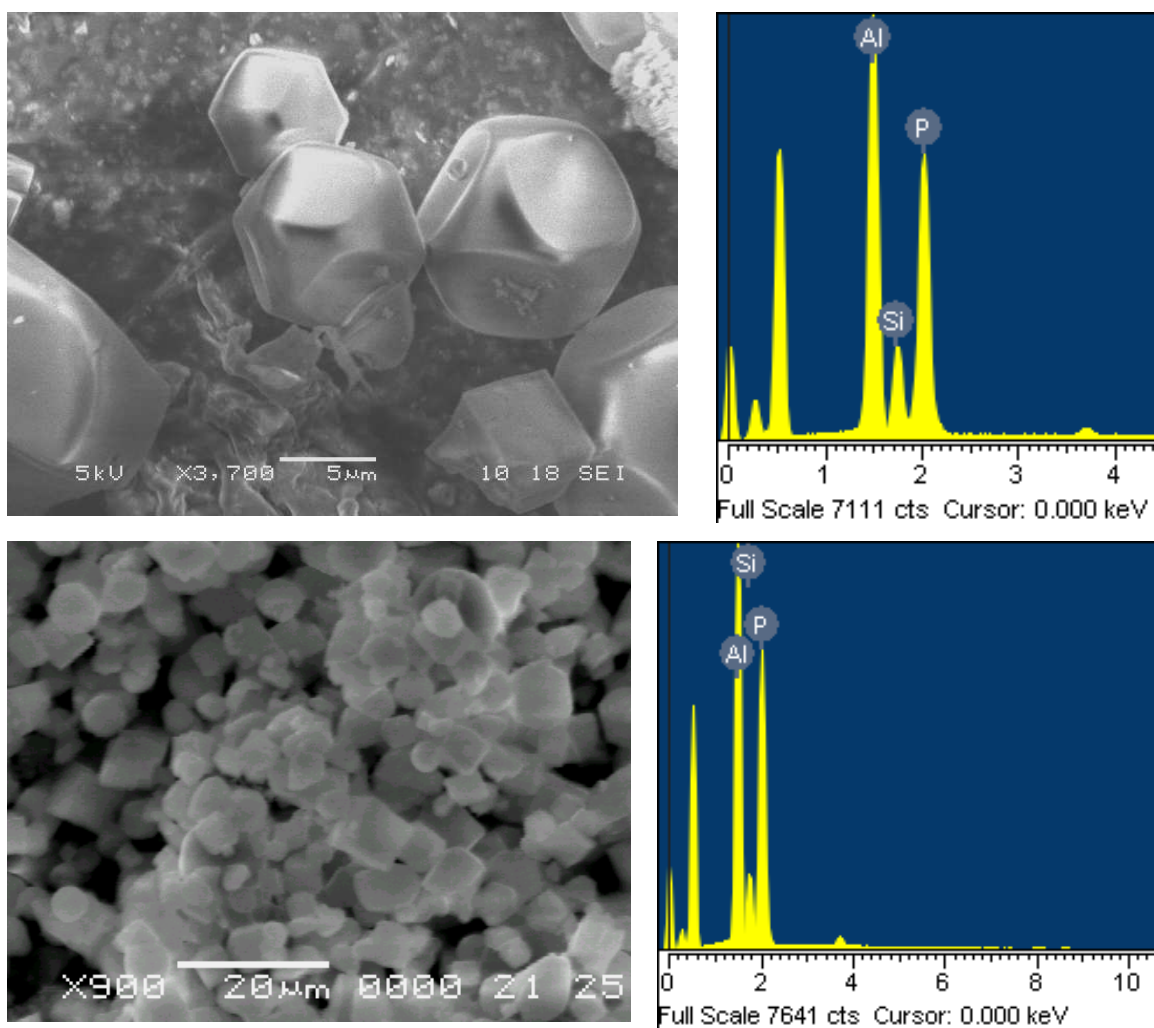


Fig. 4.22 SEM image and EDX of SAPO(20) STA-14 from a small synthesis (top) and a scaled-up synthesis (bottom).

This morphology is not suitable for the IFM technique that requires crystals with parallel faces of minimum dimensions of $20 \times 20 \mu\text{m}$. In order to obtain a material that is stable in the calcined form and that has suitable morphology for this method, the synthesis of MgAPSO materials was performed. Including silicon should provide stability and including magnesium should favour the formation of the cubic morphology. To find out the best silicon and magnesium contents for the gel, the results of the synthetic study of SAPO and MgAPO STA-14 materials was taken into account. SAPO(30) STA-14 gives little SAPO-42 impurity and might provide more thermal stability to compensate the magnesium incorporation than SAPO(20) STA-14 and MgAPO STA-14 with suitable morphology is obtained using Mg/P ratios 0.10 and 0.20 in gel. From this rationalisation, the following ratios in the gel were therefore used: (a) 0.1Mg : 0.9Al : 0.7P : 0.3Si and

(b) 0.2Mg : 0.8Al : 0.7P : 0.3Si and the samples denoted in the text as MgAPSO(1:3) and MgAPSO(2:3) STA-14 respectively.

The XRD patterns in both cases show the formation of KFI topology, although for MgAPSO(2:3) the formation of LTA impurity is more pronounced (Fig. 4.23). The lattice parameters slightly increases by replacing some of the Al with Mg, consistent with Mg 2^+ (tetrahedral) being larger than Al 3^+ (tetrahedral), 0.57 Å and 0.39 Å respectively.

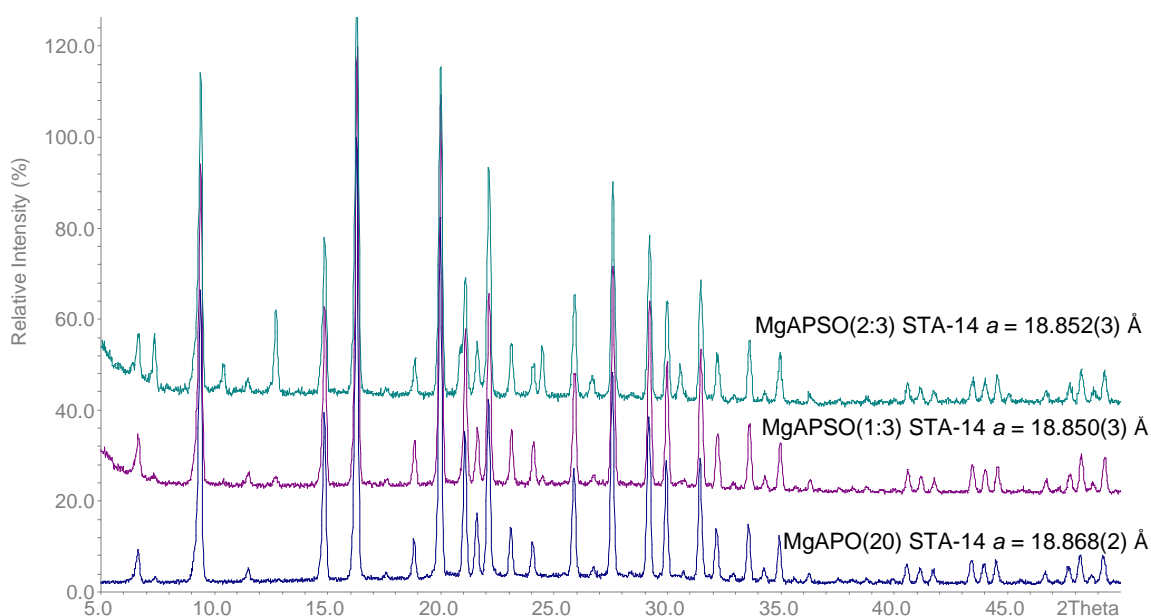


Fig. 4.23 XRD patterns of MgAPO(20) (blue), MgAPSO(1:3) (purple) and MgAPSO(2:3) (cyan) STA-14.

EDX indicates that the samples contain magnesium and silicon and MAS NMR proves that these elements are incorporated into the framework (see section 4.3.3.2 and 4.3.3.3). The SEM images show that in both syntheses the incorporation of magnesium into the SAPO gel promotes the formation of simple cubic crystals. MgAPSO(1:3) STA-14 shows only one type of morphology: cube of up to 40 µm truncated by an octahedron (Fig 4.24 a and c). MgAPSO(2:3) STA-14 shows two types of morphologies: cubic and cubic highly truncated by an octahedron typical of MgAPO and SAPO STA-14 respectively, with sizes up to 50 and 20 µm (Fig. 4.24 b, d and e). Because this sample shows SAPO-42 (LTA) impurity, some of the cubes could be attributed to it. EDX performed in the two morphologies present in MgAPSO(2:3) shows that the simple cubes have less silicon

content and higher magnesium content than the cubes that are strongly truncated by octahedral. The unit cell composition (by EDX) for MgAPSO(1:3) STA-14 is $\text{Mg}_4\text{Al}_{44}\text{P}_{37}\text{Si}_{11}\text{O}_{192}$ and for MgAPSO(2:3) STA-14 cubic and cubic highly truncated by an octahedron morphologies $\text{Mg}_9\text{Al}_{39}\text{P}_{44}\text{Si}_4\text{O}_{192}$ and $\text{Mg}_7\text{Al}_{41}\text{P}_{42}\text{Si}_6\text{O}_{192}$, respectively.

This observation leads to the conclusion that the presence of silicon slows down the growth of $\{111\}$ planes and therefore the final crystal morphology exhibits them. As a result, in MgAPSO(1:3), the magnesium favours the formation of cubes and therefore the $\{100\}$ planes, but the cubes present corners, the topological manifestation of the $\{111\}$ planes growing slowly due to silicon introduction. For MgAPSO(2:3), at higher magnesium content, magnesium and silicon compete and therefore the product shows the two topologies characteristic for pure MgAPO and SAPO STA-14. Crystals with higher magnesium content showed that magnesium controls the final crystal shape formed (well defined) and the crystals with higher silicon content exhibit the formation of $\{111\}$ planes to give cubes that are highly octahedrally truncated.

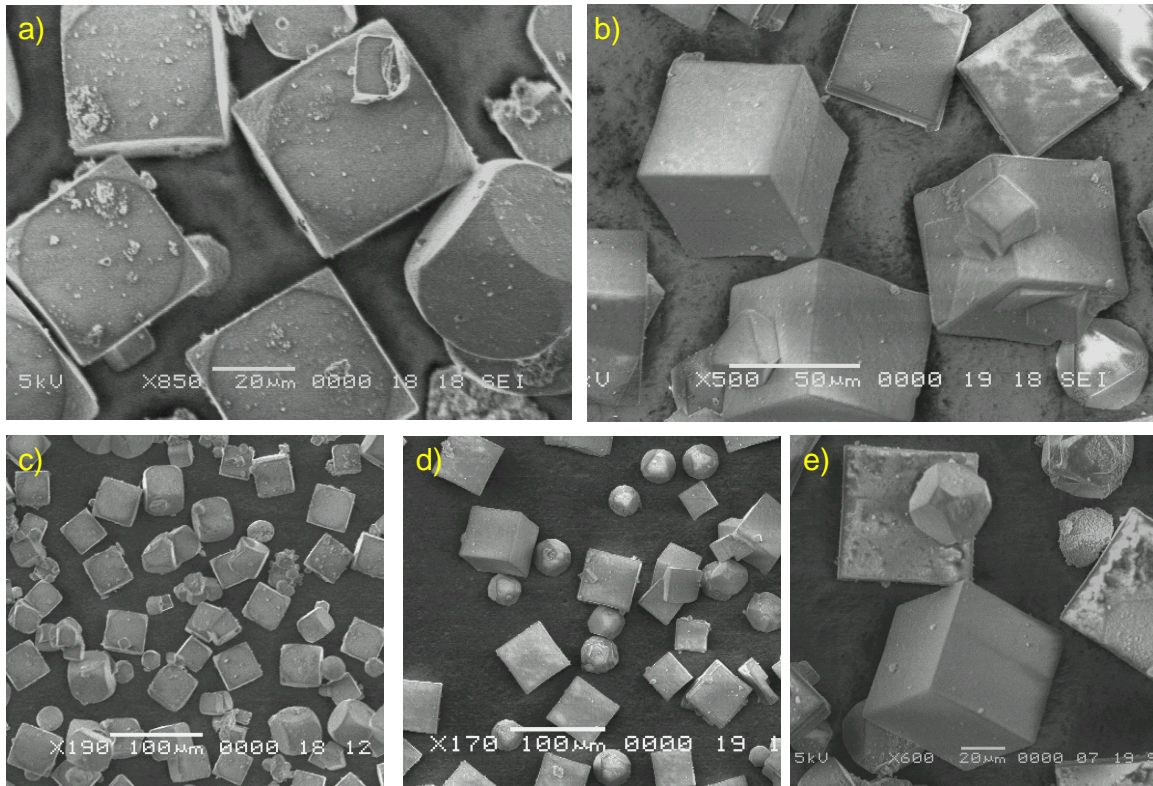


Fig. 4.24 SEM images of MgAPSO(1:3) STA-14 (a and c) and MgAPSO(2:3) STA-14 (b, d and e).

4.3.3 Characterisation of As-Prepared Materials

4.3.3.1 SXRD and Modelling in MgAPO and SAPO STA-14

In the case of STA-14, modelling was used prior to the synthetic study and showed TEA as the best co-template for the MER cage, with the tt.tt configuration. SXRD performed on a cubic crystal of MgAPO STA-14 confirmed the KFI topology and located the TEA within the MER cage in the tt.tt configuration predicted by modelling (Fig. 4.25 and 4.26).

The STA-14 space group Pn-3n has lower symmetry than the space group of the pure zeolite with KFI topology (ZK-5) Im-3m (Table 4.6). The ordered Al-O and P-O bonds in the zeotype STA-14 break the mirror planes. The structure was refined with a final $R_{\text{int}} = 0.19$ (full crystallographic details in Tables A.9 to A.12 in Appendix A).

Table 4.6 Comparison of the crystallographic data of STA-14 and ZK-5.

| Material | | Unit Cell Parameter (Å) | Space Group |
|----------|---------|-------------------------|-------------|
| STA-14 | zeotype | 18.9056(7) | Pn-3n |
| ZK-5 | zeolite | 18.6 | Im-3m |

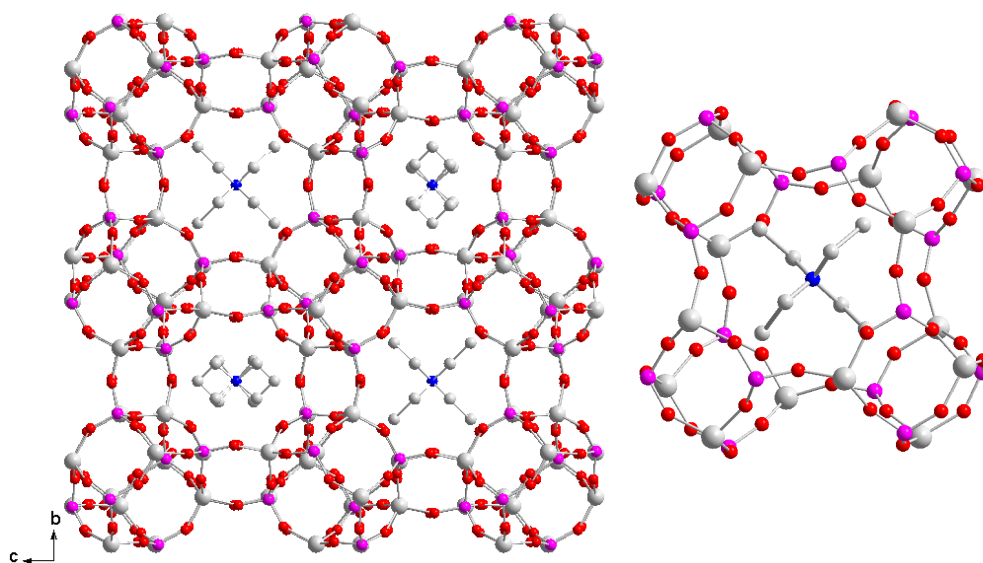


Fig. 4.25 Structure of STA-14 (left) with TEA in MER cages. The measured tt.tt configuration of TEA in MER cage of STA-14 (right) as determined from SXRD. One of two symmetry-related configurations is shown.

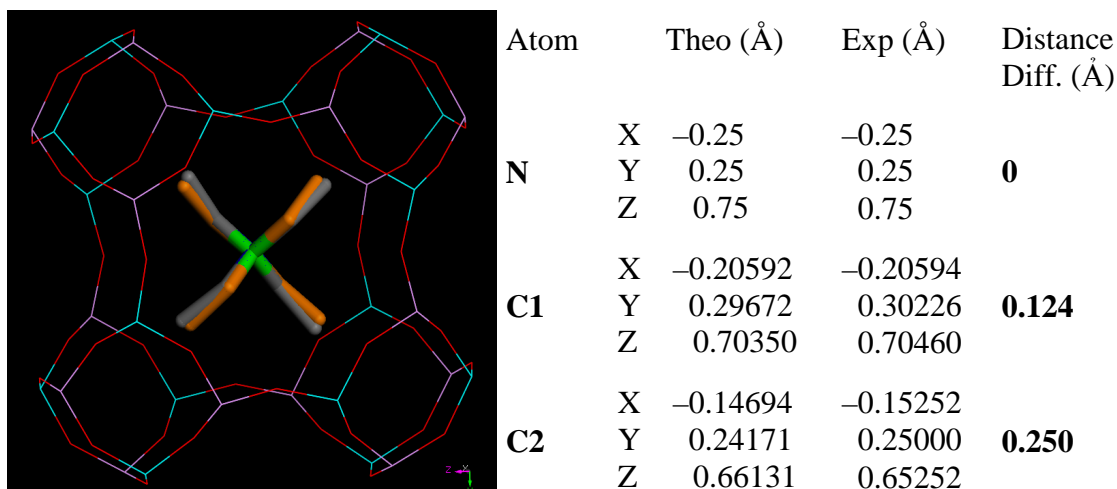


Fig. 4.26 Comparison between modelling (grey) and experimental (coloured) coordinates of TEA in MER cage of AlPO KFI modelled framework.

SXRD analysis was also conducted on a crystal of the SAPO(20) STA-14 form with similar results, where TEA was located using the same model N-C1-C2 and $R_{\text{int}} = 0.1754$ and bond distances Al-O 1.738(6) Å and P-O 1.531(6) Å.

4.3.3.2 MAS NMR on STA-14 MgAPOs

^{13}C MAS NMR shows that both organic species, K222 and TEA, have been incorporated intact within the structure. The two first sharp resonances centred at 7.5 ppm and 51.5 ppm are attributed to TEA and the rest at 55.0 ppm, 63.8 ppm and 70.9 ppm to diprotonated K222. These shifts are similar to those observed for K222 in acidic solution and within AlPO-42 where the charge balance is possible due to fluoride ions or hydroxyl groups coordinated to framework aluminium cations in the structure (see Fig.4.27).²

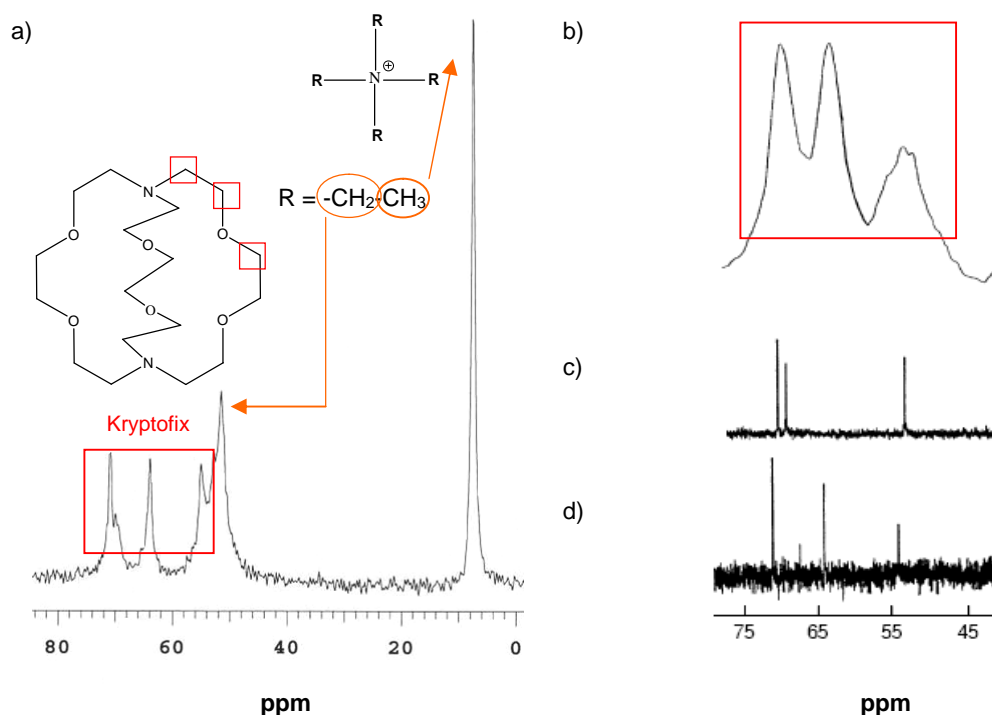


Fig. 4.27 ^{13}C MAS NMR of MgAPO(20) STA-14 showing the resonance of the two templates (a). For the case of AlPO-42 the spectrum shows the peaks of K222 at chemical shift positions very similar to STA-14 (b). That means that in both cases K222 has the same degree of protonation. From the data of ^{13}C solution-state NMR spectra of K222 in basic (c) and acidic (d) media, it seems that K222 in the solids is diprotonated.²

The results of ^{27}Al and ^{31}P MAS NMR of MgAPO(20) STA-14 are similar to those of MgAPO(20) STA-7 but show better resolution (Fig. 4.28). The ^{31}P MAS NMR spectrum exhibits four resonances centred at -28.8 ppm, -25.7 ppm, -22.4 ppm and -17.8 ppm attributed to $\text{P}(4\text{Al})$, $\text{P}(3\text{Al},1\text{Mg})$, $\text{P}(2\text{Al},2\text{Mg})$ and $\text{P}(1\text{Al},3\text{Mg})$ environments respectively also observed for MgAPO(15) and MgAPO(50) STA-14. The results in STA-14 are similar to those observed for STA-7. A maximum uptake of magnesium (by EDX) is again observed, at a Mg/P ratio of 0.26 for the sample MgAPO(50) STA-14, which means that magnesium replace a maximum of 26% of the aluminium positions in the framework. The magnesium that is not incorporated forms an extra magnesiumphosphate phase, as observed for MgAPO(50) STA-7, as suggested by the ^{31}P MAS NMR spectrum (Fig. 4.29).

The maximum magnesium content in STA-7 is slightly higher than in STA-14, 31% and 26% respectively, since for STA-14 the ratios K222:TEA is 1:3, whereas for STA-7 cyclam:TEA is 2:2. The total charge due the templates will be greater in STA-7 than in STA-14, where TEA has 1⁺ and the templates in both cases 2⁺.

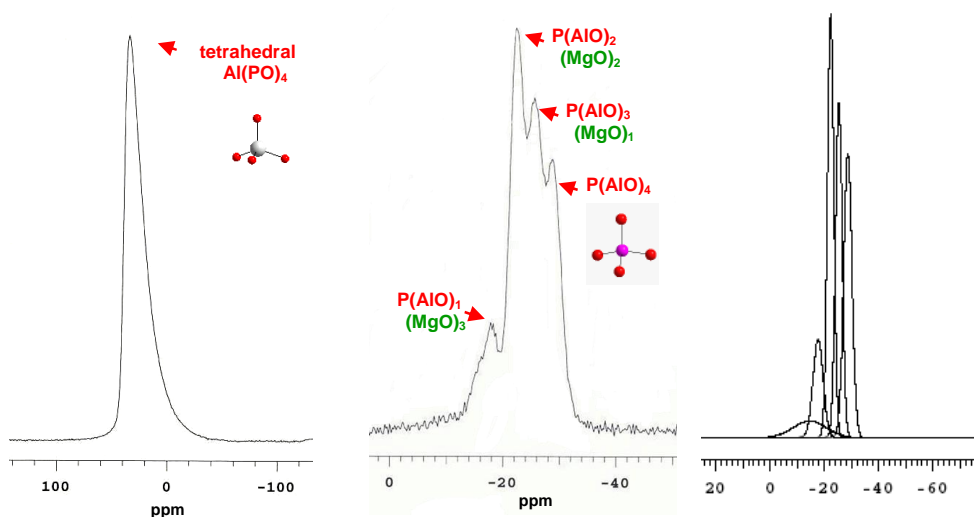


Fig. 4.28 ^{27}Al (left) and ^{31}P (middle, included the deconvoluted curves) MAS NMR of MgAPO(20) STA-14.

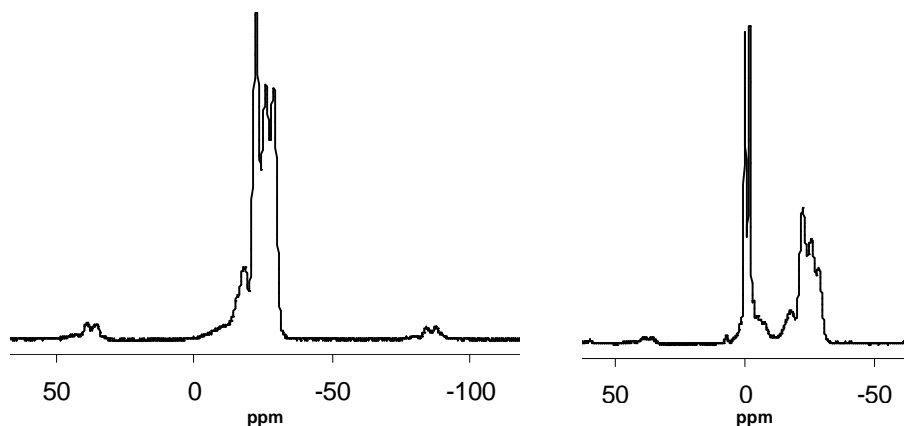


Fig. 4.29 ^{31}P MAS NMR of MgAPO(15) and MgAPO(50) STA-14.

Based on the method developed by Barrie and Klinowski,⁷ the spectrum can be deconvoluted and framework P/Al and P/Mg ratios calculated by the equation 4.1:

$$[\text{Mg}] = \frac{\sum_{n=0}^4 (4-n) \cdot I_{\text{P}(n\text{Al})}}{8 \sum_{n=0}^4 I_{\text{P}(n\text{Al})}} \quad \text{Eq. 4.1}$$

The calculated Mg/P ratio in framework for MgAPO(20) STA-14 of 0.34 is in reasonable agreement with the semi-quantitative EDX value 0.20 using the deconvoluted values 28.3, 27.0, 31.7 and 12.9 for $n = 4, 3, 2$ and 1 respectively. The discrepancy is likely to derive from errors in determining the intensity of the $n = 3$ and $n = 4$ resonances in the presence of a broader underlying signal (Fig. 4.28).

The intensities of the experimental spectra do not follow a random distribution. This was observed by the calculation of the relative intensities if magnesium were incorporated in a random fashion into the aluminium site using the binomial theorem (Table 4.7).

Table 4.7 Theoretical relative intensities of the ^{31}P MAS NMR spectra for a random incorporation of magnesium into the framework, x is the aluminium fraction.

| P(0Mg) | P(1Mg) | P(2Mg) | P(3Mg) | P(4Mg) |
|--------|-------------|---------------|-------------|-----------|
| x^4 | $4x^3(1-x)$ | $6x^2(1-x)^2$ | $4x(1-x)^3$ | $(1-x)^4$ |

Using this formula, the intensity distributions at different magnesium loadings are shown in figure 4.30. These are compared with the distribution obtained from the deconvoluted experiment showing that the incorporation of magnesium into the framework is non random since the random intensities do not match with the deconvoluted values.

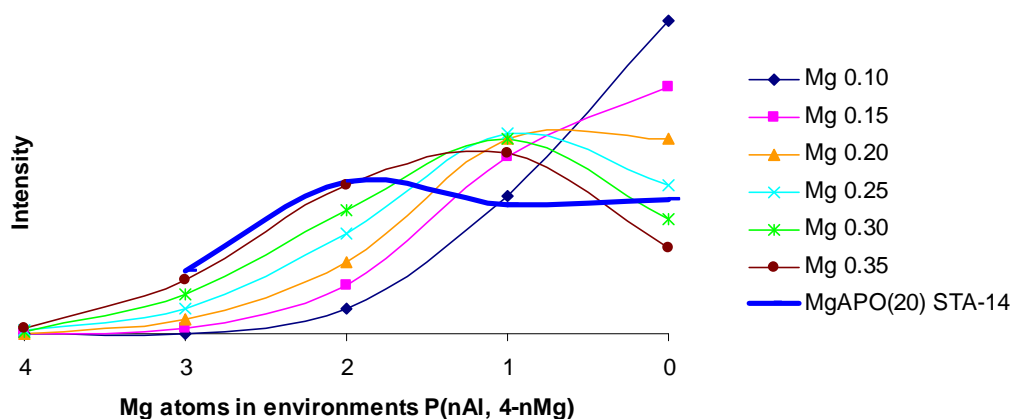


Fig. 4.30 Theoretical integral intensities at different magnesium loads in the ^{31}P MAS NMR spectra.

4.3.3.3 MAS NMR on STA-14 SAPOs

The samples SAPO(20) and SAPO(30) STA-14 were studied by MAS NMR (Fig. 4.31). As in the case of STA-7 the ^{27}Al MAS NMR shows a sharp resonance due to tetrahedral aluminium at 36.4 ppm and an extra broad signal, centred at 7.9 ppm and 8.4 ppm for SAPO(20) and (30) respectively. This broad resonance can be attributed to Al(1Si,3P) environments rather than extra-coordinated aluminium according to the results of MAS NMR STA-7. The ^{27}Al MQ MAS NMR spectrum corroborates that showing the Al(1Si,3P) resonance for SAPO(20) STA-14 (Fig. 4.32). The ^{31}P MAS NMR spectra show the resonance of the tetrahedral phosphorous at -28.9 ppm. The ^{29}Si MAS NMR spectra provide information about the incorporation of the silicon into the framework. For SAPO(20) STA-14 this is by substitution of phosphorus positions in an Si(4Al) environment whereas for SAPO(30) STA-14 islands are denoted by the signals at -96.0 , -97.5 and -110 ppm for Si(3Al), Si(2Al) and Si(4Si) environments, respectively.

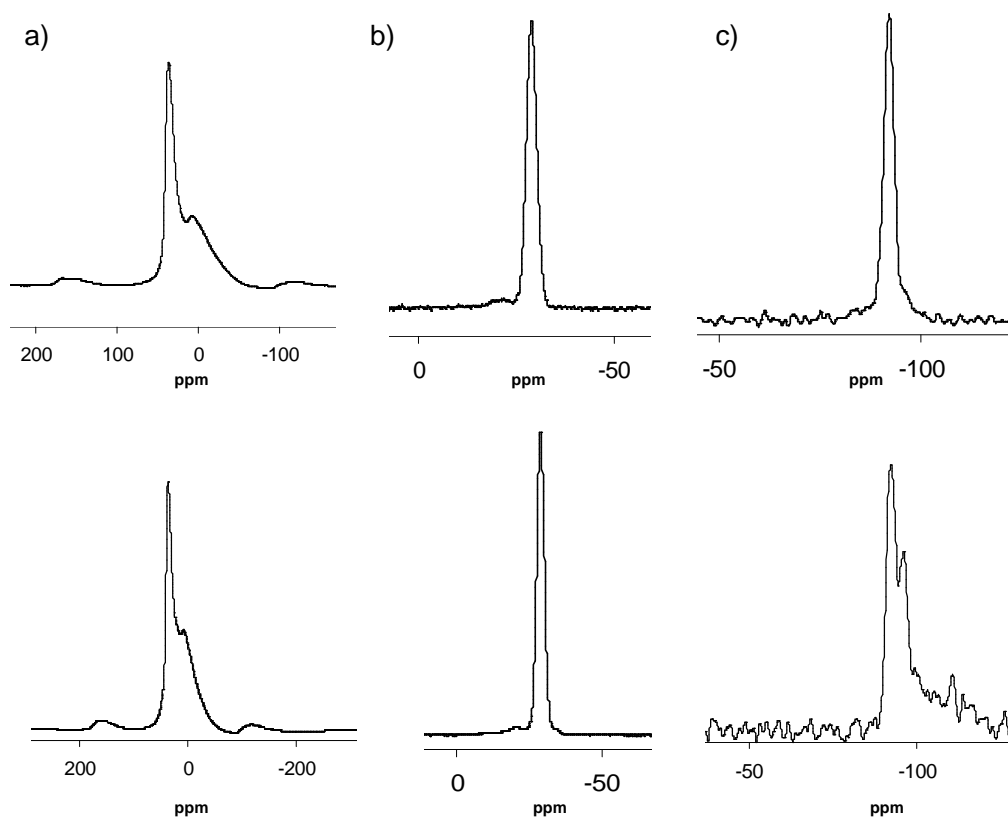


Fig. 4.31 (a) ^{27}Al , (b) ^{31}P , (c) and ^{29}Si MAS NMR for SAPO(20) and SAPO(30) STA-14, above and below respectively.

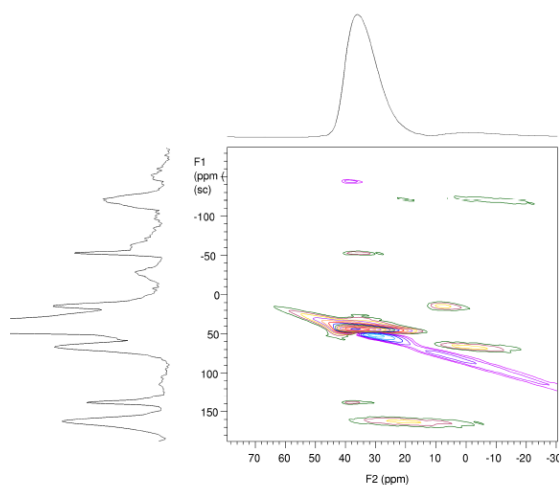


Fig. 4.32 ^{27}Al MQ MAS NMR of SAPO(20) STA-14.

4.3.4 Characterisation of Calcined Materials

STA-14 was synthesised with different chemical compositions: MgAPO, SAPO and MgAPSO. Those materials could be used for adsorption and catalysis if they remain stable after calcination. The study of their calcined forms is given below.

4.3.4.1 Calcined SAPO STA-14

TGA and Optimum Temperature for Template Removal

As in the case of STA-7, STA-14 possesses a three-dimensionally connected pore system, connected via 8MR windows. As a consequence, the rate of loss of organic species upon calcination is rapid, with all organic species being removed in a single event, despite there being two different organic species present.

The TGA profile (Fig. 4.33) shows that the calcination conditions required to remove completely the organic species is higher than in the case of STA-7, probably due to the quantity of organic species to remove. In the case of STA-7, the organic content per unit cell are two molecules of TEA and two of cyclam, whereas for STA-14 per unit cell there are six molecules of TEA and one of K222 (which corresponds to the weight loss of 20% in the profile). The chosen temperature to calcine STA-14 samples was 650 °C in a stream of dry oxygen with a ramp rate of 1.5 °C/min for 12 hours.

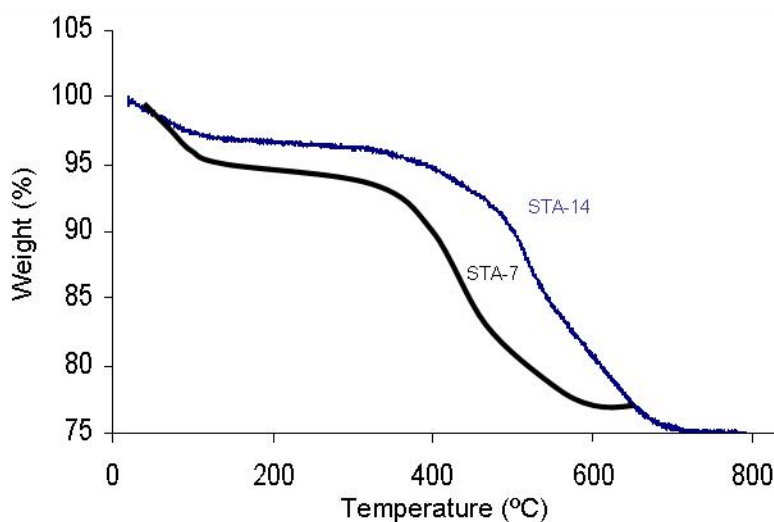


Fig. 4.33 Typical TGA thermogram of SAPO(20) STA-14 and SAPO(20) STA-7.

Once the organics were removed, X-ray powder diffraction was conducted to check the crystallinity. The following XRD patterns prove the stability of SAPO(20) STA-14 after calcination in comparison with MgAPO STA-14 which shows a considerable loss of crystallinity broadening the diffraction peaks.

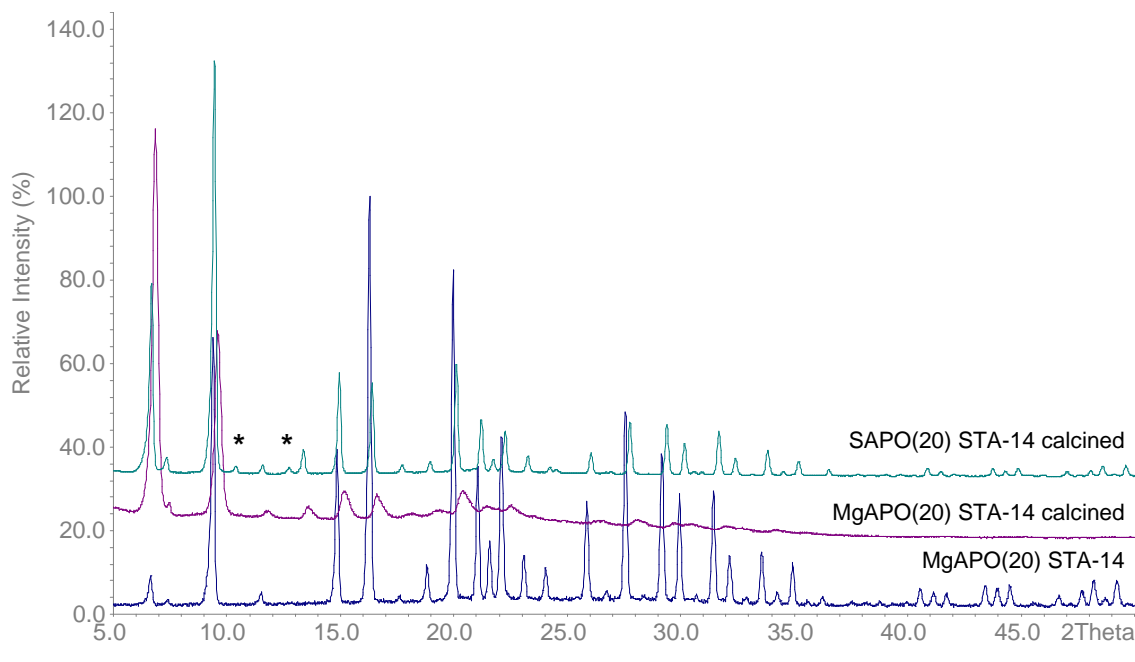


Fig. 4.34 XRD patterns of MgAPO(20) STA-14 as prepared (blue) and calcined dehydrated and SAPO(20) STA-14 calcined dehydrated (cyan), LTA impurity peaks marked with asterisks.

N₂ isotherm

Nitrogen adsorption was conducted gravimetrically on the calcined SAPO(20) STA-14 sample at 77 K. The resulting isotherm exhibits a typical type I profile (Fig. 4.35). A maximum uptake of 27% by mass suggests an internal pore volume of 0.31 cm³/g. The adsorption properties of this and other related materials obtained from this work will be discussed in detail in Chapter 7.

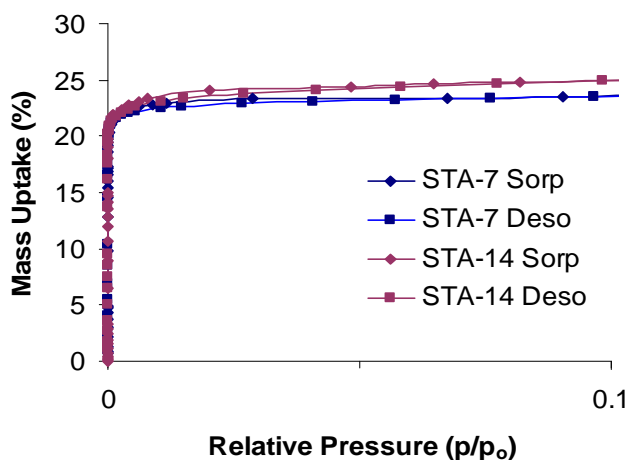


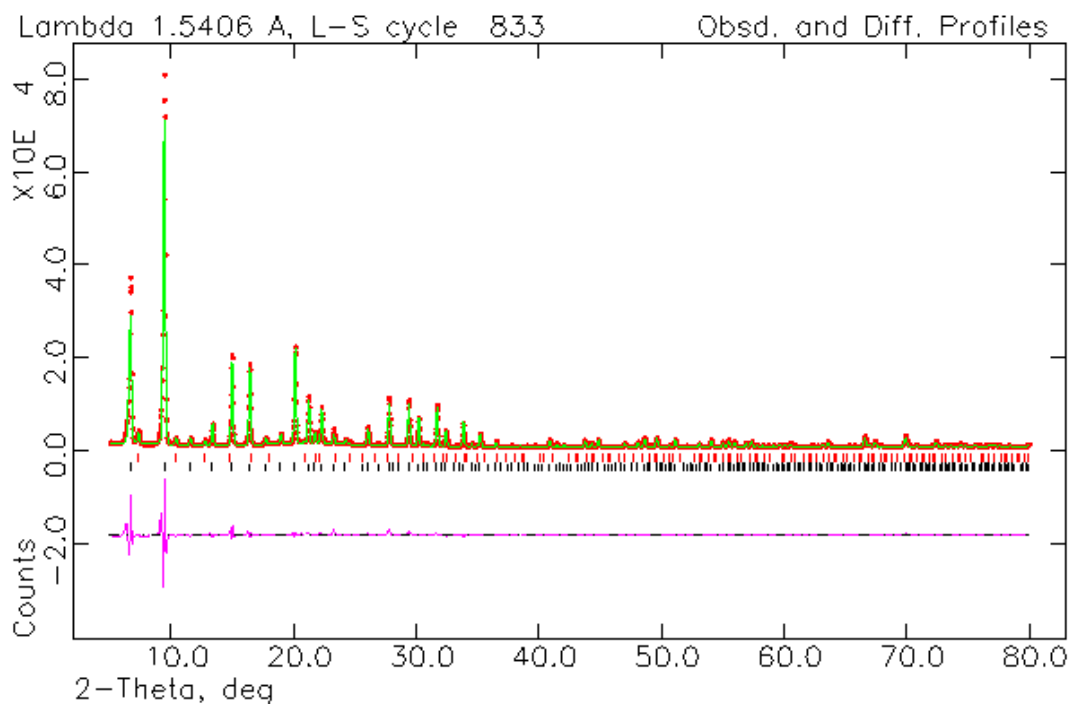
Fig. 4.35 Nitrogen adsorption/desorption isotherm for calcined SAPO(20) STA-14 and STA-7.

Structure Refinement

Rietveld refinement of the calcined form of SAPO STA-14 was performed to confirm the stability of the framework after template removal. The GSAS program suite was used and the atomic coordinates of MgAPO STA-14 and AlPO-42⁸ determined by SXRD as a starting point for phase 1 and 2. Instrumental parameters (background –type 2 and 32 terms-, zero point, peak profile coefficients -pseudo-Voigtian peak shape-) and structural parameters (unit cell, atomic coordinates, thermal parameters for phase 1) were refined, keeping restraints in bond distances with overall weight 10.

The final fit was achieved with $R_{wp} = 11.59\%$ and $R_p = 7.39\%$ and 2.5% of LTA impurity, the refinement plot is shown in figure 4.36. The refined unit cell parameters obtained are: $a = 18.7354(4)$ Å in P-3n with bond lengths P-O = 1.54(14) Å and Al-O = 1.73(14) Å. The atomic coordinates and further structural details are in the Appendix B (Tables B.4, B.5 and B.6). That proves its thermal stability for further applications (Chapter 7).

a)



b)

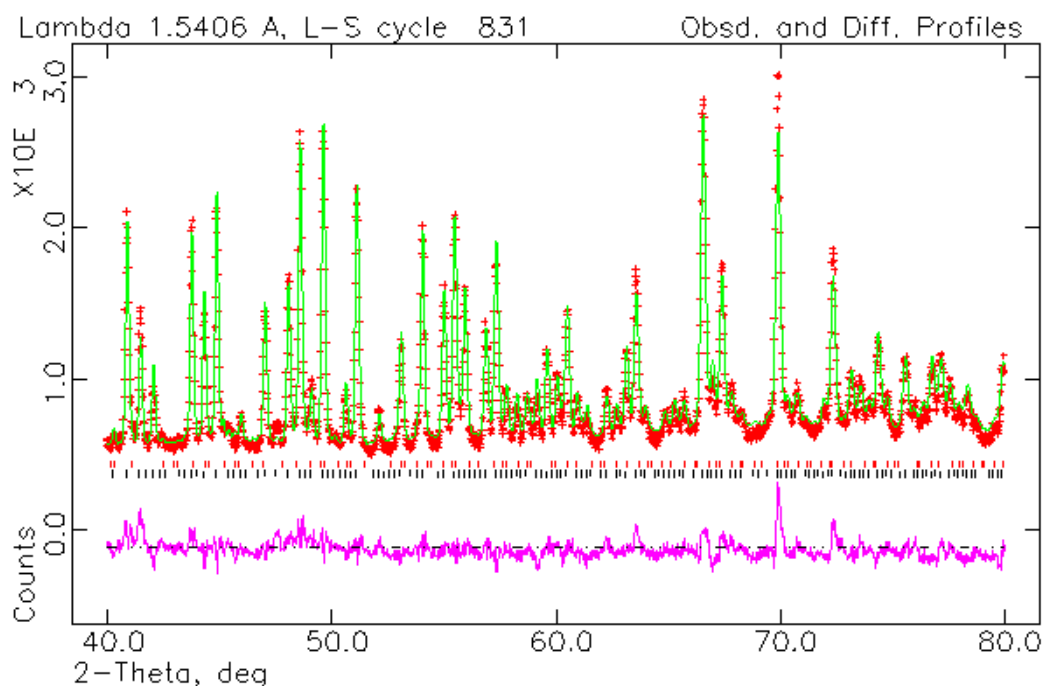


Fig. 4.36 (a) Rietveld refinement plot of calcined dehydrated SAPO(20) STA-14 (red: experimental data; green: simulated pattern; purple: difference plot; reflexion peaks of main phase KFI in black and in red of the LTA impurity), (b) expanded high angle region.

4.3.4.2 Calcined MgAPSOs STA-14

The samples MgAPSO(1:3) and MgAPSO(2:3) STA-14 were calcined and their stability checked immediately by XRD, so the samples were exposed to air for the minimum time possible. The XRD of the calcined materials show more stability upon calcination than the pure MgAPO materials (Fig. 4.37), giving the possibility of their examination as adsorbents and diffusion measurements by the IFM technique.

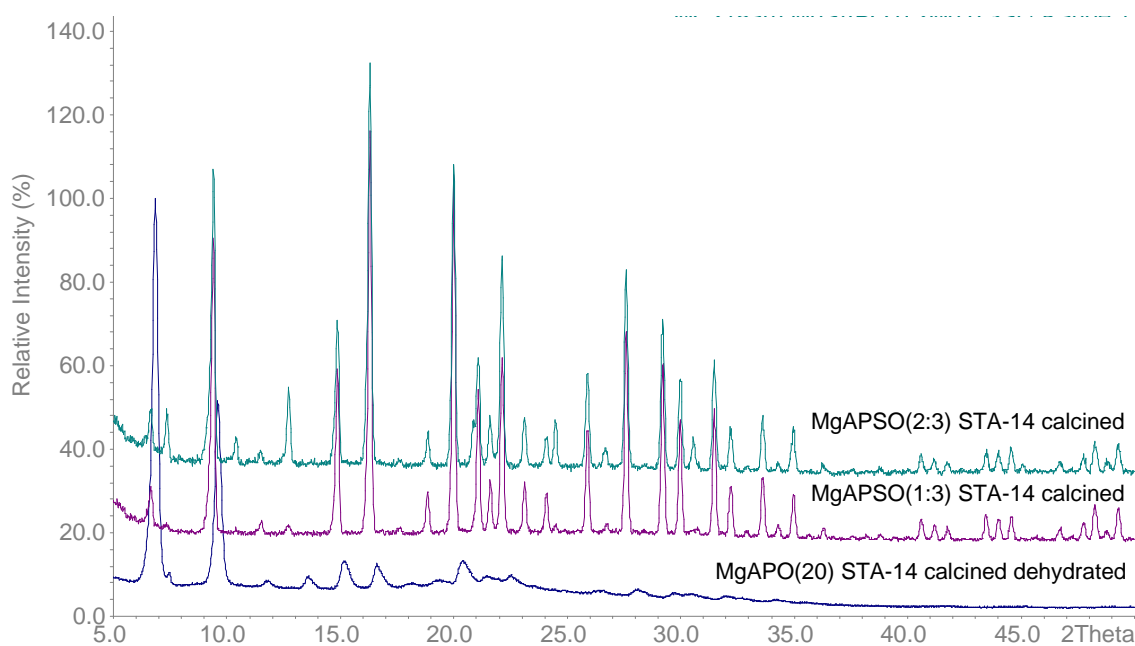


Fig. 4.37 XRD patterns of calcined dehydrated MgAPO(20) STA-14 and calcined MgAPSO(1:3) and MgAPSO(2:3) STA-14 (blue, purple and cyan respectively).

MgAPSO STA-14 materials have suitable morphology for the diffusion application IFM, and remain stable once calcined. Synchrotron X-ray diffraction was performed to confirm the space group. The data clearly shows the presence of the (4 2 1) reflexion, indicating the space group is primitive (without systematic absences, in contrast with the body centred space group of ZK-5 zeolite Im-3m, where only reflexions with Miller indices $h+k+l = 2n$ are allowed). That supports the refinement in Pn-3n (Fig. 4.38).

N₂ adsorption for MgSAPO(1:3) STA-14 gives a maximum uptake of 17% by mass suggesting an internal pore volume of 0.21 cm³/g, lower than pure SAPO(20) STA-14, showing its stability upon exposure to moisture (Fig. 4.39).

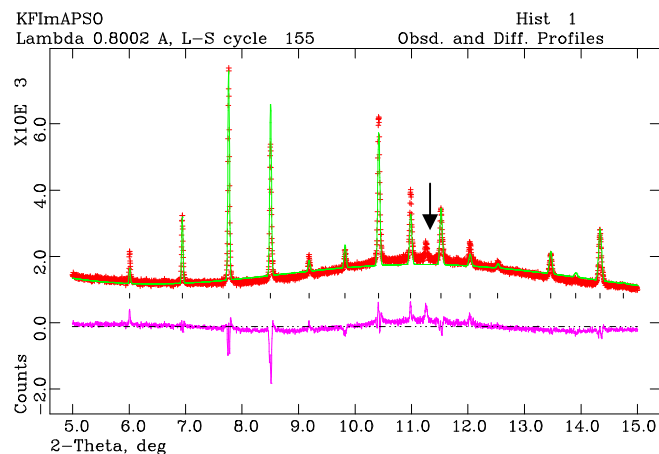


Fig. 4.38 XRD Data collected in Synchrotron for calcined MgAPSO(2:3) refined using as model the parameters of zeolite ZK-5 (space group $Im\bar{3}m$). The arrow denotes the experimental reflexion peak (4 2 1) characteristic for primitive space group; (red: experimental data, green: simulated pattern, black marks: theoretical peak positions, purple: difference)

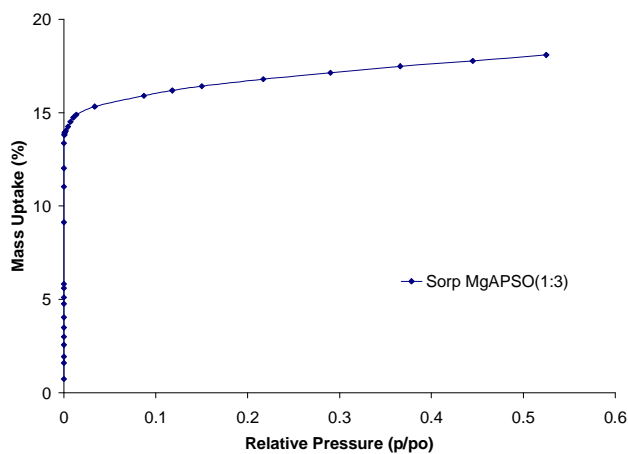


Fig. 4.39 Nitrogen adsorption/desorption isotherm for calcined MgAPSO(1:3) STA-14.

4.3.4.3 Porosity of STA-14 Materials

Table 4.8 summarises data on the most promising samples of STA-14 for CO₂ adsorption:

Table 4.8 Summary of STA-14 materials with potential adsorption properties.

| N ₂ Isotherms | | |
|--------------------------|-----------|--------------------------------|
| STA-14 | | |
| Sample | % by mass | Pore Volume cm ³ /g |
| SAPO(20) STA-14 | 25.16 | 0.31061728 |
| SAPO(30) STA-14 | 24.33 | 0.30037037 |
| MgAPSO(1:3) STA-14 | 17.00 | 0.20987654 |

4.4 Summary & Conclusions

Using a strategy of co-templating supported by modelling the novel zeotype STA-14 with the KFI topology was prepared using the suggested template/co-template pair K222/TEA. SXRD of the as-prepared materials shows the tt.tt conformation of the TEA cation within the MER cage as suggested by modelling. This underlines its co-templating effect and the agreement between experiment and host-guest calculations. This is the first reported example of a designed synthesis for a novel zeotype material. For instance, R. Xu *et al.*⁹ in 2005 applied similar rationalisation of the synthesis in combination with modelling and combinatorial approach to obtain AIPO-21 (AWO) with the rational selection of templates proposed. Our methodology endeavours to use the co-templating approach supported by modelling for novel materials built up from more than one kind of cage. The modelling approach could be improved by implementation of *de novo*¹⁰ rather than rational selection of potential templates.

STA-14 has been successfully obtained in a variety of MAPO, SAPO and MAPSO compositions but as in the case of STA-7 the pure AIPO remained elusive. This suggests that this kind of topologically very similar materials cannot incorporate into the framework hydroxyl or fluoride groups that could help to balance the charge of the organic cations. Therefore the design of the synthesis through modelling is important but also the implementation of combinatorial or high-throughput synthesis is fundamental to find the optimum conditions, since the precise mechanism of crystallisation is still incompletely understood.

From all the STA-14 materials presented here the most promising for adsorption applications is SAPO(20) STA-14. It is interesting to observe that the silicon content slow the growth of the (111) faces and that the gel composition influence the morphology. More generally organic species show different tendencies to act as SDAs, for instance TMA directs formation of the SOD cage more strongly than K222 templates the α -cage of the LTA structure. The following section discussed in detail the conclusions of crystallisation of ‘double six ring’ (D6R) materials.

-
1. W. M. Meier, G. T. Kokotailo, *Z. Kristallogr.*, 1965, **121**, 211.
 2. L. Schreyeck, F. D'Agosto, J. Stumbe, P. Caullet, J. C. Mougénel, *Chem. Commun.*, 1997, 1241.
 3. M. J. Maple, E. F. Philp, A.M. Z. Slawin, P. Lightfoot, P.A. Cox, P.A. Wright, *J. Mater. Chem.*, 2001, **11**, 98.
 4. M. M. J. Treacy, J. B. Higgins, '*Collection of simulated XRD Patterns for Zeolites*', 4th Edition, Elsevier, Amsterdam, 2001.
 5. S. Wilson, B. M. Lok, C. A. Messina, T. R. Cannan, E. M. Flanigen, *J. Am. Chem. Soc.*, 1982, **104**, 1146.
 6. H. Robson, K. P. Lillerud, '*Verified Synthesis of Zeolitic Materials*', 2nd Edition, Elsevier, Amsterdam, 2001, 113.
 7. P. J. Barrie, J. Klinowski, *J. Phys. Chem.*, 1989, **93**, 5972.
 8. G. W. Noble, *Synthesis of New Microporous Solids by Template Design*, PhD Thesis, University of St Andrews, 2000.
 9. Y. Song, J. Li, J. Yu, K. Wang, R. Xu, *Topics in Catalysis*, 2005, **35**, 3.
 10. D. W. Lewis, D. J. Willock, C. R. A. Catlow, J. M. Thomas, G. J. Hutchings, *Nature*, 1996, **382**, 604.

Chapter 5: D6R Family Conclusions

5.1 Introduction

Chapters 3 and 4 show the importance of the use of a second base acting as co-template to achieve target topologies built up from more than one cage type, STA-7 (SAV) and STA-14 (KFI). They also show how modelling can be a tool to find the optimum co-template to design a hydrothermal synthesis of a particular target structure.

This chapter discusses the relation of STA-7, STA-14 and the polytypic materials AlPO-18 (AEI) and SAPO-34 (CHA), all built up from D6Rs with different stacking arrangements, followed by the study of the crystal growth in SAPO STA-7. This work was performed via high resolution scanning electron microscopy (HRSEM) and atomic force microscopy (AFM) in collaboration with the groups of Prof M. Anderson (UMIST) and Prof O. Terasaki (Stockholm University). The study has identified spiral growth features on the surfaces and these have been imaged and compared on the same crystal by the two different methods. Here, these data are presented to support the hypothesis of the crystal growth in which the D6R is the unit building block of such materials.

This chapter concludes with synthetic studies to observe the interaction of the templates used in STA-7 and STA-14: cyclam, K222 and TEA. Due to the topological similarities it might be possible to form intergrowths of STA-7 and STA-14. Furthermore, attempts to use three co-templates for a zeotype with the tschörtnerite structure (TSC) containing three types of cages (SOD, LTA and TSC) are reported.

5.2 Synthetic Results from Chapter 3 and 4: the D6R Family.

CHA, AEI, SAV and the novel zeotype reported here with the KFI topology are all built up from D6Rs (Fig. 5.1), and their topological similarities lead to the hypothesis of the D6R as a building unit block.

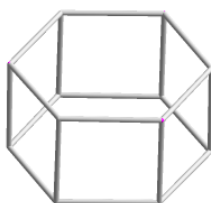


Fig. 5.1 A double six ring (D6R), vertices represent the alternating tetrahedrally coordinated aluminium and phosphorus and lines represent the oxygen bridges.

In the case of CHA, the D6Rs in each layer are tilted in the same way and each layer is stacked along the z direction in AAA fashion. The same type of D6R layer appears in AEI but stacked in ABA fashion, so each layer has an opposite tilt to the next along the z direction. For SAV the D6R have opposite tilts along x and y but each layer of D6Rs along the z direction is identical. For KFI the tilts of D6Rs alternate in orientation along each of the three crystallographic directions (Fig. 5.2).

CHA and AEI have only one type of cage, but SAV and KFI contain two types of cages, so the co-templating approach is an attractive strategy to move from one structure to the other. ^{31}P MAS NMR in STA-7 and STA-14 give similar results, suggesting that the incorporation of magnesium proceeds by the same general mechanism.

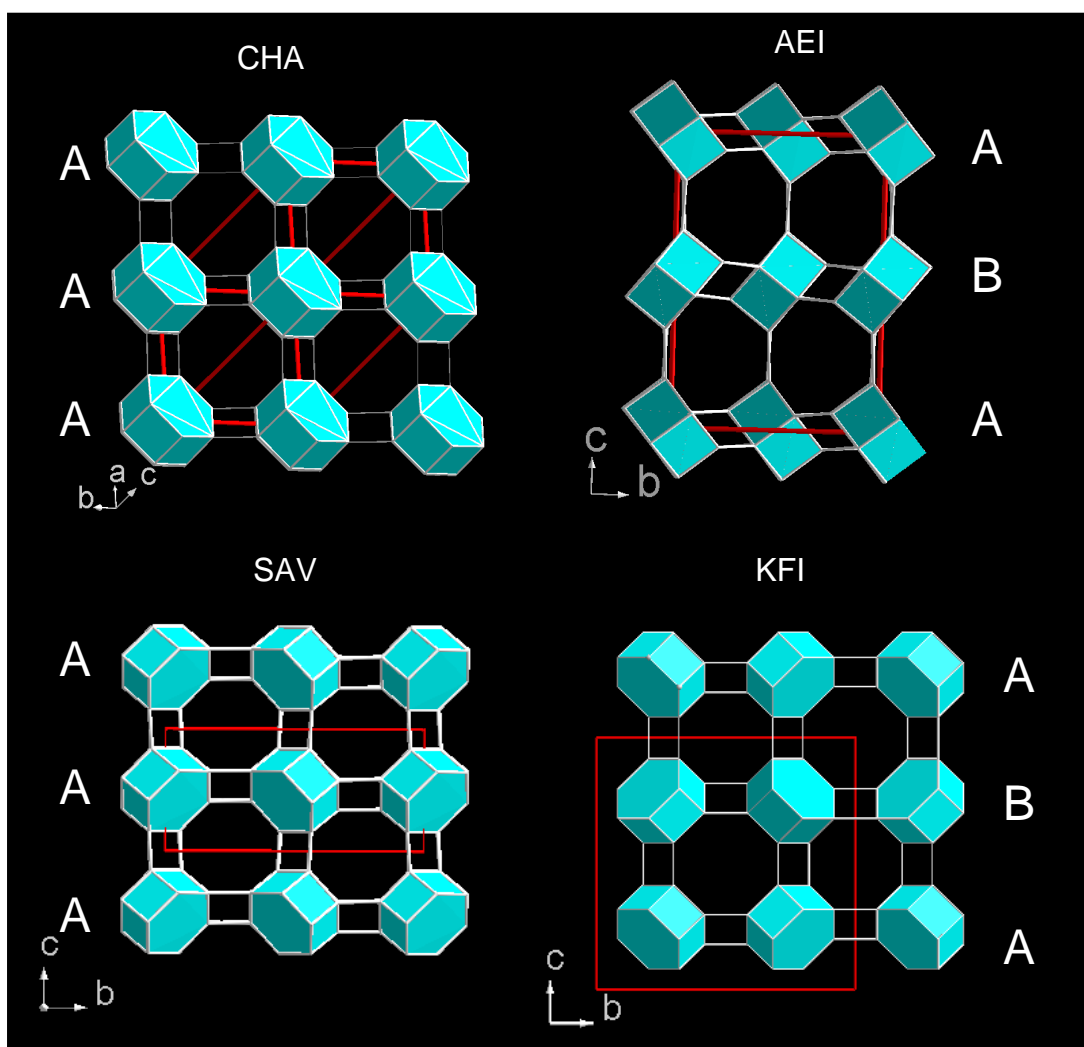


Fig. 5.2 The D6R materials with the stacking sequence layer by layer.

STA-7 and STA-14 are built up only from D6Rs, with a different stacking arrangement. Furthermore, the $\langle 001 \rangle$ surfaces of the SAV structure are topologically identical to the $\langle 100 \rangle$ surfaces of KFI. Related D6R materials AlPO-18 (AEI) and SAPO-34 (CHA) have been also produced during this work using the cyclam/TEA pair. Elemental analysis show that the TEA cation dominates cyclam in the case of AlPO-18 ($C/N = 5.6$), corroborating the information found in the literature that TEA cation stabilises the AlPO-18 structure.¹ For AlPO(F)-34, the elemental analysis shows only the presence of cyclam ($C/N = 2.3$). STA-7 was not obtained in the AlPO regime because cyclam/TEA pair could not act together. The same scenario appears in the STA-14 system, where in the AlPO composition only K222 is occluded within the framework leading to AlPO-42, the AlPO

version of zeolite A.² The following table summarises the products in these systems using two co-bases.

The co-templating role of TEA cation is proved by its change of conformation from tg.tg to tt.tt when moving from the cage A (STA-7) to the MER cage (STA-14). Such organic-inorganic interaction leading to a structure-directed aluminophosphate crystallisation has been reported for the case of MAPO-34 (M = Zn, Co, Mn) and AlPO-5, with TEA in tg.tg and tt.tt conformations, respectively.³

Table 5.1 Summary of syntheses using cyclam/TEA and K222/TEA with typical products. Syntheses of only TEAOH in SAPO, MAPO or MAPSO conditions were not conducted.

| Template | Co-temple | Gel Composition | Product (by XRD) |
|----------|-----------|---|----------------------------|
| Cyclam | TEAOH | AlPO with HF | AlPO-34 (CHA) |
| | | | only cyclam occluded |
| | | AlPO (no HF) aging conditions [*] | AlPO-18 (AEI) |
| | | | mainly TEA occluded |
| | | AlPO (no HF) aging conditions ^{**} | AlPO-5 (AFI) |
| | | MgAPO Mg/P = 0.5 | intergrowth AEI-CHA |
| | | | (by SXRD) |
| | | MgAPO Mg/P < 0.5 | } STA-7 (SAV) |
| | | CoAPO Co/P = 0.2 | |
| | | SAPO Si/P = 0.1 to 0.4 | |
| | | MgSAPO | |
| | | MnSAPO | |
| K222 | TEAOH | AlPO | AlPO-42 (LTA) |
| | | | only K222 occluded |
| | | MgAPO Mg/P = 0.2 to 0.5 | } STA-14 (KFI) |
| | | CoAPO Co/P = 0.2 | |
| | | SAPO Si/P = 0.1 to 0.3 | |
| | | MgSAPO | |
| | | | K222 and TEA |
| | | | occluded |

^{*} 1 h and 80 °C; ^{**} 1.5 h and 80 °C or 5 h and 60 °C or 7 h and 60 °C.

These results show the synthetic connections between the D6R materials. Possible intergrowths due to potential structural relationships are summarised as follows and described schematically in figure 5.3:

- MgAPO(CHA) and MgAPO(AEI) have been observed to intergrow. Structurally this is possible because they share a face in common, and it is the way in which subsequent layers are orientated that determines which structure forms. The resulting cages have slightly different shapes.
- The AEI and SAV structures could intergrow, because they share a face in common. In fact, some XRD patterns of STA-7 show an extra peak at $20.5^\circ 2\theta$ that may be attributed to the SAPO/MgAPO/MgAPSO-18 phase. This is explained later when discussing AFM results, and is thought to occur at the later stages of crystallisation as the cyclam becomes exhausted and TEA cation dominates.
- The relationship of the SAV and KFI topologies would permit intergrowth via a common plane, $(001)_{\text{SAV}} = \{100\}_{\text{KFI}}$.

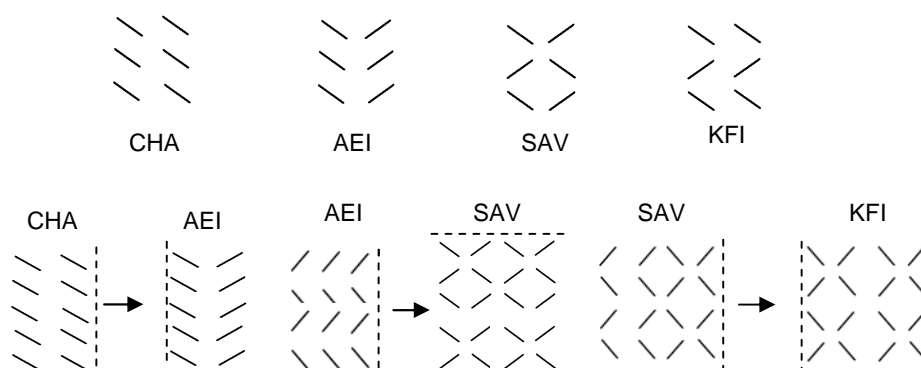


Fig. 5.3 Schematic description of the D6R structure types CHA, AEI, SAV and KFI (top) and their interconnections by face sharing (bottom): CHA/AEI, AEI/SAV and SAV/KFI from the left to the right.

CHA and AEI structures in the SAPO form are active and selective for MTO reaction (Table 5.2).^{4,5} Therefore the research of the related structures SAV and KFI was of interest in understanding the effect of pore geometry on the performance in adsorption and the MTO reaction, as covered in Chapter 7.

Table 5.2 *D6Rs materials in the SAPO form and their catalytic applications.*

| Material | Discovery Year | Reference | Applications |
|-------------------|--------------------|------------------------|-------------------|
| SAPO-34 (CHA) | 1984 ⁶ | Flanigen <i>et al.</i> | MTO ⁷ |
| SAPO-18 (AEI) | 1994 ⁸ | Chen <i>et al.</i> | MTO |
| SAPO STA-7 (SAV) | 2003 ⁹ | Wright <i>et al.</i> | MTO reported here |
| SAPO STA-14 (KFI) | 2007 ¹⁰ | Castro <i>et al.</i> | MTO reported here |

5.3 Exploring the D6R Hypothesis: Crystal Growth in SAPO STA-7.

In order to achieve a better understanding of the crystal growth of STA-7 and the role of the D6R, SAPO STA-7 was studied via polarised microscopy (sample denoted as SAPO(20) in Chapter3), single crystal X-ray diffraction (SXRD) and, in collaboration with Manchester and Stockholm University, via AFM (Atomic Force Microscopy) and HRSEM (High Resolution Scanning Electron Microscopy).

Polarised Microscopy and SXRD, a layer by layer growth of D6Rs hypothesis

SAPO STA-7 crystals show mainly tetragonal prismatic morphology. Under the optical microscope the projection observed is mainly rectangular but in a few cases a square shape is also present (Fig. 5.4 a). To establish the Miller indices of the faces of such crystals a combination of polarised light microscopy and single crystal diffraction was performed.

Under polarised light and using crossed polars extinction results for all orientations of crystals that show square projections as the position of the crystal is changed by rotating the microscope stage. That means that the light moves in an isotropic fashion along this projection. For tetragonal crystals this occurs only along the z direction,¹¹ so the square shaped face is the end-on view of the crystal and therefore the (001) face. In the other directions light is broken in two rays travelling at different velocity, therefore the rectangular projection is the (100) face along [100] (Fig. 5.4 b and c). These results were confirmed by indexing these faces as (001) and (100) via SXRD using the face indexing

routine ‘RAX Shape’ (data collected by Prof. Alex Slawin): ‘essentially the various faces of the crystal are drawn and input into the program which compares them with the orientation matrix and indexed cell to determine the indices of the external faces’.¹²

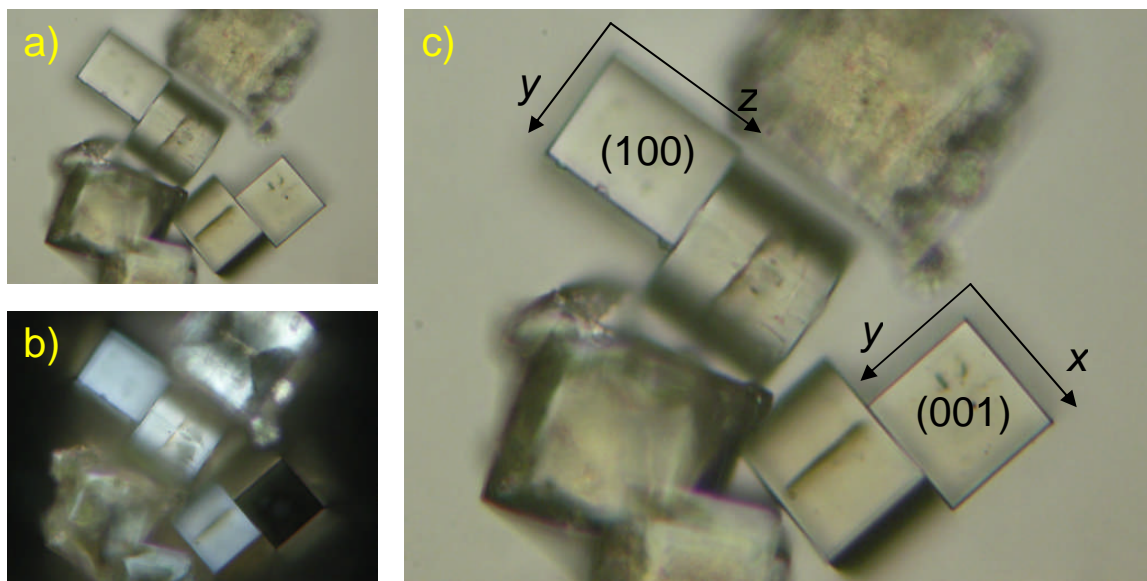


Fig. 5.4 (a) Light microscope image of SAPO(20) STA-7 crystals showing tetragonal and square projections. (b) The same crystals under polarised light shows that the square crystal turned dark and remained when crystal position changed. (c) That leads to the face indices of both projections.

AFM and HRSEM and the D6R layer growth hypothesis.

Neither light microscopy nor SEM has the resolution to give sufficiently detailed information about the surface of the crystal to prove the layer growth in SAPO STA-7. Higher resolution techniques are required. Here I present and comment on the results obtained at Manchester (Dr Pablo Cubillas) and Stockholm (Sam Stevens) using AFM (Atomic Force Microscopy) and HRSEM (High Resolution Scanning Electron Microscopy) in the content of the synthetic results obtained in this thesis.

Using these high resolution techniques, the imaging of SAPO STA-7 crystals shows the presence of multiple spiral shaped growth on (100) and [001]. The following figure 5.5 shows HRSEM (b) and AFM images (a and c) of a growth spiral in the [001] direction of an STA-7 crystal on the (001) plane. The multiple terrace growth in spiral shape can be observed in the HRSEM image. Height measurements on the AFM image give an individual step height of approximately 0.9 nm.

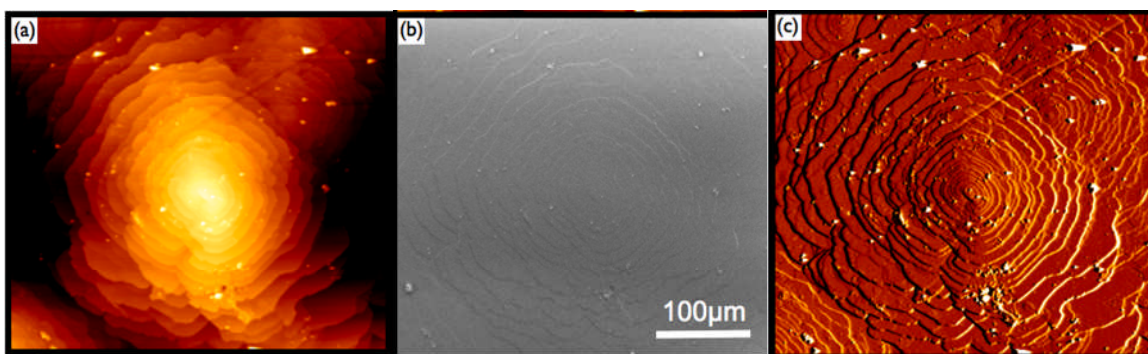


Fig. 5.5 HRSEM (b) and AFM image (a, c) for SAPO STA-7 showing the spiral growth type in the same crystal (courtesy of Sam Stevens and Pablo Cubillas, Manchester and Stockholm Universities).

This information can be translated to an atomic level to understand the crystal growth mechanism in STA-7. From the HRSEM and AFM information, STA-7 seems to grow by stacking layers along [001] in spirals, where the thickness of each layer is 0.9 nm, or 9 Å.

The atomic structural composition of such layer can be determined using a STA-7 structure model viewed along [100] obtained from single X-ray diffraction. The STA-7 3-dimensional structure can be split in layers by cutting it in slices along (001). The structure will be more easily split where fewer bonds have to be broken. From this observation, the most likely layer is formed by the D6Rs. The width of such a layer (9.4 Å) is in accordance with the value obtained by HRSEM and AFM. These observations strongly support the hypothesis of the D6R as a building block for SAV (Fig. 5.6). This hypothesis cannot differentiate between scenarios in which the D6R remains stable in solution or where smaller units are attached very rapidly during the crystallisation to form the D6Rs on the surface.

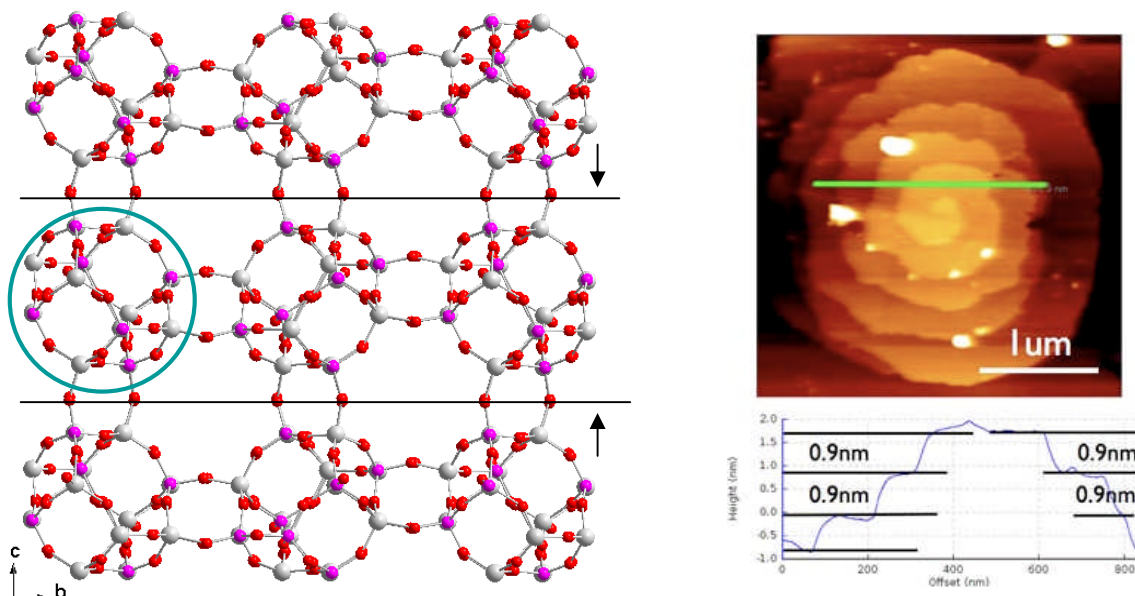


Fig. 5.6 STA-7 structure built up by stacking 2D layers of D6Rs along [001] (right), AFM image with individual step height of approximately 0.9 nm (left) (courtesy of Dr. Pablo Cubillas, Manchester University).

Understanding the formation of the spiral growth

To prepare a perfect crystal, growth should occur layer by layer so the steps disappear once the full crystal layer is formed (Fig 5.7 a), but in this case the growth appears in spirals. This shows the presence of screw dislocations that act as steps for layer growth as reported in other studies such as the synthetic zeolite A crystal (Fig 5.7 b).¹³

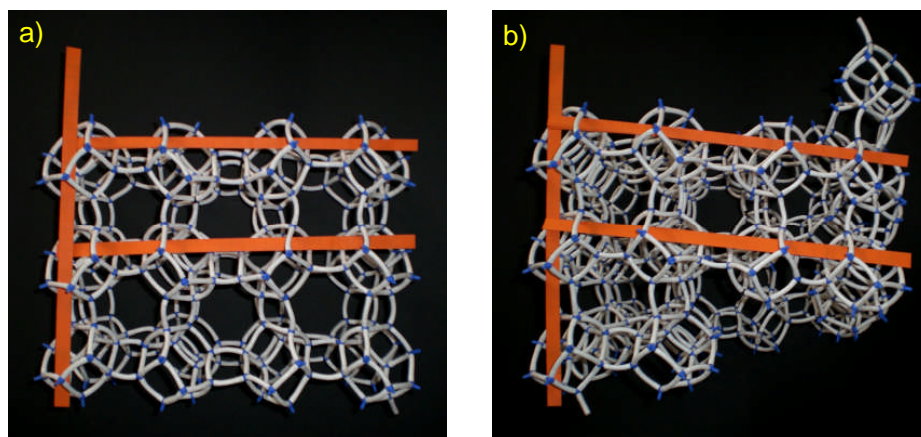


Fig. 5.7 STA-7 models: (a) the perfect structure grows along the z direction by adding layers of D6R and (b) as observed by AFM, as screw dislocation with a Burger vector of [001] is the mechanism for growth along [001].

In SAPO STA-7, along the z direction, AFM shows spirals with a step height of 0.9 nm. A model was used to understand the formation of the dislocation step by step as follows (see Fig. 5.8): (a) the D6Rs in STA-7 are orientated in four ways along the z direction, (b) in an ideal framework a D6R chain is removed along z to form the distorted model, (c1) the D6Rs can be attached to each other around this defect without breaking the symmetry to form a spiral growth along c axis with the (c2) Burger vector equal to the length observed with AFM. By removing the D6R chain along z direction, dangling bonds P-OH and Al-OH are formed, with an associated energy cost. (d1) The empty space can be filled with D6Rs with (d2) little distortion in the symmetry so the structure remains stable for continuation of the growth along this direction, suggesting that the screw dislocation is energetically favourable and therefore the crystal growth along this direction is faster.

Along [100] and [010] more complex growth patterns are observed and are at the moment under investigation with the hypothesis of the formation of AEI layers at the surface of the crystal in a final step of crystallisation.

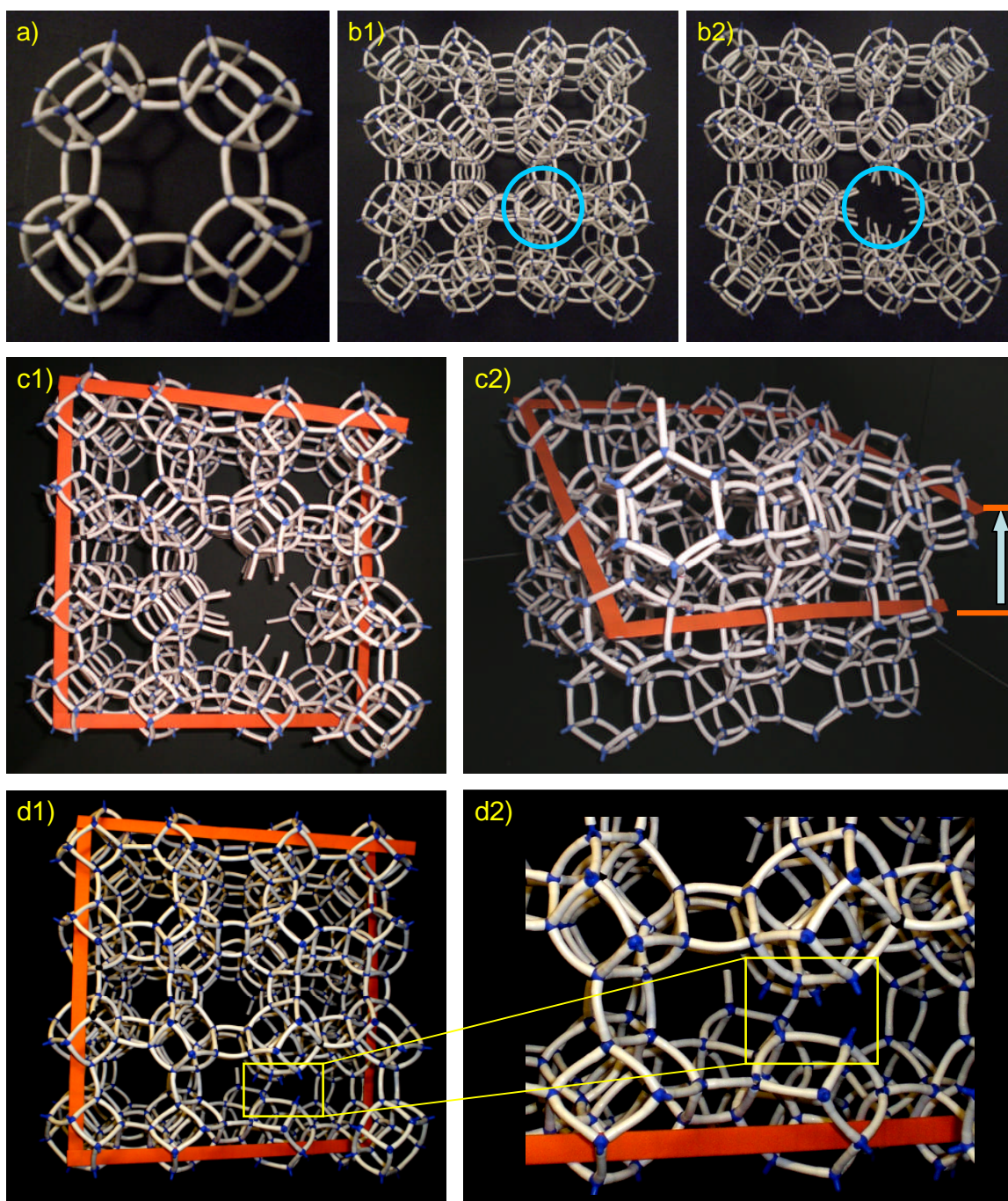


Fig. 5.8 Model of the screw axis along z direction in STA-7: the four orientations of the D6Rs along z (a), by stacking the D6Rs in the four orientations an ideal model of the structure of STA-7 is formed (b1); this model can be distorted (b2) by removing a coulomb of D6Rs along $[001]$; the growth of the material can be done stacking D6Rs in spirals around the distortion (c1) and the Burger vector of growth (c2), denoted as a light blue arrow along z has a length of a D6R layer width; the dangling bonds originated by the removal of the D6R coulomb attach D6Rs (d1) and as a result, there are disconnections of the D6Rs due to the screw dislocation (d2).

5.4 Further Work

5.4.1 Exploratory Synthesis Using the Templates of STA-7 and STA-14: Cyclam/K222/TEA

The formation of an intergrowth of STA-7 and STA-14 is theoretically possible, due to the identical topology of the (001) surface of the SAV structure and the $\langle 100 \rangle$ faces of KFI. In practice, the simultaneous addition of cyclam, K222 and TEA to raise the pH up to 7 gives STA-7 as observed in the XRD pattern and also the SEM (Fig. 5.9 and 5.10 respectively), see Table 5.3 for summary of the synthesis. The morphology of STA-7 in these preparations is similar to the one reported previously^{9, 14} and also in this investigation (section 3.3.1.1). These results indicate that cyclam acts with a stronger structure directing effect than the K222. This suggests that TEA is influenced by the templating effect of cyclam and orientates with the tg.tg configuration, controlling the next orientation of the layer making incorporation of K222 into the cages unfavourable.

Table 5.3 Summary of the syntheses using cyclam/K222/TEA in MgAPO gels at Mg/P ratio 0.2.

| Template STA-14 | Template STA-7 | Co-template | Product (by XRD) |
|-----------------|----------------|----------------|------------------|
| 0.5 K222 | 0.5 cyclam | TEA up to pH 7 | STA-7 |
| 0.3 K222 | 0.7 cyclam | TEA up to pH 7 | STA-7 |

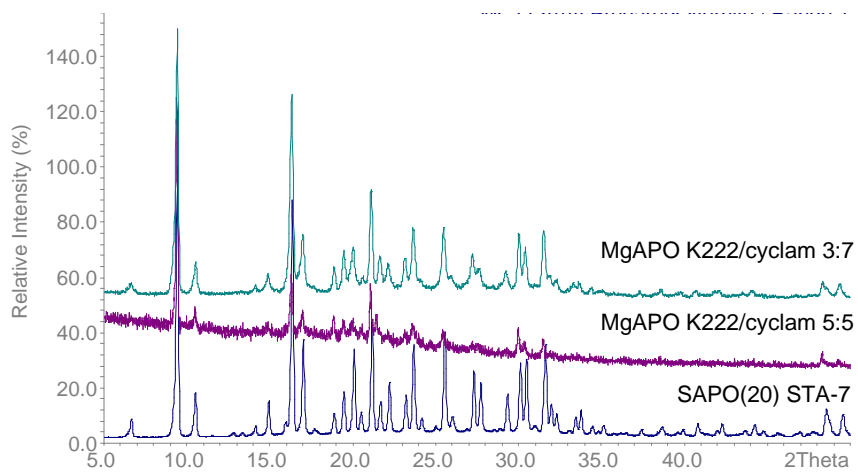


Fig. 5.9 XRD patterns of the products: K222/cyclam ratio 5:5 (purple) and 3:7 (cyan). The XRD pattern of pure STA-7 is given for comparison (blue).

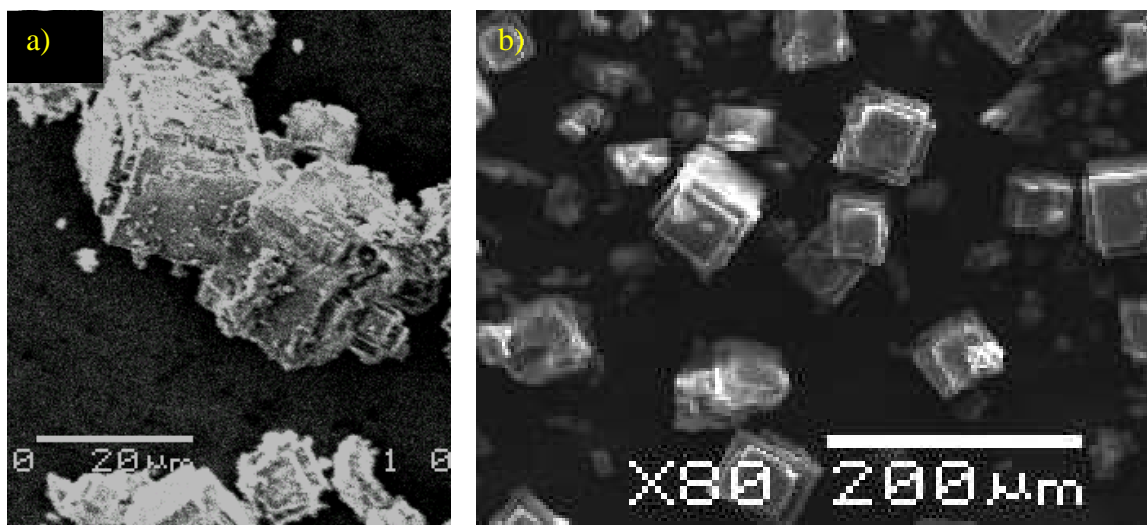


Fig. 5.10 (a) SEM image for the product from synthesis K222/cyclam ratio 3:5 and for comparison (b) typical faced cubes of STA-7 as reported in section 3.3.1.1.

Further work in this synthetic route could explore the molar ratio, increasing the ratio of K222 contain to cyclam as well as aging the gel or changing the addition sequence of the templates.

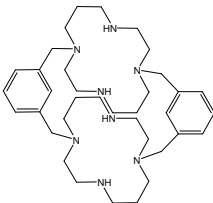
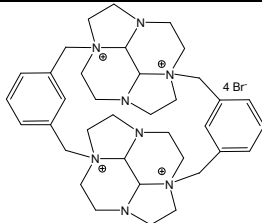
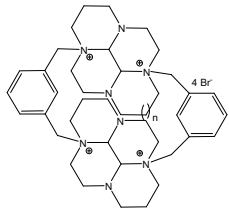
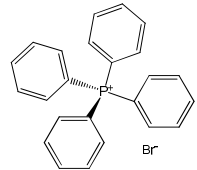
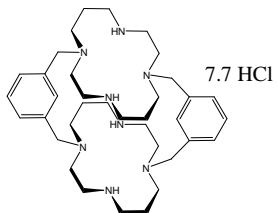
5.4.2 Exploration of the Use of Three Templates; the K222/Co-Base/‘Large Template’ System in MgAPO gel; A Novel Layer Phase

The system K222/co-base was further explored by adding a third template in an attempt to form the Tschörtnerite (TSC) topology in zeotype. The TSC topology has three types of cages: SOD, LTA and TSC (Fig. 5.11), therefore the use of TMA, K222 and as the third template (i) a selection of novel large macrocycles* based on cyclam or cyclen and (ii) tetraphenylphosphonium bromide was investigated (see Table 5.4 for the chemical formula and abbreviations of these templates).

Prior to synthetic work, modeling was performed to visualise the TSC cage and the fit of the third large template into this cage.

* Templates obtained from V. Patinec (University of Brest, Normandy).

Table 5.4 Chemical formula of the macrocycles (*based on cyclam or **cyclen) and tetraphenylphosphonium bromide (TPP) applied.

| Chemical Formula of co-template 2 | Abbreviation | Chemical Formula of co-template 2 | Abbreviation |
|--|-----------------|--|------------------|
|  | Cyclam1* |  | Cyclen1** |
|  | Cyclam2* |  | TPP |
|  | Cyclam3* | | |

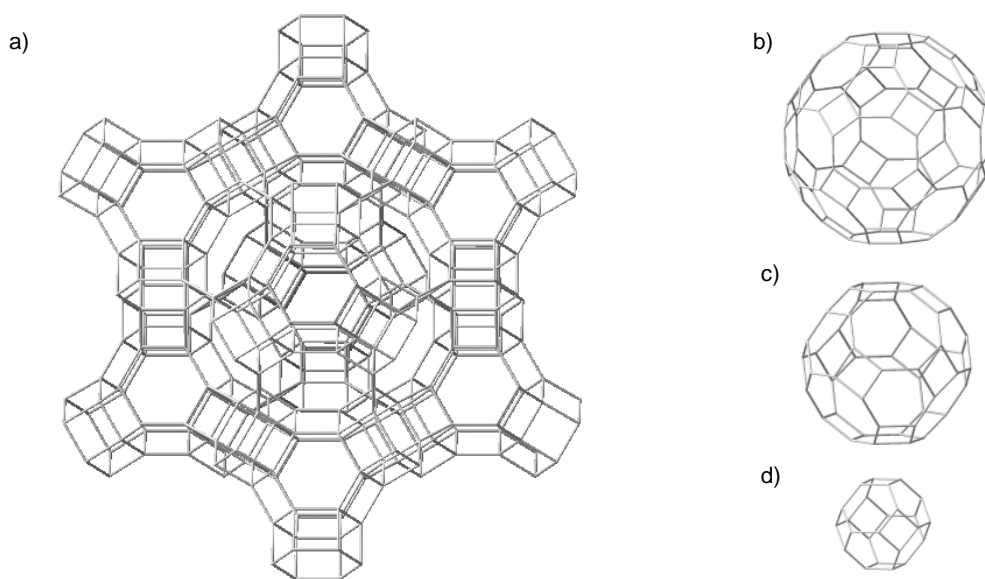


Fig. 5.11 Tschörtnerite (TSC) framework (a) and the three cages within this structure: TSC (b), LTA (c) and SOD (d).

5.4.2.1 Modelling Results

TSC zeolite was used as a model framework. The macrocycle abbreviated as Cyclam1 was modeled as a potential template. The following figures (Fig. 5.12 and 5.13) shows that such organic species could be occluded into the larger cage of TSC, but without a perfect fit between template and cage. Such templates are quite flat and are not large enough to fill the cage in three dimensions.

From a modelling basis, TSC was therefore not very likely to be obtained using the cyclam-derived templates. In an attempt to use a template with a more spherical geometry the use of tetraphenylphosphonium (TPP), as bromide form, was tried experimentally.

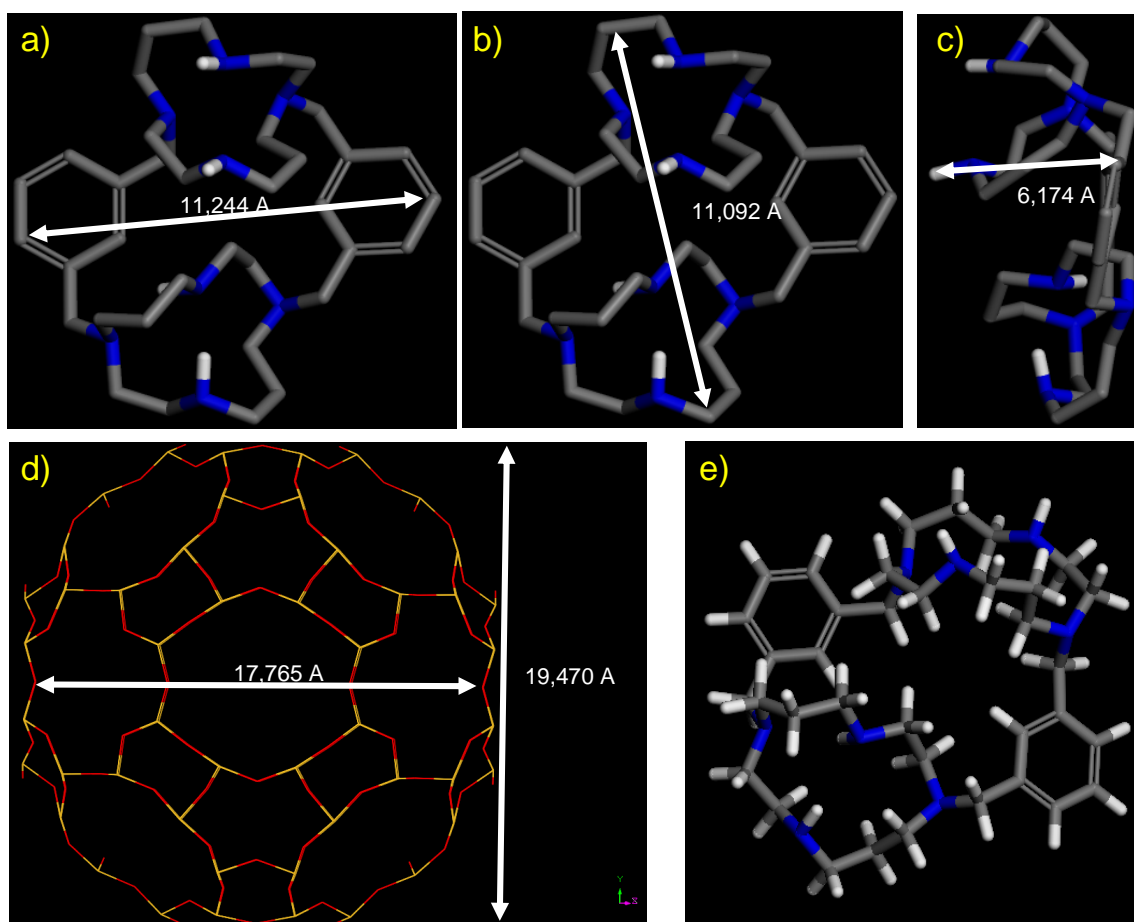


Fig. 5.12 Modelled template Cyclam1(a, b, c and e) after geometry optimisation and the larger cage of TSC structure (b).

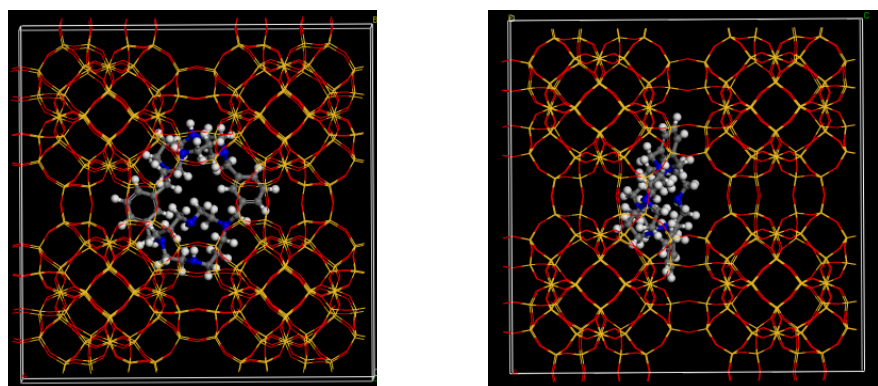


Fig. 5.13 Modelled template *Cyclam1* within the larger cage of TSC along *c*-axis and *a*-axis (left and right respectively).

5.4.2.2 Syntheses Results

The products formed (Table 5.5) do not have the tschörtnerite structure (TSC), but rather MgAPO-20 (SOD), templated by TMA; MgAPO-42 (LTA) in which the templating effect of K222 dominates; and a novel layered phase prepared in the presence of TPP, K222 and TPA. Elemental analysis indicates no nitrogen is present in this novel material, suggesting it is templated by TPP alone. The material shows hexagonal plate morphology and loses its crystallinity once calcined (Fig. 5.14). The Mg/P ratio in this material is 0.27 (by EDX).

Table 5.5 Summary of MgAPO products obtained from K222/co-base/large-template, denoted in bold the organic species acting as SDAs in each synthesis.

| Template | co-base 1 | co-template 2 | Product (by XRD) |
|-------------|--------------------|---------------|--------------------------------|
| K222 | TMA | TPP | MgAPO-20 (SOD) |
| K222 | TMA | Cyclam1 | SOD + LTA |
| K222 | TMA and TPA | TPP | SOD + novel Layer Phase |
| K222 | TPA | TPP | novel Layer Phase |
| K222 | TPA | Cyclam1 | MgAPO-42 (LTA) |
| K222 | TPA | Cyclam2 | LTA mainly |
| K222 | Pyridine | TPP | LTA + MAPO-39 (ATN) |
| K222 | Piperazine | TPP | LTA + SOD |
| K222 | DPA | Cyclen1 | LTA |
| K222 | DPA | Cyclam3 | LTA |

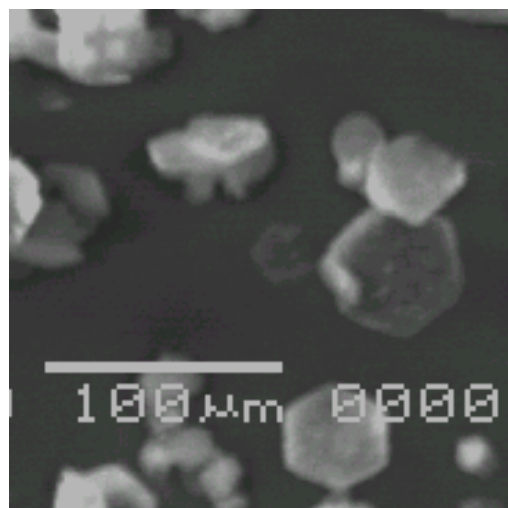
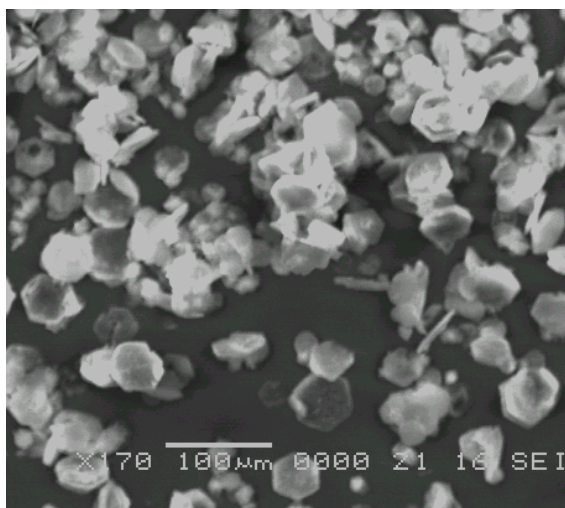
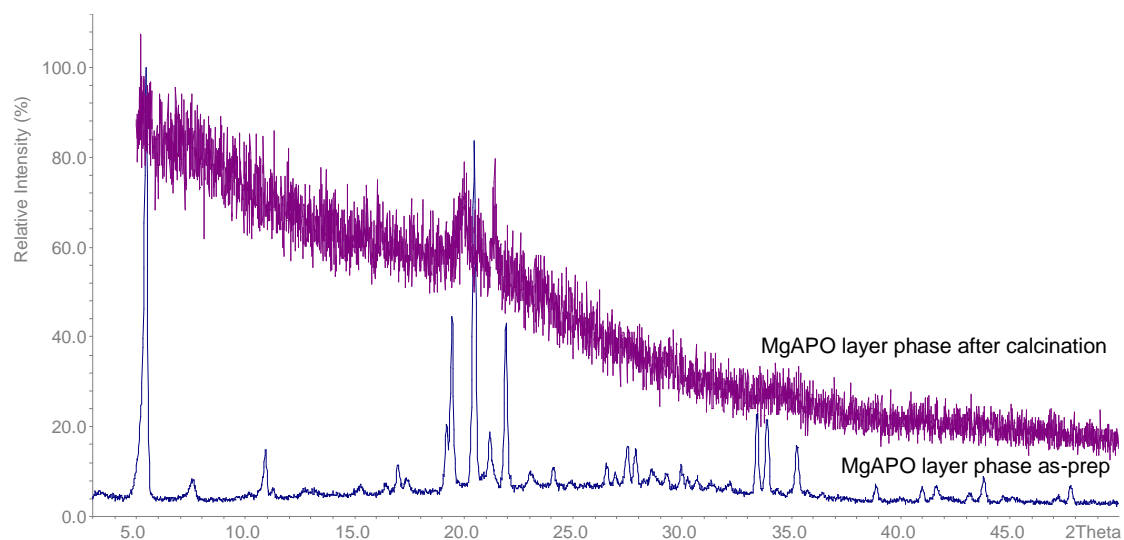


Fig. 5.14 XRD pattern (top) of novel layer phase as prepared (blue) and after calcination (purple); SEM image (bottom) showing pure phase and typical morphology of the novel phase.

5.4.2.3 SXRD of Novel Phase

SXRD data of this phase are of relatively poor quality ($R_{\text{int}} = 25\%$) but show the structural characteristics of the novel layer phase, although the template structure is not completely determined due to its disorder. The layer is formed by D6Rs attached to each other forming a honeycomb with water molecules situated in the centre of the 6MR faces (Fig. 5.15). TGA shows two steps of weight loss, a first one for the water molecules and the other from the template (Fig. 5.16). Table 5.6 gives the unit cell and space group, the atomic coordinates and further details from SXRD refinement are provided in Appendix A, Tables A.13, A.14 and A.15.

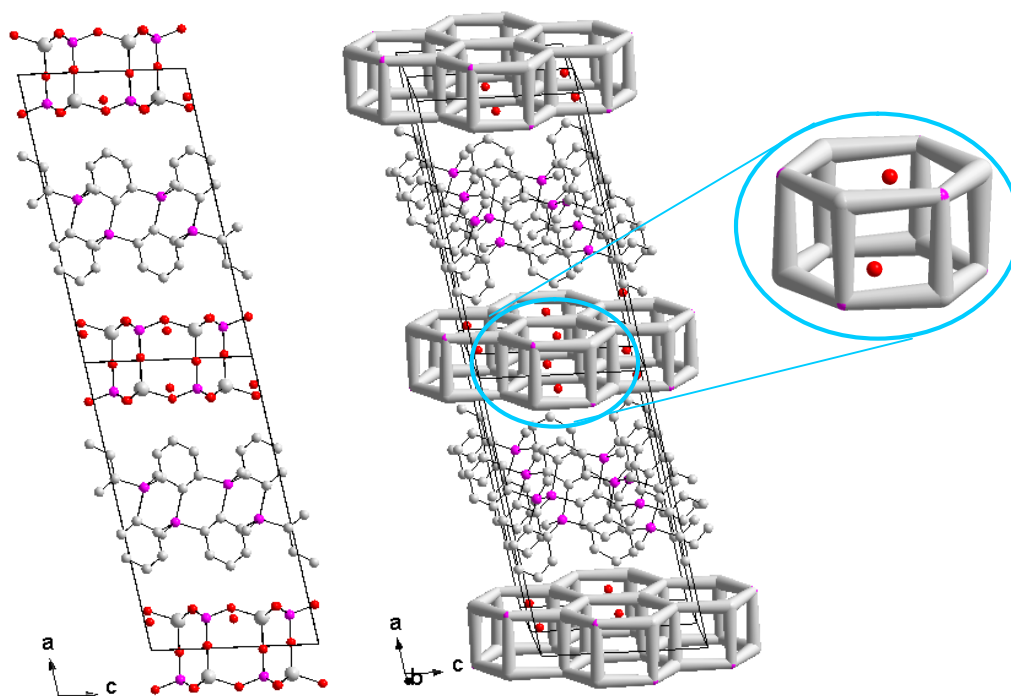


Fig. 5.15 (left) Structure of the layer phase solved from SXRD data showing the template in between the layers; (right) honey comb layers with a D6R detailed showing location of the water molecules (O atoms removed for clarity).

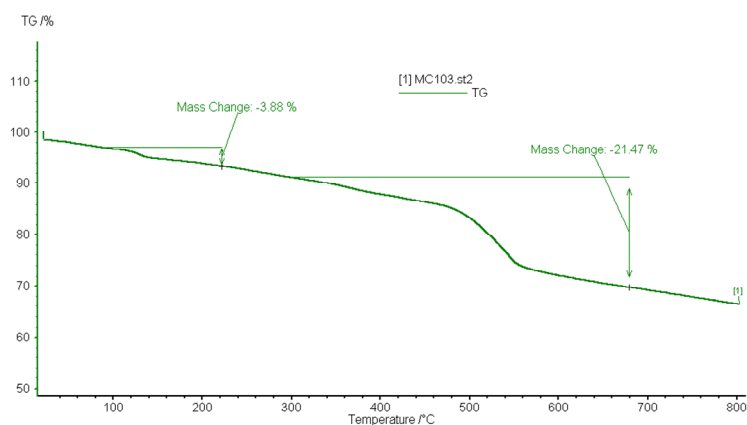


Fig. 5.16 TGA thermogram of novel layer phase.

Table 5.6 Unit cell parameters and space group obtained from the refinement of SXRD data.

| a (Å) | b (Å) | c (Å) | $\alpha = \gamma$ | β | Space Group |
|--------------|-------------|-------------|-------------------|--------------|-------------|
| 16.4854(600) | 5.3775(180) | 9.3237(340) | 90° | 100.809°(16) | P2(1)/c |

This novel structure differs from the typical structure of layered silicates (phyllosilicates). For phyllosilicates, octahedral sheets are intercalated between the infinite silicon tetrahedral sheets so there is no formation of D6Rs (Fig. 5.17 bottom right). In this case, the apical oxygen atoms of the tetrahedra form 6MRs with the hydroxyl group of the octahedral cations. In contrast, for the layered phase of this work the water molecules are in the same plane as the shared oxygen atoms from the tetrahedral making possible the formation of D6Rs. The figure 5.17 shows the differences between the novel layer phase and talc, a representative phyllosilicate mineral:

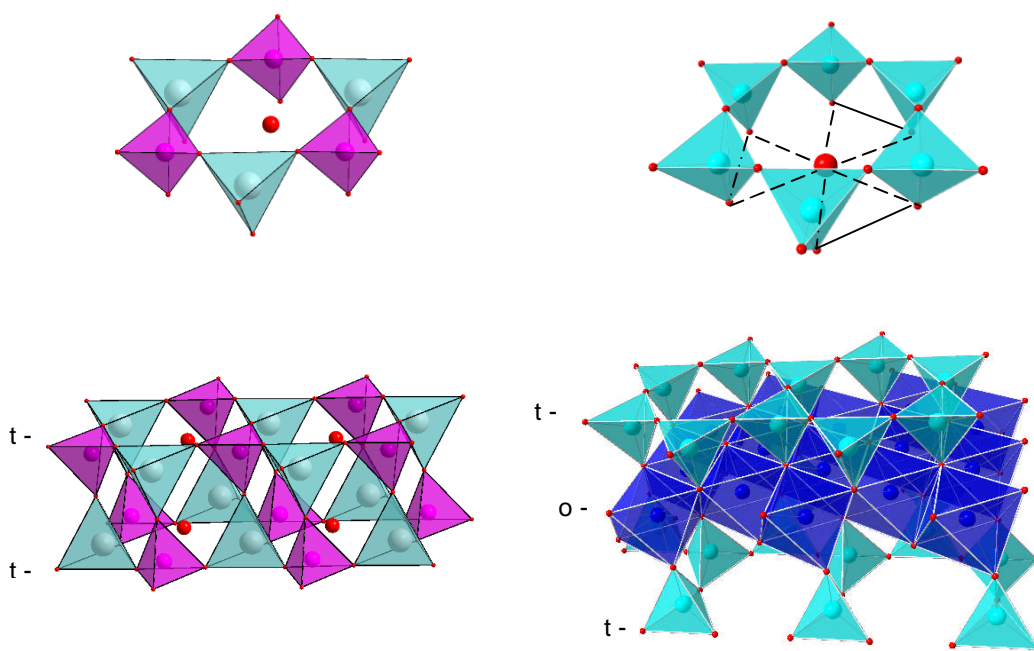


Fig. 5.17 Structures of the novel layer phase and talc (left and right, respectively); at the top, view of the 6MR showing the location of the extra framework oxygen and at the bottom the layer to layer attachment in tetrahedral to tetrahedral for the novel phase and tetrahedral-octahedral-tetrahedral layer for talc.

This novel topology has been reported as a part of hypothetical frameworks by R. Bell (Fig. 5.18).¹⁵ Bell *et al.* report that in contrast with the observation by Brunner and Meier¹⁶ that all very large pore solids appear to possess 3MRs in the framework “there is theoretically no evidence for any topological, geometric, or energetic constraint on framework density and pore size”. They show low-density and/or large-pore siliceous materials are possible with energies similar to those obtained experimentally. The aluminophosphate VFI structure for example, can be elongated hypothetically by the inclusion of strips of double six member rings (D6Rs) in the pore walls. These strips have

similarity with the experimental structure determined in this work. The key to obtain such materials therefore relates to the limitation in the organic species used as SDA rather than to their framework stability.

This experimental result indicates an area for further work: the combination of organic species to act cooperatively as structure directing agents (SDAs) to give novel phases.

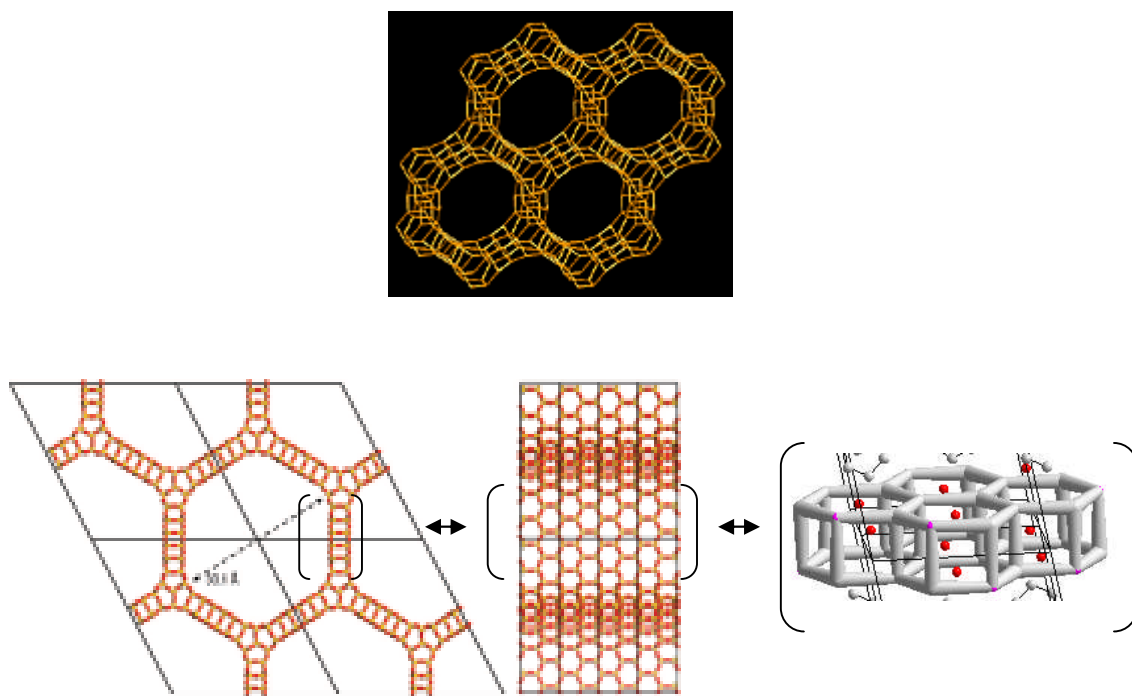


Fig. 5.18 The extension of VFI (top) by the layer phase computationally obtained from reference 13 (bottom left) and that it has been experimentally here obtained (bottom right).

5.5 Conclusions

As observed, hydrothermal synthesis using the combination of two templates leads to novel materials. Although it has not yet been possible to use three co-templates in synthesis, the use of tetraphenylphosphonium ions (TPP) has resulted in the crystallisation of a novel layered magnesiumaluminophosphate.

In many cases the two (or three) templates do not act cooperatively. TMA strongly favours MgAPO-20 (SOD), and K222 in the presence of many templates gives LTA, whereas the TEA/cyclam and TEA/K222 pairs do work in a combined fashion.

The change in the template, and consequent requirement for charge balancing, makes the synthesis of AlPOs problematical, when they do not have a ready mechanism to incorporate negative charge.

In cases where two templates are included together, it will be of interest to see the effect of changing the template ratio to understand the relative ‘templating activities’.

The initial step of modelling has helped rank potential templates and target specific co-templates. In the case of the TSC material, modelling showed that the organic species to template the large cage were not optimum. The synthesis of this material might be achievable if another organic template with a closer fit to the TSC cage could be found.

Ultimately a database of potential organic species for specific cages could permit the realisation of many of the hypothetical (but energetically feasible) structures that have been suggested in the literature.

-
1. A. Simmen, L. B. McCusker, C. Baerlocher, W. M. Meier, *Zeolites*, 1991, **11**, 654.
 2. L. Schreyeck, F. D'Agosto, J. Stumbe, P. Caullet, J. C. Mougénel, *Chem. Commun.*, 1997, 1241.
 3. M. G. O'Brien, A. M. Beale, C. R. A. Catlow, B. M. Weckhuysen, *J. Am. Chem. Soc.*, 2006, **128**, 11744.
 4. W. G. Song, J. F. Haw, J. B. Nicholas, C. S. Heneghan, *J. Am. Chem. Soc.*, 2000, **122**, 10726; W. G. Song, J. F. Haw, *J. Am. Chem. Soc.*, 2001, **123**, 4749.
 5. J. Chen, P. A. Wright, J. M. Thomas, S. Natarajan, L. Marchese, S. M. Bradley, G. Sankar, C. R. A. Catlow, P. L. Gai-Boyes, R. P. Townsend, C. M. Lok, *J. Phys. Chem.*, 1994, **98**, 10216.
 6. B. M. Lok, C. A. Messina, R. L. Patton, R. T. Gajek, T. R. Cannan, E. M. Flanigen, *J. Am. Chem. Soc.*, 1984, **106**, 6092.
 7. M. Stoecker, *Micropor. Mesopor. Mater.*, 1999, **29**, 3.
 8. J. S. Chen, J. M. Thomas, P. A. Wright, R. P. Townsend, *Catalysis Letters*, 1994, **28**, 241.
 9. R. Garcia Salas, *Synthesis and Characterisation of Aluminophosphate-based Materials Prepared with Nickel Complexes as Structure Directing Agents*, PhD Thesis, University of St Andrews, 2003.
 10. M. Castro, R. Garcia, S. J. Warrender, P. A. Wright, P. A. Cox, A. Fecant, C. Mellot-Draznieks, N. Bats, *Chem. Commun.*, 2007, 3470.

11. C. Klein, C. S. Hurlbut, '*Manual of mineralogy*', 21st edition, John Wiley & Sons, New York, 1993, 296.

12. RAXShape Guide, Draft Version, Rigaku, Jan 2007.

13. A. M. Walker, B. Slater, J. D. Gale, K. Wright, *Nature*, 2004, **3**, 715.

14. S. J. Warrender, *Structure Direction in the Formation of Zeolitic Materials*, PhD Thesis, University of St Andrews, 2007.

15. M. A. Zwijnenburegh, R. G. Bell, *Chem. Mater.*, 2008, **20**, 3008.

16. G. O. Brunner, M. W. Meier, *Nature*, 1989, **337**, 146.

Chapter 6: STA-2

6.1 Introduction

The microporous aluminophosphate STA-2 was first reported in 1997¹ and further studied in 2003.² Like STA-7 (SAV) and STA-14 (KFI), the aluminophosphate STA-2 (SAT) is known to be a stable small pore solid, containing two types of cages: one elongated and the other smaller, denoted as a cancrinite cage. Its properties for adsorption can only be attributed to the elongated cages. In this project the original aim was to prepare the material in both AIPO and SAPO forms and compare the CO₂ uptake.

The template previously used in the synthesis of STA-2 (bisquinuclidinium-butane, [(C₇H₁₃N)(CH₂)₄(NC₇H₁₃)](OH)₂, QuinC4) is prepared from an expensive reagent (quinuclidine) and tends to give as an impurity a material of similar topology, AIPO-56 (AFX). In order to predict new templates for STA-2, molecular modelling was applied in collaboration with A. Fecant at IFP-Lyon. As a result a diquaternary salt using diazabicyclooctane (DABCO_C4) was suggested as a suitable and much cheaper alternative. This template, as well as DABCO_C5 and QuinC4, was synthesised and applied in hydrothermal syntheses to give a range of solid products, including the AIPO

form of STA-2 as a pure phase from DABCO_C4. Table 6.1 gives the structural formulae of these organic species and their abbreviation in this thesis.

Literature describes the use of DABCO_C4 for zeolite synthesis to produce SSZ-16 (AFX).³ In addition, the same material can be obtained using QuinC4 as a template.⁴ Although there are no examples of the application of DABCO_C4 in the zeotype regime, its similar templating behaviour in the zeolite system to that of QuinC4 made it a promising alternative for the synthesis of STA-2. The use of modelling to design a cheaper template has been successfully applied already in the synthesis of the zeolite ZSM-18.⁵ Therefore the results of this thesis corroborate the positive impact of molecular modelling and a rational design of the synthesis.

Furthermore, previous studies suggested that AlPO STA-2 can be obtained in the absence of charge balancing fluoride anions (F^-), but structural details have not been reported.² This chapter covers the structural characterisation of AlPO STA-2 in the as-prepared form by refinement of the structure against powder data collected at the ESRF synchrotron in Grenoble and MAS NMR in combination with solution NMR giving information about the charge balancing by hydroxide groups attached to the structure and the protonation form of the template.

The following figures introduce the main structural characteristics of STA-2. This material is part of the so called ABC family which can be considered as made up of flat 6-membered rings (6MRs) that are parallel to a hexagonal *ab* plane. These 6-rings may have their centres at (0,0), (1/3, 1/3), or (2/3, 2/3) positions in the *ab* plane, and link to other 6-rings above and below them along the *c* axis which have also their centres at (0,0), (1/3, 1/3) or (2/3, 2/3), denoted as A, B or C position respectively. Therefore these structures can be described in terms of repeating stacking sequences; for example cancrinite (CAN) has the sequence AB, chabazite (CHA) the sequence AABBC and AlPO-56 (AFX) the sequence AABBCB. Using this nomenclature, the framework of STA-2 has the sequence ABBCBCCACAAB, the most complex of the family (Fig. 6.1 a).

⁶ The cavities of STA-2 are arranged in columns parallel to the *c* axis and it possesses

four different tetrahedral positions, two for Al (Al1 and Al2) and two for P (P1 and P2) (Fig. 6.1 b and c respectively).

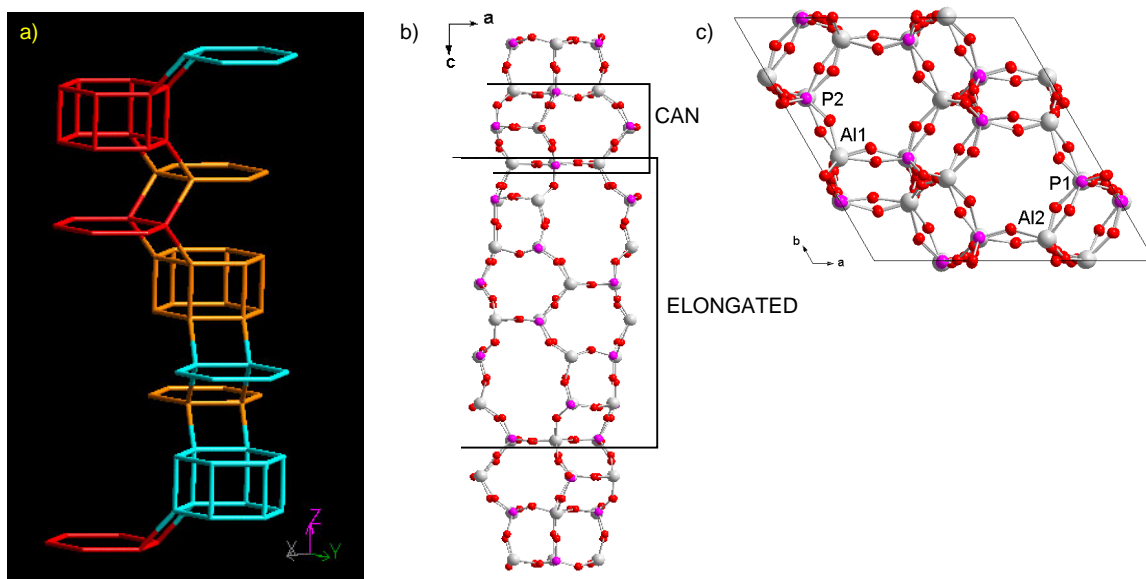
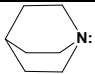
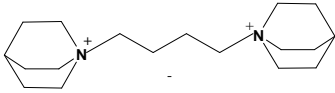
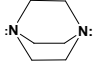
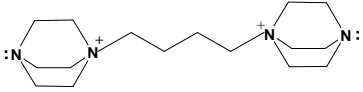
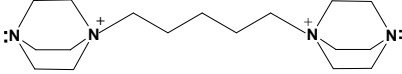


Fig. 6.1 (a) ABC stacking of the 6-ring sequence in STA-2 (A is red, B is blue and C is yellow to give ABBCBCCACAAB sequence, diagram taken from *Atlas of Zeolites Structures*⁷). (b) Column of STA-2 framework showing the two types of cages (cancrinite (CAN) and elongated) linked along c axis via D6R (left). (c) The unit cell with a pair of joining columns showing the four tetrahedral positions.

Table 6.1 Organic molecules applied in this chapter and their abbreviations.

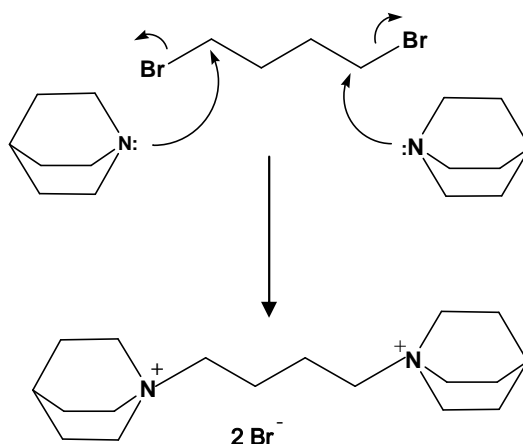
| Organic Species | Chemical Formula | Abbreviation |
|---------------------------------|--|--------------|
| Quinuclidine |  | - |
| Bisquinuclidinium-butane |  | QuinC4 |
| 1,4-Diazabicyclo (2,2,2) octane |  | DABCO |
| Bisdiazabicyclooctane-butane |  | DABCO_C4 |
| Bisdiazabicyclooctane-pentane |  | DABCO_C5 |

6.2 Experimental

Synthesis of Templates

The templates used in this chapter (QuinC4, DABCO_C4 and DABCO_C5) are prepared by routes that follow the Menshutkin reaction mechanism.⁸ This reaction is of S_N2 type (nucleophilic substitution via bimolecular reaction).

The reaction takes place between the amine (diquinuclidine or DABCO) and the dibromoalkane to form the quaternary diammonium salt as shown in the scheme 6.1:



Scheme 6.1 Menshutkin reaction showing the formation of 1,4-diquinuclidinium butane dibromide.

The synthesis of QuinC4 and DABCO_C4 was straightforward using reported methods.^{6,9} The experiments were performed using a 1:2 molar ratio of dibromoalkane and amine, refluxing at 80 °C in ethanol for 24 and 5 hours, respectively. Once cool, the excess of ethanol was removed on a rotary evaporator and the resulting residue allowed to crystallise overnight under refrigeration to give a white solid. That was washed with acetone, cold ethyl acetate and acetonitrile. The product was allowed to dry at room temperature in air. The typical yield of both templates is 97%. For the case of DABCO_C5, a synthetic procedure was not found. The work of Abbiss and Mann concerning the reaction of DABCO with dibromoalkanes was used as a general procedure for DABCO_C5.¹⁰ In this way, dibromopentane and DABCO were used in a 1:2 molar ratio. DABCO was dissolved in dry MeOH (13.0 ml) and the dibromopentane added

drop-wise under stirring, ensuring the temperature remained at 50 °C. This solution was allowed to stir at room temperature for 2 hours. Any unreacted amine was washed away with cold diethylether using a separatory funnel and the product was decanted as a yellow pale oil. The right mixture of solvents to crystallise the product was found experimentally by a combination of solvents. By doing that, the oil turned milky and eventually crystallised under refrigerated conditions to form a white solid with 40% yield (the isolation of the template from solvents is important to eliminate any possible complications during the hydrothermal treatment).

All the products were characterised by ^1H NMR, ^{13}C NMR (Fig. 6.2, 6.3 and Table 6.2) and CHN analysis (Table 6.3). The peaks are assigned as shown below in figure 6.2 (the signal 1.3 is only for QuinC4 which has an apical carbon instead of nitrogen):

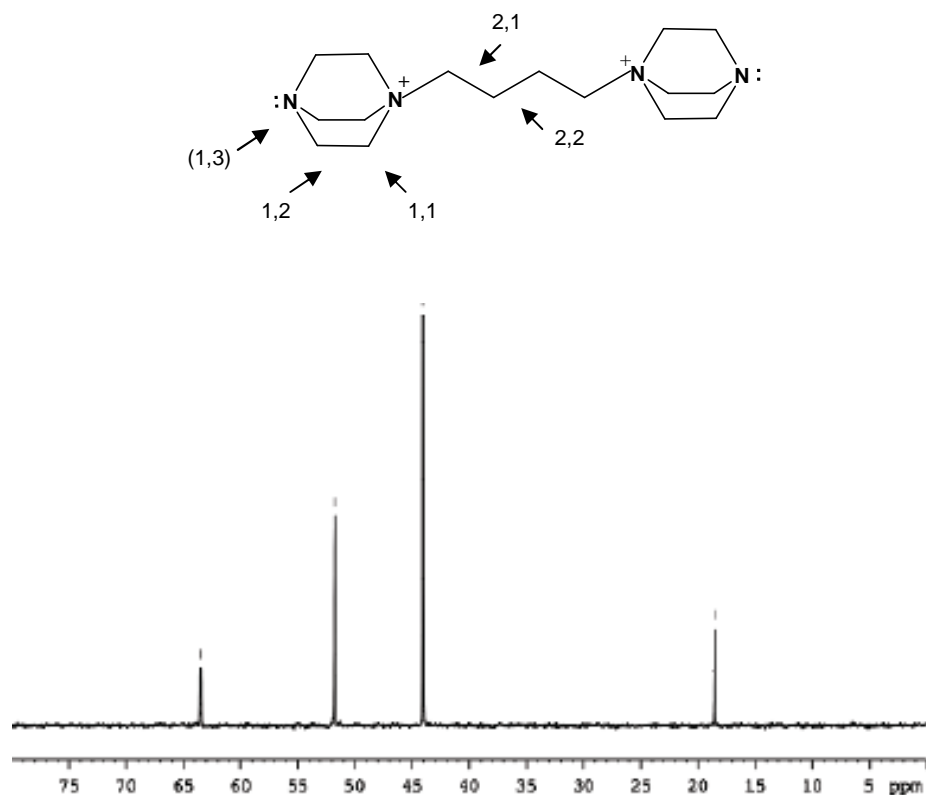


Fig. 6.2 ^{13}C NMR spectrum of DABCO_C4.

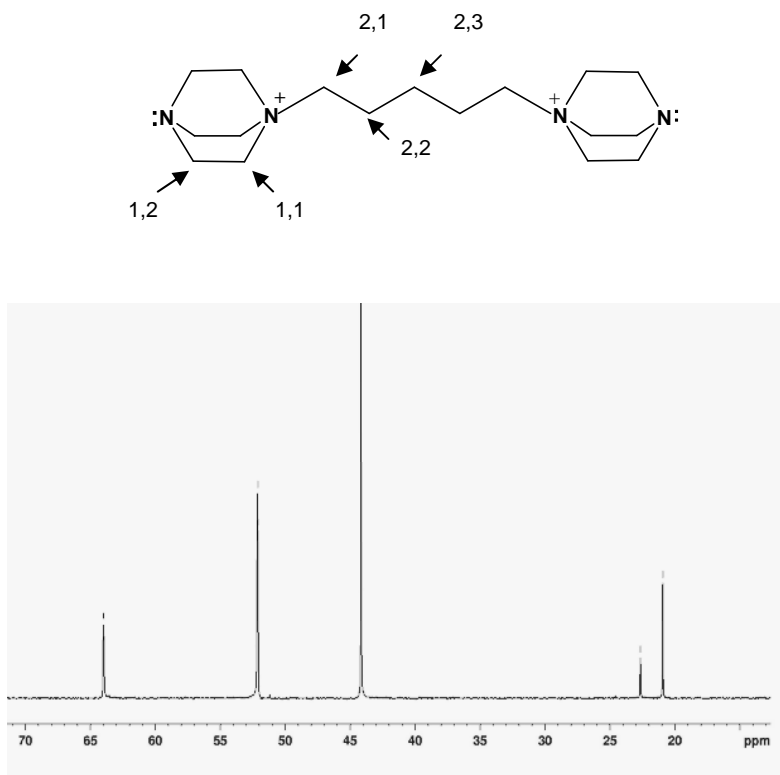


Fig. 6.3 ^{13}C NMR spectrum of DABCO_C5 sample.

Table 6.2 ^{13}C NMR chemical shift (δ) summary for the templates applied in this section.

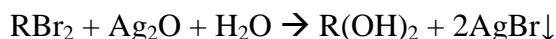
| | δ (ppm) | | | | | |
|----------|----------------|-------|-------|-------|-------|-------|
| Molecule | 1,1 | 1,2 | 1,3 | 2,1 | 2,2 | 2,3 |
| QuinC4 | 54.68 | 23.19 | 18.95 | 63.08 | 18.9 | |
| DABCO_C4 | 52.15 | 44.11 | | 63.29 | 18.53 | |
| DABCO_C5 | 52.1 | 44.11 | | 63.94 | 20.87 | 22.62 |

Table 6.3 Results of microanalysis of the templates applied here, to verify their purity.

| | %C | | %H | | %N | |
|----------|-----------|--------|-----------|--------|-----------|--------|
| Molecule | Predicted | Actual | Predicted | Actual | Predicted | Actual |
| QuinC4 | 49.34 | 45.38 | 7.77 | 7.98 | 6.40 | 5.33 |
| DABCO_C4 | 43.65 | 41.18 | 7.27 | 7.69 | 12.73 | 12.03 |
| DABCO_C5 | 44.95 | 42.57 | 7.49 | 7.51 | 12.34 | 11.91 |

Before being used, each bromide salt was converted to the hydroxide form with silver (I) oxide. A basic form of the template is required to increase the initial pH of the gel from 2 up to 7, the optimum pH for the synthesis of aluminophosphates. The typical procedure is

to mix the template with silver (I) oxide in molar ratio 1:1.2 in water overnight, covering the beaker with aluminium foil as silver halides are photosensitive. The black slurry is filtered and washed with distilled water until the filtrate containing the template in the hydroxide form has a neutral pH. The filtrate is then concentrated using a rotary evaporator into a form for the use in the aluminophosphate synthesis. The chemical equation that describes this conversion is as follows:



Preparation of gels and hydrothermal synthesis

The template is added up to pH 7, the gels were heated at 190 °C for two or seven days for AlPO and SAPO gels, respectively. The seeds of AlPO or MgAPO from previous synthesis were added at 0.1% of the water amount used in the gel (pre-digested for 24 h at 100 °C in an aqueous solution of the template).

Synchrotron data

High resolution X-ray powder diffraction data were collected on station ID-31 of the ESRF synchrotron at Grenoble by Irena Margiolaki, using radiation of wavelength 0.79989667 Å, on a sample of the as-prepared AlPO STA-2 (DABCO_C4).

Solid-State NMR data

MAS NMR spectra were collected at the EPSRC solid-state NMR Facility in Durham University by Dr David Apperley on two samples of AlPO STA-2 in the as-prepared form synthesised using QuinC4 (**1**) and DABCO_C4 (**2**) as templates, respectively. Experiments were performed on a Varian VNMRs 400 spectrometer, using a 4 mm probe for all except for the case of ^{15}N that used a 6 mm probe. Table 6.4 summarises the conditions of the experiments.

The NMR standard, at 0 ppm, was defined as the shift for 1M aqueous AlCl_3 , 85% H_3PO_4 and nitromethane, for ^{27}Al , ^{31}P and ^{15}N respectively.

Solution-State ^{14}N and ^1H - ^{15}N HMQC NMR data

^{14}N NMR and ^1H - ^{15}N HMQC (Hetero Multiple Quantum Correlation) spectra were collected at St Andrews University by Dr Tomas Lebl on two samples of the bromide DABCO_C4 salt dissolved in D_2O at neutral (**3**), acidic (**4**) and basic (**5**) pH.

^{14}N and ^1H - ^{15}N HMQC experiments were performed on Bruker AVANCE 400 and 500 spectrometers respectively. Table 6.5 summarises the conditions of experiments: NH_3 was chosen as a reference for the spectra.

- Sample preparation in acid solution was performed by dissolving 200 mg of the bromide salt of DABCO_C4 on 0.45 ml of D_2O and adding 80 μL of HCl (36% in weight) corresponding to two equivalents of H^+ .
- Sample preparation in basic solution was performed by dissolving 100 mg of the bromide salt of DABCO_C4 in 0.45 ml of D_2O and adding 11.2 mg of NaOH corresponding to two equivalents of OH^- .

DFT Calculations on DABCO_C4

DFT calculations (B3LYP hybrid functional and 6-31G+ (d,p) level of theory) were performed by Diego Carnevale to evaluate the influence of the three possible nitrogen environments for DABCO_C4 (NR_4^+ , $:\text{NR}_3$ and NR_3H^+) on the chemical shift and quadrupolar constant (C_Q). The calculation of the isotropic magnetic shieldings and the C_Q values were obtained with the CSGT method (Continuous Set of Gauge Transformation)¹¹ and NH_3 was chosen as reference shielding.

Table 6.4 Experimental parameters for ^{27}Al , ^{31}P , ^{13}C and ^{15}N MAS NMR spectra on samples **1** and **2**, (DP = Direct Polarisation, CP = Cross Polarisation, DD = Direct Detected, ID = Indirect Detected).

| Sample | Freq (MHz) | Acq time (ms) | Relaxation delay (s) | Polaris | Contact time (ms) | Pulse time (μs) | Spin rate (kHz) | |
|---------------------|---------------|---------------------|----------------------------|---------|-------------------------|-----------------------|-----------------------|-----|
| ²⁷ Al | | | | | | | | |
| 1 | 104.199 | 10.0 | 0.1 | DP | - | 1.0 | 12 | |
| 2 | 104.199 | 10.0 | 0.1 | DP | - | 1.0 | 14 | |
| ²⁷ Al MQ | | | | | | | | |
| 1 | 2 | 104.199 | 5.0 | 0.1 | DD (F2) ID (F1) | 3.8 and 1.2 | 14 | |
| ³¹ P | | | | | | | | |
| 1 | 2 | 161.876 | 10.0 | 1.0 | CP | 1.0 | - | 12 |
| 1 | 2 | 161.876 | 20.0 | 30.0 | DP | - | 4.0 | 12 |
| ¹³ C | | | | | | | | |
| 1 | 2 | 100.562 | 40.0 | 2.0 | CP | 1.0 | - | 6.8 |
| ¹⁵ N | | | | | | | | |
| 1 | 2 | 40.527 | 40.0 | 2.0 | CP | 5.0 | - | 6.8 |

Table 6.5 Experimental parameters for ^{14}N and ^1H - ^{15}N HMQC solution NMR spectra on samples **3**, **4** and **5**. Np_t2 and Np_t1 are the number of points acquired in the indirect and direct dimension respectively.

| Sample | | | Freq (MHz) | Acq time (s) | Np_t2 | Np_t1 | Relaxation delay (s) | Pulse (μs) |
|--------------------------------------|---|---|---------------|-----------------|-------|-------|-------------------------|---------------|
| ¹⁴ N | | | | | | | | |
| 3 | 4 | 5 | 28.914 | 0.10 | 4096 | - | 0.19 | 14.2 |
| ¹ H- ¹⁵ N HMQC | | | | | | | | |
| 3 | | | 50.66 | 0.46 | 4096 | 128 | 1.58 | 10.3 |
| 4 | | | 50.66 | 0.51 | 4096 | 225 | 1.57 | 14.0 |
| 5 | | | 50.66 | 0.51 | 4096 | 225 | 1.57 | 10.5 |

6.3 Results & Discussion

6.3.1 Modelling

As mentioned in the Introduction, molecular modelling was used to design an alternative template for STA-2. In addition, the precursor DABCO has nitrogen atoms in the apical positions instead of carbon atoms which could influence charge balance and even the phase that crystallises.

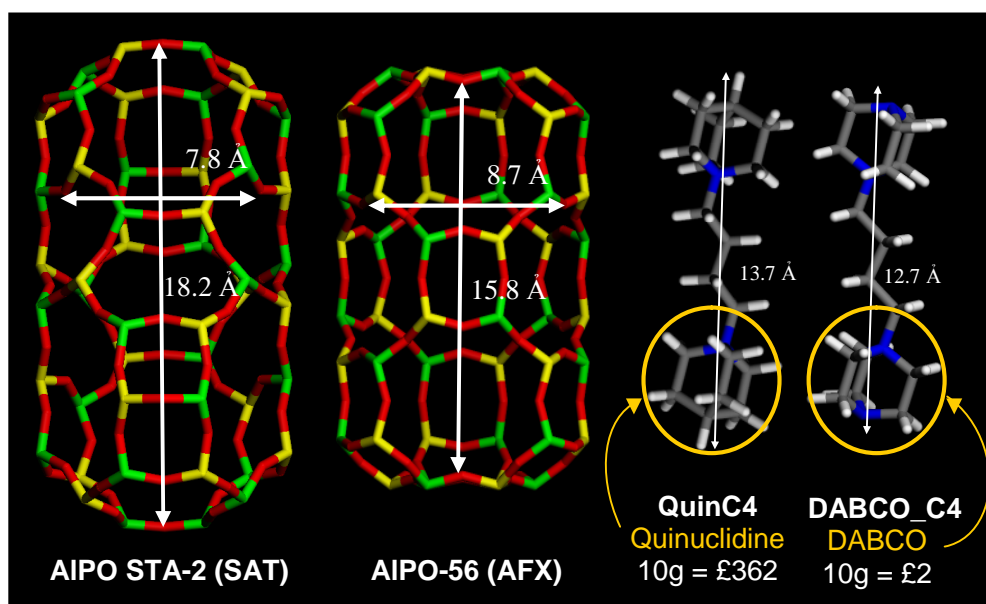


Fig. 6.4 Diagram showing the cage similarities between SAT and AFX structures and the similarities between the formal template for STA-2 QuinC4 and the designed DABCO_C4.

The same modelling method and parameters used in studies of templating of STA-7 and STA-14 were applied here. The AIPO STA-2 and -56 frameworks and a series of templates based in DABCO and quinuclidine with different alkane chain length (from C3 up to C6) were modelled in the cages of both structures and their adsorption energies calculated. The DABCO templates were modelled with the apical nitrogen atoms unprotonated (experimentally it is observed that DABCO templates are non-protonated, as described in the characterisation of AIPO STA-2 section 6.3.3). The results are summarised in the following graphs (Fig. 6.5).

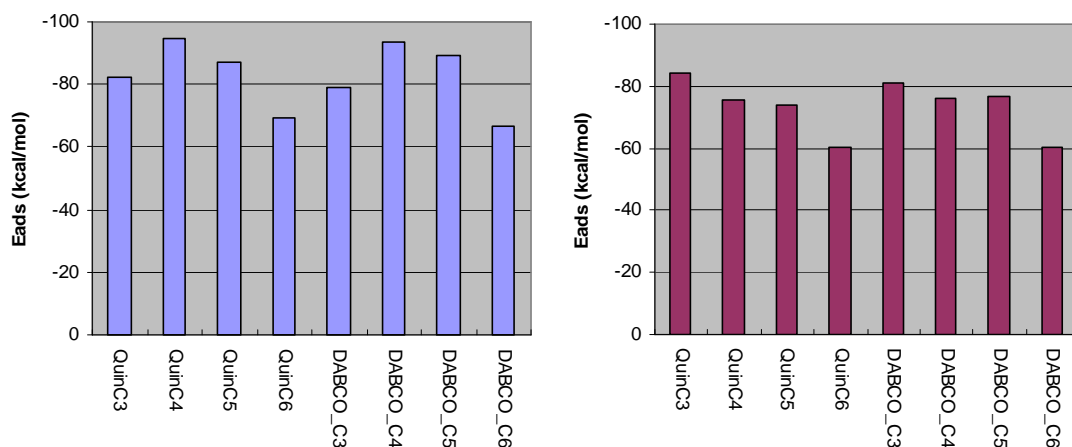


Fig. 6.5 Adsorption energies of templates based in quinuclidinium and DABCO in AlPO STA-2 (left) and AlPO-56 (right).

Prior to a discussion of the results it is important to take into account that total enthalpy values cannot be directly compared between structures because each one has a large structure-dependent value.

The modelling results for QuinCn and the novel DABCO_Cn series are very similar in both structures. Therefore, it should be possible to replace the QuinCn templates by the DABCO_Cn analogues.

These results in the QuinCn series for STA-2 are in agreement with previous experimental results performed in MgAPO gels:⁶ QuinC4 and QuinC5 form STA-2 with MAPO-56 or layered phase as impurities respectively; QuinC3 leads to MAPO-17 (ERI), and QuinC6 to MgAPO-36 (ATS) or MgAPO-5 (AFI). In the case of AlPO-56, modelling shows QuinC3 as the most favourable template followed by QuinC4 and QuinC5. These predictions contrast with experimental results where only QuinC4 forms MgAPO-56, whereas QuinC3 has a tendency to form MgAPO-17, which has an even shorter cage than MgAPO-56.

These families of templates are long and quite flexible. Another parameter that could give further information applicable to find the optimum template against competition is the torsion energy. The torsion energy estimates the adaptability of the organic molecules

within the structure. In this case, results can be compared from one structure to the other because this value is only related to the organic species (Fig. 6.6).

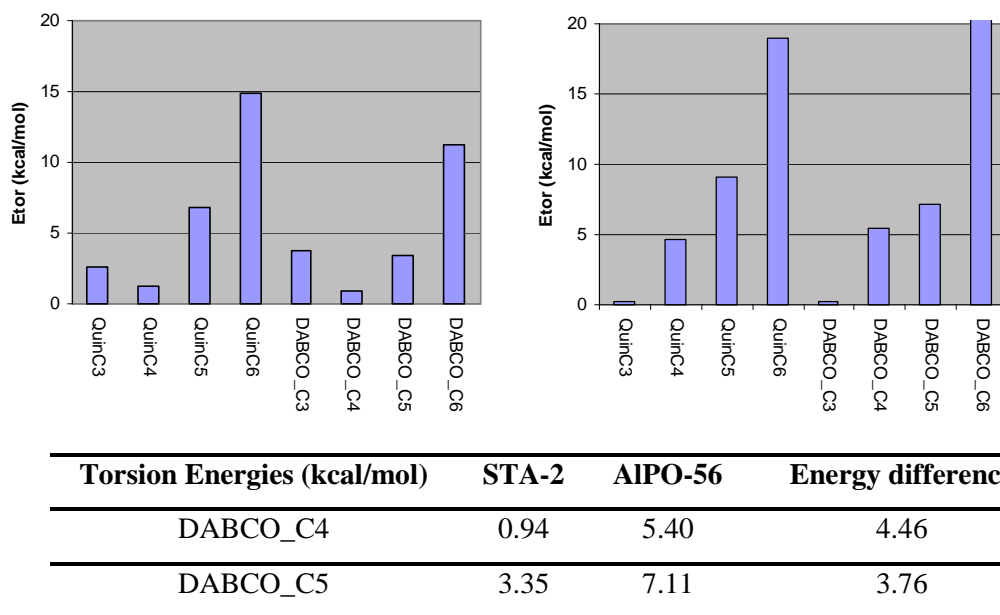


Fig. 6.6 Torsion energies of QuinCn and DABCO_Cn series for STA-2 (left) and -56 (right). Table shows the values for the more promising novel templates.

From the data presented in Fig. 6.6, the torsion energies of QuinC4 and DABCO_C4 are low in the STA-2 structure, suggesting that the molecules do not have to distort significantly to fit into the cage. For the AIPO-56 structure these templates shows higher energy values, making them less favourable for this structure. The C5 analogues, when compared with the C4, possess higher values in both structures. Therefore, if the torsion energy is an important parameter, the C4 analogues of QuinC4 and DABCO_C4 are the favoured templates for STA-2.

Figures 6.7 and 6.8 show the fit between the templates within the STA-2 and AIPO-56 cages, respectively. As observed from the results, when the template is too short or too large the torsion energy makes them unfavourable, and it is easy to see for example, how the C6 templates need to twist in order to fit into the cage.

From this information, the most promising novel templates for this study are DABCO_C4 and C5, and particularly DABCO_C4. Although they are unlikely to avoid

the formation of -56 as an impurity because both series of templates have similar trends in their adsorption energies, at least they could replace their more expensive analogues.

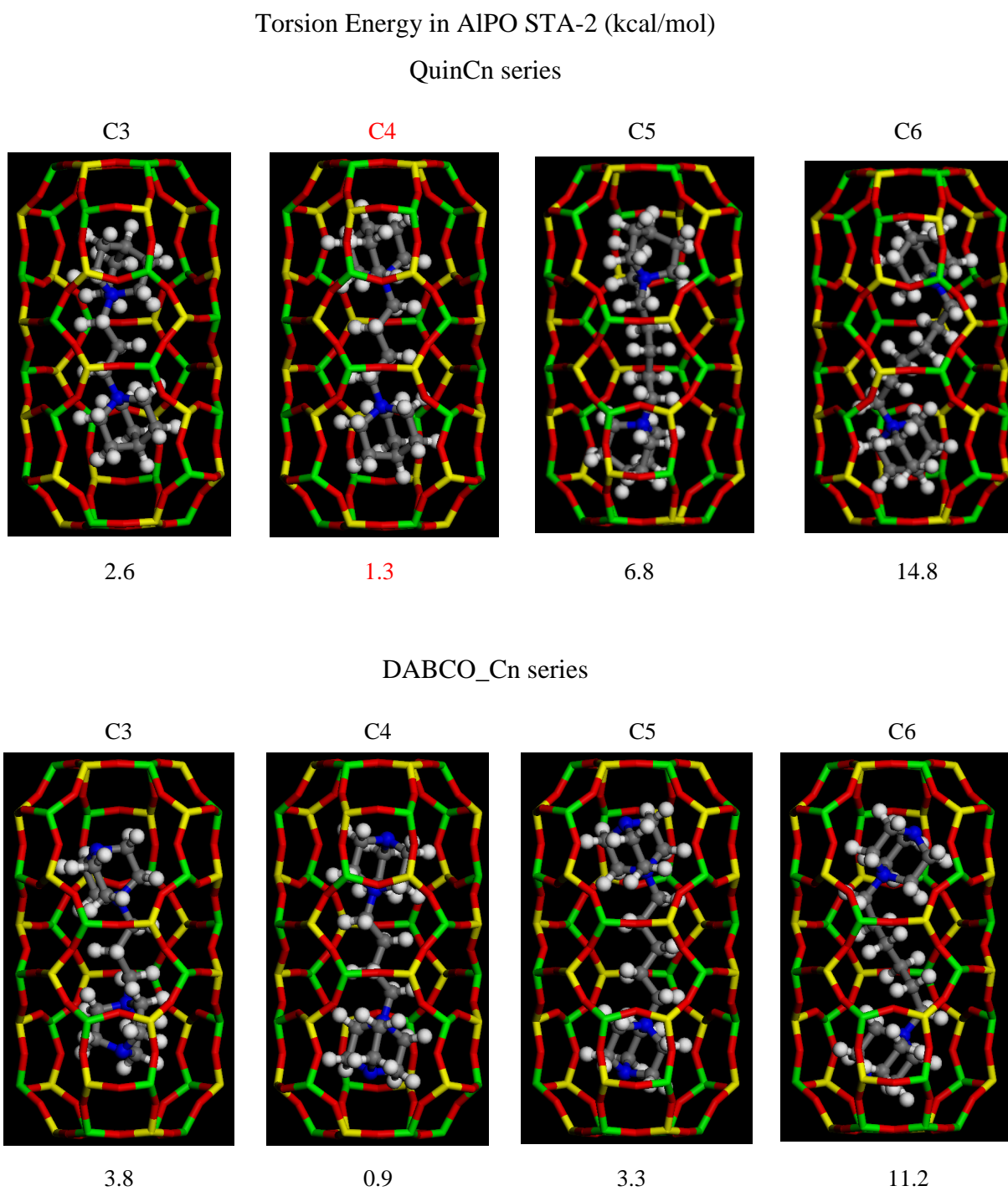


Fig. 6.7 Visualisation of the torsion energies for QuinCn and DABCO_Cn series in AlPO STA-2.

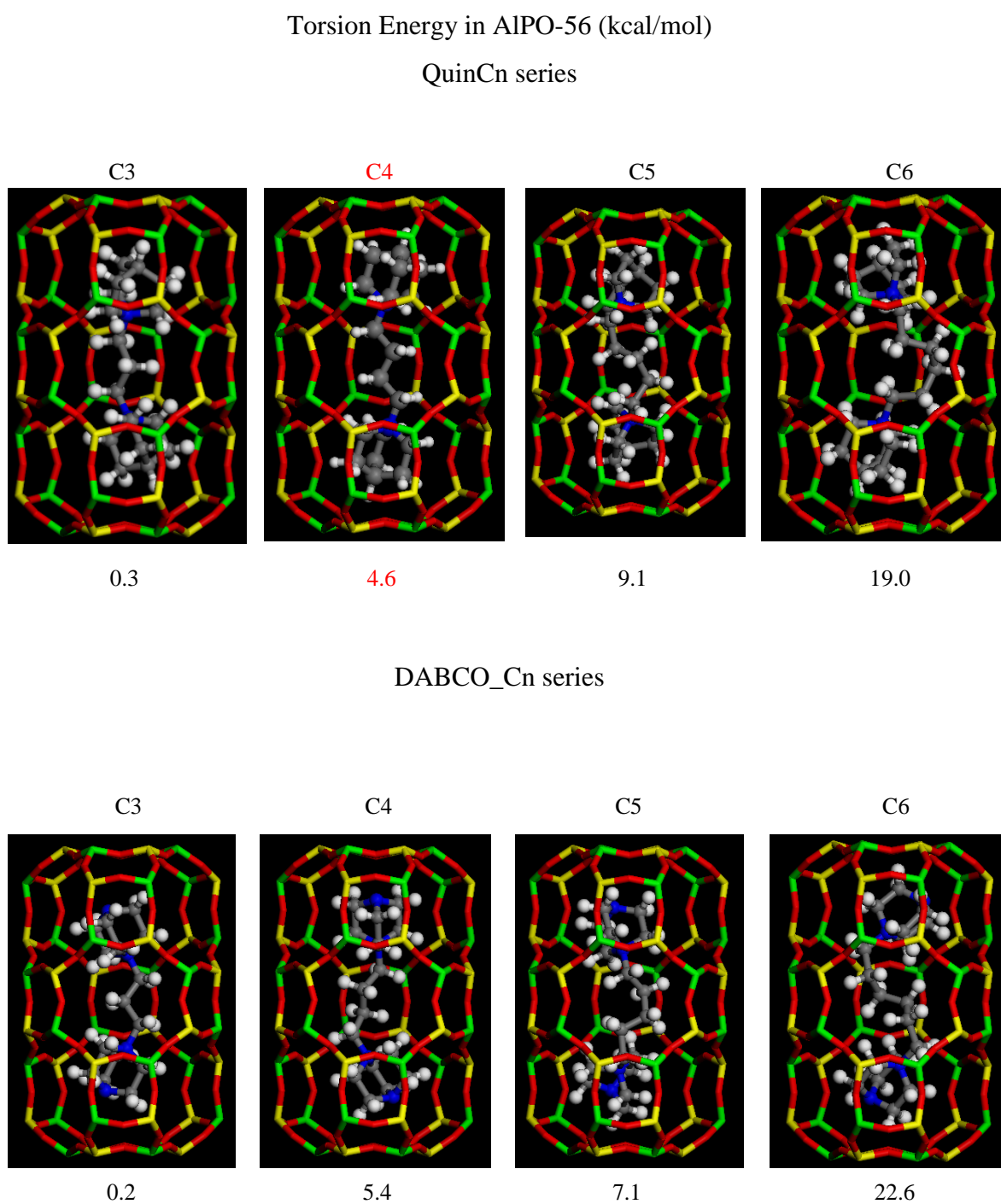


Fig. 6.8 Visualisation of the torsion energies for QuinCn and DABCO_Cn series in AlPO-56.

6.3.2 Synthesis

The new templates suggested by modelling (DABCO_C4 and C5) were used in hydrothermal synthesis and compared with QuinC4 (Table 6.6).

Table 6.6 Summary of synthesis using DABCO_C4, DABCO_C5 and QuinC4. The most promising products for further characterisation are denoted in bold. (Asterisks denotes the use of seeds).

| Template (R) | Gel Composition | | Product (by XRD) |
|-----------------|---------------------------------|---|---|
| QuinC4 | AlPO | HF/R = 0.8 | STA-2 main phase |
| | | no HF | STA-2 |
| | MgAPO | Mg/P = 0.1 | STA-2 poor crystalline |
| | | Mg/P = 0.2 | MAPO-56 |
| | SAPO | Colloidal SiO ₂ : Si/Al = 0.2* | STA-2, SAPO-56 and extra phase |
| DABCO_C4 | AlPO | no HF* | STA-2 |
| | | no HF and no Seeding | STA-2 |
| | MgAPO | Mg/P = 0.2* | STA-2 and MAPO-56 |
| | SAPO | Colloidal SiO ₂ : Si/Al = 0.2* | STA-2, MAPO-56, extra phase |
| DABCO_C5 | AlPO | HF/R = 0.8 | Layer phase |
| | | HF/R = 0.4 | “ |
| | | No HF | “ |
| | MgAPO | Mg/P = 0.1* | STA-2, layer phase |
| | | Mg/P = 0.2* | STA-2 and -56 |
| | SAPO | Colloidal SiO ₂ : Si/Al = 0.2* | SAPO STA-2 and -56 |
| | | Fumed SiO ₂ : Si/Al = 0.2* | SAPO-56 |
| | | Si/Al = 0.3* | SAPO-56 |
| | MgAPSO Fumed SiO ₂ : | | MgAPSO-56 |
| | | 0.05 Mg:0.15 Si* | |
| | Fumed SiO ₂ : | | MgAPSO-56 |
| | | 0.20 Mg:0.30 Si | |

The results given in Table 6.6 can be summarised. (i) The use of DABCO_C4 formed pure AIPO STA-2, (ii) the introduction of SiO₂ gave a variety of results for the three templates and (iii) DABCO_C5 as template gave a complex range of products.

AIPO synthesis using DABCO_C4

DABCO_C4 produces pure AIPO STA-2 with and without seeding in non-fluoride gels. The good quality of the sample gives high quality synchrotron data to elucidate structural details. The XRD pattern is given in this section (Fig. 6.9) and SEM in section 6.3.3.

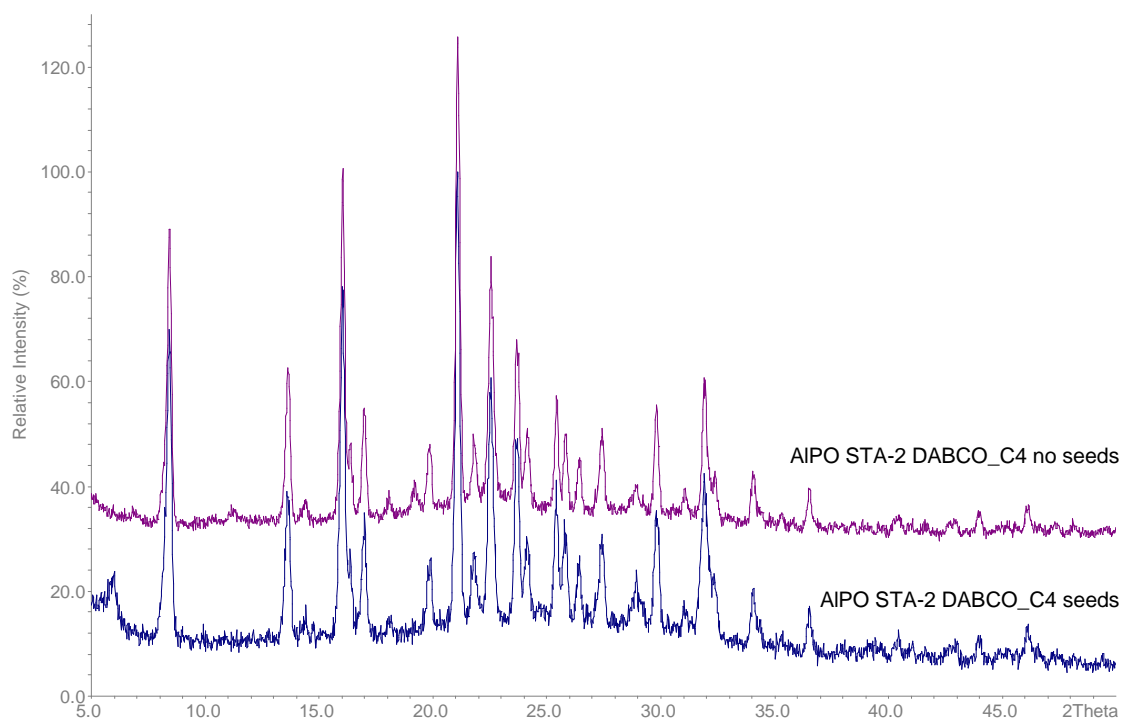


Fig. 6.9 XRD patterns of AIPO STA-2 (DABCO_C4) with and without seeds (blue and purple, respectively).

SAPO synthesis using DABCO_C4 and QuinC4

The inclusion of silicon atom into the AIPO framework using DABCO_C4 and QuinC4 was examined. The most promising sample was obtained using QuinC4, seeds of AIPO STA-2 and colloidal silica as the silicon source. The XRD pattern is given here (Fig. 6.10) and further structure characterisation is provided in section 6.3.4.

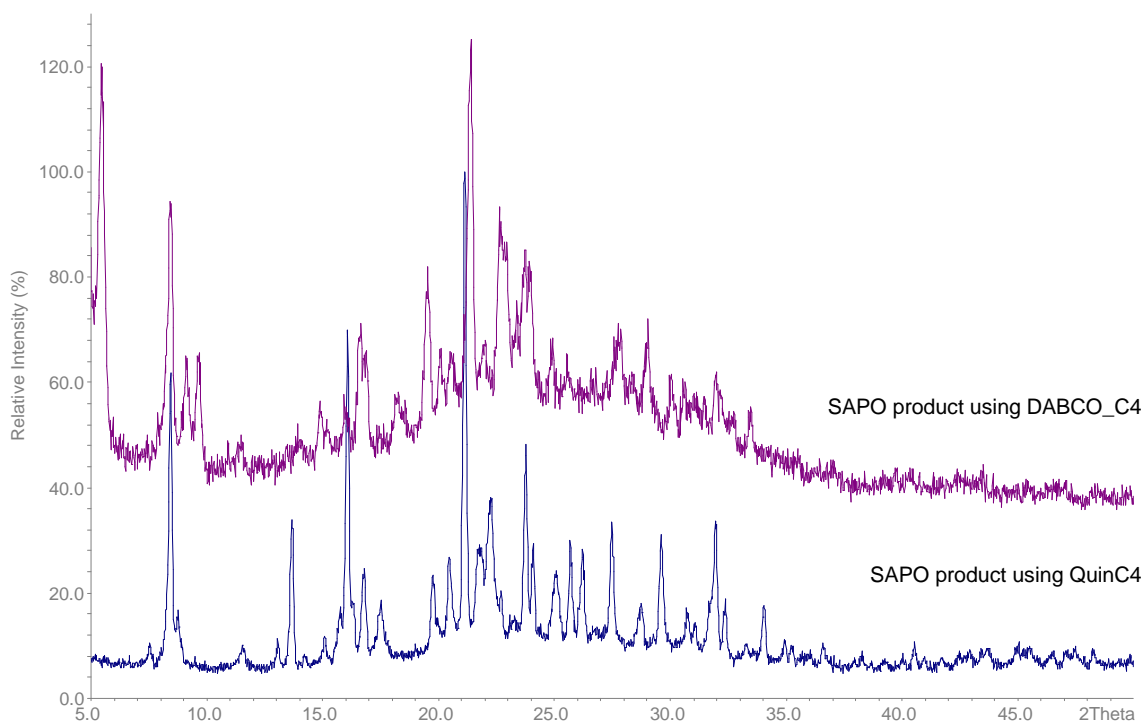


Fig. 6.10 XRD patterns of SAPO synthesis with DABCO_C4 and QuinC4 (purple and blue, respectively).

DABCO_C5 in synthesis

The DABCO_C5 system is very complex and the change in the gel composition strongly influences the phase formation. DABCO_C5 in the AlPO regime (with or without the addition of fluoride ions) forms a layer phase. The amount of this phase decreases upon adding magnesium into the gel, when Mg/P reaches 0.2 the layer phase disappears and STA-2 and MgAPO-56 are formed as two discrete phases with octahedral and hexagonal plate morphologies respectively (Fig. 6.11 and 6.12 shows the XRD patterns and the SEM images respectively). Probably the structure directing role of DABCO_C5 is stronger in magnesium-containing gels as charge-balancing becomes important.

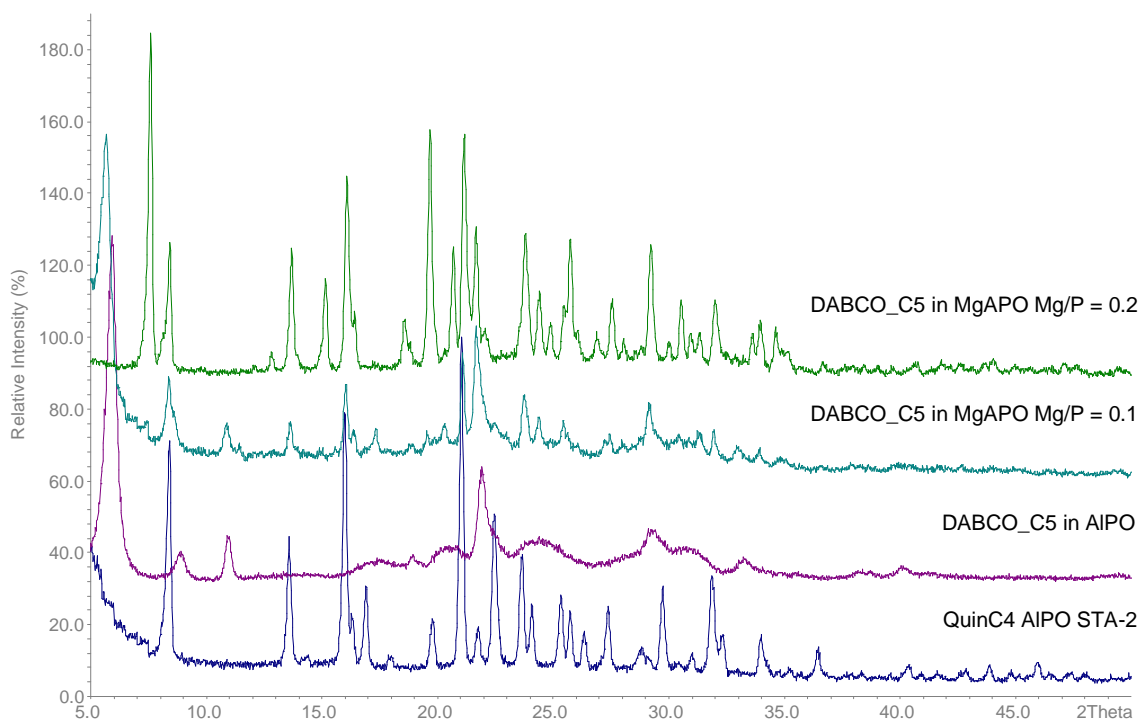


Fig. 6.11 XRD patterns of the products using DABCO_C5 in AlPO and MgAPO gels; for comparison XRD pattern of AlPO STA-2 using QuinC4.

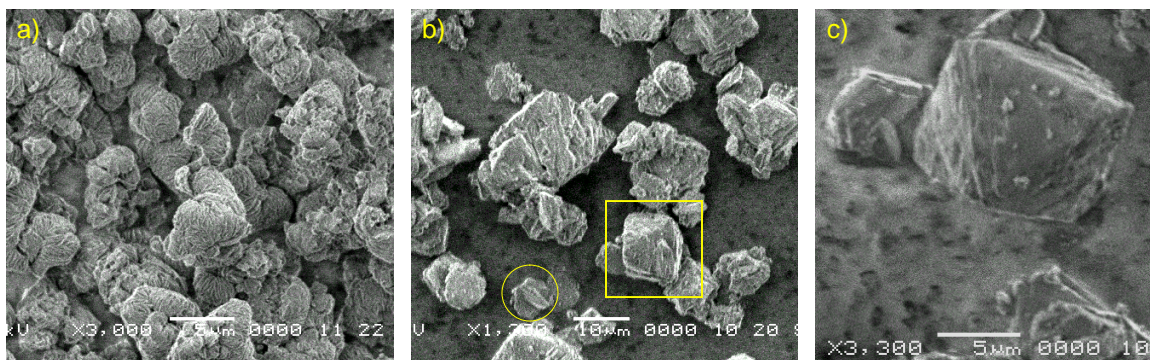


Fig. 6.12 SEM image of DABCO_C5 products in AlPO (a) and MgAPO Mg/P = 0.2 gels (b and c).

DABCO_C5 in the SAPO regime forms a mixture of STA-2 and SAPO-56 using colloidal silica as silicon source, whereas using fumed silica tends to give SAPO-56 (Fig. 6.13). This tendency remains when magnesium is incorporated into the gel but also an extra phase appears. In fact, SEM of this sample shows very well defined octahedral morphology for STA-2 which appears in small fraction as well as the flat planes of -56 and the new phase appears as main phase with plate like morphology (Fig 6.14).

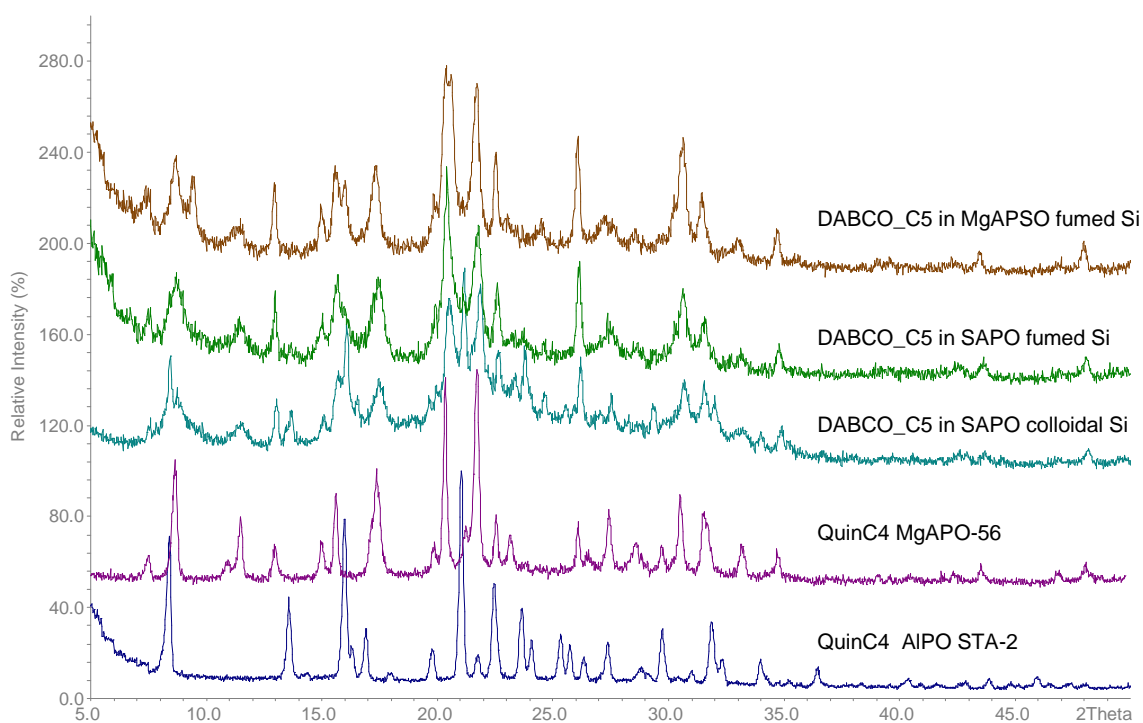


Fig. 6.13 XRD patterns of the products using DABCO_C5 in SAPO and MgAPSO gels; for comparison XRD pattern of AlPO STA-2 and MgAPO-56 using QuinC4.

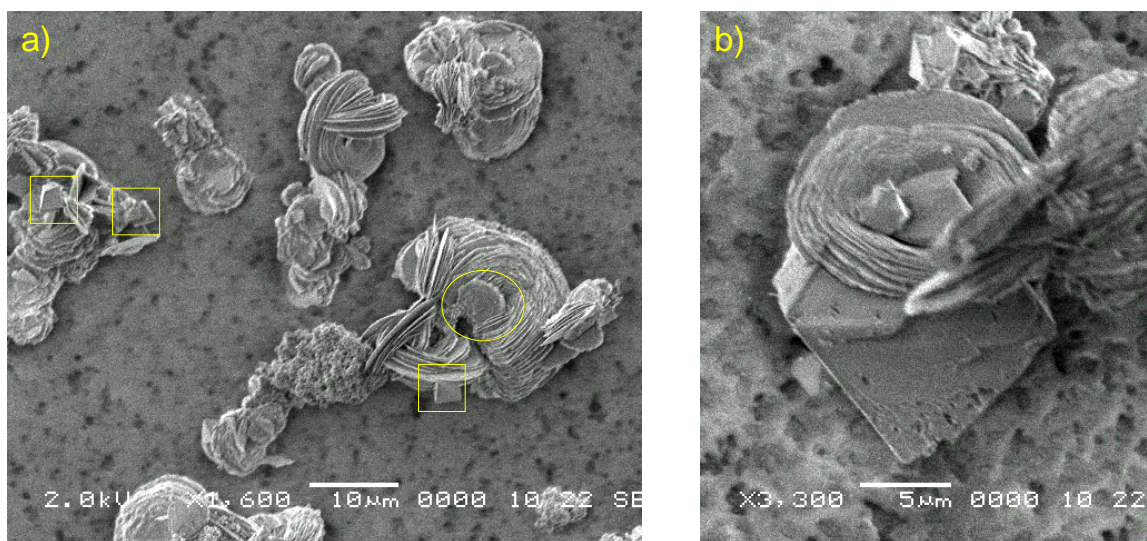


Fig. 6.14 SEM images of DABCO_C5 product using a MgAPSO gel.

6.3.3 Characterisation of As-Prepared AlPO STA-2

The AlPO version of STA-2 was successfully prepared using the DABCO_C4 template. The as-prepared material has been characterised by SEM, high resolution X-ray powder diffraction and solid-state NMR, and compared with AlPO STA-2 prepared using the QuinC4 template, also under fluoride-free conditions.

AlPO STA-2 in both cases is prepared in highly crystalline form, as crystals 2 μm in dimension (Fig. 6.15).

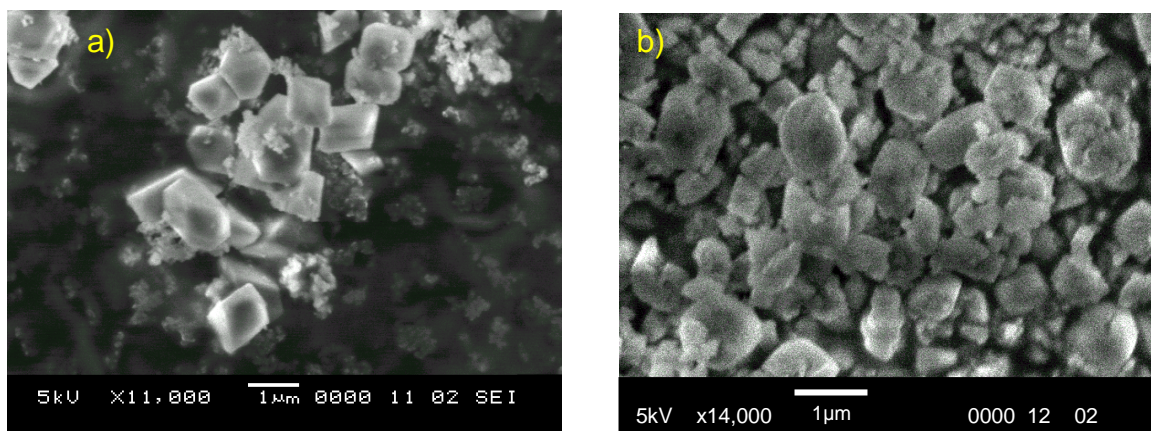


Fig. 6.15 SEM image of AlPO STA-2 using DABCO_C4(a) and QuinC4 (b) in the absence of fluoride.

Rietveld refinement of the structure against high resolution X-ray powder diffraction data of the as-prepared AlPO STA-2 (DABCO_C4) was performed with the GSAS program suite. As a starting model, the SXRD structure of MgAPO STA-2 with QuinC4 as template from the literature was used.¹ The refined unit cell is very similar to that reported by Maple² for AlPO STA-2 as-prepared with QuinC4 in the presence of fluoride, and distorted with respect to the MgAPO form, being shorter by 4.6% along the c axis and extended by 2.4% along the a and b axes (Table 6.7). The background was fitted using a 32 term cosine function, and reflection profiles were modelled using a pseudo-Voigtian peak shape. The starting model was improved by replacing the atomic coordinates QuinC4 by those of DABCO_C4 obtained from the modelled location within the large cage of STA-2. The occupancies and displacement parameters of template atoms were allowed to refine with suitable constraints. Atomic coordinates of the

framework were initially allowed to refine, with the application of soft restraints to ensure acceptable bond lengths and tetrahedral geometry. As the refinement proceeded the restraints were relaxed and ultimately removed, keeping constraints on the thermal parameters, giving a sensible Al-O = 1.708(19) Å and P-O = 1.520(15) Å. This last refinement without restrains in bonds supports that the space group is correct giving Al, P order and therefore the two distinctive sites A and B for hydroxyl groups.

Table 6.7 Table with STA-2 unit cell of MAPO, AlPO(F), AlPO(QuinC4) and AlPO(DABCO_C4).

| Unit Cell | MgAPO ¹ | AlPO(F) ² | AlPO (QuinC4) | AlPO (DABCO_C4) |
|----------------------|--------------------|----------------------|---------------|-----------------|
| $a = b / \text{\AA}$ | 12.726(2) | 13.0245(5) | 13.0341(4) | 13.0301(1) |
| $c / \text{\AA}$ | 30.939(6) | 29.598(1) | 29.605(1) | 29.531(3) |
| $V / \text{\AA}^3$ | 5010.6(15) | 5020.9(3) | 5029.5(3) | 5013.9(5) |

Previous structural work performed on a sample of AlPO(F) STA-2 using QuinC4 as template from laboratory X-ray diffraction data and MAS NMR suggests that STA-2 contains disordered water molecules and hydroxyl groups coordinated to aluminium attached to the structure to balance the positive charge from protonated template. These studies were complicated by the likely presence of both fluoride ions and hydroxide ions coordinated to the framework.² This information was taken into account and difference Fourier maps were calculated to observe the electron density related to these disordered water molecules and hydroxyl groups (the TGA in Fig. 6.28 shows a weight loss step of 8wt% at 100 °C proving the presence of water molecules in the as-prepared form of AlPO STA-2).

The following figure shows that the highest peaks of electron density are around the template and within the cancrinite cage (Fig. 6.16).

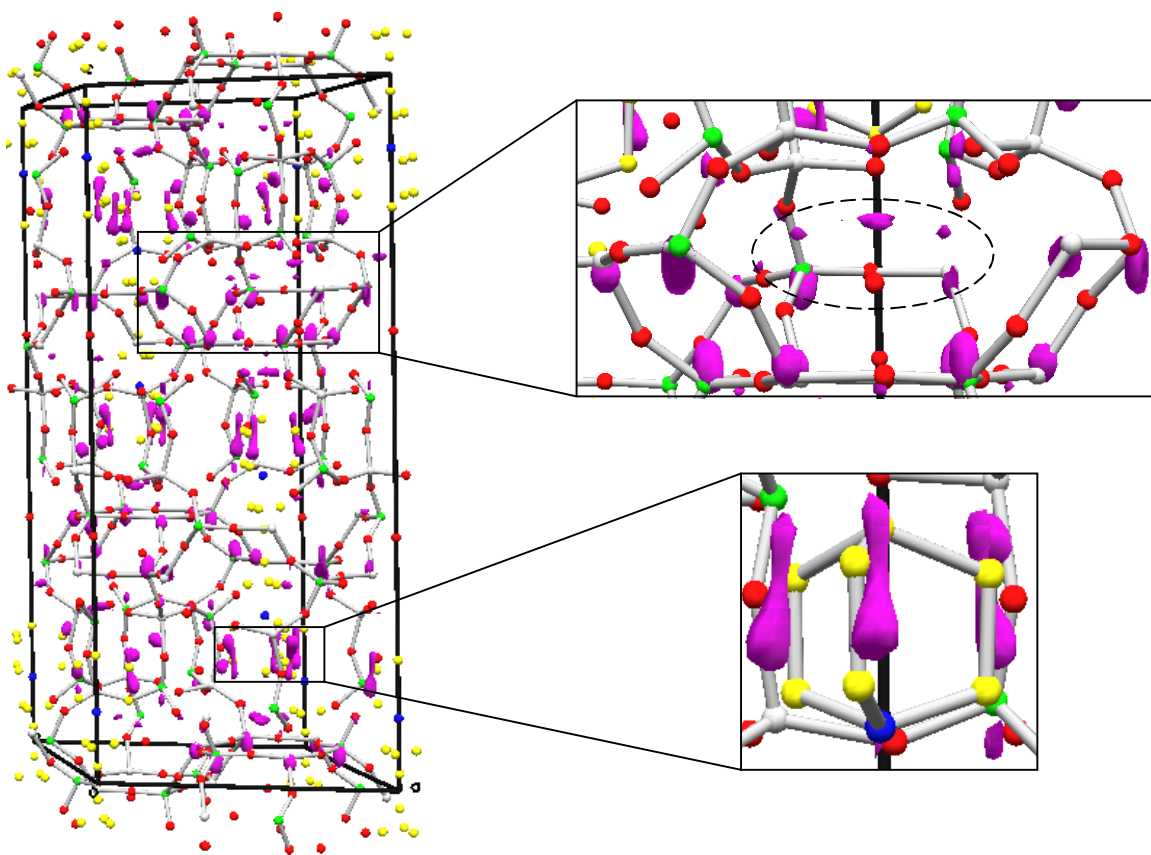


Fig. 6.16 Difference Fourier maps of AlPO STA-2 model using SXRD coordinates of MgAPO STA-2 with QuinC4 as template from previous work¹ (extra electron density denoted in magenta); in detail the cancrinite cage -an oxygen atom in the middle of the cage found by Fourier and refined is included- (top) and quinuclidium ring (bottom).

By refinement of the framework, inclusion of modelled positions for the template, and refinement of the extra framework species observed in the difference Fourier maps, the fit was improved to a final $R_{wp} = 11.16\%$ and $R_p = 8.6\%$. The refined unit cell parameters obtained are: $a = 13.03007(11)$ Å and $c = 29.5413(26)$ Å in R-3 (hexagonal setting) and bond lengths P-O = 1.534(9) Å and Al-O = 1.708(8) Å. The region between 0 and 4° 2θ was excluded (Fig. 6.17). Atomic coordinates, temperature factors and selected bond lengths and angles are given in Appendix B, Tables B.7, B.8 and B.9, respectively.

Three extra framework sites for oxygen atoms within the cancrinite cage were found by difference Fourier maps. The A site, due to Al(1)-OH-Al(2), at 2.8 Å from Al1 and 2.4 Å from Al2, refined to an occupancy of 0.257. The B site maybe also assigned to hydroxyl

groups close to P1 and P2 at 2.0 Å and refined to an occupancy of 0.138. The water molecule was found in the centre of the cancrinite cage in a special position, with a refined occupancy of 0.189. The refinement of this structure is complicated by the partial occupancy of hydroxyl groups in site A and B, which presumably results in distortion of the framework. Further investigation was performed using MAS NMR to study the different aluminium and phosphorus environments and investigate the possible locations of hydroxyl groups in the A and B sites (Fig. 6.18).

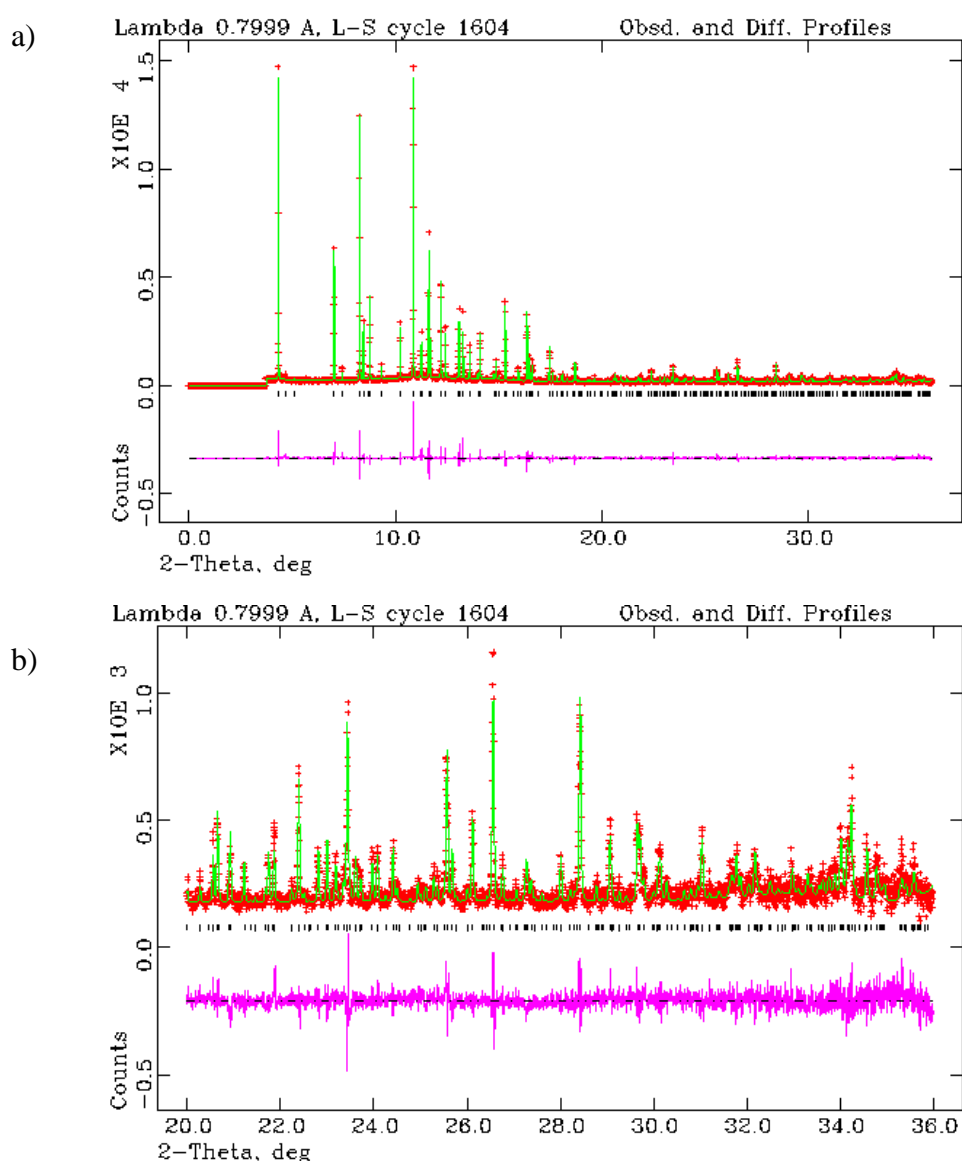


Fig. 6.17 (a) Rietveld refinement plot of AlPO STA-2 DABCO_C4 (red: experimental data, green: model, purple: difference plot), (b) expanded low angle region.

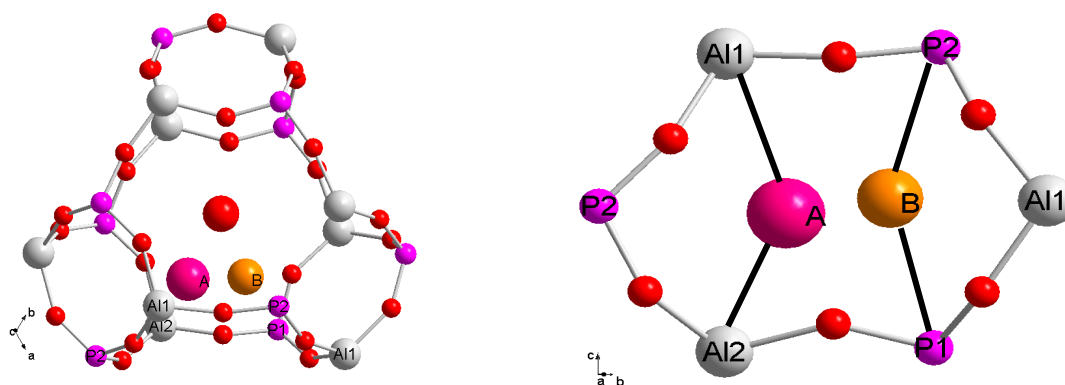


Fig. 6. 18 The two possible sites of hydroxyl groups, A and B and the water molecule in the centre of the cancrinite cage by difference Fourier maps of AlPO STA-2 DABCO_C4 (left). The A and B positions in detail (right).

MAS NMR of AlPO STA-2 using QuinC4 and DABCO_C4 as templates. Solution NMR of DABCO_C4

Solid-state MAS NMR was performed on AlPO STA-2 (QuinC4) and AlPO STA-2 (DABCO_C4) samples, and the information is complementary to that available from diffraction.

The ^{27}Al and ^{31}P MAS NMR spectra of AlPO STA-2 prepared with QuinC4 and DABCO_C4 are similar (Fig. 6.19). In the ^{27}Al spectra there are two main resonances, one centered at 37 ppm and other much broader at *ca.* 14 ppm. These signals are assigned to aluminium in tetrahedral and 5-coordination environments respectively. These environments were examined in more detail by ^{27}Al MQ MAS NMR (Fig. 6.20) and are again similar for the two AlPO samples. MQ MAS NMR clearly resolves the two crystallographically distinct tetrahedral aluminium sites (Al(1) and Al(2)) with isotropic chemical shifts of 43 and 34 ppm. In addition there are one or two distinct five-fold coordinated aluminium species at 12 ppm. This indicates that AlPO STA-2 is based on a tetrahedrally-connected framework, but with a part of the aluminium cations coordinating additional species, as indicated by the Rietveld analysis. These additional species could be hydroxyl groups, to facilitate charge balance of the alkylammonium cations, and are tentatively assigned to $\text{O}_4\text{Al}(1)\text{-OH-Al}(2)\text{O}_4$ groups (site A).

The ^{31}P MAS NMR DP spectra are more complex and show three lines at about -31 , -27 and -22 ppm and a broader resonance at *ca.* -10 ppm. (There are also two minor ^{31}P signals in the spectrum of AlPO STA-2 (QuinC4) close to 0 ppm). These spectra are deconvoluted as four main signals* and the main signal at about -27 ppm is assigned to the phosphorus in tetrahedral coordination within an undistorted tetrahedrally coordinated framework. The rest of the signals could be a consequence of the interaction of phosphorus with the hydroxyl group at the B site found in the Rietveld refinement ($\text{O}_3\text{P-OH}$). To investigate this, CP spectra were collected. The sharper resonances are only slightly enhanced by CP, so it is unlikely that the corresponding phosphorus atoms have directly bonded hydroxyl groups. The broad signal at -12 ppm in the spectra of the DABCO_C4 sample increases in intensity with CP, therefore this signal is attributed to P atoms with attached hydroxyl groups. It is not possible to completely determine the structure of this as-prepared AlPO material, and it is likely that there is a complex structural arrangement to enable the charge on the template to be accommodated by the AlPO framework. This ‘defect’ is likely to be disordered over different positions within the cacrinite cages of AlPO STA-2.

The formation of Al1-OH-Al2 (site A) may interrupt the Al-O-P connectivity and open up the structure, making a P-OH bond possible (site B). A similar situation has been reported in an AlPO-34 related material (CHA) containing a Ni- complex, where the formation of Al-OH-Al bridges in 5-coordination breaks the Al-O-P connectivity and P atoms interact with the Ni(II) complex to form an unusual P-O-Ni-O-P bridge. In this case after calcination the CHA framework is fully recovered.¹² As a continuation of the MAS NMR study, this sample will be calcined and fully characterised.

*The deconvoluted intensities for the ^{31}P MAS NMR DP spectra for AlPO STA-2 (QuinC4) and AlPO STA-2 (BABCO_C4) are given in Appendix C (Table C.1 and C.2).

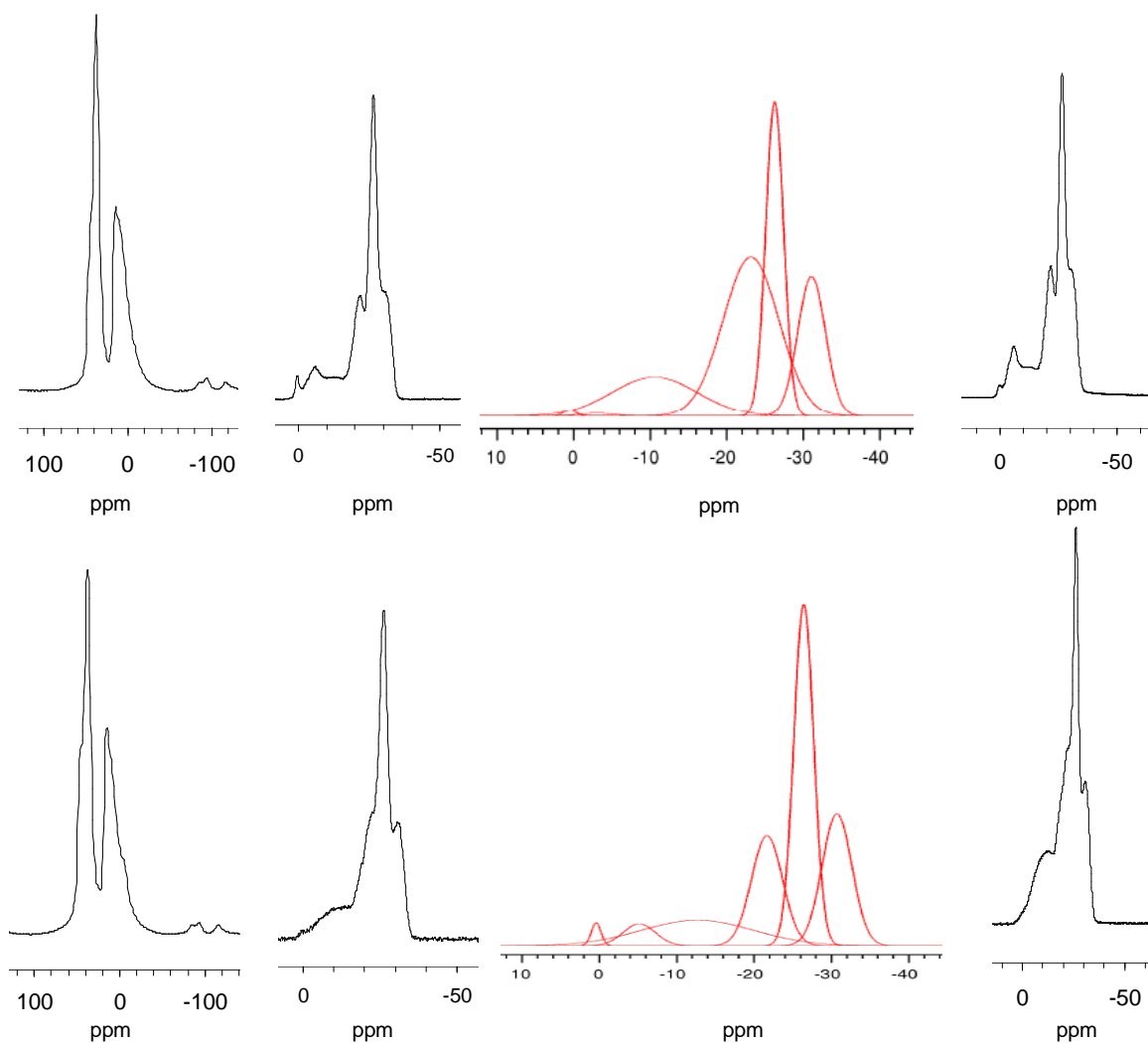


Fig. 6.19 From the left to the right: ^{27}Al , ^{31}P DP, DP deconvoluted curves and ^{31}P CP MAS NMR spectra for AlPO STA-2 QuinC4 (top) and DABCO_C4 (bottom).

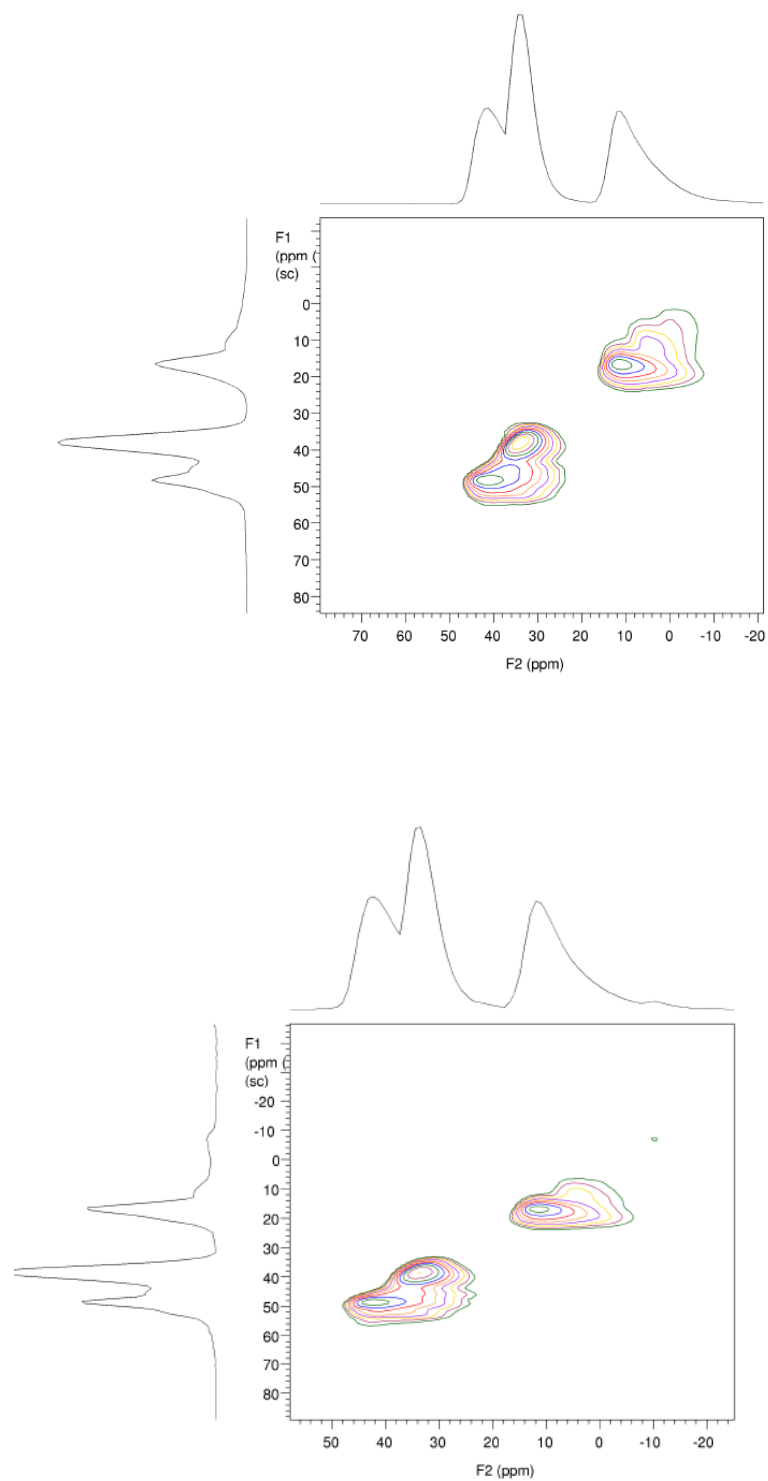


Fig. 6.20 ^{27}Al MQ MAS NMR spectra for AlPO STA-2 QuinC4 (top) and DABCO_C4 (bottom).

Details of the included template molecules were obtained by solid-state ^{13}C and ^{15}N MAS NMR (Fig. 6.21) in combination with solution-state ^{14}N and ^{15}N NMR.

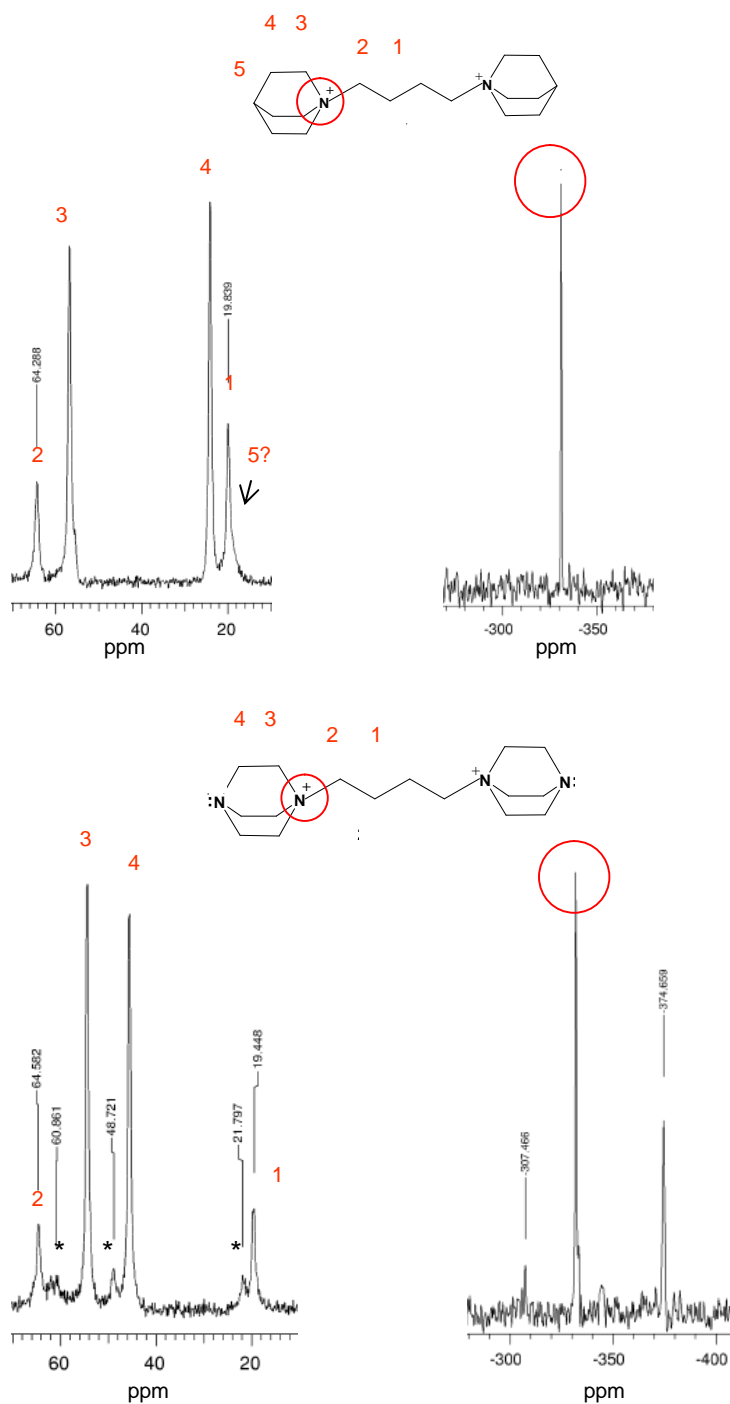


Fig. 6.21 From left to right: ^{13}C and ^{15}N MAS NMR spectra for AlPO STA-2 QuinC4 (top) and DABCO_C4 (bottom). In the case of DABCO_C4 the possibility exists of the apical nitrogen atoms being protonated or non-protonated related to the peak at -374.7 ppm. Solution NMR was applied to elucidate the assignment of this peak to the non-protonated nitrogen environment. So, the template within the cages is 2^+ charged.

^{13}C MAS NMR shows in both cases that the templates are incorporated largely intact. Signals are assigned for both templates in figure 6.21. For QuinC4 the signals appear at 64.3, 56.7, 24.0 and 19.8 ppm related to C2, C3, C4 and C1, respectively. A weak shoulder could be assigned as the apical C5. For DABCO_C4, some extra weak peaks appear that could be attributed to break down products, the main signals appearing at 64.6, 54.3, 45.5 and 19.5 ppm related to C2, C3, C4 and C1 respectively.

^{15}N MAS NMR was performed to observe the differences upon protonation between QuinC4 and DABCO_C4: QuinC4 is 2^+ charged whereas DABCO_C4 could be 2^+ , 3^+ or 4^+ , if the apical nitrogen atoms were protonated. As expected, the spectrum for QuinC4 shows one single signal at -331.2 ppm for the quaternary nitrogen atoms (NR_4^+). The DABCO_C4 spectrum shows two major signals, one at -332.0 ppm related to the quaternary nitrogen atoms and another at -374.7 ppm related to the apical nitrogen atoms that could be either in non-protonated ($:\text{NR}_3$) or protonated (NR_3H^+) environment. DFT calculations and solution ^{14}N and ^{15}N NMR were applied to elucidate the assignment of this signal.

The isotropic magnetic shieldings of nitrogen environments in DABCO_C4 were calculated with the CSGT method by D. Carnevale. These data predict $:\text{NR}_3$ as most shielded, followed by NR_3H^+ at 30 ppm deshielded and NR_4^+ at 20 ppm further deshielded (Fig. 6.22 left). The quadrupolar constant (C_Q) shows that only $:\text{NR}_3$ has a large and therefore NMR-relevant C_Q value (5.8 MHz at the highest level of theory) (Fig. 6.22 right). These results mean that either for ^{15}N ($I = 1/2$) or ^{14}N ($I = 1$) spectra the chemical shift positions will follow the order $:\text{NR}_3 < \text{NR}_3\text{H}^+ < \text{NR}_4^+$.

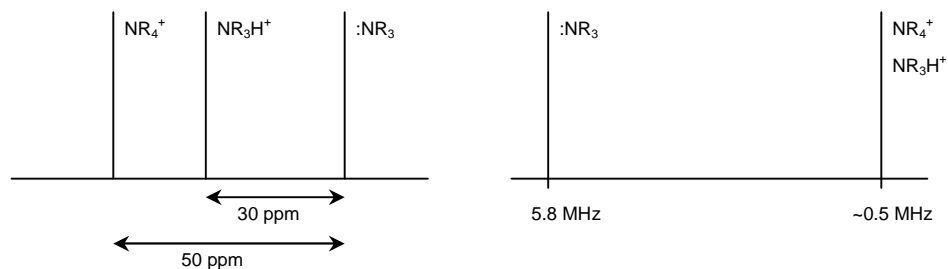


Fig. 6.22 Schematically description of the chemical shift differences (left) and C_Q values (right) for the nitrogen environments in DABCO_C4 molecule.

The solution ^{14}N ($I = 1$) spectrum of sample **3**, DABCO_C4 dissolved at neutral pH, shows only one resonance at 47.7 ppm that must be assigned to the quaternary nitrogen atoms (Fig. 6.23). The apical nitrogen atoms, are expected in D_2O to be in equilibrium between the protonated and the non-protonated forms. This dynamics take place on a much shorter time scale than the NMR phenomenon itself. Therefore, both forms are expected to be recorded as a single resonance in a water solution. The lack of this resonance in the spectrum indicates the equilibrium is highly shifted to the non-protonated form ($:\text{NR}_3$) which is not easily detected due to its large quadrupolar constant.

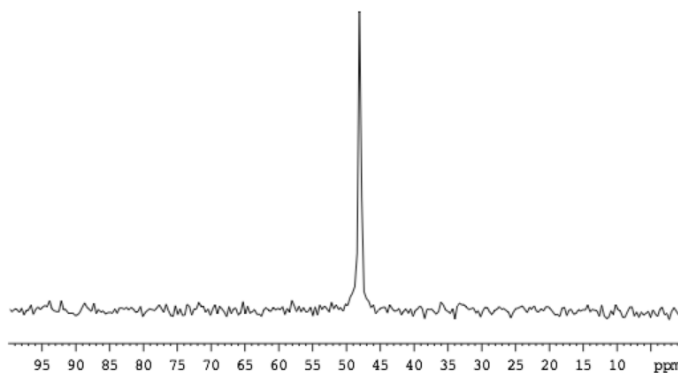


Fig. 6.23 ^{14}N spectrum of sample **3**, DABCO_4 at neutral pH.

In contrast, when the equilibrium is shifted towards the protonated form (NR_3H^+), sample **4**, this environment appears in the spectrum as a much broader signal at 33.1 ppm (Fig. 6.24 c). A schematic representation of this signal upon acid addition is presented in Fig. 6.24 b) which shows that the signal will progressively become narrower as the protonated form becomes more representative in the acquisition time and as a result there is a shift to low field.

From these results it can be concluded that the apical nitrogen in DABCO_C4 at pH seven, the typical pH for the synthesis of AlPO STA-2, is mainly in non-protonated form ($:\text{NR}_3$). Therefore the total charge of the template DABCO_C4 in solution is 2^+ (the same as QuinC4).

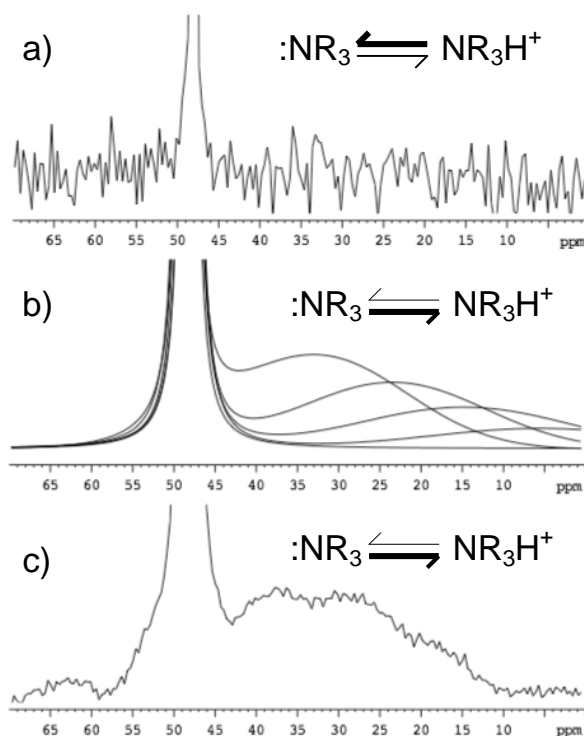


Fig. 6.24 Experimental ^{14}N spectrum of sample 4 (a) and 3 (c) and simulated behaviour of the ^{14}N resonances of the DABCO_C4 as function of the acidification of the solution (b).

Furthermore, ^{15}N spectra were collected on samples 3, 4 and 5. Although ^{15}N is characterised by low natural abundance (0.36%), its detection was possible to record as indirect dimension of a ^1H -acquired 2D correlation experiment denoted as ^1H - ^{15}N HMQC. The isotropic behaviour ^{15}N ($I = 1/2$) gives narrower resonances as it can be observed in the spectra where the signal related to the apical nitrogen atoms shifts depending on the tendency of the equilibrium towards the protonated or non-protonated form. For sample 3 (DABCO_C4 at neutral pH) this signal appears at 16.2 ppm, whereas for sample 4 (DABCO_C4 at acid pH) the signal is shifted towards lower field (δ 30 ppm) due to the NR_3H^+ environment and for sample 5 (DABCO_C4 at basic pH) the signal is shifted to higher field (δ 11.1 ppm) due to the $:\text{NR}_3$ environment (Fig. 6.25). The difference in chemical shifts between the signals of ^{15}N quaternary and apical non-protonated of about 40 ppm in the experiments for the samples 3, 4 suggests that the signal at -374.7 ppm in ^{15}N MAS NMR is related to $:\text{NR}_3$. This direct observation concludes that DABCO_C4 in the solid is 2^+ .

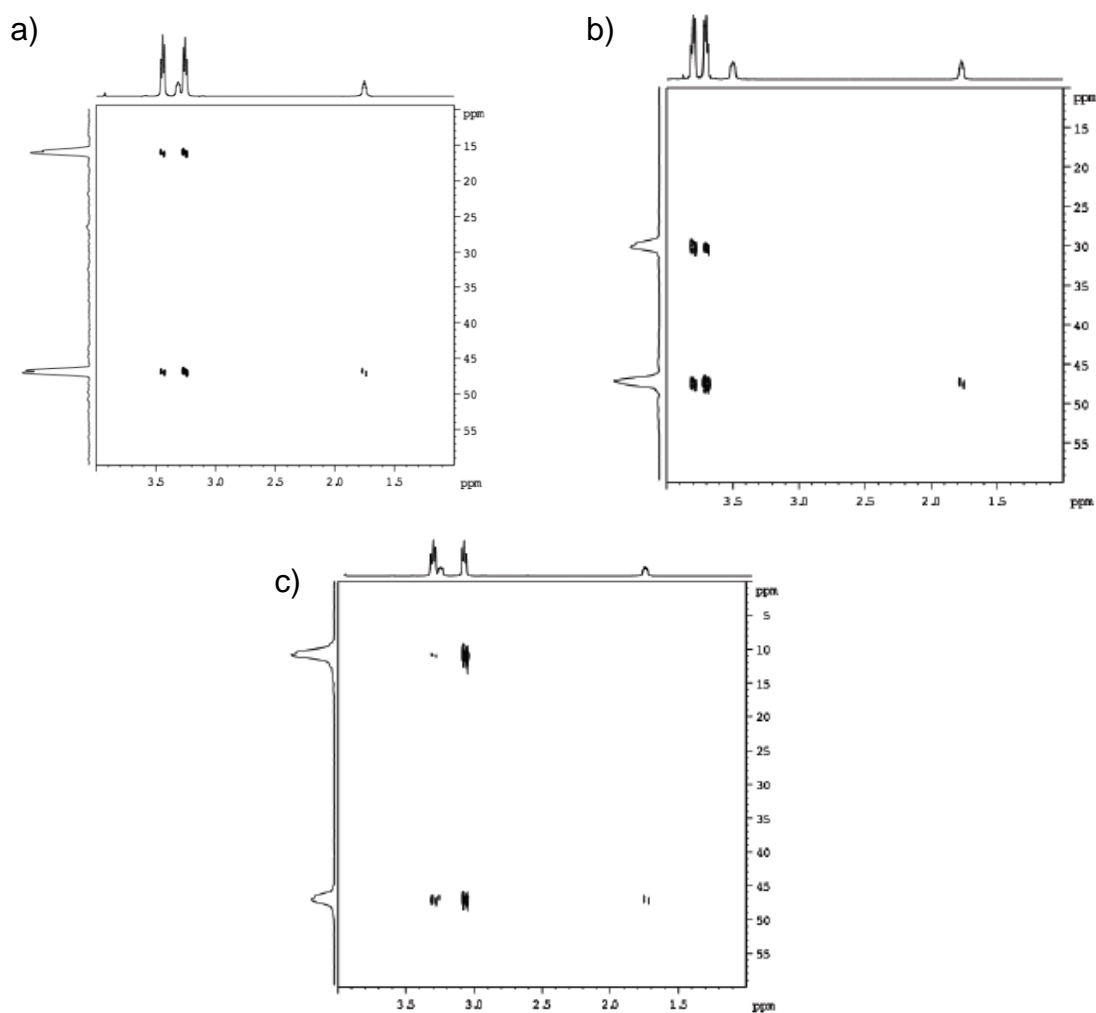


Fig. 6.25 ^1H - ^{15}N HMQC spectra of samples **3**, **4** and **5** (DABCO_C4 at neutral (a), acidic (b) and basic (c) pH respectively).

As a conclusion from the structural study on as-prepared AIPO STA-2 it can be said that DABCO_C4 can act as a substitute for QuinC4 in the STA-2 synthesis and it is incorporated into the solid as 2^+ (the same charge as QuinC4). The complex environments around the framework cation sites are reflected in both XRD and MAS NMR data. These data show that AIPO STA-2 certainly possesses 5-coordinated aluminium environments and also phosphorus environments that are strongly distorted by the effects of aluminium cations in the tetrahedral framework being additionally coordinated by hydroxyl groups.

6.3.4 Characterisation of As-Prepared SAPO STA-2

As an extension to this work, the incorporation of silicon into the AlPO STA-2 framework was attempted. SAPO STA-2 was not obtained using DABCO_C4 or C5. The best defined sample was synthesised using QuinC4 with seeds of AlPO STA-2 and colloidal silica as the silicon source. The structural characterisation of this product is briefly described here.

SEM and EDX

The XRD pattern of this product shows STA-2 as the main phase with SAPO-56 peaks as an impurity phase.

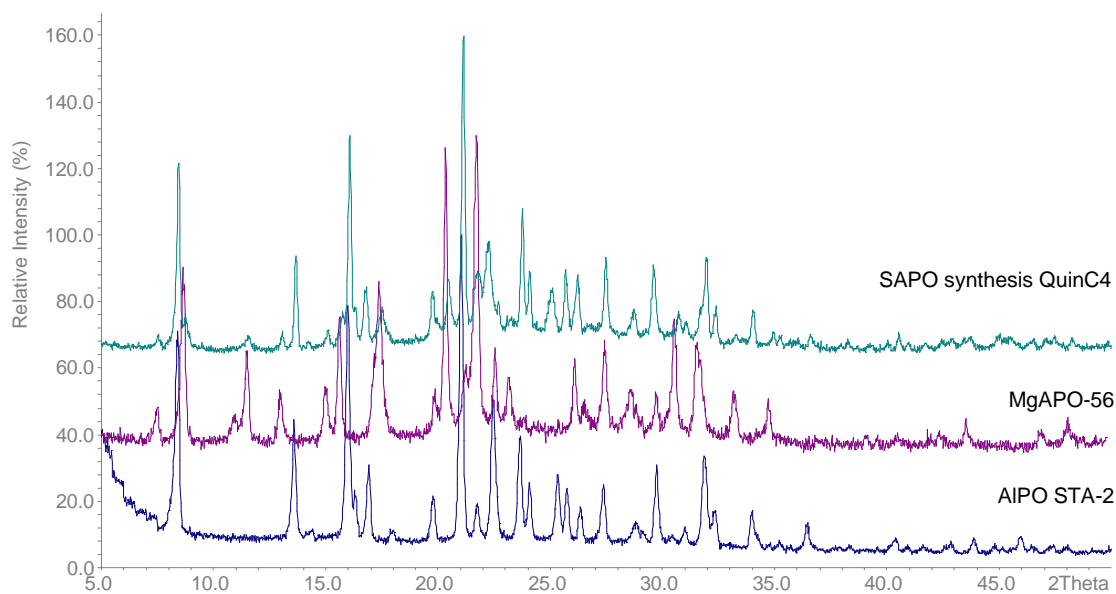


Fig. 6.26 XRD Pattern of the product from SAPO STA-2 synthesis (cyan) and for comparison pattern of AlPO STA-2 (blue) and MgAPO-56 (purple), both prepared with QuinC4 as template.

SEM show three types of particles: a main component comprising oblate spheroidal particles of 30 μm , a second one with cuboidal morphology and some amorphous material. The main component phase and cuboidal particles have a SAPO composition with $\text{Al/Si} = 0.4$ by EDX analysis, whereas the poorly defined material is mainly unreacted silica with traces of aluminium and phosphorus.

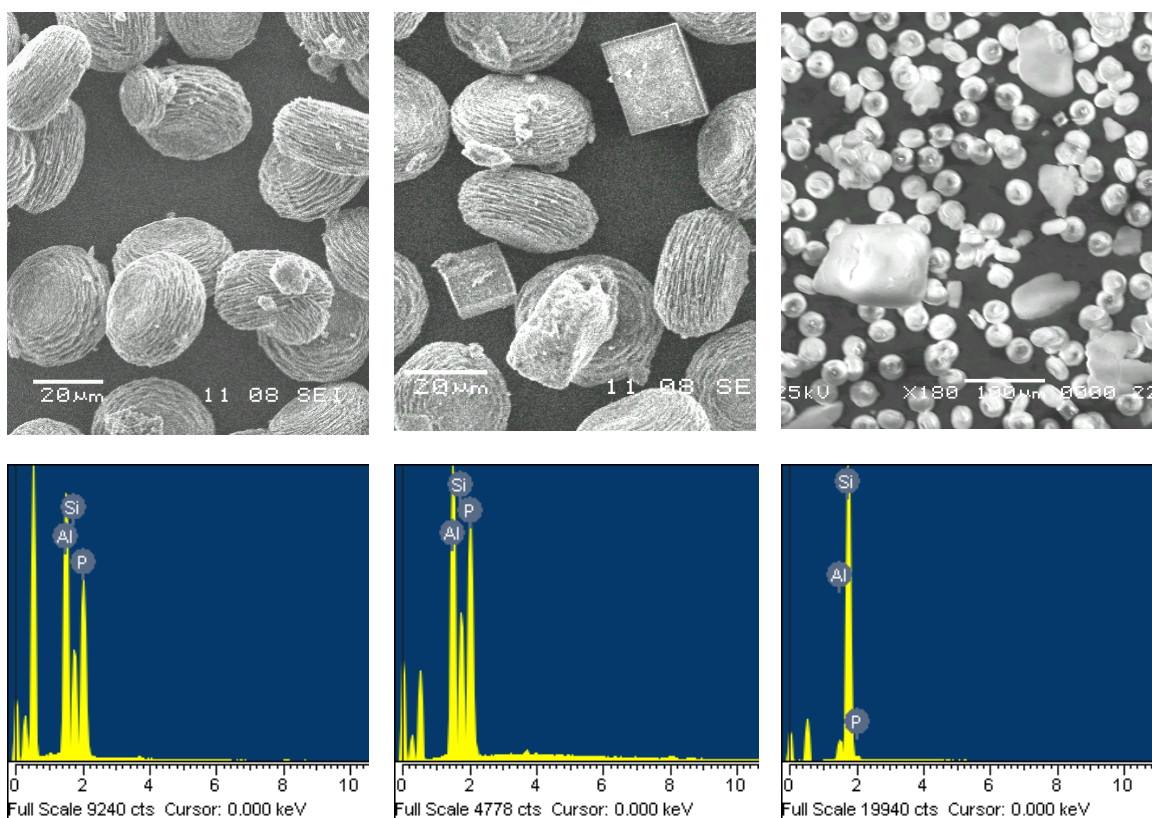


Fig. 6.27 SEM (top) and EDX (bottom) of main (left), cuboidal (middle) and amorphous (right) particles.

The cuboidal particles cannot be attributed to the SAPO-56 impurity because their morphology is incompatible with the symmetry of SAPO-56 (trigonal, space group P-31c).¹³ Previous work, using a MgAPO gel and different synthesis conditions, formed hexagonal plates for MgAPO-56 and single crystals with octahedral shape for MgAPO STA-2.¹ It is therefore concluded that the intergrowth particles include a mixture of SAPO STA-2 and -56 crystallites. They are polytypes and can form with the template QuinC4. Furthermore there are common crystallographic planes between the two solids. Because the product is a mixture, NMR was not helpful. Nevertheless, the adsorption was measured to compare with that of the AlPO STA-2.

6.3.5 Porosity of STA-2 Materials

TGA profiles of AlPO STA-2 (DABCO_C4 and QuinC4, see Fig. 6.28) gave one weight loss step at 100 °C, due to water lost, of 8wt%, and a second, due to template removal, of 17wt% which corresponds to 100% occupancy of the template within the solid. The XRD pattern of the calcined material shows that AlPO STA-2 remains stable as reported in previous work which demonstrated MgAPO and AlPO STA-2 are stable to template removal and have reported the structure of the calcined phases (Fig. 6.29).^{2,7} In this work, nitrogen adsorption was conducted gravimetrically on the calcined samples at 77 K to determine their porosity. STA-2 displays an isotherm of type I with some type II character, probably due to the small particle size that makes the external surface area significant. Maximum uptakes of 17% and 18.5% by mass suggest internal pore volumes of 0.21 and 0.23 cm³/g for AlPO STA-2 and SAPO STA-2/-56 respectively.

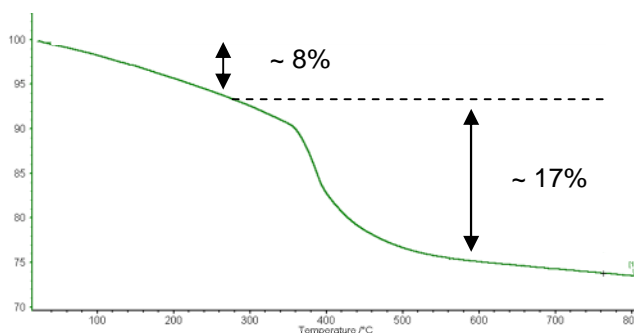


Fig. 6.28 Typical TGA thermogram of AlPO STA-2 (DABCO_C4).

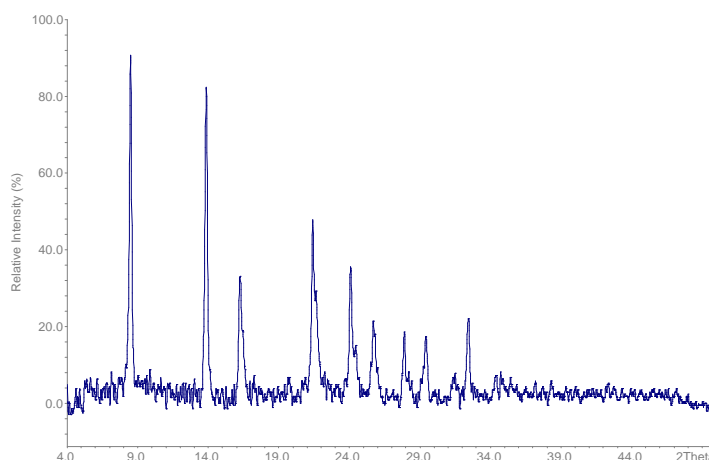


Fig. 6.29 Typical XRD pattern of calcined AlPO STA-2.

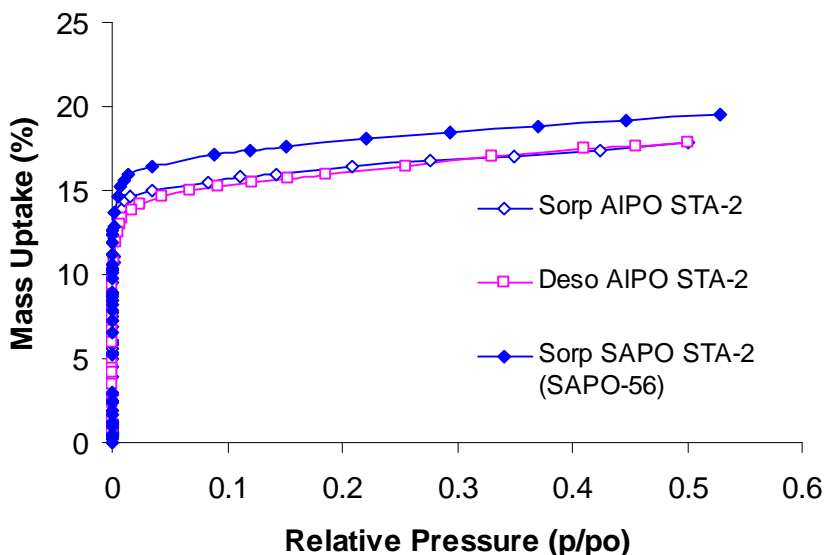


Fig. 6.30 Nitrogen adsorption/desorption isotherm for AIPO STA-2 and SAPO STA-2 (SAPO-56).

6.4 Summary & Further Work

The synthesis of pure AIPO STA-2 with a much cheaper template suggested by modelling underlines the value of this technique as a preliminary step in hydrothermal synthesis.

Although the current literature does not provide examples of DABCO_C4 and C5 as templates for aluminophosphates, this section demonstrates their potential use in this regime. In addition, the DABCO_C5 system is complex and further work would benefit from a high throughput approach to obtain novel phases. Such an approach was applied for the commercial template hexamethonium by EXXON to give a range of solids including the novel EMM-3 material.¹⁴ In addition, the use of the analogue QuinC5 in zeolite synthesis gives five different structures depending on the gel composition and structural studies demonstrate the different host-guest interactions.¹⁵

The refinement of AIPO STA-2 (DABCO_C4) shows a complex structure due to the inclusion of hydroxyl groups into the framework to accommodate the charged template.

The charge of the novel template has been investigated in detail by solution NMR which shows that, included in the solid, DABCO_C4 has the same charge (2^+) as the analogous QuinC4. Further XRD and solid-state NMR studies in the calcined form should show the differences in the framework with the as-prepared form since the removal of the template should result in a fully tetrahedral structure. In addition, solid-state NMR could resolve and assign the four crystallographic tetrahedral positions in the framework, Al1, Al2, P1 and P2, by virtue of their characteristic connectivity (Fig. 6.31).

| T site | T coordinate | T site | T coordinate | T site | T coordinate | T site | T coordinate |
|--------|--------------|--------|--------------|--------|--------------|--------|--------------|
| Al1 | P2 | Al2 | P1 | P1 | Al2 | P2 | Al1 |
| | P2 | | P1 | | Al2 | | Al1 |
| | P2 | | P1 | | Al2 | | Al1 |
| | P1 | | P2 | | Al1 | | Al2 |

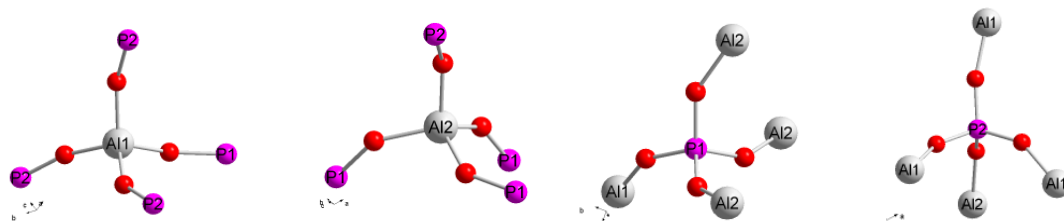


Fig. 6.31 Coordination of the *T* positions in STA-2.

-
1. G. W. Noble, P. A. Wright, A. J. Kvik, *Chem. Soc., Dalton Trans.*, 1997, 4485.
 2. M. J. Maple, *Structure and Catalytic Properties of Micoporous Aluminophosphates*, PhD Thesis, University of St Andrews, 2003.
 3. S. I. Zones, 1993, US patent 5194235.
 4. R. F. Lobo, S. I. Zones, R. C. Medrud, *Chem. Mater.*, 1996, **8**, 409.
 5. K. D. Schmitt, G. J. Kennedy, *Zeolites*, 1994, **14**, 635.
 6. G. W. Noble, *Synthesis of New Microporous Solids by Template Design*, PhD Thesis, University of St Andrews, 1998.
 7. <http://www.iza-online.org/>
 8. R. A. Sheldon, *Current Opinion in Solid State & Materials Scinece*, 1996, **1**, 101.
 9. V. Patinec, Pers. Comm.
 10. T. P. Abbiss, F. G. Mann, *Journal of the Chemical Society*, 1964, 2248.
 11. T. A. Keith, R. F. W. Bader, *Chem Phys. Lett.*, 1993, **210**, 223; J. R. Cheeseman, G. W. Trucks, T. A. Keith, M. J. Frish, *J. Chem. Phys.*, 1996, **104**, 5497.
 12. A. Meden *et al.*, *Micopor. Mesopor. Mater.*, 2001, **47**, 269.
 13. R. F. Lobo, S. I. Zones, R. C. Medrud, *Chem. Mater.*, 1996, **8**, 2409.

-
14. M. Afeworki, D. L. Dorset, G. J. Kennedy, K. G. Strohmaier, *Chem. Mater.*, 2006, **18**, 1697.
 15. S.-H. Lee, C.-H. Shin, D.-K. Yang, S.-D. Ahn, I.-S. Nam, S. B. Hong, *Micropor. Mesopor. Mater.*, 2004, **68**, 97.

PART 3

Adsorption Performance & other Applications of Zeotypes

Adsorption of Greenhouse Gases

- **At High Pressures**
- **At Low Pressures**

Diffusion & Catalysis

Summary & Further Work

Synopsis

This section studies the performance of the zeotypes developed during this work (STA-7, STA-14 and STA-2) in typical applications for microporous materials.

The main purpose is to study their potential application in gas adsorption and separation to remove greenhouse gases in different industrial processes. The adsorption of CO₂ and CH₄ as well as CO was performed at high and low pressures, at IFP-Lyon and the University of St Andrews. In addition, selected materials were tested for other applications in a collaborative manner sending the samples to other laboratories where the experimental data were collected. These results are presented and related to the structural features.

The adsorption performance of zeotypes is compared with related microporous materials such as the zeolite NaX and the metal organic framework (MOF) MIL-101, concluding that although zeotypes could offer advantages over zeolites the novel MOFs are also very promising, so further work should focus on both types of materials.

Chapter 7: Applications

7.1 Adsorption of Greenhouse Gases at High Pressures

7.1.1 Introduction

This INDENS project focuses on the potential use of zeotypes to adsorb and separate CO₂ from gas mixtures. Normally large scale removal of this gas from different gas streams is accomplished using amine-based absorption systems, which suffer from inherent regeneration cost of the solvent and inefficiency.^{1,2} Cryogenic technology is also applied but is rather complicated and costly.³ In contrast to these methods, the use of an adsorption process could be a cheaper possibility. Pressure Swing Adsorption (PSA) is a technology that separates gas species from a mixture of gases by varying pressure between one and several bar and ideally operates at room temperature for the regeneration of the adsorbent. Therefore the energy and infrastructure required are less expensive than the processes mentioned previously. The main requirement of PSA is to have a selective adsorbent for the gas molecule in question, in our case CO₂.

Microporous carbons and zeolites have long been used in PSA processes for the separation of nitrogen and oxygen from air. Carbons act as true molecular sieves. Their small pore size enable the smaller oxygen molecules to be adsorbed, leaving the gas

enriched in the larger nitrogen molecules (90-95%). In the case of zeolites the sites of interaction with the gases are the extra framework cations that have a stronger electrostatic interaction with the quadrupolar N_2 , leaving oxygen enriched to 95%. In the case of zeolites, the application of heat (TSA) or vacuum (VSA) is necessary to regenerate the adsorbent.⁴ Because zeotypes are similar structurally to zeolites but possess a less polar framework they could be of interest for application in PSA, where they could interact with a quadrupolar gas such as CO_2 (making possible its separation from a gas mixture) but the interaction would not be strong enough that regeneration would need the application of heating or vacuum.

PSA technology would be interesting for the following gas mixtures if suitable adsorbents were obtained:

- CO_2/N_2 . The application of CO_2 sequestration from flue gas. Flue gases from combustion of fossil fuels and by-products in the industrial processes contain nitrogen (typically more than two-thirds) as well as the greenhouse gas CO_2 . That creates the necessity of technologies for separation, capture and storage of CO_2 from CO_2/N_2 gas mixtures.⁵ For this purpose zeolite 13X has been already investigated using the PSA process (Fig. 7.1 left).⁶
- CO_2/CH_4 . The application in methane purification. This gas mixture is of importance in the biogas purification, where the presence of CO_2 reduces the energy content and also gives rise to acidity in the presence of water, consequently corroding the gas pipes (Fig. 7.1 right). A PSA process could be used to increase the concentration of methane: in the case of zeolites, zeolite 13X has been studied using high pressures.^{7,8}
- CO_2/CO . CO is an important reactant in many industrial process and most sources of CO are gas mixtures containing CO_2 , N_2 and H_2 .⁹



Fig. 7.1 *Emitted flue gas from a power plant (left) and a pipe containing biogas (right).*

With these applications in mind it is interesting to compare the CO_2 adsorption performance of zeolites, zeotypes and novel families of microporous materials in the PSA regime.

The adsorption performance of SAPO STA-7, SAPO STA-14 and related materials at high pressures relevant to Pressure Swing Adsorption (PSA) was measured in collaboration with Dr. Y. Belmabkhout and Dr. G. Pirngruber (INDENS) at IFP-Lyon. The results are compared with the performance of zeolite NaX (FAU)¹⁰ and zeotype SAPO-34 (CHA),¹¹ which are microporous solids used in industry.

7.1.2 Experimental

The adsorption isotherms of the samples were recorded gravimetrically on a set-up incorporating a Rubotherm magnetic suspension balance (T226) at the IPF-Lyon laboratory (Fig. 7.2), using a high pressure cell. Prior to measurement the samples were outgassed at 673 K for 4 hours under vacuum to remove adsorbed water. Due to concerns about their thermal stability, MgSAPO STA-14 and Cu SAPO STA-7 were outgassed at 573 K.

All adsorption isotherms were recorded at 373 K. This temperature was chosen for practical reasons. The high pressure version of the Rubotherm set-up used is less precise at low pressures (0 to 0.5 bar) and therefore not ideally suited to discriminate adsorbents in the low pressure regime of the isotherm. The use of a high measurement temperature

shifts the adsorption isotherm to higher pressures and accentuates the differences between the samples. Between 150 and 500 mg of sample were used for each measurement. After recording an adsorption isotherm, the samples were regenerated under the same conditions as those used for initial activation and an adsorption isotherm measured with the next gas of interest.

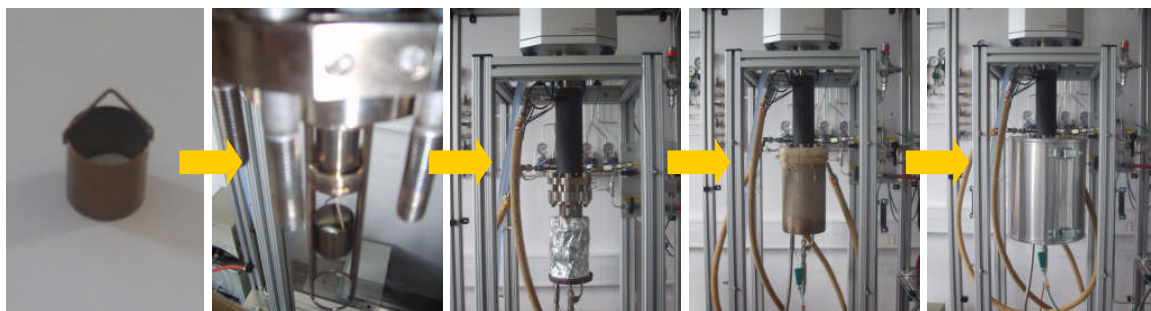


Fig. 7.2 Steps for the set up at high pressures using the gravimetric method: the sample is loaded in ‘the basket’, which is placed in the instrument hanging from the balance. The system is isolated from the surroundings by several jackets.

The samples used in this study are summarized in the following Table 7.1:

Table 7.1 Summary of the samples selected for gas adsorption at high pressures. Samples Si-CHA and NaX were provided by IFP-Lyon. The sections that describe the synthesis of these samples are as follows: for (†) 3.3.1.2; (††) 3.3.3.2; (♦) 4.3.2.3; (♦♦) 4.3.2.4; (‡) from verified synthesis recipe reference 12. The composition of the samples was determined by EDX assuming $Al/(Si+P) = 1$.

| Sample | Cation Exchanged | Composition (by EDX) | | | | V_p^* cm^3/g |
|---|----------------------|----------------------|------|------|------|---------------------|
| | | Al | P | Si | Mg | |
| SAPO(20) STA-7 [†] (SAV) | H ⁺ | 1.00 | 0.73 | 0.27 | - | 0.29 |
| Cu-SAPO(20) STA-7 ^{††} (SAV) | Cu ²⁺ | 1.00 | 0.73 | 0.27 | - | 0.23 |
| SAPO(20) STA-14 [♦] (KFI) | H ⁺ | 1.00 | 0.69 | 0.21 | - | 0.31 |
| MgSAPO (1:3) STA-14 ^{♦♦} (KFI) | H ⁺ | 0.90 | 0.77 | 0.23 | 0.10 | 0.21 |
| Si-CHA (CHA) | - | - | - | 1 | - | 0.32 |
| SAPO-34 [‡] (CHA) | H ⁺ | 1.00 | 0.67 | 0.33 | - | 0.28 |
| NaX (FAU) | Na ⁺ 100% | 1.00 | - | ~1.2 | - | 0.28 |

*The internal pore volumes were determined for St Andrews samples from N₂ adsorption isotherms at 77 K.

7.1.3 Results

7.1.3.1 CO₂ Adsorption on SAPO STA-7 Compared with that on a Zeolite (NaX)

The behaviour of the zeotype SAPO(20) STA-7 was compared with that of the industrial zeolite NaX to find out if SAPO(20) STA-7 could be a suitable material for PSA. From the isotherms of CO₂ at 373 K (Fig. 7.3), it can be observed that the uptake in the zeolite is higher than in the zeotype at each pressure even though the total pore volume is similar. This tendency is accentuated at low pressures due to the strong interaction of the extra framework cation Na⁺ and the quadrupolar gas molecule CO₂. The strong adsorption of the zeolite at 1 bar, even at this elevated temperature, means that the amount adsorbed from 1 to 12 bar, 2.2 mmol(CO₂)g⁻¹, is smaller than that for SAPO(20) STA-7, 2.5 mmol(CO₂)g⁻¹, (Fig. 7.3) and that at 300 K SAPO(20) STA-7 could show a greater increase of uptake of CO₂ from 1 to 20 bar than the NaX does over the same pressure range. Published data indicates that SAPO STA-7 uptake increases by 4 mmol(CO₂)g⁻¹ from 1 to 20 bar at 303 K,¹³ whereas for NaX the uptake increases by *ca.* 2.2 mmol(CO₂)g⁻¹ over the same range.¹⁴ Therefore, zeotype materials could be suitable substitutes over zeolites for pressure swing adsorption (PSA) technology.

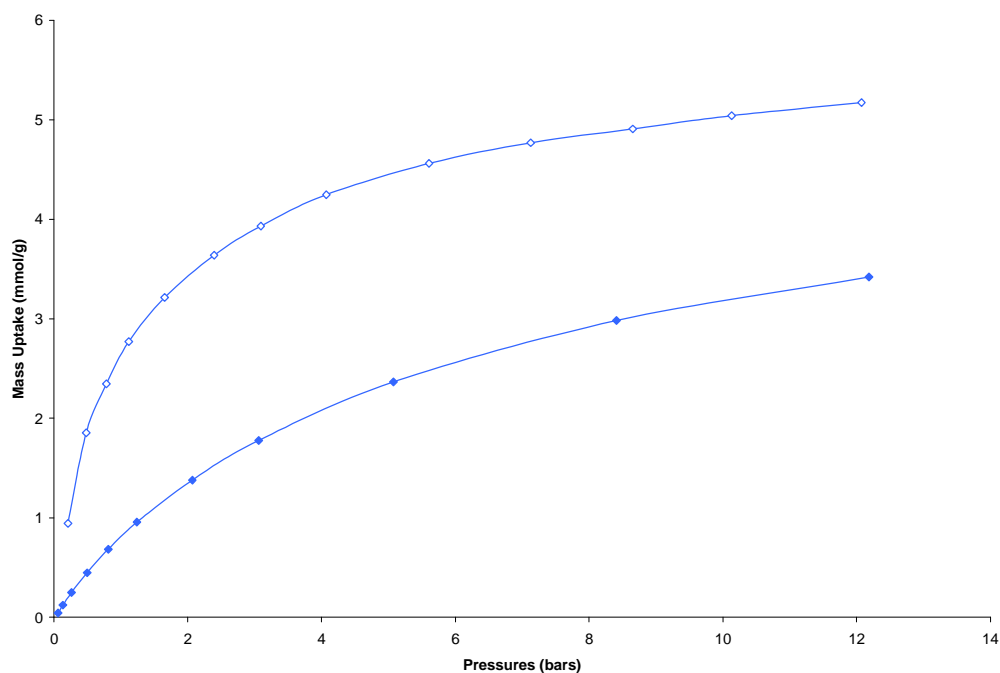


Fig. 7.3 Adsorption isotherms of CO₂ on NaX (empty symbols) and SAPO STA-7 (full symbols) at 373 K.

7.1.3.2 CO₂ Adsorption on D6R Polytypes (SAV, KFI and CHA) in SAPO Form

CO₂ adsorption isotherms at 373 K were also measured for SAPO samples with similar composition, but different pore structures, STA-7 (SAV), STA-14 (KFI) and SAPO-34 (CHA). SAPO STA-7 and STA-14 were developed in this thesis using the procedure to obtain SAPO(20) STA-7 and STA-14 in Part 2 of this thesis and SAPO-34 was synthesised using a literature procedure.¹² Framework densities of these polytopic structures are expected to be very close (since all are composed only of D6R units).

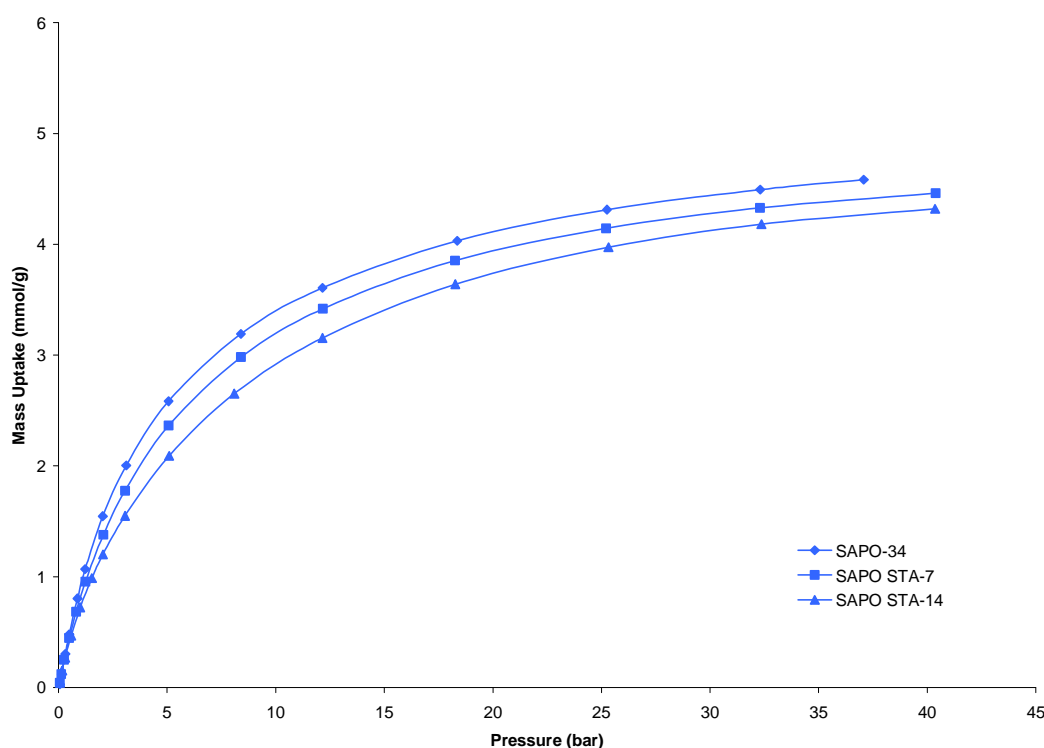


Fig. 7.4 Adsorption isotherms of CO₂ on SAPO-34 (diamonds), STA-7 (squares) and STA-14 (triangles) at 373 K.

The measured uptakes of the three materials are very similar, with the adsorption uptake of CO₂ decreasing slightly in the order CHA > SAV > KFI.

In attempting to rationalise the observed sequence of adsorption uptake amounts, both the silicon content of the samples and the structure should be taken into account. The silicon content in the framework is responsible for the formation of Brønsted acid sites, which are likely to be the main adsorption sites, particularly at low coverages. EDX analysis

indicates that the SAPO-34 sample has a Si/Al ratio of 0.33, whereas for SAPO STA-7 and STA-14 this is 0.31 and 0.20 respectively. This could result in the highest adsorption uptake being achieved for SAPO-34.

The structure may play a role even among polytypes. The three materials contain 4 cages per 48 T sites but these are of different types: SAPO-34 has only one, slightly elongated cage type (CHA), whereas STA-7 and STA-14 have two types of cages. In the same volume of structure STA-7 contains two larger (B) and two smaller (A) cages and STA-14 one large cage (α -cage) and three small cages (MER). In the case of STA-7 and STA-14 the size of the smaller cages could result in less efficient packing, decreasing the total adsorption uptake. The difference of cage sizes is more significant for STA-14 and this may explain its lower adsorption uptake value.

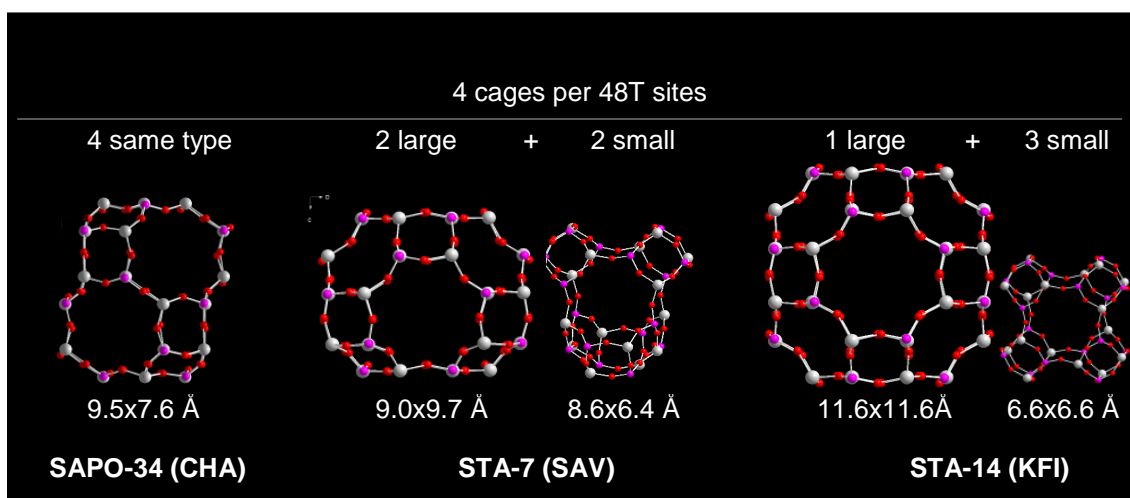


Fig. 7.5 SAPO-34, STA-7 and STA-14 cage types per 48 T sites, cage dimensions included.

To study further the influence of the composition, specific structure types with modified compositions were compared:

For the CHA topology the adsorption behaviour of a purely siliceous sample with a corresponding SAPO was compared. As expected, the SAPO structure shows a higher uptake of CO₂ due to its greater framework polarity.

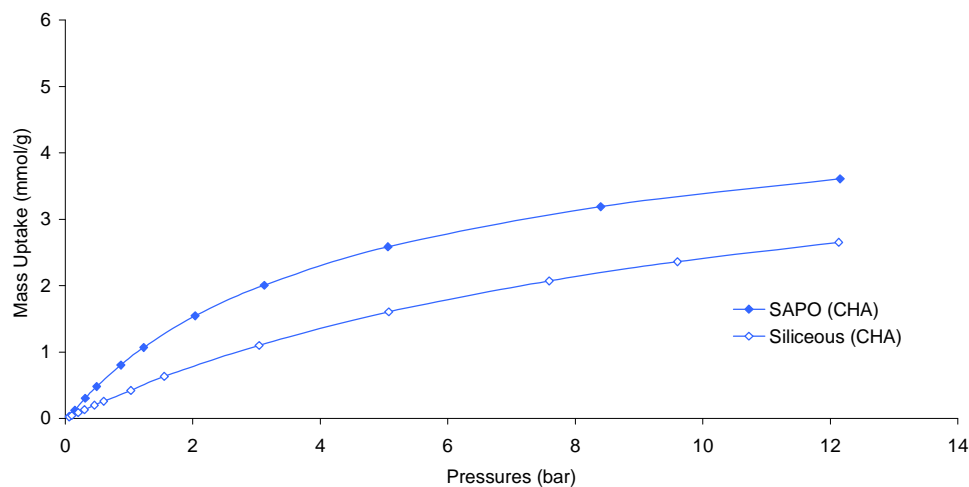


Fig. 7.6 Adsorption isotherms of CO_2 in CHA topology as SAPO (full symbols) and pure siliceous form (empty symbols) at 373 K..

For the SAV structure, the presence of Cu^{2+} cations slightly reduces its adsorption capacity for CO_2 . The presence of Cu^{2+} cations in the pores of the solid both increases the weight of the sample (by *ca.* 4%) and decreases the total available space within the pores by occupying free space within the cage (Fig. 7.7).

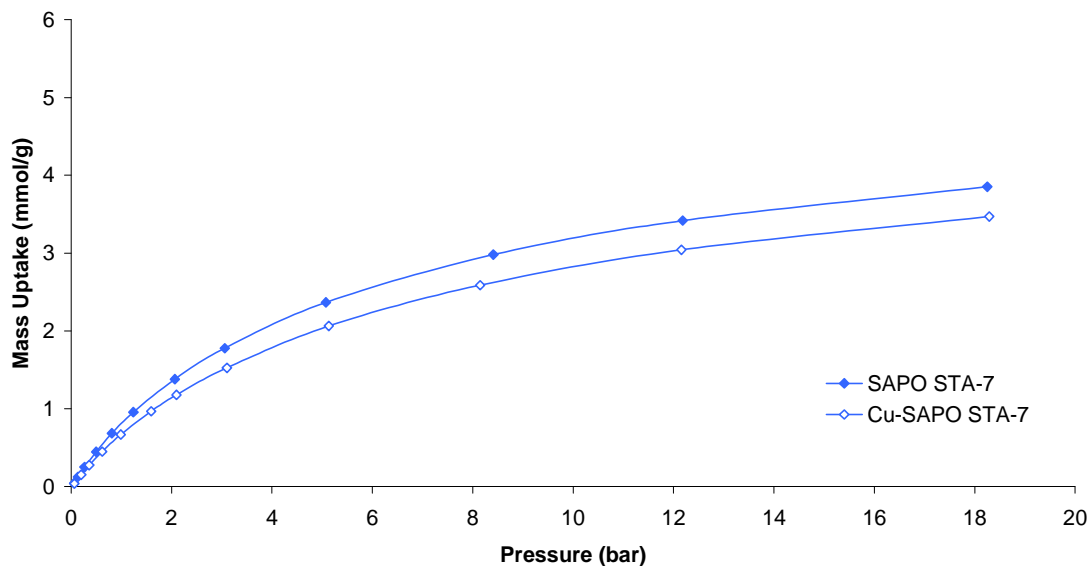


Fig. 7.7 Adsorption isotherms of CO_2 in SAPO and Cu-SAPO STA-7 at 373 K.

For the KFI topology the adsorption behaviour of MgSAPO STA-14 is very similar to that of the corresponding SAPO STA-14. If it is calcined and kept from contact with moisture it would be amenable for IFM measurements of diffusion due to its suitable morphology.

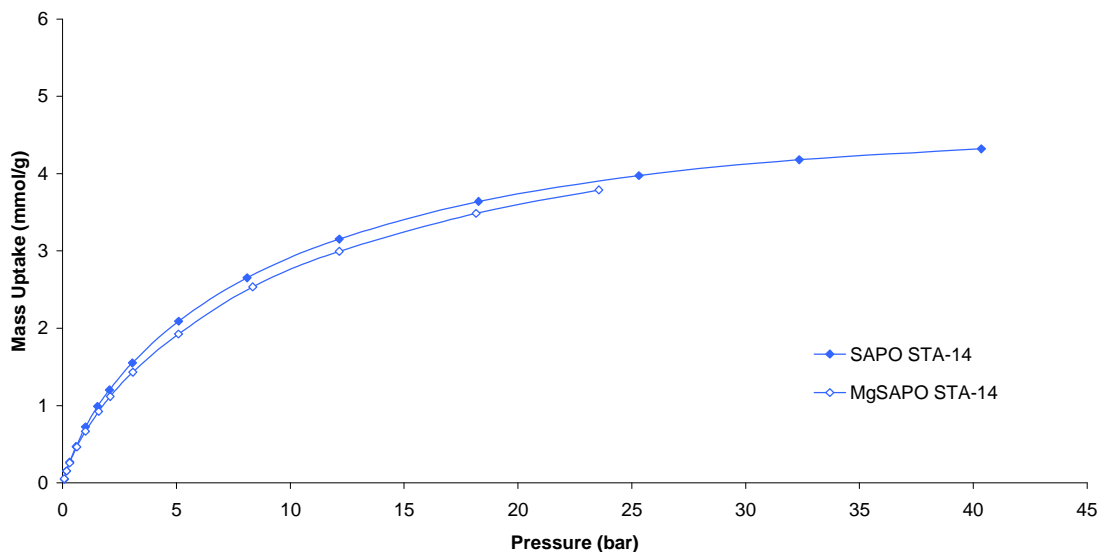


Fig. 7.8 Adsorption isotherms of CO_2 in SAPO and MgSAPO STA-14 at 373 K.

7.1.3.3 The Polarity of the Gas Influences Adsorption in a SAPO Framework: the Basis for Gas Mixture Separation

The following isotherms in SAPO-34, SAPO STA-7 and SAPO STA-14 frameworks (Fig. 7.9) show that the adsorption of CH_4 and CO follows the same trend as found for CO_2 : $\text{CHA} > \text{SAV} > \text{KFI}$. These materials have a preferential uptake of CO_2 over CO and CH_4 , because of stronger interactions of the quadrupole moment of CO_2 with the charged adsorbent framework. Notably, whereas the uptake of CO is greater than that of CH_4 for the cationic zeolite NaX, where the cation-dipole interaction predominates, the selectivity is reversed over the silicoaluminophosphates (discussed later in this section).

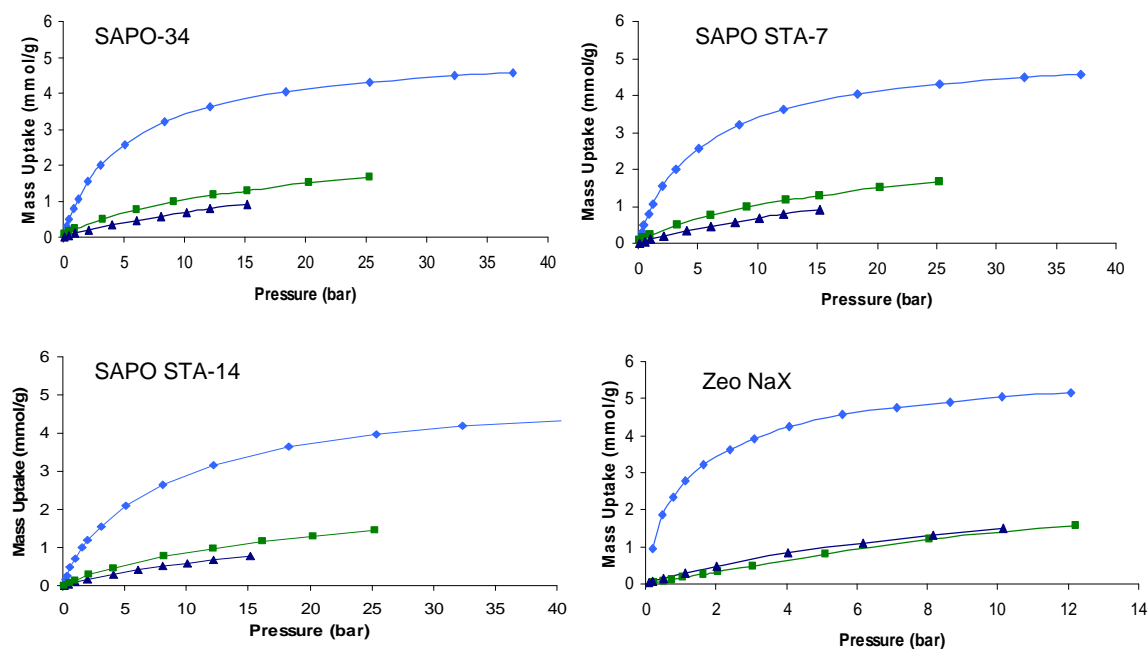


Fig. 7.9 Adsorption isotherms of SAPO-34, SAPO STA-7, SAPO STA-14 and NaX using as probe gases: CO_2 (diamonds), CH_4 (squares) and CO (triangles) at 373 K.

In summary, SAPO materials possess a different selectivity from that of zeolite NaX. The total uptake is lower compared with the zeolite: in all cases there is preferential uptake of CO_2 . Figure 7.10 compares the uptakes (and indirectly the selectivities) for CO_2 , CH_4 and CO on NaX and SAPO STA-7.

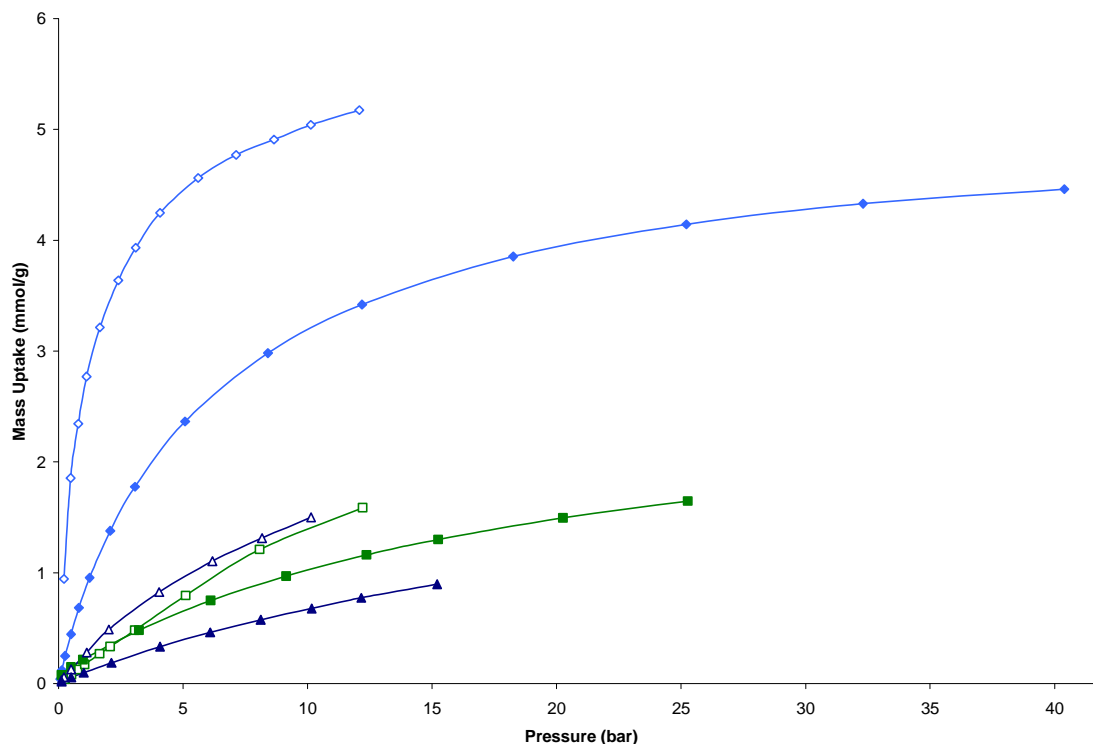


Fig. 7.10 Adsorption isotherms of NaX (empty symbols) and SAPO STA-7 (filled symbols) using as probe gases: CO₂ (diamonds), CO (triangles) and CH₄ (squares) at 373 K.

Compared with NaX, the adsorption capacity of the SAPO sample, at least at the pressures used here, is lower. This is not surprising. In NaX the main adsorption sites are the Na⁺ cations. There are 0.45 Na⁺ cations per tetrahedral atom. In SAPO the main adsorption sites are the Brønsted hydroxyl groups created by the replacement of phosphorous in the AlPO structure by silicon, so that for 30% silicon substitution into the phosphorus site there should be a maximum of 0.15 Brønsted acid sites per tetrahedral atom. The Brønsted acid adsorption sites are expected to show weaker coulombic effects: although the proton is smaller than a sodium cation, its coulombic effect will be reduced by being bound to oxygen of the framework, where some of the electron density of the oxygen atom is polarized by the proton.

NaX adsorbs slightly more CO than CH₄. Generally the interaction of CH₄ and CO (adsorption enthalpy determined from the isosteric heat from IFP-Lyon) is more or less equal for NaX zeolites.¹⁵ However, the nature of the interaction is not exactly the same for the two molecules. CH₄ is only attracted by van de Waals interactions, while in the

case of CO, van de Waals and polarisation forces play a role. Van de Waals forces do not depend very much on the composition (the molecules only interact with the lattice oxygen atoms, but not with the T atoms), but polarisation forces are a function of the electric field in the adsorbent. The electric field in a faujasite is stronger than in SAPO STA-7, which may explain the inversion of the CH₄/CO selectivity in NaX compared to SAPOs. It is likely that the charge is lower and more delocalised on the SAPOs, so that dispersive interactions with the CH₄ become more important.

7.1.3.4 Comparison of Different Families of Materials for their Application in CO₂ Adsorption and Separation

In order to compare the SAPO materials (STA-7, STA-14 and SAPO-34) with zeolites and MOFs under conditions relevant to PSA (1-20 bar, room temperature) data has been compared in table 7.2. In addition to STA-7 and STA-14 and the commercial zeolite NaX the data from one of the largest pore metal organic frameworks MIL-101(Cr)¹⁶ is presented, which possesses a pore volume of 2.15 cm³/g and has pores in the mesoporous range (smaller cage diameter of 29 Å and larger of 34 Å). The adsorption uptakes of these materials are summarised in the table 7.2:

Table 7.2 Adsorption uptakes of CO₂ for different microporous materials.
Data collected at room temperature.

| Microporous Family | Material | Vp* cm ³ /g | CO ₂ uptake at 1 bar (mmol/g) | CO ₂ uptake at 5 bar (mmol/g) |
|--------------------|----------|---------------------------|---|---|
| Zeolite | NaX | 0.28 | 4.5 | 5.8 |
| Zeotype | STA-7 | 0.29 | 3.0 | 4.5 ¹⁷ |
| MOF | MIL-101 | 2.15 | 3.5 | 9.0 ¹⁴ |

*The internal pore volume was determined for St Andrews sample from N₂adsorption isotherms at 77 K.

For PSA application it is the difference in uptake between 1 bar and a higher pressure (taken in Table 7.2 as 5 bar) that is the usable capacity. On this basis the STA-7 is competitive with the zeolite, because the strength of the Na⁺...CO₂ interaction results in a higher uptake already at 1 bar. It should be noted that the novel MOF materials have much higher usable capacities, and therefore advantages, if issues of stability and selectivity can be resolved.

7.1.4 Conclusions

The data of adsorption at high pressure show that zeotypes with similar framework topologies adsorb in a similar way. The affinity of adsorption in all of them is the same and follows the trend $\text{CO}_2 \gg \text{CH}_4 > \text{CO}$ whereas zeolite NaX gives the adsorption order $\text{CO}_2 \gg \text{CO} > \text{CH}_4$. Due to the preferential uptake for CO_2 it can be concluded that zeotypes could be effective adsorbents for the room temperature separation of CO_2 from CO_2/CH_4 and CO_2/CO mixtures in PSA processes.

7.2 CO_2 Adsorption at Low Pressures (0-1 bar)

7.2.1 Introduction

The high pressure adsorption study gives information about the performance under industrially relevant conditions. Under these conditions the D6R materials perform similarly. To understand in more detail the interaction of the framework with adsorbate molecules at low coverages, low pressure adsorption of CO_2 was carried out. This section covers the study of surface- CO_2 interactions as a function of the composition of the material or in the presence of extra framework cations. In addition to STA-7 (SAV), STA-14 (KFI) and SAPO-34 (CHA) frameworks, STA-2 (SAT) is included for comparison.

The adsorption apparatus to measure the isotherms is based on a gravimetric method, recording the amount of CO_2 adsorbed in grams as a function of the equilibrium gas pressure. The isotherm is the plot of the values of CO_2 mass adsorbed at the specific gas pressure at a constant temperature.

CO_2 isotherms were collected, when possible, at different temperatures to determine the heats of adsorption. The heat of adsorption gives information about the strength of the surface-gas interaction. The method to obtain the heat of adsorption has two steps: first the collection of adsorption isotherms at different temperatures and then the calculation

of enthalpy of adsorption at constant uptake, via the measurement of the equilibrium pressure at the constant uptake at the different isothermal temperatures.

Assuming reversible adsorption, the plots of $\ln P$ as a function of $1/T$ at constant coverage (isosteres) give straight lines that follow the Clausius-Clapeyron equation (Eq. 7.1). The plot of $\ln P$ vs. $1/T$ and the fit of the data by linear regression gives the enthalpy of adsorption via the slope ($-\Delta H_{\text{ads}}/R$).

The Clausius-Clapeyron equation:

$$\ln P = - \frac{\Delta H_{\text{ads}}}{RT} + C$$

$$\text{where } R = 8.31 \text{ Jmol}^{-1}\text{K}^{-1}$$

Eq. 7.1

7.2.2 Experimental

Low pressure CO_2 isotherms were collected gravimetrically using the Hiden IGA instrument with a procedure similar to that described for N_2 adsorption. In this case a thermostatted water bath controlled the temperatures. Temperatures were chosen to give reasonable uptakes and to achieve equilibrium in acceptable times. Where equilibrium was not completely achieved, equilibrium adsorption values were calculated by mathematical analysis of the asymptotic increase of weight within a 1 hour time period by the software controlling the IGA instrument.

Prior to the measurement, the samples were outgassed at 573 K for 4 hours under high vacuum to remove adsorbed water (10^{-6} mbar). The isotherms were recorded at temperatures between 273 K and 303 K in cycles of adsorption/desorption/adsorption until fully reversible behaviour was achieved. Typically there was an irreversible uptake on the first adsorption/desorption cycle on these aluminophosphate samples (0 – 0.5 wt%) which was attributed to strong adsorption at defect sites.^{18,*}

* Similar effects were not seen on MOF samples such as the scandium terephthalate $\text{Sc}_2(\text{O}_2\text{CC}_6\text{H}_4\text{CO}_2)_3$ analysed on the Hiden IGA instrument.

Subsequent adsorption/desorption cycles were fully reversible, and these are illustrated in this section.

The samples used in this study are summarised in the following table:

Table 7.3 Summary of samples for CO₂ adsorption performed at low pressures at the University of St Andrews. The sections that describe the synthesis of the samples here used are as follows for: (†) 3.3.1.2; (††) 3.3.3.2; (♦) 4.3.2.3; (‡) 3.3.1.4; (‡‡) from verified synthesis recipe reference 12; (§ and §§) 6.3.4. The composition of the samples was determined by EDX assuming Al/(Si+P) = 1.

| Sample | Cation Exchanged | Composition (by EDX) | | | Vp*** cm ³ /g |
|---|---------------------|----------------------|------|------|-----------------------------|
| | | Al | P | Si | |
| SAPO(20) STA-7 [†] (SAV) | H ⁺ | 1.00 | 0.73 | 0.27 | 0.29 |
| SAPO STA-7* (SAV) | H ⁺ | 1.00 | 0.69 | 0.31 | |
| K-SAPO(20) STA-7 ^{††} (SAV) (microcalorimetry data)** | K ⁺ 63% | 1.00 | 0.73 | 0.27 | 0.18 |
| SAPO(20) STA-14 [♦] (KFI) | H ⁺ | 0.90 | 0.77 | 0.23 | 0.33 |
| AIPO-34 [‡] (CH) | - | 1.00 | 1.00 | - | 0.23 |
| SAPO-34 ^{‡‡} (CHA) | H ⁺ | 1.00 | 0.67 | 0.33 | 0.28 |
| AIPO STA-2 [§] (SAT) | - | 1.00 | 1.00 | - | 0.21 |
| SAPO STA-2 ^{§§} (SAT) | H ⁺ | 1.00 | 0.56 | 0.44 | 0.23 |

*The SAPO STA-7 sample was provided by S. Warrender (synthesised in presence of fluoride).

**K-SAPO STA-7 sample was analysed by adsorption and associated microcalorimetry at MADIREL, Marseille, within the INDENS project.

***The internal pore volumes for all the samples were determined from N₂ adsorption isotherms at 77 K.

7.2.3 Results

7.2.3.1 CO₂ Adsorption on AIPO and SAPO STA-2

The total uptake of CO₂ on a microporous solid depends on both its structure and composition. It was observed previously that for the CHA topology, the neutral SiO₂ composition adsorbs much less strongly than the SAPO composition. Fig. 7.11 compares the adsorption isotherms for AIPO-34 and SAPO STA-7 (with very similar structures) and also AIPO STA-2 and SAPO STA-2.

The most important factor is the structure. Whereas in the D6R materials SAPO STA-7 and AIPO-34 only the volume within the D6Rs is inaccessible to CO₂, in STA-2 both the D6Rs and the CAN cages are inaccessible. This is apparent from the pore volumes measured by N₂ adsorption and also from the CO₂ uptakes, comparing either SAPO or AIPO compositions.

The framework composition also has a strong effect. Inclusion of silicon in the framework and its associated framework charge strongly enhances CO₂ uptake. In fact at low pressures between zero up to 0.5 bars, SAPO STA-2 shows higher uptake than AIPO-34 due to the stronger interaction of the Brønsted sites of the framework (related to the silicon content) with the quadrupolar CO₂. (N.B. The uptake in the sample of SAPO STA-2 is likely to be slightly higher than in pure SAPO STA-2 because this sample contains admixed SAPO-56, which has a slightly larger specific adsorption uptake because its structure does not have inaccessible cancrinite cages).

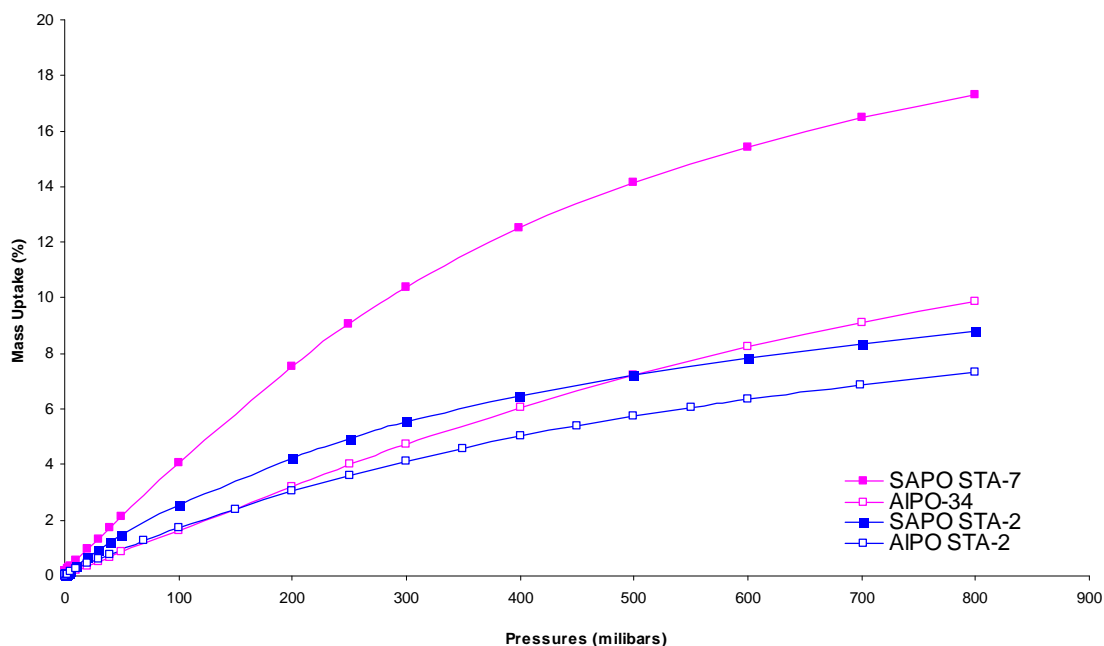


Fig. 7.11 Adsorption isotherms for CO₂ at 273 K for SAPO and AIPO STA-2, SAPO STA-7 and AIPO-34.

7.2.3.2 CO₂ Adsorption on SAPO STA-7 with Different Silicon Distribution

Comparison of samples of SAPO STA-7 with different silicon distribution and AIPO-34 indicates that the AIPO framework has the lowest CO₂ uptake. The CO₂ uptake depends not only on the silicon content but also on its distribution within the framework. The

SAPO STA-7 sample containing silica islands Si(4Si) possesses a lower uptake in comparison with the same material at same silicon content but with only Si(4Al) environments. The reason is that in silica islands Si(4Si), the silicon atom in the central position of the island (see the diagram of Fig. 7.12) imparts no negative charge, in contrast with Si(4Al) environments where all the silicon atoms impart a negative charge because they substitute for phosphorus (V).

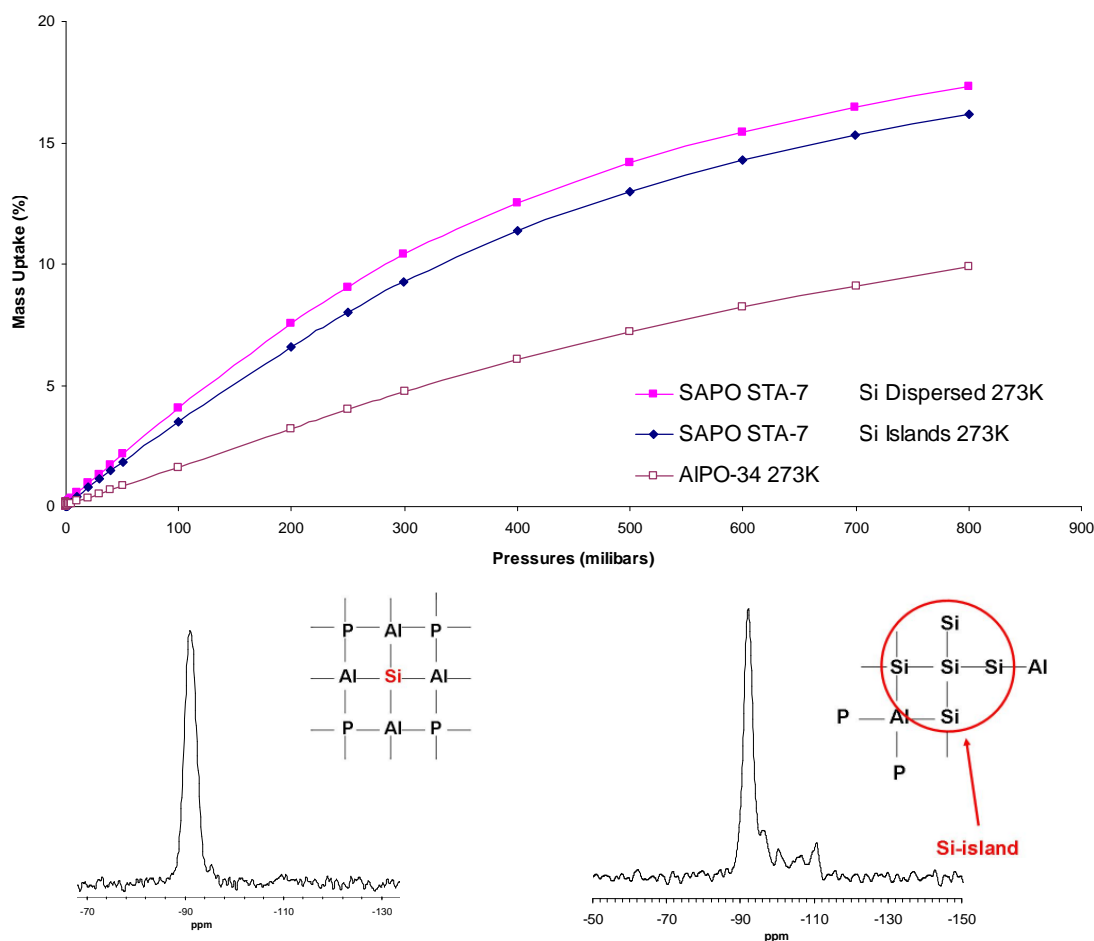


Fig. 7.12 Adsorption isotherms for CO₂ at 273 K of SAPO STA-7 with Si/Al ratio ca. 0.3 and silica islands (²⁹Si MAS NMR bottom right) and without silica islands (²⁹Si MAS NMR bottom left) and AIPO-34.

7.2.3.3 Heats of Adsorption

In order to obtain heats of adsorption of CO₂ in the SAPO ‘D6R’ materials STA-7 (SAV), STA-14 (KFI) and SAPO-34, CO₂ isotherms were collected at three or four temperatures (Fig. 7.13).

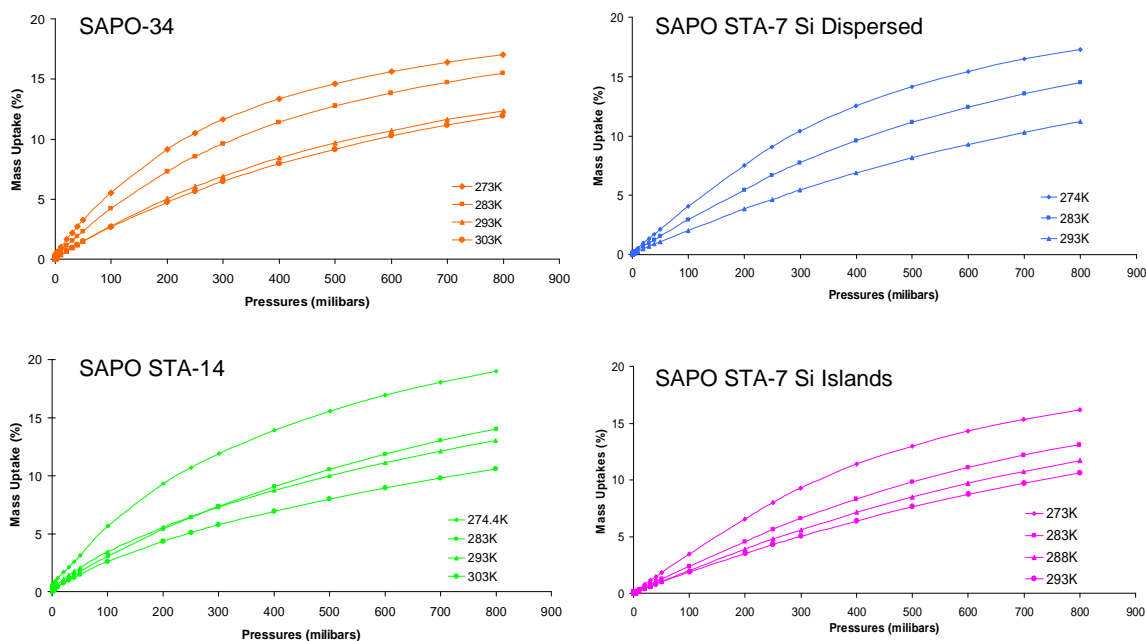


Fig. 7.13 CO_2 reversible adsorption isotherms at four temperatures of SAPO-34, SAPO STA-7 with the two different distributions of silicon and SAPO STA-14.

From these data the isosteres were plotted using the pressure values for 10wt% of coverage (at which the data have good resolution) giving the following heats of adsorption summarised in Table 7.4:

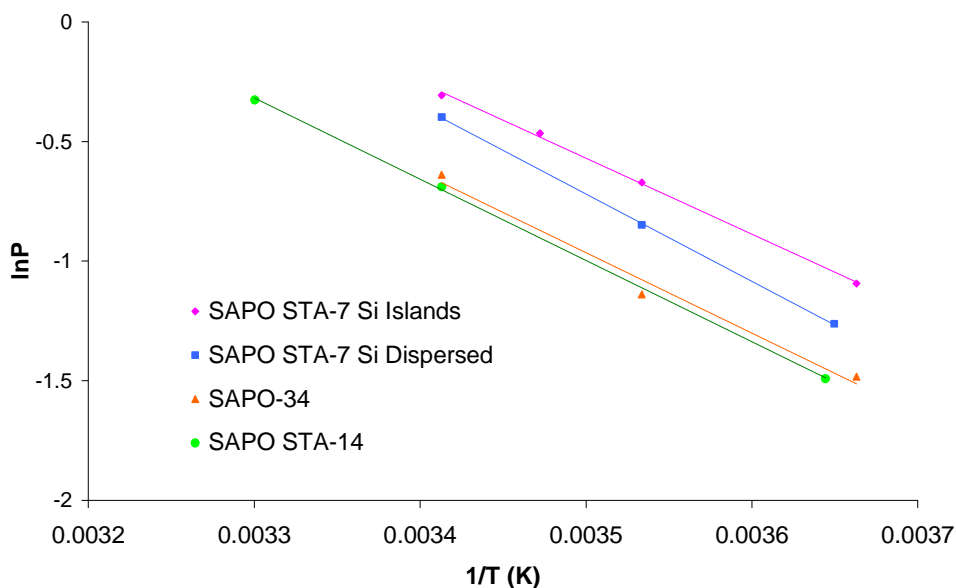


Fig. 7.14 Isosteres presented using the experimental data (dots) and the linear regression fits to obtain from the slope the heats of adsorption summarised in Table 7.4.

Table 7.4 *Heats of adsorption for the SAPO version of D6R materials at 10wt% uptake.*

| Sample | Heats of Adsorption (kJ/mol) |
|-------------------------|------------------------------|
| | Isosteric Method |
| SAPO STA-7 Si Dispersed | 30.4(1) |
| SAPO STA-7 Si Islands | 28.3(1) |
| SAPO STA-14 | 26.4(1) |
| SAPO-34 | 28.0(1) |

The heats of adsorption obtained for all the materials are similar due their topological similarities, at about 30 kJ/mol. The adsorption behaviour on SAPO STA-7 has been studied in more detail by INDENS partners based in Marseille (MADIREL) and Montpellier, the first experimentally by adsorption and associated microcalorimetry and the second using theoretical approaches (DFT). Their results (Fig. 7.15) give heats of adsorption closer to 40 kJ/mol. In addition, SAPO STA-7 was studied experimentally by these partners after cation exchange with K^+ , see Table 7.5. The CO_2 isotherm shows a lower uptake due to the decrease of the total pore volume ($0.18 \text{ cm}^3/\text{g}$) and there is no strong increase in the associated enthalpies of adsorption.

Table 7.5 *Comparison of the values of heats of adsorption obtained by three different methods at 10wt% of coverage.*

| Sample | ΔH_{ads} (kJ/mol) | | |
|--------------|----------------------------------|-------------------|-----|
| | Isosteric | Microcalorimetric | DFT |
| SAPO STA-7 | 30 | 40 | 39 |
| K-SAPO STA-7 | - | 40 | - |

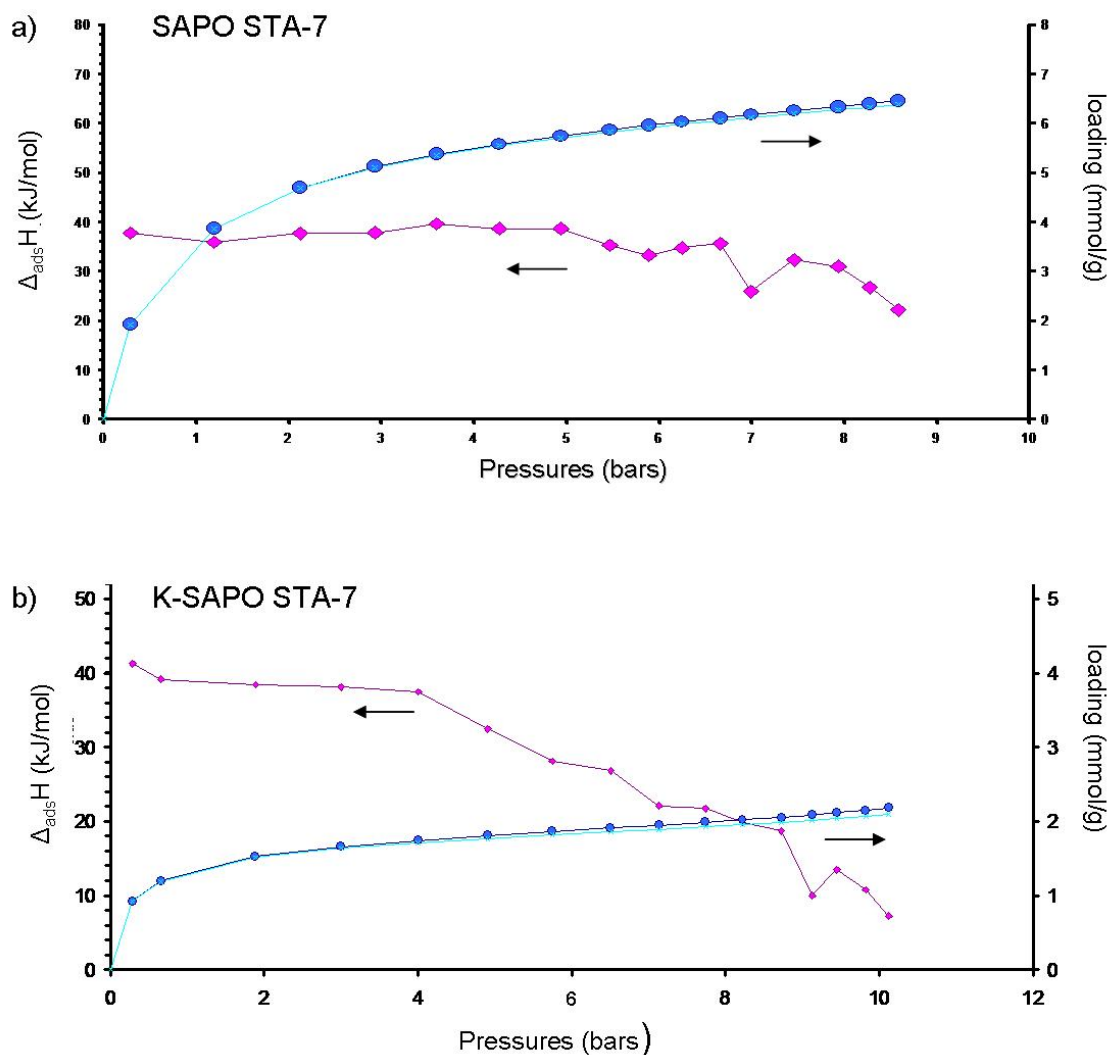


Fig. 7.15 Enthalpy of adsorption vs CO₂ isotherm for SAPO STA-7(a) and the K⁺ ion exchange form (b) which shows a lower uptake due to the decrease of the total pore volume (0.18 cm³/g) without strong increase in the associated enthalpies of adsorption. Data collected by L. Gaberova at MADIREL (INDENS).

7.2.4 Conclusions

This section shows that the CO₂ uptake depends strongly on the topology type of the framework, which determines the internal pore volume. The silicon content also plays an important role in the uptake as observed when comparing the uptake of SAPO STA-7 vs. AlPO-34. Finally the distribution of the silicon within the framework can influence the uptake, as observed for the uptake of SAPO STA-7 with silica islands. All these parameters should be taken into account to optimise the uptake of SAPO materials. By contrast, attempts to improve the adsorption properties by cation exchange with potassium ions were not successful.

7.3 Other Applications of Zeotypes

The D6R silicoaluminophosphate materials synthesised and characterised fully in this thesis were also used for further studies of adsorption, diffusion and catalysis in collaboration with external laboratories.

7.3.1 Argon Adsorption as a Method to Give Details of Pore Structure Unresolved by N₂ Adsorption

During the course of this project very well defined samples of silicoaluminophosphates STA-7 and STA-14 were obtained, in each of which there were two types of cages of different size accessible to small molecule adsorbates. As a result, it was felt that these would act as interesting model compounds to calibrate the use of argon porosimetry to determine the pore size of SAPOs with cage structures.

Argon shows almost ideal behaviour for pore size analysis because it is spherical and does not give specific interactions with surface functional groups or extra framework cations during adsorption. As a consequence, argon fills micropores of dimension 5 to 10 Å at much higher relative pressure ($10^{-5} < P/P_o < 10^{-3}$) than nitrogen and therefore its adsorption is able to resolve between pores of similar sizes.

High-resolution isotherms of argon at 87.3 K were measured and analysed to investigate if the small differences in pore size and geometry of the cages within STA-7 and STA-14 could be resolved. These measurements were performed by Dr. Fernando Rey Garcia at the Instituto de Tecnología Química in Valencia (Spain). Experimental conditions are given in Appendix (section A.1.1).

The following graphs (Fig. 7.16) show the argon isotherms at 87 K and the pore distribution for SAPO STA-7 and STA-14, calculated using the Horvath-Kawazoe model applying a modified interaction parameter relevant to aluminophosphates (this method was first reported for activated carbons).¹⁹

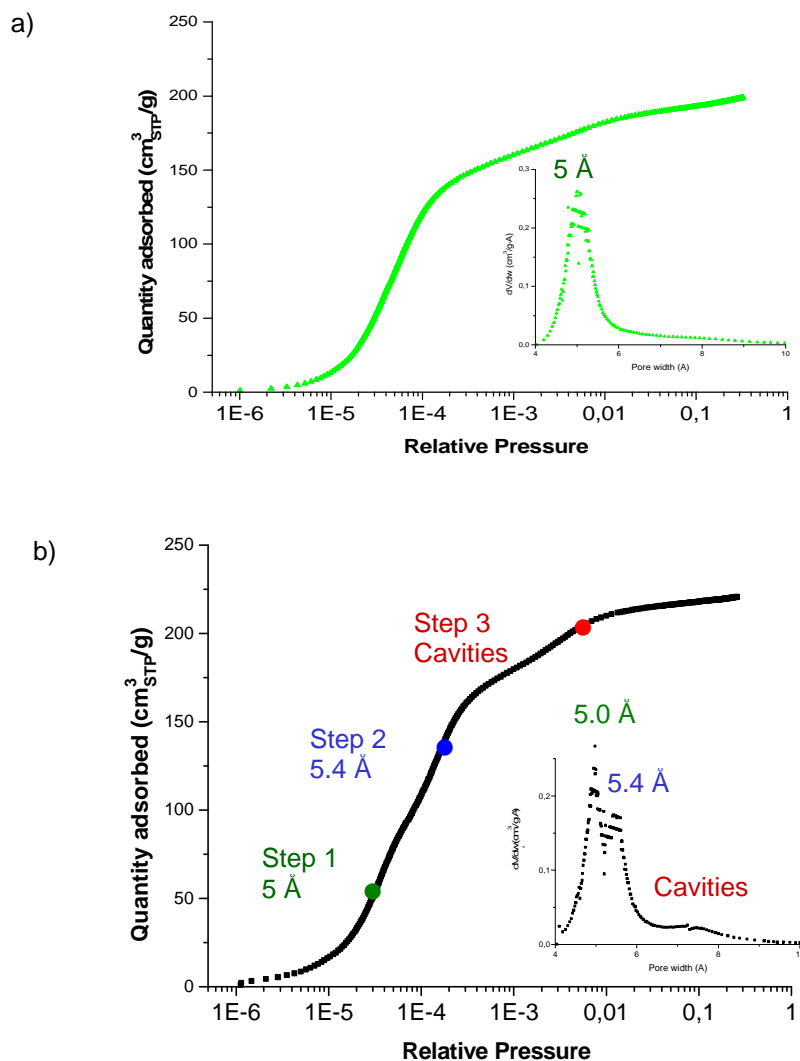


Fig. 7.16 Argon isotherms and pore distribution for SAPO STA-7 (a) and STA-14 (b).

For the case of STA-7 (Fig. 7.16 a), the first step observed is attributed to the monolayer of argon adsorbed close to the cage walls. A step at high partial pressure is probably due to occluded argon molecules in the centre of the larger cavities (B cage) where the adsorption uptakes correspond to 1-2 atoms of argon per cage. Although STA-7 possesses two types of cages (Fig. 7.17), the resolution of the argon adsorption is insufficient to distinguish between them (7.5 mmol/g or $170\text{ cm}^3_{\text{STP/g}}$).

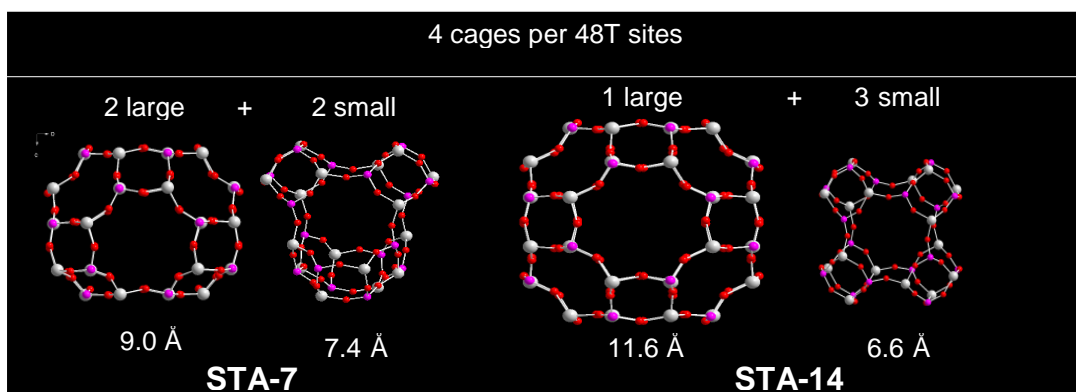


Fig. 7.17 STA-7 and STA-14 cages with their minimum diameter within the cage.

By contrast, the argon isotherm for STA-14 shows three steps (Fig.7.16 b). These can be attributed to the monolayer of argon in the two cages -the smaller cages in STA-14, the MER cages are filled first (4.0 mmol/g or 90 cm³_{STP}/g) followed by the larger α -cages (3.7 mmol/g or 85 cm³_{STP}/g)- and a third step corresponds to argon molecules adsorbed in the centre of the α cavities, corresponding to nine atoms of argon per α -cage.

The following graph (Fig. 7.18) shows the plot of the relative pressures at which the maxima of the pore distribution appears for STA-7 and STA-14 vs. the diameter of the largest sphere inscribed in the cages. It can be observed that the pressure of the uptake of argon increases depending on the size of the cage. For STA-14, the two cages can be distinguished due their large difference in size and therefore in uptake pressure. For STA-7 the uptake for each cage is unresolved because the size difference between cages is not so large.

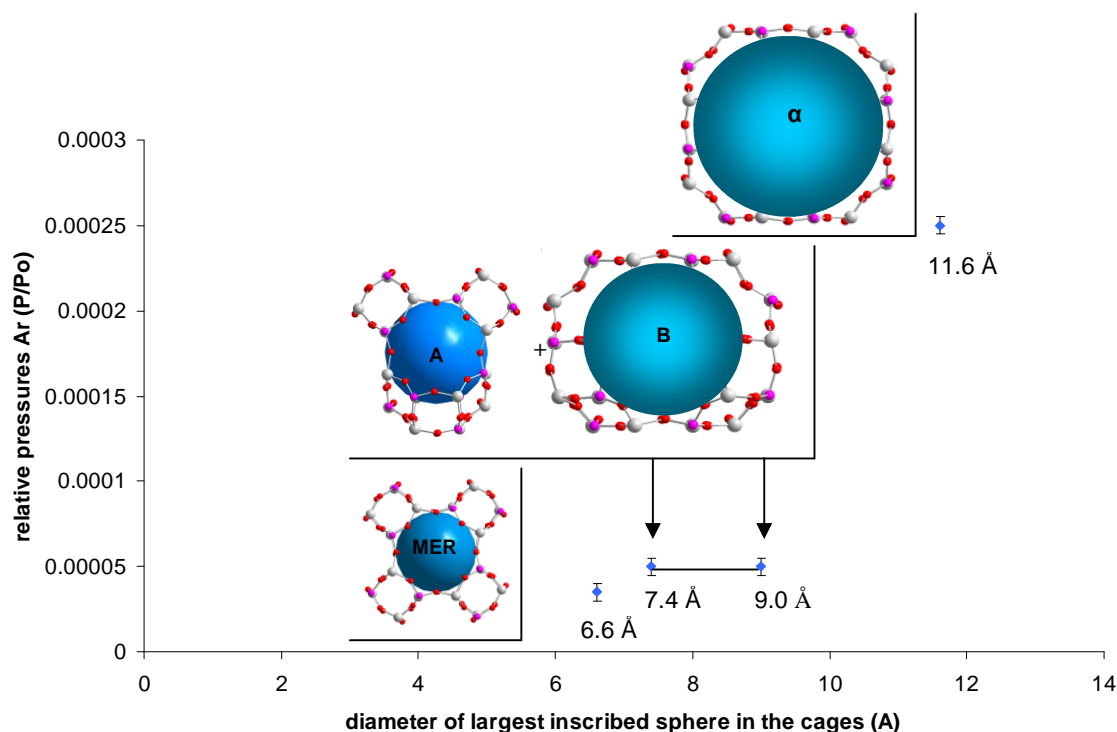


Fig. 7.18 Graphic showing the uptakes of argon for the different cages of STA-7 (A and B cages) and STA-14 (MER and α -cages).

In conclusion, argon isotherms at 87 K discriminate the differences in cage sizes between STA-7 and STA-14. These differences will influence their properties.

7.3.2 Direct Observation of the Diffusion of Methanol in a Single Crystal of SAPO STA-7 by Interference Optical Microscopy (IFM)

Diffusion of adsorbate molecules through the free pore space of microporous materials is an essential step in processes such as adsorption and catalysis. Diffusion results from numerous displacements caused by the interaction between the particle (in our case the gas molecules) and the surroundings (the pore channels or cages within the structure) resulting in their motion.

Diffusion studies performed with PFG (Pulsed Field Gradient) NMR (which monitors molecular displacement in the direction of the applied magnetic field) give diffusion information at equilibrium (self diffusion, D_s), see Fig. 7.19. In this case, the uptake has

achieved thermodynamic equilibrium, with the chemical potential of the adsorbed molecules being equal to the chemical potential of the molecules in gas phase. Although this gives a macroscopic picture it does not directly reveal the process. Diffusion depends strongly on the interaction between the gas molecules and the framework and therefore structural defects (such as stacking faults, growth defects and surface barriers) play an important role. This information can be obtained under non-equilibrium conditions (transport diffusion, D_t), see Fig. 7.19. Recently, the technique of interference microscopy (IFM) has been developed to follow diffusion on the microscopic scale under non-equilibrium conditions. IFM provides a method for the direct observation of transport diffusion on a micron scale when a single crystal is exposed to gas molecules by monitoring the intracrystalline concentration profiles.

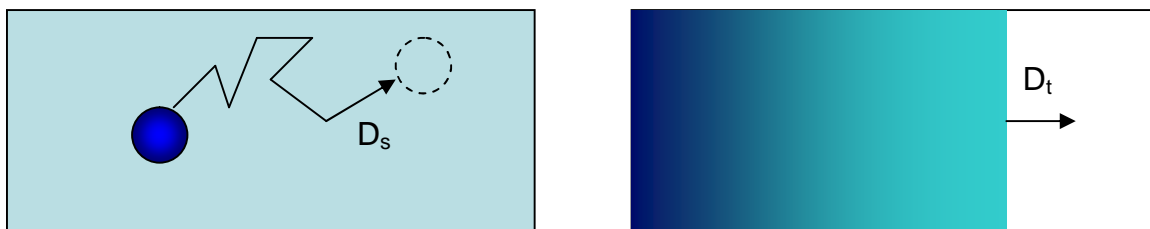


Fig. 7.19 Schematic description of self diffusion to study at equilibrium state (left) and transport diffusion to study diffusion under non-equilibrium conditions (right).

Zeolites are in general optically transparent. So it is possible to monitor the internal concentration profiles by optical observation. In this way, the IFM method is based on the fact that the refractive index (n) of a medium is a function of its composition, in this case of the concentration of the guest molecules within the crystal. The difference in the optical densities between the crystallite and the surroundings produces a phase difference in the respective beams. The change of the intracrystalline concentration of sorbents affects the phase difference of a beam light passing through the crystal. That makes it possible to obtain transport diffusivities as a function of loading under non-equilibrium conditions at spatial and temporal resolutions of $0.5 \times 0.5 \mu\text{m}^2$ and 10 seconds, respectively, for each direction of the crystal.

As part of the INDENS project, SAPO(20) STA-7 crystals up to 50 μm in size were prepared with perfect tetragonal prismatic morphology and used as a model system for IFM for the measurement of methanol diffusion at room temperature. The measurements were carried out by Despina Tzoulaki (INDENS) and other members of the Leipzig group of Professor Karger, and it has been possible for the first time to extract anisotropic concentration diffusion coefficients (parallel to the a , b and c axes of STA-7).²⁰

As already described, STA-7 possesses two types of cages that differ in shape and size (A and B) connected to each other via windows made up of rings of eight tetrahedral cations and eight oxygen atoms (8MRs). These cages are three dimensionally connected; along the z direction the connectivity of STA-7 is via two parallel paths: one between A cages only (window size of 3.2 \AA) and the other between only B cages (window size of 4.1 \AA), see Fig. 7.20. In x and y direction there is only one path connecting A and B cages (window size of 3.5 \AA).

The self diffusivity coefficients related to each direction were obtained (Table 7.6). These values show anisotropic transport in perfect agreement with the inner cage description of STA-7 where in the z direction the value is twice as large as in the x and y direction. This is likely to be because inter-cage diffusion along z direction is mainly possible via the larger windows along the path that connect B cages (4.1 \AA) rather than along x and y direction where the smallest pore diameter is 3.5 \AA .

Table 7.6 Self diffusivity coefficients along x , y and z related to the inner cage description of STA-7 with the windows size obtained from the refinement data of the calcined form assuming van der Waals radii of the oxygen atoms of 1.35 \AA , see also Fig. 7.20.

| STA-7 (SAV) | Direction | | | |
|---|-----------|----------|----------|--------|
| | x | y | z | |
| Path Type | A-B | A-B | B | A |
| Window Size (\AA) | 3.5 | 3.5 | 4.1 | 3.2 |
| Window Shape | flat | flat | flat | curved |
| Self Diff Coef (m^2/s) $\cdot 10^{-14}$ | 4.5 | 4.2 | 8.5 | |

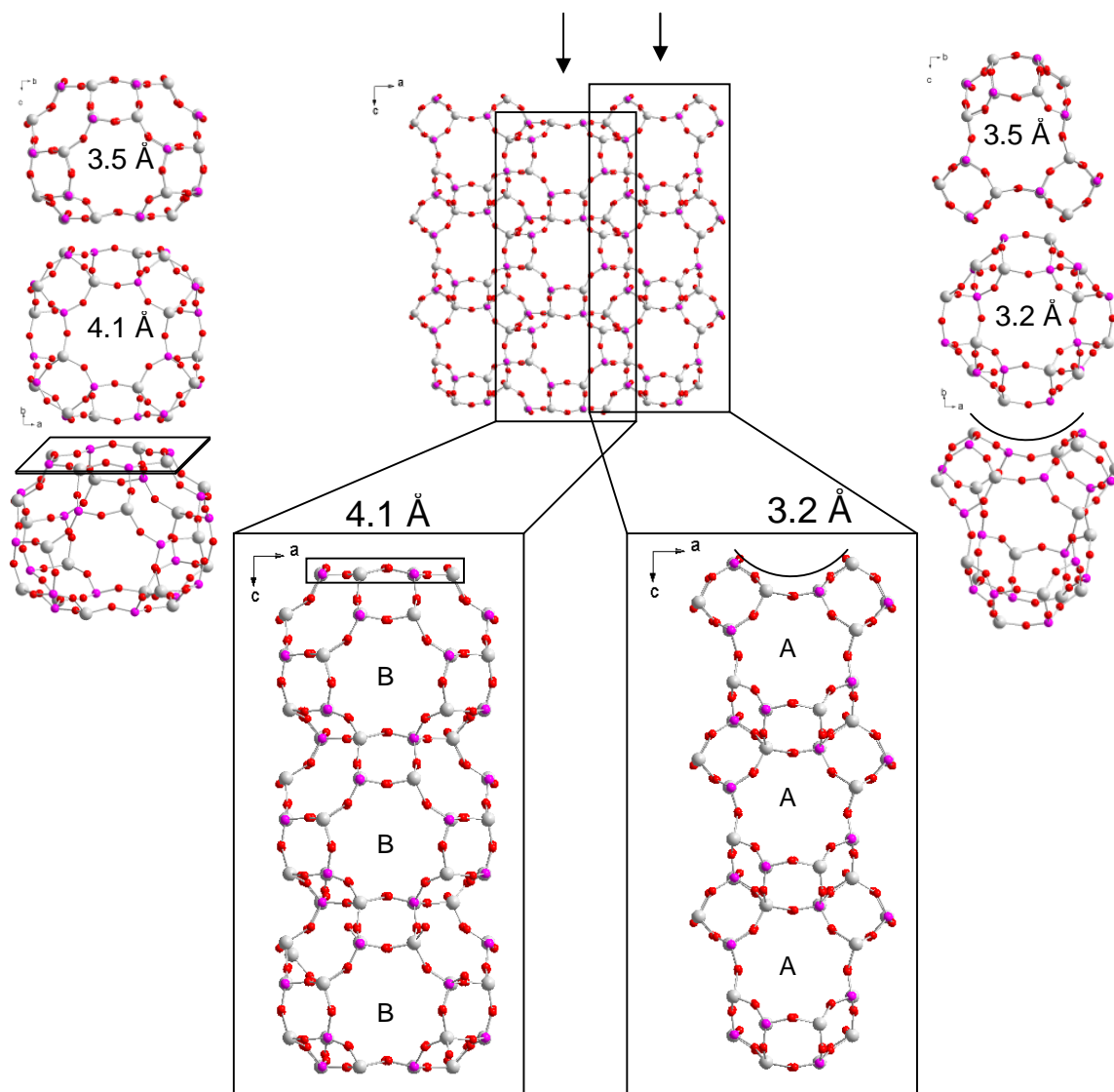


Fig. 7.20 STA-7 structure viewed along *b* axis, showing in detail the two paths that run along the *z* direction, one connecting only B cages with a flat window of 4.1 Å and the other connecting A cages with a much smaller oval window of 3.2 Å making it very difficult for the gas probe molecule to access the pore. Along *x* and *y* directions both cages are intercalated one after the other having the same window size of 3.5 Å.

In conclusion, interference microscopy (IFM) shows the influence of the structure of the framework in determining rates of diffusion. The following figure (Fig. 7.21) summarises the IFM technique and the results on SAPO STA-7. This information is fundamental to the performance of STA-7 in the methanol-to-olefins (MTO) conversion described in the next section.

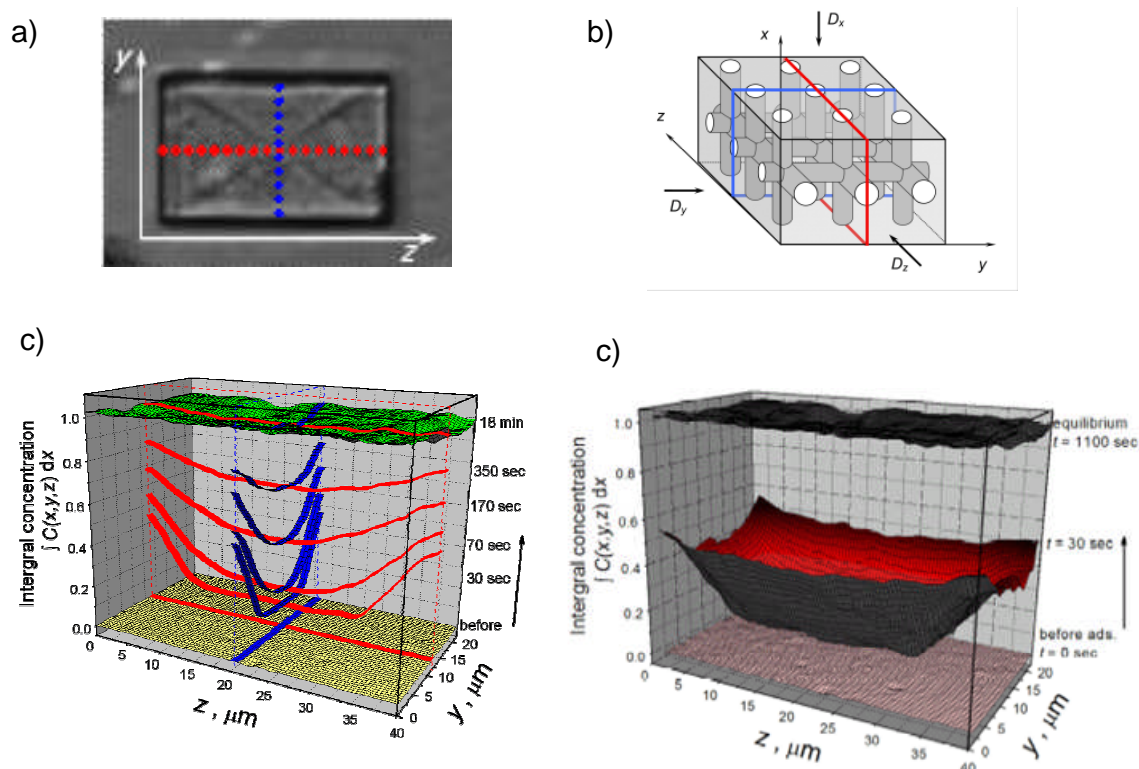


Fig. 7.21 Interference optical microscopy of the adsorption of methanol into perfect single crystals* of SAPO STA-7 shows directly how the alcohol diffuses into the crystal as a function of time (a). The schematic pore system of the crystal with the two light beams, one passing through the crystal and the other unperturbed through the surroundings (b). Time dependent concentration profiles measured in orthogonal sections (c) and the full concentration profile after 30 seconds (d). * This technique requires transparent single crystals with a minimum size of $20\ \mu\text{m} \times 20\ \mu\text{m}$. (Courtesy of P. Kurtunov, D. Tzoulakis, J. Kaerger, Leipzig University).

7.3.3 Catalysis: the Conversion of Methanol to Olefins (MTO)

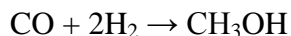
Aluminosilicate zeolites are widely used as solid acid catalysts in industrial important reactions, including isomerisation, alkylation, oligomerisation and the cracking of alkanes, alkenes and aromatics.²¹ For example the highly siliceous synthetic zeolite ZSM-5 (MFI) was introduced in 1972 as a powerful heterogeneous catalyst,²² its acid strength being similar to H_2SO_4 (80%).²³

In addition, aluminophosphate microporous solids modified by inclusion of tetravalent silicon cations (SAPOs) or divalent metal cations (MAPOs) into the frameworks give solid acid catalysts which are in general less strongly acidic than zeolites. These materials

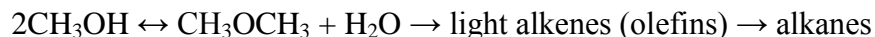
also have industrial applications; in particular SAPOs as catalysts for the methanol-to-hydrocarbons technology (MTHC).

MTHC had been developed since the '70s energy crisis to find an alternative route to crude oil products.²⁴ This technology is based on methanol and can make a range of products. Two important reactions due their potential economic impact are methanol-to-gasoline (MTG) and methanol-to-olefins (MTO) technologies.

Methanol itself can be produced from syngas (a mixture of carbon monoxide and hydrogen) via the reaction:



The MTO reaction steps are as follows:



Methanol is dehydrated to dimethyl ether (DME) and water in equilibrium. Light olefins (alkenes) are formed using a small pore catalyst such as SAPO zeotypes, whereas a medium pore catalyst such as the zeolite ZSM-5 (MFI) tends to form paraffins and aromatics (MTG).

One example of a SAPO material used commercially in MTO is SAPO-34 (CHA) by UOP /Norsk Hydro to obtain ethylene and propylene selectively, two important monomers for plastic production.¹¹

This section covers the conversion of methanol-to-olefins reaction (MTO) using as acid catalysts SAPO STA-7 (SAV) and the novel SAPO STA-14 (KFI), and having as a reference catalyst SAPO-34 (CHA).

The previous section (7.3.2) showed that methanol diffused into the SAV structure of STA-7 and showed that this diffusion was anisotropic.

MTO reactions were performed at POSTECH (South Korea) in collaboration with Dr. Suk Bong Hong and his student Hyung-Ki Min, who also provided the SAPO-34(s) sample (experimental details are included in Appendix D, section D.2). The following table 7.7 summarises the materials used:

Table 7.7 *Composition of catalysts applied for the MTO reaction (SEM images in Fig. 7.22). The sections that describe the synthesis of the samples used here are as follows: (†) 3.3.1.2; (◆) 4.3.2.3; (‡) from verified synthesis recipe modified by eliminating the addition of water in step (6) of the preparation from reference 12.*

| Material | Synthetic Method | Si/Al (EDX) | Crystal Size | SEM image |
|--|---|----------------|---------------------|--------------|
| SAPO(20) STA-7 [†] (SAV) (large = l) | Scale-up Static and Teflon liner | 0.31 | ~50 μm | a) |
| SAPO STA-7 (SAV) (small = s) | Provided by S. Warrender | 0.20 | 10-15 μm | b) |
| SAPO(20) STA-14 [◆] (KFI) | Scale-up Static and Teflon liner | 0.21 | 5-10 μm | c) |
| SAPO-34 [‡] (CHA) (large = l) | St Andrews Modified recipe Ref ¹² | 0.44 | ~20 μm | d) |
| SAPO-34 (CHA) (small = s) | POSTECH | 0.21 | 2-5 μm | e) |

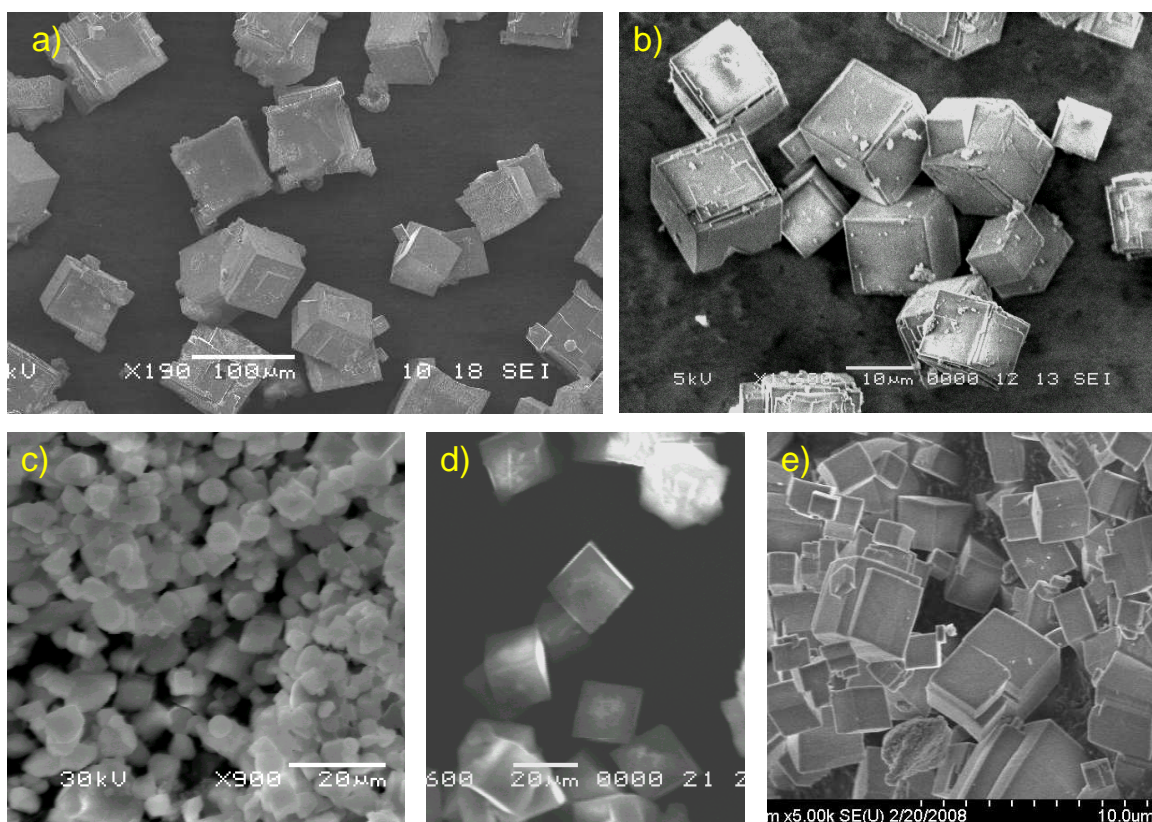


Fig. 7.22 SEM images of the catalyst applied for the MTO reaction disclosed in Table 7.7.

Prior to MTO reaction, the strength and density of Brønsted acid sites were characterised by temperature-programmed desorption (TPD) of a base, in this case ammonia (NH_3). Once the samples are degassed, ammonia vapour is adsorbed at 373 K. The experiment starts by heating in a temperature-programmed manner and passing an inert gas through the sample. The amount of ammonia desorbed is detected. The area under desorption curves are related to the number of acid sites, while the temperature of desorption is related to the acid strength.

The profiles for the five samples are very similar with one main desorption peak around 400 °C for SAPO-34(s) and SAPO STA-14, 430 °C for SAPO-34(l) and SAPO STA-7(s) and in the case of SAPO STA-7(l) at 450 °C (Fig. 7.23). That means that in all samples the Brønsted acid sites are of similar strength and present in similar quantity. This enables their performance in MTO to be related to particle size and structure.

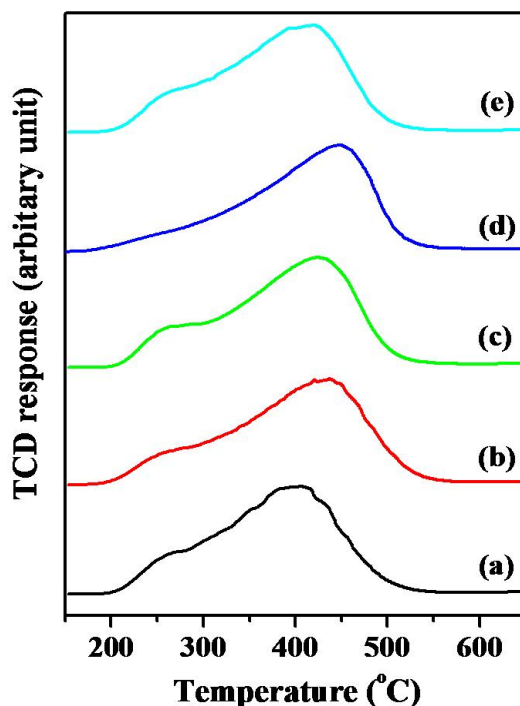


Fig. 7.23 NH_3 -TPD profiles of (a) SAPO-34(s), (b) SAPO-34(l), (c) SAPO STA-7(s), (d) SAPO STA-7(l), and (e) SAPO STA-14.

The results of the MTO reaction (Fig. 7.24) show that the best performance is for SAPO-34(s), followed closely by the novel SAPO STA-14, for which the conversion starts to decrease after 100 min. The sample SAPO-34 with larger crystals shows a much more rapid loss of activity compared with the sample with smaller crystal size, due to diffusion difficulties that arise as the pores become filled with aromatic molecules. SAPO STA-7 shows a rapid loss of activity for both crystal sizes. This can in part be explained with reference to the diffusion measured on this material by IFM, i.e. the presence of the small windows that connect A and B cages along x and y directions with $3.5 \times 3.5 \text{ \AA}$ windows, making this SAPO effectively a material with a one-dimensional pore system leading to severe diffusional limitations.

The catalysts remain crystalline after the MTO reaction showing similar stability to SAPO-34. (See figure 7.26 where the XRD patterns of the samples are compared before and after MTO reaction).

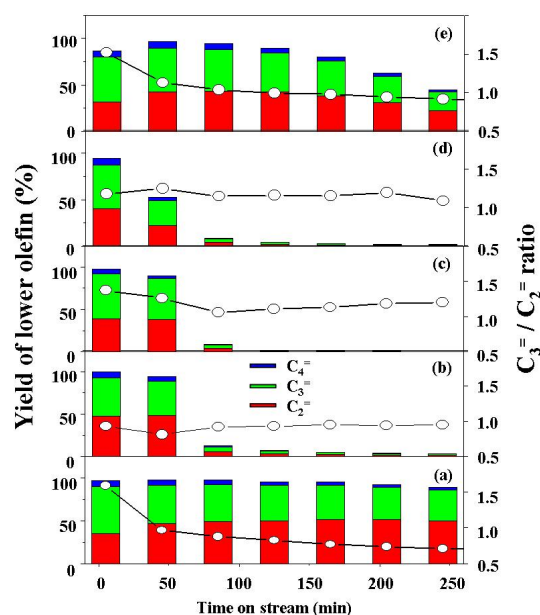


Fig. 7.24 Yield of lower olefins over (a) SAPO-34(s), (b) SAPO-34(l), (c) STA-7(s), (d) STA-7(l), and (e) STA-14 in the MTO reactions with the time on stream at 350 °C and 0.67 h⁻¹ WHSV.

The SAPO STA-14 performs at rates closer to the optimum material SAPO-34(s) because it is acting as a true three dimensional system, where the flat 8MR window of the α -cage is also the merlionite cage window, giving to SAPO STA-14 a better accessibility to the acid sites and also promoting the diffusion of the molecules (Fig. 7.25). Table 7.8 summarises the dimensions of the 8MR windows for each catalyst.

Table 7.8 Table with the size and shape of 8MR windows along the three directions for the catalysts apply in MTO reaction, (c: curve window; f: flat window).

| | | |
|--|--|--|
| CHA* | $3.8 \times 3.8 \text{ \AA}$ | |
| STA-14 (KFI)** | $4.2 \times 4.2 \text{ \AA}$ (f) α -cage | $4.2 \times 4.2 \text{ \AA}$ MER cage (f) $3.6 \times 3.6 \text{ \AA}$ MER cage (c) |
| STA-7 (SAV)** | $3.2 \times 3.2 \text{ \AA}$ path A (c) [001] $4.1 \times 4.1 \text{ \AA}$ path B (f) [001] | $3.5 \times 3.5 \text{ \AA}$ path (F) <100> |
| * IZA Atlas of Zeolites | | |
| **SAPO STA-14 and STA-7 data from refined structures in calcined form. | | |

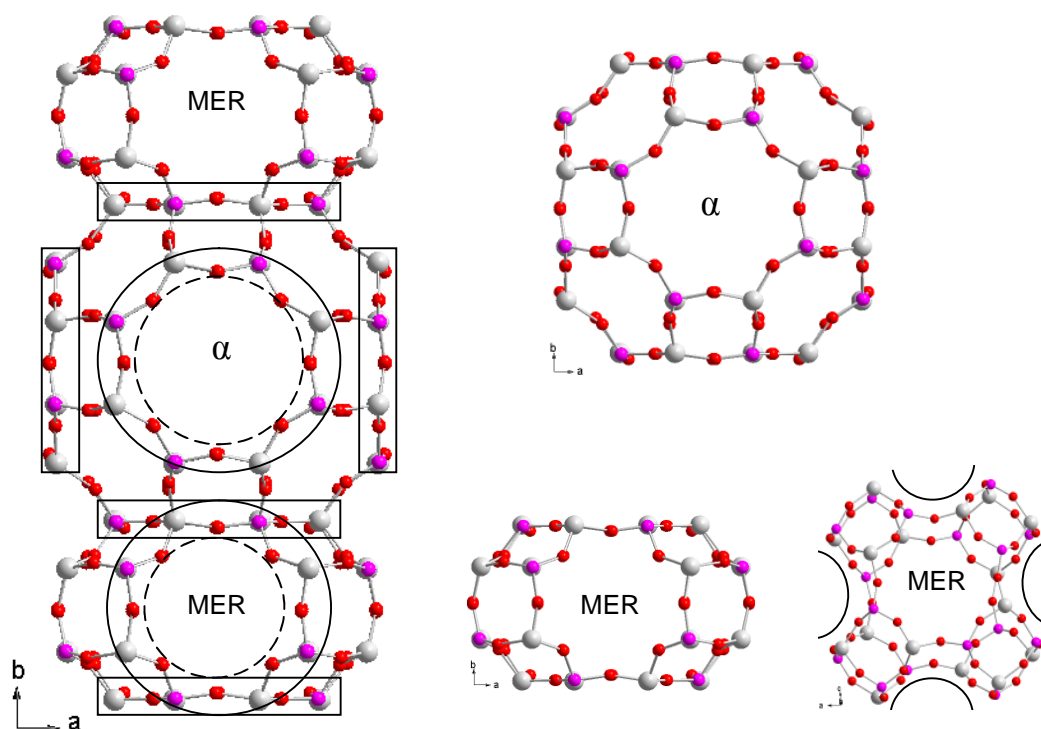


Fig. 7.25 SAPO STA-14 cage interconnection between the 8MR flat windows of MER and α -cages along x , y and z direction (left). In detail, alpha cage and MER cage (right).

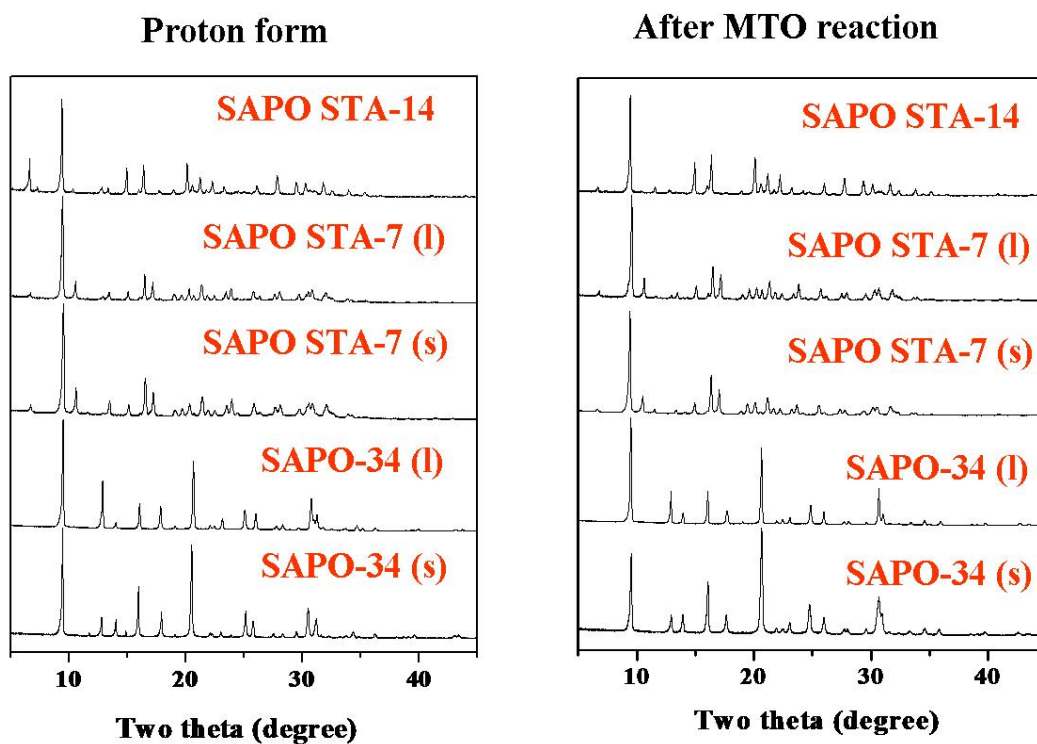


Fig. 7.26 XRD patterns of SAPO-based catalysts before and after MTO reaction at 350 °C for 250 min.

In conclusion, the best activity and lifetime is possessed by the small SAPO-34 crystals, followed by SAPO STA-14. The topology plays an important part in the catalytic performance of the materials, suggesting that in SAPO STA-14 the interconnected pore system act as a true three dimensional system whereas SAPO STA-7 acts as a one-dimensional material. That shows that although the crystal size can influence the performance, as observed for SAPO-34, the structural features are also important to determine the performance of SAPOs in catalytic reactions of this sort.

As further work, experiments will be continued on using very small crystals of SAPO STA-7.

-
1. A. Veawab, P. Tontiwachwuthikul, A. Chakma, *Ind. Eng. Chem. Res.*, 1999, **38**, 3917.
 2. R. J. Hook, *Ind. Eng. Chem. Res.*, 1997, **36**, 1779.
 3. S.S. Kapdi *et al.*, *Renewable Energy*, 2004, **20**, 1.
 4. P. A. Wright, '*Microporous Framework Solids*', RSC, Cambridge, 2008, 302.
 5. N. Konduru, P. Lindner, N. M. Assaf-Anid, *AIChE Journal*, 2007, **53**, 3137.
 6. V. G. Gomes, K. W. K. Yee, *Separation and Purification Technology*, 2007, **28**, 161.
 7. J. A. Delgado, M. A. Uguina, J. L. Sotelo, B. Ruiz, M. Rosario, *Journal of Natural Gas Chemistry*, 2007, **16**, 235.
 8. S. Cavenati, C. A. Grande, A. E. Rodrigues, *J. Chem. Eng. Data*, 2004, **49**, 1095.
 9. N. N. Dutta, G. S. Patil, *Gas Separation & Purification*, 1995, **9**, 277.
 10. D. P. Dee, R. L. Chiang, 2004, US Patent 6824590.
 11. M. Stoecker, *Micropor. Mesopor. Mater.*, 1999, **29**, 3.
 12. H. Hobson, K. P. Lillerud, '*Verified Synthesis of Zeolitic Materials*', 2nd Edition, Elsevier, Amsterdam, 2001.
 13. I. Deroche, L. Gaberova, G. Maurin, M. Castro, P.A. Wright, P. Llewellyn, *J. Phys. Chem.*, 2008, **112**, 50.48.
 - 14 G. Maurin, P. Llewellyn, R. G. Bell, *J. Phys. Chem. B*, 2005, **109**, 16084.
- 270

-
15. Y. Belmabkhout, G. Pirngruber, E. Jolimaître, A. Methivier, *Adsorption*, 2007, **13**, 341.
 16. P. Llewellyn, S. Bourrelly, C. Serre, A. Vimont, M. Daturi, L. Hamon, G. De Weireld, J. Chang, D. Hong, Y. K. Hwang, S. H. Jhung, G. Férey, *Langmuir*, 2008, 10.1021/la800227x.
 17. I. Déroche, L. Gaberova, G. Maurin, P. Llewellyn, M. Castro, P. Wright, *Adsorption*, 2008, **14**, 207.
 18. S. R. Miller, P. A. Wright, C. Serre, T. Loiseau, J. Marrot, G. Férey, *Chem. Commun.*, 2005, 3850.
 19. G. Horwath, K. Kawazoe, *Journal of Chemical Engineering of Japan*, 1983, **16**, 470.
 20. L. Heinke, P. Kortunov, D. Tzoulaki, M. Castro, P. A. Wright, J. Kaerger, *European Physics Letters*, 2008, **81**, 26002.
 21. A. Corma, *Chem. Rev.*, 1995, **95**, 559.
 22. R. J. Argauer, G. R. Landolt, 1972, US Patent 3702886.
 23. P. A. Wright, '*Microporous Framework Solids*', RSC, Cambridge, 2008, 319.
 24. K. W. Betz, 'Remembering the Energy Crisis', *Energy User News*, 1998, December, 4.

Chapter 8: Summary & Further Work

The aim of this research was the synthesis of zeotype materials for the INDENS project and the study of their performance in gas adsorption and separation particularly of CO₂. The importance of this relates to the increasing demand for capture and storage of CO₂, the main greenhouse gas implicated in the global warming effect on Earth.

Zeotype materials were chosen due their similarities to zeolites which have been applied for PSA technology for CO₂ adsorption and separation but that require high pressures or temperature for regeneration of the sorbent due to strong interaction between the gas molecule and the extraframework cations present in cationic zeolites.

As a key material for the project, SAPO STA-7 (SAV) prepared from previous synthesis work was investigated in detail and its synthesis modified. As a result the new route gave perfect single tetragonal crystals which are interesting not only for adsorption but for other techniques such as interference microscopy and atomic force microscopy in combination with high resolution scanning electron microscopy. One of the scientific fundamentals of this thesis was to investigate the co-templating effect in cage-like

materials to control the final structure of the material. The experimental results in STA-7 demonstrated the co-templating effect of TEA in the small cage of STA-7 to favour its crystallisation over that of STA-6, the phase in competition. Further in this line of research, the implementation of modelling approaches to design potential co-templates gave the novel zeotype STA-14 which possesses two types of cages. As a continuation in the application of modelling, the design of a cheaper template for STA-2 was predicted and experimentally proven.

In our opinion under the optimal gel conditions, the use of more than one template in cage materials is the key factor to control the synthesis. The use of modelling as a preliminary step increases the success of the experimentally efforts, decreasing cost and time, since it is able to hypothetically screen the co-bases with potential role as structure directing agents (SDAs).

Structural details have been provided, where the co-template tetraethylammonium cation (TEA) shows different conformations when it is templating the A cage and the MER cage for STA-7 and STA-14, respectively. The pure AlPO version of those materials using the template/co-template pair was not prepared, due to structural features that make impossible the formation of Al-OH or Al-F species in the structure to provide the charge balance to accommodate the charged template. That is demonstrated with the successful synthesis for the first time of the pure AlPO(OH) version of STA-2, where the synchrotron refinement data suggests the formation of Al-OH-Al bonds, making possible the incorporation of the template DABCO_C4^{2+} .

The materials, STA-7, STA-14 and STA-2 were tested at high and low pressures for CO_2 adsorption and their performance compared with industrial zeolite NaX (FAU) and the zeotype SAPO-34 (CHA). It is observed that these materials could be competitive in performance with zeolites because the total uptake is very similar and at low pressures when the regeneration of the sorbent would take place its uptake is lower than for NaX, where already at 1 bar the uptake is high. (For zeolites, therefore regeneration requires

the application of heat or vacuum). It has been proved the SAPO STA-7 remains stable after calcination and it does not loss crystallinity with time once calcined.

Furthermore, the adsorption data were compared with the novel metal organic framework MIL-101. These new materials have higher uptakes compared to zeolites and zeotypes due to very large cages in their structures and for MIL-101 at 1 bar the uptake is in the same range as zeotypes (Table 5.2). Their thermal and chemical stability will determine whether they will be substitutes for zeolites in specific applications, but these materials already have a strong investment recently from industry and academia. For example, the company BASF SE works in collaboration with one of the strongest groups focused in this area led by Omar M. Yaghi (Caltech).

As further work the synthesis of metal organic frameworks is evidently interesting and as a result, the synthesis of yttrium and ytterbium metal organic frameworks was undertaken in an attempt to obtain analogues of the scandium terephthalate microporous material recently reported by Miller *et al.*¹ This research has so far given six novel phases, mainly layered materials. One of them, $\text{Yb}_2(\text{O}_2\text{CC}_{12}\text{H}_8\text{CO}_2)_3$, (Fig. 8.1) is made up of isolated YbO_6 linked by biphenyl groups and exhibits structural features for the formation of open frameworks due to the low ytterbium coordination (octahedral) and simple mode of ligand binding, encouraging further exploratory synthesis.

The other topic to develop is the use of designed templates for zeotypes materials in combination with the co-templating approach to obtain hypothetical structures or only presented as zeolites build up from more than one cage.

Both areas of research would be strongly benefited from high-throughput synthesis and modelling approaches. For the case of zeotypes, the implementation of a modelling method where ‘*de novo*’ design of templates could be obtained as well as a data base with all the possible combinations guest-host will be very useful to designed the synthesis for a tailor structure. In the case of metal organic frameworks, modelling approaches to give

the favoured combination of metal-organic clusters would help in the investigation of a reticular synthesis.

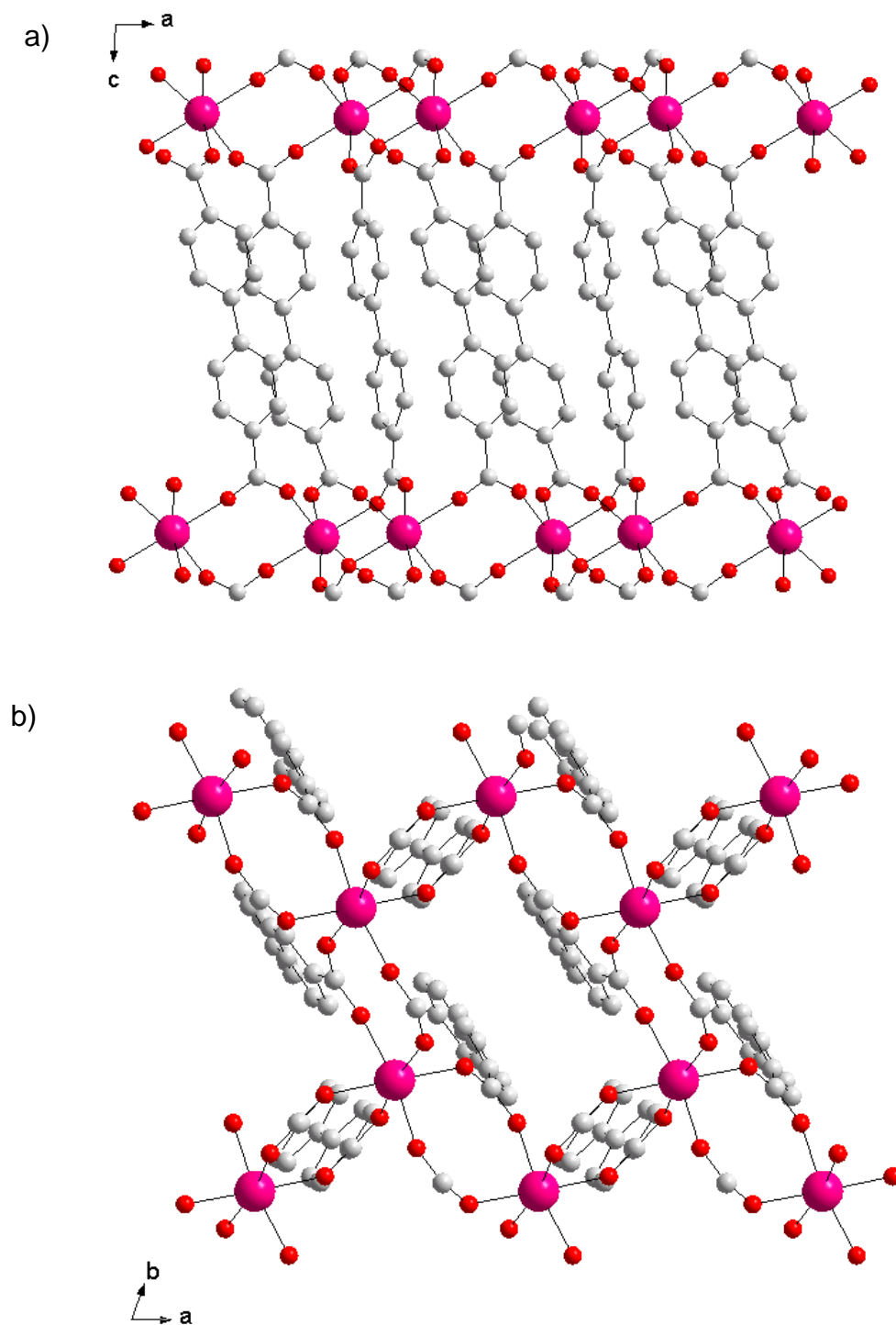


Fig. 8.1 The framework of $\text{Yb}_2(\text{O}_2\text{CC}_{12}\text{H}_8\text{CO}_2)_3$ viewed down the *a*-axis (a) and *c*-axis (b).

-
1. S. R. Miller, P. A. Wright, C. Serre, T. Loiseau, J. Marrot, G. Férey, *Chem. Comm.*, 2005, 3850.

Appendix A

Single X-Ray Data

In this Appendix atomic coordinates and temperature factors obtained by single X-ray diffraction are presented for as-prepared SAPO(20) STA-7, Cs-SAPO(20) STA-7, as-prepared MgAPO(20) STA-14 and the novel MgAPO layer phase. Selected bond lengths and angles are also given. Tables were provided by Prof. A. M. Z. Slawin.

Table A.1 *Crystal data and structure refinement for as-prepared SAPO(20) STA-7 (SAV).*

| | |
|-----------------------------------|---|
| Empirical formula | C32.40 H97.60 Al24 N9 O107 P18.50 Si5.50 |
| Formula weight | 3700.55 |
| Temperature | 93(2) K |
| Wavelength | 0.71073 Å |
| Crystal system | Tetragonal |
| Space group | P4/n |
| Unit cell dimensions | $a = b = 18.656(15)$ Å $\alpha = \beta = \gamma = 90^\circ$. $c = 9.378(7)$ Å |
| Volume / Z | $3264(4)$ Å ³ / 1 |
| Density (calculated) | 1.883 Mg/m ³ |
| Absorption coefficient | 0.578 mm ⁻¹ |
| F(000) | 1878 |
| Crystal size | 0.0300 x 0.0280 x 0.0100 mm ³ |
| Theta range for data collection | 1.54 to 25.37°. |
| Index ranges | -22 ≤ h ≤ 16, -21 ≤ k ≤ 19, -11 ≤ l ≤ 11 |
| Reflections collected | 22423 |
| Independent reflections | 2985 [R(int) = 0.2217] |
| Completeness to theta = 25.00° | 99.1 % |
| Absorption correction | Multiscan |
| Max. and min. transmission | 1.0000 and 0.0566 |
| Refinement method | Full-matrix least-squares on F ² |
| Data / restraints / parameters | 2985 / 0 / 200 |
| Goodness-of-fit on F ² | 1.180 |
| Final R indices [I > 2σ(I)] | R1 = 0.1027, wR2 = 0.1940 |
| R indices (all data) | R1 = 0.1581, wR2 = 0.2180 |
| Largest diff. peak and hole | 0.594 and -0.559 e.Å ⁻³ |

Table A. 2 Atomic coordinates ($\times 10^4$) and equivalent isotropic displacement parameters ($\text{\AA}^2 \times 10^3$) for as-prepared SAPO(20) STA-7 (SAV). $U(eq)$ is defined as one third of the trace of the orthogonalised U^{ij} tensor.

| Atom | x | y | z | U(eq) |
|-------|----------|-----------|------------|----------|
| P(1) | 10671(1) | -1662(1) | 904(2) | 9(1) |
| O(1) | 9976(3) | -1575(3) | 38(5) | 20(1) |
| O(2) | 10570(3) | -1294(3) | 2344(5) | 16(1) |
| O(3) | 11307(3) | -1338(3) | 100(5) | 19(1) |
| O(4) | 10828(3) | -2446(3) | 1186(5) | 18(1) |
| Al(1) | 9545(1) | -1658(1) | -1586(2) | 11(1) |
| P(2) | 8343(1) | -492(1) | -1603(2) | 12(1) |
| O(5) | 8725(3) | -1229(3) | -1562(5) | 20(1) |
| O(6) | 8422(3) | -143(3) | -115(5) | 22(2) |
| O(7) | 7548(3) | -615(3) | -1970(6) | 19(1) |
| O(8) | 8664(3) | -7(3) | -2791(6) | 23(2) |
| Al(2) | 8335(1) | 639(1) | 856(2) | 10(1) |
| P(3) | 9439(1) | 656(1) | 3363(2) | 9(1) |
| O(9) | 8749(3) | 600(3) | 2483(5) | 20(1) |
| O(10) | 9838(3) | -57(3) | 3231(5) | 17(1) |
| O(11) | 9902(3) | 1286(3) | 2885(5) | 22(2) |
| O(12) | 9222(3) | 782(3) | 4923(5) | 14(1) |
| Al(3) | 10639(1) | -520(1) | 3345(2) | 10(1) |
| N(1) | 7500 | 2500 | 5000 | 28(4) |
| C(1A) | 8030(11) | 2948(11) | 4098(19) | 22(4) |
| C(1B) | 8035(14) | 2063(14) | 4120(30) | 48(7) |
| C(2) | 8414(7) | 2508(7) | 2967(12) | 49(4) |
| O(21) | 7500(20) | 20(20) | -5320(40) | 98(14) |
| O(22) | 8690(20) | -1320(20) | 2120(40) | 86(12) |
| O(23) | 7500 | -2500 | -3460(140) | 100(40) |
| O(24) | 7500 | -2500 | -2100(300) | 180(120) |
| O(25) | 7500 | -2500 | -1500(400) | 150(120) |
| O(26) | 7500 | -2500 | -900(200) | 140(90) |

Table A.3 Bond lengths (Å) and angles (°) for as-prepared SAPO(20) STA-7 (SAV).

| | | | |
|---------------|----------|----------------------|-----------|
| P(1)-O(4) | 1.515(6) | N(1)-C(1A)#6 | 1.546(19) |
| P(1)-O(2) | 1.527(5) | N(1)-C(1A) | 1.546(19) |
| P(1)-O(3) | 1.530(5) | N(1)-C(1A)#5 | 1.546(19) |
| P(1)-O(1) | 1.538(6) | N(1)-C(1A)#7 | 1.546(19) |
| O(1)-Al(1) | 1.729(5) | C(1A)-C(2) | 1.52(2) |
| O(2)-Al(3) | 1.727(5) | C(1A)-C(1B) | 1.65(3) |
| O(3)-Al(2)#1 | 1.718(6) | C(1A)-C(1B)#5 | 1.69(3) |
| O(4)-Al(2)#2 | 1.722(6) | C(1A)-C(1B)#6 | 1.99(3) |
| Al(1)-O(7)#2 | 1.726(6) | C(1B)-C(2) | 1.54(3) |
| Al(1)-O(5) | 1.727(6) | C(1B)-C(1A)#7 | 1.69(3) |
| Al(1)-O(11)#1 | 1.740(6) | C(1B)-C(1A)#6 | 1.99(3) |
| P(2)-O(7) | 1.539(6) | O(23)-O(24) | 1.2(3) |
| P(2)-O(6) | 1.547(5) | O(24)-O(25) | 0.6(5) |
| P(2)-O(5) | 1.549(6) | O(24)-O(26) | 1.1(4) |
| P(2)-O(8) | 1.555(5) | | |
| O(6)-Al(2) | 1.726(6) | O(4)-P(1)-O(2) | 107.7(3) |
| O(7)-Al(1)#3 | 1.726(6) | O(4)-P(1)-O(3) | 108.5(3) |
| O(8)-Al(3)#1 | 1.711(6) | O(2)-P(1)-O(3) | 110.7(3) |
| Al(2)-O(9) | 1.712(5) | O(4)-P(1)-O(1) | 110.9(3) |
| Al(2)-O(3)#1 | 1.718(6) | O(2)-P(1)-O(1) | 108.4(3) |
| Al(2)-O(4)#3 | 1.722(6) | O(3)-P(1)-O(1) | 110.6(3) |
| P(3)-O(11) | 1.526(6) | P(1)-O(1)-Al(1) | 147.9(4) |
| P(3)-O(10) | 1.530(6) | P(1)-O(2)-Al(3) | 147.9(4) |
| P(3)-O(9) | 1.532(5) | P(1)-O(3)-Al(2)#1 | 149.2(4) |
| P(3)-O(12) | 1.535(5) | P(1)-O(4)-Al(2)#2 | 149.1(4) |
| O(10)-Al(3) | 1.729(6) | O(7)#2-Al(1)-O(5) | 107.2(3) |
| O(11)-Al(1)#1 | 1.740(6) | O(7)#2-Al(1)-O(1) | 110.5(3) |
| O(12)-Al(3)#4 | 1.717(5) | O(5)-Al(1)-O(1) | 111.0(3) |
| Al(3)-O(8)#1 | 1.711(6) | O(7)#2-Al(1)-O(11)#1 | 109.9(3) |
| Al(3)-O(12)#4 | 1.717(5) | O(5)-Al(1)-O(11)#1 | 110.4(3) |
| N(1)-C(1B)#5 | 1.53(3) | O(1)-Al(1)-O(11)#1 | 107.8(3) |
| N(1)-C(1B)#6 | 1.53(3) | O(7)-P(2)-O(6) | 110.9(3) |
| N(1)-C(1B) | 1.53(3) | O(7)-P(2)-O(5) | 108.4(3) |
| N(1)-C(1B)#7 | 1.53(3) | O(6)-P(2)-O(5) | 107.9(3) |

| | | | |
|----------------------|-----------|-----------------------|-----------|
| O(7)-P(2)-O(8) | 107.4(3) | C(1B)#6-N(1)-C(1A)#6 | 64.9(12) |
| O(6)-P(2)-O(8) | 111.4(3) | C(1B)-N(1)-C(1A)#6 | 80.5(12) |
| O(5)-P(2)-O(8) | 110.9(3) | C(1B)#7-N(1)-C(1A)#6 | 66.5(11) |
| P(2)-O(5)-Al(1) | 145.0(4) | C(1B)#5-N(1)-C(1A) | 66.5(11) |
| P(2)-O(6)-Al(2) | 145.3(4) | C(1B)#6-N(1)-C(1A) | 80.5(12) |
| P(2)-O(7)-Al(1)#3 | 148.7(4) | C(1B)-N(1)-C(1A) | 64.9(12) |
| P(2)-O(8)-Al(3)#1 | 147.6(4) | C(1B)#7-N(1)-C(1A) | 171.1(12) |
| O(9)-Al(2)-O(3)#1 | 108.7(3) | C(1A)#6-N(1)-C(1A) | 113.7(14) |
| O(9)-Al(2)-O(4)#3 | 106.4(3) | C(1B)#5-N(1)-C(1A)#5 | 64.9(12) |
| O(3)#1-Al(2)-O(4)#3 | 108.2(3) | C(1B)#6-N(1)-C(1A)#5 | 66.5(11) |
| O(9)-Al(2)-O(6) | 113.1(3) | C(1B)-N(1)-C(1A)#5 | 171.1(12) |
| O(3)#1-Al(2)-O(6) | 109.2(3) | C(1B)#7-N(1)-C(1A)#5 | 80.5(12) |
| O(4)#3-Al(2)-O(6) | 111.0(3) | C(1A)#6-N(1)-C(1A)#5 | 107.4(7) |
| O(11)-P(3)-O(10) | 111.7(3) | C(1A)-N(1)-C(1A)#5 | 107.4(7) |
| O(11)-P(3)-O(9) | 111.7(3) | C(1B)#5-N(1)-C(1A)#7 | 80.5(12) |
| O(10)-P(3)-O(9) | 107.8(3) | C(1B)#6-N(1)-C(1A)#7 | 171.1(12) |
| O(11)-P(3)-O(12) | 108.2(3) | C(1B)-N(1)-C(1A)#7 | 66.5(11) |
| O(10)-P(3)-O(12) | 109.8(3) | C(1B)#7-N(1)-C(1A)#7 | 64.9(12) |
| O(9)-P(3)-O(12) | 107.6(3) | C(1A)#6-N(1)-C(1A)#7 | 107.4(7) |
| P(3)-O(9)-Al(2) | 148.9(4) | C(1A)-N(1)-C(1A)#7 | 107.4(7) |
| P(3)-O(10)-Al(3) | 148.3(4) | C(1A)#5-N(1)-C(1A)#7 | 113.7(14) |
| P(3)-O(11)-Al(1)#1 | 148.1(4) | C(2)-C(1A)-N(1) | 113.1(13) |
| P(3)-O(12)-Al(3)#4 | 144.9(4) | C(2)-C(1A)-C(1B) | 57.8(12) |
| O(8)#1-Al(3)-O(12)#4 | 109.6(3) | N(1)-C(1A)-C(1B) | 57.1(12) |
| O(8)#1-Al(3)-O(2) | 111.8(3) | C(2)-C(1A)-C(1B)#5 | 142.3(16) |
| O(12)#4-Al(3)-O(2) | 106.7(3) | N(1)-C(1A)-C(1B)#5 | 56.3(11) |
| O(8)#1-Al(3)-O(10) | 110.5(3) | C(1B)-C(1A)-C(1B)#5 | 94.8(16) |
| O(12)#4-Al(3)-O(10) | 109.4(3) | C(2)-C(1A)-C(1B)#6 | 118.3(14) |
| O(2)-Al(3)-O(10) | 108.7(3) | N(1)-C(1A)-C(1B)#6 | 49.4(9) |
| C(1B)#5-N(1)-C(1B)#6 | 106.9(9) | C(1B)-C(1A)-C(1B)#6 | 89.7(15) |
| C(1B)#5-N(1)-C(1B) | 106.9(9) | C(1B)#5-C(1A)-C(1B)#6 | 83.5(14) |
| C(1B)#6-N(1)-C(1B) | 114.8(19) | N(1)-C(1B)-C(2) | 113.1(17) |
| C(1B)#5-N(1)-C(1B)#7 | 114.8(19) | N(1)-C(1B)-C(1A) | 58.0(11) |
| C(1B)#6-N(1)-C(1B)#7 | 106.9(9) | C(2)-C(1B)-C(1A) | 56.8(12) |
| C(1B)-N(1)-C(1B)#7 | 106.9(9) | N(1)-C(1B)-C(1A)#7 | 57.2(11) |
| C(1B)#5-N(1)-C(1A)#6 | 171.1(12) | C(2)-C(1B)-C(1A)#7 | 142.8(19) |

| | | | |
|-----------------------|-----------|-------------------|-----------|
| C(1A)-C(1B)-C(1A)#7 | 96.6(16) | C(1A)-C(2)-C(1B) | 65.4(13) |
| N(1)-C(1B)-C(1A)#6 | 50.1(10) | O(25)-O(24)-O(26) | 0.00(8) |
| C(2)-C(1B)-C(1A)#6 | 117.3(17) | O(25)-O(24)-O(23) | 180.00(8) |
| C(1A)-C(1B)-C(1A)#6 | 90.3(15) | O(26)-O(24)-O(23) | 180.00(3) |
| C(1A)#7-C(1B)-C(1A)#6 | 85.0(14) | | |

Table A.4 Anisotropic displacement parameters ($\text{\AA}^2 \times 10^3$) for as-prepared SAPO(20) STA-7 (SAV). The anisotropic displacement factor exponent takes the form: $-2p^2 [h^2 a^{*2} U^{11} + \dots + 2 h k a^* b^* U^{12}]$

| Atom | U ¹¹ | U ²² | U ³³ | U ²³ | U ¹³ | U ¹² |
|-------|-----------------|-----------------|-----------------|-----------------|-----------------|-----------------|
| P(1) | 12(1) | 4(1) | 12(1) | -2(1) | -1(1) | 0(1) |
| O(1) | 20(4) | 17(4) | 23(3) | 0(2) | -9(2) | 4(3) |
| O(2) | 24(4) | 10(3) | 13(2) | -6(2) | 3(2) | 0(3) |
| O(3) | 16(4) | 24(4) | 15(3) | 6(2) | 9(2) | -6(3) |
| O(4) | 20(4) | 8(3) | 27(3) | -3(2) | -6(2) | -3(3) |
| Al(1) | 10(1) | 6(1) | 16(1) | 2(1) | -1(1) | 1(1) |
| P(2) | 7(1) | 10(1) | 19(1) | -1(1) | 2(1) | 1(1) |
| O(5) | 13(3) | 20(4) | 27(3) | -4(2) | -3(2) | 1(3) |
| O(6) | 25(4) | 17(4) | 23(3) | -12(2) | -5(3) | 8(3) |
| O(7) | 8(3) | 20(4) | 29(3) | -8(2) | 2(2) | 1(3) |
| O(8) | 17(4) | 22(4) | 31(3) | 9(3) | 2(3) | -9(3) |
| Al(2) | 4(1) | 15(2) | 12(1) | -1(1) | 0(1) | -1(1) |
| P(3) | 7(1) | 13(1) | 8(1) | 1(1) | 0(1) | 2(1) |
| O(9) | 12(3) | 39(4) | 9(3) | 3(2) | -8(2) | -1(3) |
| O(10) | 16(3) | 11(3) | 26(3) | -4(2) | -4(2) | 7(3) |
| O(11) | 19(4) | 21(4) | 26(3) | 7(2) | 7(2) | -10(3) |
| O(12) | 17(3) | 18(3) | 7(2) | 2(2) | 2(2) | 8(3) |
| Al(3) | 14(1) | 10(1) | 7(1) | 1(1) | 2(1) | 4(1) |
| N(1) | 24(7) | 24(7) | 37(9) | 0 | 0 | 0 |
| C(2) | 60(10) | 40(8) | 47(7) | -2(6) | 22(6) | -2(7) |

Table A.5 *Crystal data and structure refinement for Cs-SAPO(20) STA-7 (SAV).*

| | |
|-----------------------------------|---|
| Empirical formula | Al ₂₄ Cs O ₉₆ P ₂₀ Si ₄ |
| Formula weight | 3048.19 |
| Temperature | 173(2) K |
| Wavelength | 1.54178 Å |
| Crystal system | Tetragonal |
| Space group | P 422 |
| Unit cell dimensions | $a = 18.508(3) \text{ Å}$ $\alpha = 90^\circ$. $b = 18.508(3) \text{ Å}$ $\beta = 90^\circ$. $c = 9.3221(12) \text{ Å}$ $\gamma = 90^\circ$. |
| Volume | 3193.3(8) Å ³ |
| Z | 1 |
| Density (calculated) | 1.585 Mg/m ³ |
| Absorption coefficient | 7.577 mm ⁻¹ |
| F(000) | 1491 |
| Crystal size | 0.02 x 0.02 x 0.02 mm ³ |
| Theta range for data collection | 3.38 to 44.68°. |
| Index ranges | -16 ≤ h ≤ 15, -16 ≤ k ≤ 16, -8 ≤ l ≤ 8 |
| Reflections collected | 15362 |
| Independent reflections | 1273 [R(int) = 0.2587] |
| Completeness to theta = 25.00° | 100.0 % |
| Absorption correction | multiscan |
| Max. and min. transmission | 0.8632 and 0.8632 |
| Refinement method | Full-matrix least-squares on F ² |
| Data / restraints / parameters | 1273 / 0 / 166 |
| Goodness-of-fit on F ² | 2.295 |
| Final R indices [I > 2σ(I)] | R1 = 0.2584, wR2 = 0.5521 |
| R indices (all data) | R1 = 0.3023, wR2 = 0.5753 |
| Largest diff. peak and hole | 3.731 and -1.176 e.Å ⁻³ |

Table A. 6 Atomic coordinates ($\times 10^4$) and equivalent isotropic displacement parameters ($\text{\AA}^2 \times 10^3$) for Cs-SAPO(20) STA-7 (SAV). $U(eq)$ is defined as one third of the trace of the orthogonalised U^{ij} tensor.

| Atom | x | y | z | U(eq) |
|-------|-----------|-----------|-----------|---------|
| Cs(1) | -2500 | 7500 | 2070(50) | 159(16) |
| P(3) | -1632(6) | 9524(8) | 1542(17) | 101(5) |
| P(5) | 530(7) | 9317(7) | 3380(14) | 86(5) |
| Si(1) | 673(8) | 8342(7) | -869(13) | 71(4) |
| Al(2) | -478(7) | 8341(6) | 1614(15) | 78(5) |
| Al(4) | -647(9) | 10500(8) | 3300(14) | 95(6) |
| Al(6) | 1655(8) | 9363(10) | 858(17) | 118(6) |
| O(1) | 546(14) | 8735(13) | -2330(20) | 79(8) |
| O(2) | 813(16) | 7574(17) | -1120(40) | 135(14) |
| O(3) | 0(20) | 8436(14) | -130(30) | 119(11) |
| O(4) | 1351(17) | 8629(14) | -70(30) | 98(9) |
| O(5) | -1282(13) | 8744(13) | 1580(40) | 112(11) |
| O(6) | -1307(18) | 10008(17) | 2810(30) | 117(11) |
| O(7) | -1545(15) | 9856(16) | -30(30) | 120(12) |
| O(8) | -2476(16) | 9272(19) | 1880(40) | 151(14) |
| O(9) | 104(13) | 10058(13) | 3060(30) | 80(8) |
| O(10) | 38(16) | 8694(16) | 2870(30) | 97(9) |
| O(11) | 1268(15) | 9403(15) | 2460(20) | 90(9) |
| O(12) | 769(13) | 9211(14) | 4940(20) | 82(9) |

Table A.7 Bond lengths (Å) and angles (°) for Cs-SAPO(20) STA-7 (SAV).

| | | | |
|---------------|-----------|---------------------|-----------|
| Cs(1)-O(5)#1 | 3.25(3) | Al(6)-O(11) | 1.66(2) |
| Cs(1)-O(5)#2 | 3.25(3) | Al(6)-O(4) | 1.71(3) |
| Cs(1)-O(5)#3 | 3.25(3) | O(1)-Al(4)#5 | 1.69(3) |
| Cs(1)-O(5) | 3.25(3) | O(2)-Al(6)#7 | 1.75(3) |
| Cs(1)-O(8)#1 | 3.28(4) | O(7)-Al(6)#5 | 1.65(3) |
| Cs(1)-O(8)#3 | 3.28(4) | O(8)-Al(2)#3 | 1.68(3) |
| Cs(1)-O(8)#2 | 3.28(4) | O(12)-Al(4)#4 | 1.74(2) |
| Cs(1)-O(8) | 3.28(4) | | |
| Cs(1)-Al(2)#1 | 4.074(13) | O(5)#1-Cs(1)-O(5)#2 | 88.9(3) |
| Cs(1)-Al(2)#2 | 4.074(13) | O(5)#1-Cs(1)-O(5)#3 | 88.9(3) |
| Cs(1)-Al(2)#3 | 4.074(13) | O(5)#2-Cs(1)-O(5)#3 | 163.9(19) |
| Cs(1)-Al(2) | 4.074(13) | O(5)#1-Cs(1)-O(5) | 163.9(19) |
| P(3)-O(5) | 1.58(3) | O(5)#2-Cs(1)-O(5) | 88.9(3) |
| P(3)-O(6) | 1.60(3) | O(5)#3-Cs(1)-O(5) | 88.9(3) |
| P(3)-O(7) | 1.59(3) | O(5)#1-Cs(1)-O(8)#1 | 43.7(7) |
| P(3)-O(8) | 1.66(3) | O(5)#2-Cs(1)-O(8)#1 | 46.4(7) |
| P(5)-O(10) | 1.55(3) | O(5)#3-Cs(1)-O(8)#1 | 132.4(8) |
| P(5)-O(12) | 1.54(2) | O(5)-Cs(1)-O(8)#1 | 135.1(8) |
| P(5)-O(11) | 1.62(3) | O(5)#1-Cs(1)-O(8)#3 | 46.4(7) |
| P(5)-O(9) | 1.61(3) | O(5)#2-Cs(1)-O(8)#3 | 135.1(8) |
| Si(1)-O(3) | 1.44(3) | O(5)#3-Cs(1)-O(8)#3 | 43.7(7) |
| Si(1)-O(1) | 1.56(3) | O(5)-Cs(1)-O(8)#3 | 132.4(8) |
| Si(1)-O(2) | 1.46(3) | O(8)#1-Cs(1)-O(8)#3 | 89.83(12) |
| Si(1)-O(4) | 1.55(3) | O(5)#1-Cs(1)-O(8)#2 | 132.4(8) |
| Al(2)-O(5) | 1.66(3) | O(5)#2-Cs(1)-O(8)#2 | 43.7(7) |
| Al(2)-O(8)#2 | 1.68(3) | O(5)#3-Cs(1)-O(8)#2 | 135.1(8) |
| Al(2)-O(10) | 1.64(3) | O(5)-Cs(1)-O(8)#2 | 46.4(7) |
| Al(2)-O(3) | 1.86(4) | O(8)#1-Cs(1)-O(8)#2 | 89.83(12) |
| Al(4)-O(6) | 1.59(3) | O(8)#3-Cs(1)-O(8)#2 | 174(2) |
| Al(4)-O(9) | 1.63(3) | O(5)#1-Cs(1)-O(8) | 135.1(8) |
| Al(4)-O(12)#4 | 1.74(2) | O(5)#2-Cs(1)-O(8) | 132.4(8) |
| Al(4)-O(1)#5 | 1.69(3) | O(5)#3-Cs(1)-O(8) | 46.4(7) |
| Al(6)-O(7)#5 | 1.65(3) | O(5)-Cs(1)-O(8) | 43.7(7) |
| Al(6)-O(2)#6 | 1.75(3) | O(8)#1-Cs(1)-O(8) | 174(2) |

| | | | |
|-----------------------|-----------|---------------------|-----------|
| O(8)#3-Cs(1)-O(8) | 89.83(11) | O(8)-Cs(1)-Al(2) | 66.4(5) |
| O(8)#2-Cs(1)-O(8) | 89.83(11) | Al(2)#1-Cs(1)-Al(2) | 168.1(13) |
| O(5)#1-Cs(1)-Al(2)#1 | 22.9(4) | Al(2)#2-Cs(1)-Al(2) | 89.38(13) |
| O(5)#2-Cs(1)-Al(2)#1 | 111.7(5) | Al(2)#3-Cs(1)-Al(2) | 89.38(13) |
| O(5)#3-Cs(1)-Al(2)#1 | 66.5(5) | O(5)-P(3)-O(6) | 109.9(18) |
| O(5)-Cs(1)-Al(2)#1 | 153.1(8) | O(5)-P(3)-O(7) | 109.2(19) |
| O(8)#1-Cs(1)-Al(2)#1 | 66.4(5) | O(6)-P(3)-O(7) | 115.2(19) |
| O(8)#3-Cs(1)-Al(2)#1 | 23.5(6) | O(5)-P(3)-O(8) | 97.1(16) |
| O(8)#2-Cs(1)-Al(2)#1 | 155.0(7) | O(6)-P(3)-O(8) | 112(2) |
| O(8)-Cs(1)-Al(2)#1 | 112.9(6) | O(7)-P(3)-O(8) | 112.1(18) |
| O(5)#1-Cs(1)-Al(2)#2 | 66.5(5) | O(5)-P(3)-Cs(1) | 47.6(10) |
| O(5)#2-Cs(1)-Al(2)#2 | 22.9(4) | O(6)-P(3)-Cs(1) | 124.7(15) |
| O(5)#3-Cs(1)-Al(2)#2 | 153.1(8) | O(7)-P(3)-Cs(1) | 120.0(14) |
| O(5)-Cs(1)-Al(2)#2 | 111.7(5) | O(8)-P(3)-Cs(1) | 49.6(12) |
| O(8)#1-Cs(1)-Al(2)#2 | 23.5(6) | O(10)-P(5)-O(12) | 111.6(17) |
| O(8)#3-Cs(1)-Al(2)#2 | 112.9(6) | O(10)-P(5)-O(11) | 114.1(15) |
| O(8)#2-Cs(1)-Al(2)#2 | 66.4(5) | O(12)-P(5)-O(11) | 105.6(15) |
| O(8)-Cs(1)-Al(2)#2 | 155.0(7) | O(10)-P(5)-O(9) | 106.9(16) |
| Al(2)#1-Cs(1)-Al(2)#2 | 89.38(13) | O(12)-P(5)-O(9) | 115.1(15) |
| O(5)#1-Cs(1)-Al(2)#3 | 111.7(5) | O(11)-P(5)-O(9) | 103.5(16) |
| O(5)#2-Cs(1)-Al(2)#3 | 153.1(8) | O(3)-Si(1)-O(1) | 103.3(18) |
| O(5)#3-Cs(1)-Al(2)#3 | 22.9(4) | O(3)-Si(1)-O(2) | 110.4(17) |
| O(5)-Cs(1)-Al(2)#3 | 66.5(5) | O(1)-Si(1)-O(2) | 109.8(19) |
| O(8)#1-Cs(1)-Al(2)#3 | 155.0(7) | O(3)-Si(1)-O(4) | 115.6(18) |
| O(8)#3-Cs(1)-Al(2)#3 | 66.4(5) | O(1)-Si(1)-O(4) | 112.3(16) |
| O(8)#2-Cs(1)-Al(2)#3 | 112.9(6) | O(2)-Si(1)-O(4) | 105.5(19) |
| O(8)-Cs(1)-Al(2)#3 | 23.5(6) | O(5)-Al(2)-O(8)#2 | 100.6(15) |
| Al(2)#1-Cs(1)-Al(2)#3 | 89.38(13) | O(5)-Al(2)-O(10) | 110.8(16) |
| Al(2)#2-Cs(1)-Al(2)#3 | 168.1(13) | O(8)#2-Al(2)-O(10) | 115.7(19) |
| O(5)#1-Cs(1)-Al(2) | 153.1(8) | O(5)-Al(2)-O(3) | 111.4(18) |
| O(5)#2-Cs(1)-Al(2) | 66.5(5) | O(8)#2-Al(2)-O(3) | 110.3(16) |
| O(5)#3-Cs(1)-Al(2) | 111.7(5) | O(10)-Al(2)-O(3) | 107.9(15) |
| O(5)-Cs(1)-Al(2) | 22.9(4) | O(5)-Al(2)-Cs(1) | 49.6(9) |
| O(8)#1-Cs(1)-Al(2) | 112.9(6) | O(8)#2-Al(2)-Cs(1) | 50.9(13) |
| O(8)#3-Cs(1)-Al(2) | 155.0(7) | O(10)-Al(2)-Cs(1) | 127.7(13) |
| O(8)#2-Cs(1)-Al(2) | 23.5(6) | O(3)-Al(2)-Cs(1) | 124.3(13) |

| | | | |
|----------------------|-----------|--------------------|-----------|
| O(6)-Al(4)-O(9) | 109.2(17) | Si(1)-O(3)-Al(2) | 145(2) |
| O(6)-Al(4)-O(12)#4 | 110.2(17) | Si(1)-O(4)-Al(6) | 141(2) |
| O(9)-Al(4)-O(12)#4 | 113.2(14) | P(3)-O(5)-Al(2) | 140.8(17) |
| O(6)-Al(4)-O(1)#5 | 114.2(16) | P(3)-O(5)-Cs(1) | 111.4(12) |
| O(9)-Al(4)-O(1)#5 | 104.7(14) | Al(2)-O(5)-Cs(1) | 107.4(11) |
| O(12)#4-Al(4)-O(1)#5 | 105.2(14) | P(3)-O(6)-Al(4) | 145(2) |
| O(7)#5-Al(6)-O(2)#6 | 110.4(16) | P(3)-O(7)-Al(6)#5 | 139(3) |
| O(7)#5-Al(6)-O(11) | 109.3(19) | P(3)-O(8)-Al(2)#3 | 142(2) |
| O(2)#6-Al(6)-O(11) | 107.5(19) | P(3)-O(8)-Cs(1) | 107.7(14) |
| O(7)#5-Al(6)-O(4) | 114.6(17) | Al(2)#3-O(8)-Cs(1) | 105.6(16) |
| O(2)#6-Al(6)-O(4) | 104.1(18) | P(5)-O(9)-Al(4) | 145.3(19) |
| O(11)-Al(6)-O(4) | 110.6(16) | P(5)-O(10)-Al(2) | 149(2) |
| Si(1)-O(1)-Al(4)#5 | 147.3(19) | P(5)-O(11)-Al(6) | 146.6(19) |
| Si(1)-O(2)-Al(6)#7 | 153(2) | P(5)-O(12)-Al(4)#4 | 144.8(16) |

Table A.8 Anisotropic displacement parameters ($\text{\AA}^2 \times 10^3$) for Cs-SAPO(20) STA-7 (SAV).
The anisotropic displacement factor exponent takes the form: $-2p^2 [h^2 a^{*2} U^{11} + \dots + 2 h k a^* b^* U^{12}]$

| Atom | U ¹¹ | U ²² | U ³³ | U ²³ | U ¹³ | U ¹² |
|-------|-----------------|-----------------|-----------------|-----------------|-----------------|-----------------|
| Cs(1) | 36(9) | 36(9) | 400(50) | 0 | 0 | 0 |
| P(3) | 48(9) | 107(12) | 149(14) | 5(10) | -14(8) | -7(7) |
| P(5) | 93(10) | 90(10) | 76(10) | -7(8) | 2(8) | 9(8) |
| Si(1) | 101(11) | 59(10) | 55(8) | 11(7) | 18(8) | 2(8) |
| Al(2) | 73(10) | 60(9) | 100(11) | -5(8) | -1(8) | -8(7) |
| Al(4) | 113(13) | 101(12) | 71(11) | 8(9) | -38(9) | 10(10) |
| Al(6) | 91(13) | 152(15) | 112(13) | -19(12) | 34(10) | -35(11) |
| O(1) | 110(20) | 74(18) | 59(18) | 12(16) | 8(16) | 16(15) |
| O(2) | 110(20) | 80(30) | 220(40) | 60(20) | 60(20) | -16(19) |
| O(3) | 190(40) | 70(20) | 100(20) | -26(17) | 30(30) | -30(20) |
| O(4) | 160(30) | 80(20) | 53(17) | -24(16) | -34(19) | 0(20) |
| O(5) | 41(16) | 53(18) | 240(30) | 0(20) | -30(20) | 10(15) |
| O(6) | 160(30) | 120(30) | 80(20) | -28(19) | -60(20) | 0(20) |
| O(7) | 110(20) | 110(20) | 130(30) | 90(20) | -50(20) | -30(20) |
| O(8) | 80(30) | 160(30) | 210(40) | 10(30) | 0(20) | 40(20) |
| O(9) | 65(18) | 71(19) | 100(20) | -20(15) | -4(15) | 28(16) |
| O(10) | 90(20) | 110(20) | 90(20) | -26(19) | 7(18) | 20(20) |
| O(11) | 110(20) | 130(20) | 35(16) | 3(16) | 32(16) | -3(17) |
| O(12) | 110(20) | 120(20) | 11(15) | 9(14) | 19(14) | 61(17) |

Table A.9 *Crystal data and structure refinement for MgAPO(20) STA-14 (KFI).*

| | | |
|-----------------------------------|---|----------|
| Empirical formula | C ₆₆ H ₂₄₆ Al ₃₈ Mg ₁₀ N ₁₀ O ₂₃₈ P ₄₈ | |
| Formula weight | 7743.63 | |
| Temperature | 93(2) K | |
| Wavelength | 0.71073 Å | |
| Crystal system | Cubic | |
| Space group | Pn-3n | |
| Unit cell dimensions | a = 18.9056(17) Å | α = 90°. |
| | b = 18.9056(17) Å | β = 90°. |
| | c = 18.9056(17) Å | γ = 90°. |
| Volume | 6757.3(11) Å ³ | |
| Z | 1 | |
| Density (calculated) | 1.903 Mg/m ³ | |
| Absorption coefficient | 0.575 mm ⁻¹ | |
| F(000) | 3950 | |
| Crystal size | 0.030 x 0.030 x 0.010 mm ³ | |
| Theta range for data collection | 3.05 to 25.33°. | |
| Index ranges | -21 ≤ h ≤ 22, -22 ≤ k ≤ 22, -22 ≤ l ≤ 22 | |
| Reflections collected | 55683 | |
| Independent reflections | 1034 [R(int) = 0.1899] | |
| Completeness to theta = 25.00° | 98.6 % | |
| Absorption correction | Multiscan | |
| Max. and min. transmission | 1.0000 and 0.9386 | |
| Refinement method | Full-matrix least-squares on F ² | |
| Data / restraints / parameters | 1034 / 0 / 68 | |
| Goodness-of-fit on F ² | 1.288 | |
| Final R indices [I > 2σ(I)] | R1 = 0.1320, wR2 = 0.2986 | |
| R indices (all data) | R1 = 0.1386, wR2 = 0.3030 | |
| Largest diff. peak and hole | 0.723 and -1.180 e.Å ⁻³ | |

Table A. 10 Atomic coordinates ($\times 10^4$) and equivalent isotropic displacement parameters ($\text{\AA}^2 \times 10^3$) for as-prepared MgAPO(20) STA-14 (KFI). $U(\text{eq})$ is defined as one third of the trace of the orthogonalised U^{ij} tensor.

| Atom | x | y | z | U(eq) |
|-------|-----------|----------|----------|---------|
| P(1) | 708(2) | 5517(1) | 6672(1) | 13(1) |
| Al(1) | -456(2) | 4317(2) | 6660(2) | 12(1) |
| O(1) | -3(4) | 5143(4) | 6602(4) | 19(2) |
| O(2) | 644(4) | 6211(4) | 6295(4) | 23(2) |
| O(3) | 866(5) | 5665(4) | 7445(4) | 28(2) |
| O(4) | 1294(4) | 5079(4) | 6367(4) | 23(2) |
| N(1) | -2500 | 2500 | 7500 | 16(5) |
| C(1) | -2059(18) | 3023(16) | 7046(18) | 44(6) |
| C(2) | -1525(11) | 2500 | 6525(11) | 50(6) |
| C(3) | -2500 | 3870(30) | 7500 | 21(11) |
| N(2) | -2500 | 7500 | 7500 | 30(12) |
| O(12) | -1300(40) | 6300(40) | 6300(40) | 130(50) |

Table A.11 Bond lengths (\AA) and angles ($^\circ$) for as-prepared MgAPO(20) STA-14 (KFI).

| | | | |
|--------------|----------|--------------|---------|
| P(1)-O(2) | 1.498(8) | N(1)-C(1)#9 | 1.55(3) |
| P(1)-O(4) | 1.499(8) | N(1)-C(1) | 1.55(3) |
| P(1)-O(3) | 1.517(8) | N(1)-C(1)#10 | 1.55(3) |
| P(1)-O(1) | 1.525(7) | N(1)-C(1)#11 | 1.55(3) |
| Al(1)-O(3)#1 | 1.772(8) | N(1)-C(1)#12 | 1.55(3) |
| Al(1)-O(4)#2 | 1.781(8) | C(1)-C(1)#9 | 1.69(4) |
| Al(1)-O(1) | 1.783(7) | C(1)-C(1)#7 | 1.69(4) |
| Al(1)-O(2)#3 | 1.800(8) | C(1)-C(2) | 1.72(4) |
| O(2)-Al(1)#4 | 1.800(8) | C(1)-C(3) | 2.00(5) |
| O(3)-Al(1)#1 | 1.772(8) | C(1)-C(1)#8 | 1.98(6) |
| O(4)-Al(1)#5 | 1.781(8) | C(2)-C(1)#8 | 1.72(4) |
| N(1)-C(1)#6 | 1.55(3) | C(3)-C(1)#9 | 2.00(5) |
| N(1)-C(1)#7 | 1.55(3) | C(3)-C(1)#7 | 2.00(5) |
| N(1)-C(1)#8 | 1.55(3) | C(3)-C(1)#11 | 2.00(5) |

| | | | |
|---------------------|----------|----------------------|-----------|
| O(2)-P(1)-O(4) | 111.1(5) | C(1)#8-N(1)-C(1)#11 | 179(3) |
| O(2)-P(1)-O(3) | 108.2(5) | C(1)#9-N(1)-C(1)#11 | 66.1(12) |
| O(4)-P(1)-O(3) | 109.1(5) | C(1)-N(1)-C(1)#11 | 101(2) |
| O(2)-P(1)-O(1) | 107.1(4) | C(1)#10-N(1)-C(1)#11 | 79(2) |
| O(4)-P(1)-O(1) | 111.2(5) | C(1)#6-N(1)-C(1)#12 | 101(2) |
| O(3)-P(1)-O(1) | 110.0(4) | C(1)#7-N(1)-C(1)#12 | 79(2) |
| O(3)#1-Al(1)-O(4)#2 | 110.8(4) | C(1)#8-N(1)-C(1)#12 | 66.1(12) |
| O(3)#1-Al(1)-O(1) | 109.6(4) | C(1)#9-N(1)-C(1)#12 | 179(3) |
| O(4)#2-Al(1)-O(1) | 109.8(4) | C(1)-N(1)-C(1)#12 | 115(3) |
| O(3)#1-Al(1)-O(2)#3 | 105.2(4) | C(1)#10-N(1)-C(1)#12 | 66.1(12) |
| O(4)#2-Al(1)-O(2)#3 | 110.3(4) | C(1)#11-N(1)-C(1)#12 | 113(3) |
| O(1)-Al(1)-O(2)#3 | 111.0(4) | N(1)-C(1)-C(1)#9 | 57.0(6) |
| P(1)-O(1)-Al(1) | 145.5(5) | N(1)-C(1)-C(1)#7 | 57.0(6) |
| P(1)-O(2)-Al(1)#4 | 146.0(5) | C(1)#9-C(1)-C(1)#7 | 90.000(6) |
| P(1)-O(3)-Al(1)#1 | 147.2(5) | N(1)-C(1)-C(2) | 105.4(18) |
| P(1)-O(4)-Al(1)#5 | 151.6(6) | C(1)#9-C(1)-C(2) | 127(2) |
| C(1)#6-N(1)-C(1)#7 | 179(3) | C(1)#7-C(1)-C(2) | 124(2) |
| C(1)#6-N(1)-C(1)#8 | 66.1(12) | N(1)-C(1)-C(3) | 92.7(17) |
| C(1)#7-N(1)-C(1)#8 | 113(3) | C(1)#9-C(1)-C(3) | 64.9(8) |
| C(1)#6-N(1)-C(1)#9 | 79(2) | C(1)#7-C(1)-C(3) | 64.9(8) |
| C(1)#7-N(1)-C(1)#9 | 101(2) | C(2)-C(1)-C(3) | 162(2) |
| C(1)#8-N(1)-C(1)#9 | 115(3) | N(1)-C(1)-C(1)#8 | 50.4(12) |
| C(1)#6-N(1)-C(1) | 113(3) | C(1)#9-C(1)-C(1)#8 | 90.7(15) |
| C(1)#7-N(1)-C(1) | 66.1(12) | C(1)#7-C(1)-C(1)#8 | 89.3(16) |
| C(1)#8-N(1)-C(1) | 79(2) | C(2)-C(1)-C(1)#8 | 55.0(10) |
| C(1)#9-N(1)-C(1) | 66.1(12) | C(3)-C(1)-C(1)#8 | 143.2(12) |
| C(1)#6-N(1)-C(1)#10 | 66.1(12) | C(1)-C(2)-C(1)#8 | 70(2) |
| C(1)#7-N(1)-C(1)#10 | 115(3) | C(1)#9-C(3)-C(1) | 50.1(15) |
| C(1)#8-N(1)-C(1)#10 | 101(2) | C(1)#9-C(3)-C(1)#7 | 74(2) |
| C(1)#9-N(1)-C(1)#10 | 113(3) | C(1)-C(3)-C(1)#7 | 50.1(15) |
| C(1)-N(1)-C(1)#10 | 179(3) | C(1)#9-C(3)-C(1)#11 | 50.1(15) |
| C(1)#6-N(1)-C(1)#11 | 115(3) | C(1)-C(3)-C(1)#11 | 74(2) |
| C(1)#7-N(1)-C(1)#11 | 66.1(12) | C(1)#7-C(3)-C(1)#11 | 50.1(15) |

Table A.12 Anisotropic displacement parameters ($\text{\AA}^2 \times 10^3$) for as-prepared MgAPO(20) STA-14 (KFI). The anisotropic displacement factor exponent takes the form: $-2\pi^2 [h^2 a^{*2} U^{11} + \dots + 2 h k a^* b^* U^{12}]$

| Atom | U ¹¹ | U ²² | U ³³ | U ²³ | U ¹³ | U ¹² |
|-------|-----------------|-----------------|-----------------|-----------------|-----------------|-----------------|
| P(1) | 26(2) | 7(1) | 8(1) | -1(1) | 2(1) | -7(1) |
| Al(1) | 13(2) | 12(2) | 11(2) | 0(1) | -2(1) | 0(1) |
| O(1) | 22(4) | 18(4) | 17(4) | 0(3) | 4(3) | -15(3) |
| O(2) | 33(4) | 11(4) | 25(5) | 10(3) | 2(4) | 5(3) |
| O(3) | 42(5) | 27(4) | 15(4) | -11(4) | 9(4) | -16(4) |
| O(4) | 31(5) | 11(4) | 26(4) | -4(3) | 8(3) | 12(3) |

Table A.13 *Crystal data and structure refinement for as-prepared novel MgAPO layer phase.*

| | |
|-----------------------------------|---|
| Empirical formula | C ₂₁ H ₁₂ Al ₁₂ N ₄ O ₂₄ P ₉ Si ₃ |
| Formula weight | 1391.11 |
| Temperature | 173(2) K |
| Wavelength | 1.54178 Å |
| Crystal system | Monoclinic |
| Space group | P 2 (b) |
| Unit cell dimensions | $a = 16.485(6)$ Å $\alpha = 90^\circ$. $b = 5.3775(18)$ Å $\beta = 100.809(16)^\circ$. $c = 9.324(3)$ Å $\gamma = 90^\circ$. |
| Volume | 811.9(5) Å ³ |
| Z | 1 |
| Density (calculated) | 2.845 Mg/m ³ |
| Absorption coefficient | 9.897 mm ⁻¹ |
| F(000) | 691 |
| Crystal size | 0.10 x 0.10 x 0.01 mm ³ |
| Theta range for data collection | 5.46 to 67.28°. |
| Index ranges | -19 ≤ h ≤ 19, -6 ≤ k ≤ 6, -11 ≤ l ≤ 11 |
| Reflections collected | 9249 |
| Independent reflections | 1426 [R(int) = 0.2761] |
| Completeness to theta = 25.00° | 99.2 % |
| Absorption correction | multiscan |
| Max. and min. transmission | 0.9075 and 0.4377 |
| Refinement method | Full-matrix least-squares on F ² |
| Data / restraints / parameters | 1426 / 2 / 50 |
| Goodness-of-fit on F ² | 1.779 |
| Final R indices [I > 2σ(I)] | R1 = 0.2581, wR2 = 0.5277 |
| R indices (all data) | R1 = 0.3272, wR2 = 0.5877 |
| Largest diff. peak and hole | 2.659 and -0.911 e.Å ⁻³ |

Table A. 14 Atomic coordinates ($\times 10^4$) and equivalent isotropic displacement parameters ($\text{\AA}^2 \times 10^3$) for as-prepared novel MgAPO layer phase. $U(eq)$ is defined as one third of the trace of the orthogonalised U^{ij} tensor.

| Atom | x | y | z | U(eq) |
|-------|-----------|-----------|------------|---------|
| P(1) | 8953(2) | -25(7) | 6321(4) | 40(1) |
| Al(1) | 10986(2) | 11(9) | 6992(4) | 42(2) |
| O(1) | 9903(5) | 68(16) | 6628(9) | 37(2) |
| O(2) | 8639(6) | -47(18) | 4688(11) | 49(3) |
| O(3) | 8636(6) | -2217(19) | 7044(10) | 50(3) |
| O(4) | 8636(6) | 2358(19) | 6949(11) | 51(3) |
| P(2) | 14381(13) | -30(40) | 8190(20) | 73(5) |
| C(1) | 14040(20) | 340(70) | 9800(30) | 29(12) |
| C(2) | 14467(15) | -1140(70) | 10920(30) | 55(16) |
| C(3) | 14069(18) | -2070(60) | 11990(30) | 24(10) |
| C(4) | 13241(17) | -1520(60) | 11950(30) | 32(12) |
| C(5) | 12812(14) | -40(70) | 10840(30) | 22(9) |
| C(6) | 13211(19) | 890(60) | 9760(20) | 50(15) |
| C(7) | 13990(40) | 2570(70) | 7240(60) | 48(16) |
| O(21) | 10980(60) | -500(200) | 10290(110) | 100(30) |

Table A.15 Bond lengths (Å) and angles (°) for as-prepared novel MgAPO layer phase.

| | | | |
|----------------|-----------|---------------------|-----------|
| P(1)-O(3) | 1.500(11) | O(4)-P(1)-O(1) | 107.9(6) |
| P(1)-O(2) | 1.513(10) | O(1)-Al(1)-O(3)#1 | 109.1(5) |
| P(1)-O(4) | 1.540(11) | O(1)-Al(1)-O(2)#2 | 109.7(5) |
| P(1)-O(1) | 1.540(8) | O(3)#1-Al(1)-O(2)#2 | 106.6(5) |
| Al(1)-O(1) | 1.754(8) | O(1)-Al(1)-O(4)#3 | 111.0(5) |
| Al(1)-O(3)#1 | 1.791(12) | O(3)#1-Al(1)-O(4)#3 | 109.7(5) |
| Al(1)-O(2)#2 | 1.789(11) | O(2)#2-Al(1)-O(4)#3 | 110.6(5) |
| Al(1)-O(4)#3 | 1.780(12) | P(1)-O(1)-Al(1) | 177.1(7) |
| O(2)-Al(1)#2 | 1.789(10) | P(1)-O(2)-Al(1)#2 | 140.5(7) |
| O(3)-Al(1)#3 | 1.791(12) | P(1)-O(3)-Al(1)#3 | 139.7(7) |
| O(4)-Al(1)#1 | 1.780(12) | P(1)-O(4)-Al(1)#1 | 140.3(7) |
| P(2)-C(7) | 1.711(10) | C(7)-P(2)-C(1) | 102(2) |
| P(2)-C(1) | 1.717(10) | C(7)-P(2)-C(3)#4 | 109(3) |
| P(2)-C(3)#4 | 1.93(9) | C(1)-P(2)-C(3)#4 | 120(2) |
| P(2)-C(2)#5 | 2.03(7) | C(7)-P(2)-C(2)#5 | 101(3) |
| C(1)-C(2) | 1.3900 | C(1)-P(2)-C(2)#5 | 92.2(16) |
| C(1)-C(6) | 1.3900 | C(3)#4-P(2)-C(2)#5 | 128(5) |
| C(2)-C(3) | 1.3900 | C(2)-C(1)-C(6) | 120.0 |
| C(2)-P(2)#5 | 2.03(4) | C(2)-C(1)-P(2) | 113(2) |
| C(3)-C(4) | 1.3900 | C(6)-C(1)-P(2) | 119(2) |
| C(3)-P(2)#6 | 1.93(3) | C(1)-C(2)-C(3) | 120.0 |
| C(4)-C(5) | 1.3900 | C(1)-C(2)-P(2)#5 | 115.9(18) |
| C(5)-C(6) | 1.3900 | C(3)-C(2)-P(2)#5 | 110.3(18) |
| | | C(4)-C(3)-C(2) | 120.0 |
| O(3)-P(1)-O(2) | 111.4(6) | C(4)-C(3)-P(2)#6 | 109.9(19) |
| O(3)-P(1)-O(4) | 108.1(6) | C(2)-C(3)-P(2)#6 | 127(2) |
| O(2)-P(1)-O(4) | 108.2(6) | C(3)-C(4)-C(5) | 120.0 |
| O(3)-P(1)-O(1) | 111.7(6) | C(6)-C(5)-C(4) | 120.0 |
| O(2)-P(1)-O(1) | 109.4(5) | C(5)-C(6)-C(1) | 120.0 |

Appendix B

Rietveld Refinement Data

In this Appendix atomic coordinates and temperature factors obtained for Rietveld refinement of powder X-ray diffraction are presented for calcined SAPO(20) materials STA-7 and STA-14 and the as-prepared AlPO STA-2 templated with DABCO_C4. Selected bond lengths and angles are also given.

Table B.1 Atomic coordinates and thermal parameters for calcined SAPO(20) STA-7 (SAV) from Rietveld profile refinement of powder X-ray diffraction data in space group $P4-n$ ($R_{wp} = 7.8\%$ and $R_p = 5.4\%$), with lattice parameters $a = 18.6931(7) \text{ \AA}$ and $c = 9.4191(5) \text{ \AA}$.

| Atom | x | y | z | Occ. | $U_{iso} (\text{\AA}^2)$ |
|------|------------|-------------|-------------|------|--------------------------|
| P1 | 1.0677(11) | -0.1669(8) | 0.0964(19) | 1.00 | 0.020(2) |
| P2 | 0.8385(9) | -0.0556(9) | -0.1526(21) | 1.00 | 0.020(2) |
| P3 | 0.9478(10) | 0.0650(10) | 0.3377(23) | 1.00 | 0.020(2) |
| Al1 | 0.8395(10) | 0.0644(12) | 0.0826(22) | 1.00 | 0.020(2) |
| Al2 | 0.6678(10) | -0.0424(9) | -0.1566(23) | 1.00 | 0.020(2) |
| Al3 | 1.0677(11) | -0.0526(11) | 0.3338(24) | 1.00 | 0.020(2) |
| O1 | 0.8803(14) | 0.0525(19) | 0.2452(27) | 1.00 | 0.020(2) |
| O2 | 0.9825(12) | 0.1398(12) | 0.2983(26) | 1.00 | 0.020(2) |
| O3 | 0.7571(10) | -0.0632(11) | -0.1837(22) | 1.00 | 0.020(2) |
| O4 | 0.8428(15) | -0.0209(12) | -0.0106(25) | 1.00 | 0.020(2) |
| O5 | 0.9894(13) | -0.0023(10) | 0.3141(23) | 1.00 | 0.020(2) |
| O6 | 1.0624(20) | -0.1326(13) | 0.2376(23) | 1.00 | 0.020(2) |
| O7 | 0.8824(10) | -0.1264(10) | -0.1639(23) | 1.00 | 0.020(2) |
| O8 | 0.9300(18) | 0.0786(16) | 0.4894(24) | 1.00 | 0.020(2) |
| O9 | 1.1369(12) | -0.1394(14) | 0.018(4) | 1.00 | 0.020(2) |
| O10 | 1.0730(10) | -0.1517(9) | 0.1123(21) | 1.00 | 0.020(2) |
| O11 | 1.0001(12) | -0.1476(15) | 0.0030(24) | 1.00 | 0.020(2) |
| O12 | 0.8664(15) | -0.0057(14) | -0.2761(28) | 1.00 | 0.020(2) |

Table B.2 *Selected bond lengths for calcined SAPO(20) STA-7 (SAV).*

| Atom-Atom | Distance (Å) | Atom-Atom | Distance (Å) |
|-----------|--------------|-----------|--------------|
| P1-O6 | 1.479(19) | Al1-O1 | 1.725(19) |
| P1-O9 | 1.575(19) | Al1-O4 | 1.821(20) |
| P1-O10 | 1.595(20) | Al1-O9 | 1.749(19) |
| P1-O11 | 1.582(20) | Al1-O10 | 1.673(24) |
| P2-O3 | 1.556(18) | Al2-O2 | 1.819(26) |
| P2-O4 | 1.489(19) | Al2-O3 | 1.733(18) |
| P2-O7 | 1.562(20) | Al2-O7 | 1.605(25) |
| P2-O12 | 1.580(20) | Al2-O11 | 1.742(26) |
| P3-O1 | 1.551(18) | Al3-O5 | 1.749(19) |
| P3-O21 | 1.586(19) | Al3-O6 | 1.752(19) |
| P3-O5 | 1.497(18) | Al3-O8 | 1.735(19) |
| P3-O8 | 1.489(18) | Al3-O12 | 1.732(20) |

Table B.3 *Selected angles for calcined SAPO(20) STA-7 (SAV), continued on next page.*

| O-T-O | Angle (°) | O-T-O | Angle (°) | O-T-O | Angle (°) |
|------------|-----------|-----------|-----------|----------|-----------|
| O6-P1-O9 | 109.4(20) | O3-P2-O4 | 105.2(16) | O1-P3-O2 | 109.5(19) |
| O6-P1-O10 | 110.5(17) | O3-P2-O7 | 115.0(16) | O1-P3-O5 | 102.3(17) |
| O6-P1-O11 | 110.3(19) | O3-P2-O12 | 103.8(16) | O1-P3-O8 | 112.6(19) |
| O9-P1-O10 | 108.6(16) | O4-P2-O7 | 113.7(18) | O2-P3-O5 | 119.6(17) |
| O9-P1-O11 | 108.8(16) | O4-P2-O12 | 112.8(19) | O2-P3-O8 | 99.5(19) |
| O10-P1-O11 | 109.2(17) | O7-P2-O12 | 106.0(17) | O5-P3-O8 | 113.7(18) |

Table B.3 Selected angles for calcined SAPO(20) STA-7 (SAV), continuation.

| O-T-O | Angle (°) | O-T-O | Angle (°) | O-T-O | Angle (°) |
|--------------|------------------|--------------|------------------|--------------|------------------|
| O1-Al1-O4 | 107.4(16) | O2-Al2-O3 | 107.9(14) | O5-Al3-O6 | 110.9(17) |
| O1-Al1-O90 | 118.4(18) | O2-Al2-O7 | 111.7(15) | O5-Al3-O8 | 105.8(15) |
| O1-Al1-O10 | 107.3(16) | O2-Al2-O11 | 106.9(16) | O5-Al3-O12 | 102.9(15) |
| O4-Al1-O9 | 115.5(17) | O3-Al2-O7 | 105.1(14) | O6-Al3-O8 | 105.1(16) |
| O4-Al1-O10 | 101.4(16) | O3-Al2-O11 | 116.0(17) | O6-Al3-O12 | 114.5(17) |
| O9-Al1-O10 | 105.2(15) | O7-Al2-O11 | 109.4(15) | O8-Al3-O12 | 117.4(17) |

Table B.4 Atomic coordinates and thermal parameters for calcined SAPO(20) STA-14 (KFI) from Rietveld profile refinement of powder X-ray diffraction data in space group $Pn-3n$ ($R_{wp} = 11.5\%$ and $R_p = 7.4\%$), with lattice parameters $a = 13.03009(11)$ Å.

| Atom | x | y | z | Occ. | U_{iso} (Å²) |
|-------------|------------|------------|-----------|-------------|--|
| P1 | 0.0716(5) | 0.5500(5) | 0.6666(5) | 1.00 | 0.003(1) |
| Al1 | -0.0468(5) | 0.4311(6) | 0.6656(6) | 1.00 | 0.003(1) |
| O1 | 0.1396(7) | 0.5068(10) | 0.6419(8) | 1.00 | 0.012(1) |
| O2 | 0.0055(6) | 0.5088(6) | 0.6542(4) | 1.00 | 0.012(1) |
| O3 | 0.0708(6) | 0.6216(6) | 0.6251(7) | 1.00 | 0.012(1) |
| O4 | 0.0826(5) | 0.5655(5) | 0.7473(8) | 1.00 | 0.012(1) |
| Ow1 | 0.25 | 0.75 | 0.25 | 0.61(2) | 0.05 |
| Ow2 | 0.25 | 0.75 | 0.00 | 0.5692) | 0.05 |

Table B.5 *Selected bond lengths for calcined SAPO(20) STA-14 (KFI).*

| Atom-Atom | Distance (Å) |
|-----------|--------------|
| P1-O1 | 1.580(14) |
| P1-O2 | 1.478(13) |
| P1-O3 | 1.550(14) |
| P1-O4 | 1.553(13) |
| Al1-O1 | 1.766(15) |
| Al1-O2 | 1.766(14) |
| Al1-O3 | 1.684(15) |
| Al1-O4 | 1.689(13) |

Table B.6 *Selected angles for calcined SAPO(20) STA-14 (KFI).*

| O-T-O | Angle (°) |
|-----------|-----------|
| O1-P1-O2 | 111.3(9) |
| O1-P1-O3 | 107.7(11) |
| O1-P1-O4 | 105.9(8) |
| O2-P1-O3 | 111.5(8) |
| O2-P1-O4 | 111.2(7) |
| O3-P1-O4 | 109.1(8) |
| O1-Al1-O2 | 106.9(8) |
| O1-Al1-O3 | 110.0(10) |
| O1-Al1-O4 | 105.5(8) |
| O2-Al1-O3 | 116.2(8) |
| O2-Al1-O4 | 110.9(7) |
| O3-Al1-O4 | 106.8(7) |

Table B.7 Atomic coordinates and thermal parameters for as-prepared AlPO STA-2 (SAT) templated with DABCO_C4 from Rietveld profile refinement of powder X-ray diffraction data in space group $R\bar{3}$ ($R_{wp} = 11.16\%$ and $R_p = 8.6\%$), with lattice parameters $a = 13.03007(11)$ Å, $c = 29.53413(26)$.

| Atom | x | y | z | Occ. | U_{iso} (Å ²) |
|------|------------|------------|-------------|----------|-----------------------------|
| P1 | 0.5731(6) | 0.9078(6) | 0.11405(30) | 1.00 | 0.0273(9) |
| P2 | 0.7601(7) | 0.0041(6) | 0.29581(29) | 1.00 | 0.0273(9) |
| Al1 | 0.7560(7) | 0.7629(8) | 0.29278(30) | 1.00 | 0.0273(9) |
| Al2 | 0.5678(7) | 0.9023(6) | 0.21912(32) | 1.00 | 0.0273(9) |
| O1 | 0.6037(10) | 0.9393(9) | 0.16415(29) | 1.00 | 0.0270(14) |
| O2 | 0.5258(7) | 0.7524(5) | 0.22476(35) | 1.00 | 0.0270(14) |
| O3 | 0.7981(7) | 0.9101(7) | 0.2927(4) | 1.00 | 0.0270(14) |
| O4 | 0.4630(7) | 0.9392(7) | 0.23182(32) | 1.00 | 0.0270(14) |
| O5 | 0.6876(8) | 0.9909(10) | 0.2526(4) | 1.00 | 0.0270(14) |
| O6 | 0.8633(8) | 0.1248(5) | 0.29663(35) | 1.00 | 0.0270(14) |
| O7 | 0.6783(12) | 0.9880(9) | 0.3347(4) | 1.00 | 0.0270(14) |
| O8 | 0.6564(9) | 0.0322(8) | 0.09265(32) | 1.00 | 0.0270(14) |
| Ow | 0.3333 | 0.6666 | 0.0288(27) | 0.189(5) | 0.0250 |
| O(A) | 0.1900(32) | 0.493(4) | 0.0550(14) | 0.257(5) | 0.0250 |
| O(B) | 0.348(6) | 0.507(6) | 0.0209(28) | 0.138(5) | 0.0250 |
| N1 | 0.33924 | 0.70201 | 0.85309 | 0.1666 | 0.04614 |
| N2 | 0.33615 | 0.64476 | 0.77184 | 0.1666 | 0.04614 |
| N3 | 0.33720 | 0.68659 | 0.56195 | 0.1666 | 0.04614 |
| N4 | 0.33413 | 0.62925 | 0.48071 | 0.1666 | 0.04614 |
| C1 | 0.32437 | 0.58109 | 0.84993 | 0.1666 | 0.04614 |
| C2 | 0.31798 | 0.54482 | 0.80141 | 0.1666 | 0.04614 |
| C3 | 0.23982 | 0.67367 | 0.78076 | 0.1666 | 0.04614 |
| C4 | 0.23826 | 0.70172 | 0.82999 | 0.1666 | 0.04614 |
| C5 | 0.45274 | 0.78798 | 0.83139 | 0.1666 | 0.04614 |
| C6 | 0.45341 | 0.75180 | 0.78301 | 0.1666 | 0.04614 |
| C7 | 0.33316 | 0.60438 | 0.72573 | 0.1666 | 0.04614 |
| C8 | 0.33632 | 0.64061 | 0.64404 | 0.1666 | 0.04614 |

| C9 | 0.34017 | 0.72701 | 0.60806 | 0.1666 | 0.04614 |
|-------------|----------|----------|----------|-------------|--|
| Atom | x | y | z | Occ. | U_{iso} (Å²) |
| C10 | 0.43334 | 0.65739 | 0.55307 | 0.1666 | 0.04614 |
| C11 | 0.43496 | 0.62932 | 0.50385 | 0.1666 | 0.04614 |
| C12 | 0.22053 | 0.54345 | 0.50238 | 0.1666 | 0.04614 |
| C13 | 0.21982 | 0.57971 | 0.55076 | 0.1666 | 0.04614 |
| C14 | 0.35566 | 0.78661 | 0.53237 | 0.1666 | 0.04614 |
| C15 | 0.34925 | 0.75027 | 0.48386 | 0.1666 | 0.04614 |
| C15 | 0.33683 | 0.69071 | 0.68976 | 0.1666 | 0.04614 |
| H1 | 0.40064 | 0.57967 | 0.86645 | 0.1666 | 0.04614 |
| H2 | 0.24157 | 0.51527 | 0.86738 | 0.1666 | 0.04614 |
| H3 | 0.22976 | 0.46281 | 0.79507 | 0.1666 | 0.04614 |
| H4 | 0.38856 | 0.52150 | 0.79557 | 0.1666 | 0.04614 |
| H5 | 0.15176 | 0.59769 | 0.77088 | 0.1666 | 0.04614 |
| H6 | 0.25465 | 0.75380 | 0.76185 | 0.1666 | 0.04614 |
| H7 | 0.15267 | 0.63289 | 0.84483 | 0.1666 | 0.04614 |
| H8 | 0.24303 | 0.24303 | 0.83427 | 0.1666 | 0.04614 |
| H9 | 0.53009 | 0.79241 | 0.84931 | 0.1666 | 0.04614 |
| H10 | 0.46258 | 0.87847 | 0.83287 | 0.1666 | 0.04614 |
| H11 | 0.52816 | 0.73324 | 0.77785 | 0.1666 | 0.04614 |
| H12 | 0.47139 | 0.82916 | 0.76193 | 0.1666 | 0.04614 |
| H13 | 0.24982 | 0.51656 | 0.72043 | 0.1666 | 0.04614 |
| H14 | 0.40974 | 0.58847 | 0.72025 | 0.1666 | 0.04614 |
| H15 | 0.41631 | 0.62954 | 0.64149 | 0.1666 | 0.04614 |
| H16 | 0.25417 | 0.55149 | 0.64078 | 0.1666 | 0.04614 |
| H17 | 0.42358 | 0.81477 | 0.61337 | 0.1666 | 0.04614 |
| H18 | 0.26367 | 0.74306 | 0.61351 | 0.1666 | 0.04614 |
| H19 | 0.52148 | 0.73322 | 0.56298 | 0.1666 | 0.04614 |
| H20 | 0.41826 | 0.57717 | 0.57198 | 0.1666 | 0.04614 |
| H21 | 0.43002 | 0.54111 | 0.49958 | 0.1666 | 0.04614 |
| H22 | 0.52063 | 0.69804 | 0.48904 | 0.1666 | 0.04614 |

| H23 | 0.21055 | 0.45289 | 0.50095 | 0.1666 | 0.04614 |
|-------------|----------|----------|----------|-------------|--|
| Atom | x | y | z | Occ. | U_{iso} (Å²) |
| H24 | 0.14328 | 0.53913 | 0.48444 | 0.1666 | 0.04614 |
| H25 | 0.20158 | 0.50231 | 0.57186 | 0.1666 | 0.04614 |
| H26 | 0.14523 | 0.59853 | 0.55586 | 0.1666 | 0.04614 |
| H27 | 0.44399 | 0.86848 | 0.53872 | 0.1666 | 0.04614 |
| H28 | 0.28526 | 0.81019 | 0.53818 | 0.1666 | 0.04614 |
| H29 | 0.43211 | 0.81597 | 0.46641 | 0.1666 | 0.04614 |
| H30 | 0.27307 | 0.75184 | 0.46732 | 0.1666 | 0.04614 |
| H31 | 0.25678 | 0.70167 | 0.69232 | 0.1666 | 0.04614 |
| H32 | 0.41893 | 0.77988 | 0.69300 | 0.1666 | 0.04614 |

Table B.8 *Selected bond lengths for as-prepared AlPO STA-2 templated with DABCO_C4 (SAT).*

| Atom-Atom | Distance (Å) | Atom-Atom | Distance (Å) |
|------------------|---------------------|------------------|---------------------|
| P1-O1 | 1.534(7) | Al1-O3 | 1.711(7) |
| P1-O2 | 1.527(10) | Al1-O6 | 1.739(9) |
| P1-O4 | 1.583(10) | Al1-O7 | 1.682(6) |
| P1-O8 | 1.564(7) | Al1-O8 | 1.700(9) |
| P2-O3 | 1.536(7) | Al2-O1 | 1.692(7) |
| P2-O5 | 1.546(7) | Al2-O2 | 1.764(7) |
| P2-O6 | 1.472(7) | Al2-O4 | 1.701(7) |
| P2-O7 | 1.509(7) | Al2-O5 | 1.715(7) |
| P2-O(B) | 1.99(8) | Al2-O(A) | 2.04(4) |

Table B.9 *Selected angles for as-prepared AlPO STA-2 templated with DABCO_C4 (SAT).*

| O-T-O | Angle (°) | O-T-O | Angle (°) |
|--------------|------------------|--------------|------------------|
| O1-P1-O2 | 107.6(8) | O3-Al1-O6 | 113.0(7) |
| O1-P1-O4 | 107.6(8) | O3-Al1-O7 | 116.2(6) |
| O1-P1-O8 | 99.2(7) | O3-Al1-O8 | 106.8(8) |
| O2-P1-O4 | 110.4(5) | O6-Al1-O7 | 108.3(7) |
| O2-P1-O8 | 116.3(8) | O6-Al1-O8 | 103.3(6) |
| O4-P1-O8 | 114.5(8) | O7-Al1-O8 | 108.4(7) |
| O3-P2-O5 | 106.5(7) | O1-Al2-O2 | 107.2(7) |
| O3-P2-O6 | 111.5(7) | O1-Al2-O4 | 106.1(7) |
| O3-P2-O7 | 115.0(7) | O1-Al2-O5 | 109.4(7) |
| O3-P2-O(B) | 68.0(19) | O1-Al2-O(A) | 163.5(12) |
| O5-P2-O6 | 108.3(7) | O2-Al2-O4 | 116.5(7) |
| O5-P2-O7 | 105.3(7) | O2-Al2-O5 | 111.5(6) |
| O5-P2-O(B) | 167.5(21) | O2-Al2-O(A) | 71.4(12) |
| O6-P2-O7 | 109.9(8) | O4-Al2-O5 | 105.8(8) |
| O6-P2-O(B) | 84.2(20) | O4-Al2-O(A) | 62.1(11) |
| O7-P2-O(B) | 68.9(18) | O5-Al2-O(A) | 85.5(11) |

Appendix C

Deconvoluted Intensities of MAS NMR Spectra

C.1 ^{31}P MAS NMR in AlPO STA-2 (QuinC4)

Table C.1 Deconvoluted intensities of ^{31}P MAS NMR of AlPO STA-2, templated with QuinC4.

| Curve | ppm | % |
|-------|-------|------|
| 1 | −30.8 | 22.0 |
| 2 | −26.5 | 37.9 |
| 3 | −21.7 | 19.1 |
| 4 | −12.8 | 15.9 |
| 5 | −5.2 | 3.9 |
| 6 | 0.3 | 1.2 |

C.2 ^{31}P MAS NMR in AlPO STA-2 (DABCO_C4)

Table C.2 Deconvoluted intensities of ^{31}P MAS NMR of AlPO STA-2, templated with DABCO_C4.

| Curve | ppm | % |
|-------|-------|------------------|
| 1 | −31.2 | 17.8 |
| 2 | −26.3 | 25.6 |
| 3 | −23.3 | 40.6 |
| 4 | −10.7 | 15.4 |
| 5 | −3.2 | 0.4 |
| 6 | 0.4 | 0.3 _o |

Appendix D

Experimental Conditions for Applications Described in Section 7.3

D.1 Experimental Procedure for Argon Isotherms

The samples were submitted to evacuation at 300 °C for 12 hours in a glass burette equipped with a seal-frit attachment to prevent any contact of the clean sample with the atmosphere.

The free spaces of the burette were calculated from the Helium expansion at room temperature (total free volume) and at 87 K (cold free volume). Prior to start the Argon isotherm, any occluded He filling the micropores of the zeotypes was removed by 'in-situ' evacuation at 200 °C for 2 hours. Then, the Argon isotherm was measured at 87.3 K (liquid Argon temperature). The high-resolution part of the isotherm (ultra-low and low pressure region) was constructed by adding 1 STP cm³/g for each point. After dosing this volume, equilibrium time was taking by continuously monitoring the pressure drop. It was consider that the equilibrium was reached when the pressure drop was less than 3% or 3 mbar (the most restrictive condition is always taken) during 10 minutes. Typically, over hundred points at relative pressures below 0.3, which allow plotting and calculating with enough accuracy the isotherm and the H-K micropore distribution. Above 0.3 P/Po, the isotherm is plot by taking points at targeted pressures and the required volumes to reach this pressure are dosing by following the same equilibrium criteria than below.

D.2 Experimental Procedure for MTO Reaction

Characterisation

Powder X-ray diffraction (XRD) patterns were measured on a PANalytical X'Pert diffractometer with an X'Celerator detector. Data were collected with a fixed divergence slit (0.50°) and Soller slits (incident and diffracted = 0.04°) and Cu K_α radiation.

Acidic properties of the SAPO molecular sieves were determined by temperature programmed desorption (TPD) of preadsorbed ammonia. The experiments were carried out in a home-made TPD instrument equipped with a thermal conductivity detector

(TCD). A sample of ca. 0.1 g was activated in flowing He ($100 \text{ cm}^3 \cdot \text{min}^{-1}$) at 550°C for 2 hours. Then, ammonia pulses were injected to the sample at 150°C for 0.5h. The treated sample was subsequently purged with He at the same temperature for 1 h to remove physisorbed ammonia. Finally, the TPD profile was obtained in flowing He ($100 \text{ cm}^3 \cdot \text{min}^{-1}$) from 150 to 650°C with a temperature ramp of $10^\circ\text{C} \cdot \text{min}^{-1}$.

Thermogravimetric analyses (TGA) were performed in air on an EXSTAR 6000 thermal analyzer, where the weight loss related to the combustion of coke deposits formed during MTO was further confirmed by differential thermal analyses (DTA) using the same analyzer.

The coke deposits formed on the SAPO catalysts after 90 min of MTO at 350°C were characterized by UV-Visible spectroscopy. The used catalysts was completely dissolved by 10% HF solutions and then neutralized with K_2CO_3 . CCl_4 (Aldrich, 99.5%) was employed to extract the organic species from the resulting solution, and water in the organic phase was removed by adding a small amount of Na_2SO_4 that was subsequently recovered using an Advantec DISMIC-13JP syringe filter. The spectra of extracted organic phases were recorded on an Agilent 8453 UV-Visible spectrophotometer, using CCl_4 as a reference.

Catalysis

A conventional continuous-flow microreactor was used to carry out the MTO reaction over various SAPO molecular sieves at atmospheric pressure. Prior to the experiments, the catalyst was routinely activated under flowing N_2 ($50 \text{ cm}^3 \cdot \text{min}^{-1}$) at 550°C for 2 hours and kept at 350°C to establish a standard operating procedure, allowing time for the product distribution to stabilize. Then, methanol vapor was fed at a rate of $0.085 \text{ cm}^3 \cdot \text{h}^{-1}$ ($\text{WHSV} = 0.67 \text{ h}^{-1}$) into the reactor containing 0.1 g of catalyst at the same temperature. The total gas flow at the reactor inlet was kept constant at $50 \text{ cm}^3 \cdot \text{min}^{-1}$. The reaction products were analyzed on-line in a Varian CP-3800 gas chromatograph equipped with a CP-PoraPLOT Q capillary column (0.25 mm x 25 m) and a flame ionization detector (FID), with the first analysis carried out after 5 min on stream. CO_2 was separated using a

packed Carbosphere column and analyzed with a TCD. The conversion of methanol was defined as the percentage of methanol consumed during the MTO reaction. Dimethylether was not considered as a product. The yield of each product was calculated as the percentage of the amount (in mole) of methanol used in obtaining it to the amount of methanol fed.